



Politecnico di Milano
Mechanical Department
Doctoral programme in Mechanical Engineering

Rapid tools in sheet metal forming processes

Doctoral Dissertation of:
Lorenzo Iorio

Supervisor:

Prof. Matteo Strano

Tutor:

Prof. Mario Guagliano

The Chair of the Doctoral Program:

Prof. Daniele Rocchi

Year 2018 – Cycle XXX

Table of contents

Abstract	1
1. State of the art	5
1.1 Introduction	5
1.2 Rigid Tools Processes.....	6
1.2.1 Deep drawing.....	6
1.2.1.1 Description of the tools setup	6
1.2.1.2 Process parameters	7
1.2.2 Tube bending	8
1.2.3 Air bending	11
1.2.4 Rigid tools: Advantages and disadvantages.....	11
1.3 Deformable tools processes.....	12
1.3.1 Fluid based processes	12
1.3.2 Rubber pad forming.....	14
1.3.2.1 Guerin process.....	14
1.3.2.2 Marform process.....	17
1.3.3 Deformable tools: Advantages and disadvantages	17
1.4 Choice of the tools materials	18
1.5 Rapid tools	21
1.5.1 Indirect tooling	22
1.5.1.1 Soft Tooling: silicon moulds	23
1.5.1.2 Soft Tooling: epoxy moulds	24
1.5.1.3 Hard tooling: spray metal tooling.....	24
1.5.1.4 Hard tooling: electroformed tooling.....	25
1.5.1.5 Hard tooling: cast metal tooling	26
1.5.1.6 Hard tooling: KelTool tooling.....	26
1.5.2 Direct tooling	27
1.5.2.1 Resin tools	27
1.5.2.2 Stereolithography tooling	28
1.5.2.3 FDM tooling	29

1.5.2.4 Laminated Tooling.....	30
1.6 Conclusion	31
1.7 References.....	34
2. Polymeric materials.....	37
2.1 Introduction.....	37
2.2 Classification	39
2.3 Material tests	43
2.3.1 Tensile tests.....	43
2.3.2 Compression tests	47
2.4 FEM simulation of the compression test	52
2.4.1 Geometry and boundary conditions	52
2.4.2 Material properties.....	54
2.4.3 Simulations results	55
2.5 References.....	58
3. Rapid tools in stamping process	59
3.1 Introduction.....	59
3.2 Case study 1: simple component	60
3.2.1 Experimental setup.....	60
3.2.2 Experimental plan and results	66
3.2.3 FEM model	71
3.2.3.1 Mesh and geometry.....	71
3.2.3.2 Material properties	75
3.2.3.3 Boundary conditions	76
3.2.3.4 Validation.....	79
3.2.4 Compensation algorithm	85
3.2.4.1 Main compensation algorithm methods	85
3.2.4.2 Description of the compensation algorithm	88
3.2.4.3 Application of the compensation algorithm on the case 1	93
3.3 Case study 2: complex industrial component	98
3.3.1 Experimental setup.....	98
3.3.2 Experimental plan and results	104
3.3.3 FEM model	106
3.3.3.1 Mesh and geometry.....	106

3.3.3.2	Material properties	107
3.3.3.3	Boundary conditions	108
3.3.3.4	Validation	111
3.3.3.5	Compensation algorithm results	113
3.4	Tools life evaluation.....	118
3.4.1	Introduction	118
3.4.2	Experimental setup and plan description.....	119
3.4.3	Experimental results.....	122
3.5	Conclusions	127
3.6	References	128
4.	Rapid tools in air bending process	131
4.1	Introduction	131
4.2	Economical comparison	132
4.3	Experimental plan and tools setup	135
4.4	Experimental results	140
4.5	FEM model.....	154
4.5.1	Geometry and mesh.....	154
4.5.2	Material properties.....	157
4.5.3	Boundary conditions.....	166
4.5.4	Simulation results	167
4.6	Conclusions	176
4.7	References	177
5.	Rapid tools in tube bending	179
5.1	Introduction	179
5.2	Brief description of the previous study on rotary draw bending process ...	179
5.3	FEM model with Rapid Tools	180
5.3.1	Geometry and mesh.....	180
5.3.2	Material properties.....	182
5.3.3	Boundary conditions.....	183
5.4	Comparison of the results between rigid and deformable tools setup.....	185
5.5	Design improvement.....	191
5.6	Conclusions	196
5.7	References.....	197

Conclusions	199
Appendix A	203
A-1. Tensile Tests results of polyurethane material	203
A-2. Compression Tests results of polyurethane material.....	212
Appendix B.....	227
B-1. Description of the local 2D offset	227
Appendix C	231
C-1. Tensile Tests results of metal specimens used in the bending experiments 231	
C-2. Plan designed for sheet metal bending experiments.....	245
C-3. Statistical analysis of experimental data with metal tools	246

List of figures

Figure 1. 1: Scheme of traditional deep drawing process.	7
Figure 1. 2: schematic example of drawbead.	7
Figure 1. 3: nomogram used for evaluate the ratio D/t	9
Figure 1. 4: nomogram used for choosing the best curvature method.	9
Figure 1. 5: schemes of the described tube bending processes: rotary draw (a), compression (b), roll (c) and push (d) bending.	10
Figure 1. 6: scheme of the air bending process.	11
Figure 1. 7: scheme of aquadraw (a) and Hydroforming process (b).	13
Figure 1. 8: scheme of the flexforming process.	13
Figure 1. 9: scheme of Guerin process.	15
Figure 1. 10: typical shape realized by Guerin process.	16
Figure 1. 11: scheme (a) and practical example of Guerin process (b).	16
Figure 1. 12: scheme of the Marform process.	17
Figure 1. 13: minimization of Machining Energy and Price of for the materials used in tools manufacturing.	19
Figure 1. 14: comparison between Yield strength and Fatigue Strength	20
Figure 1. 15: comparison between Young's modulus and Poisson's ratio.	21
Figure 1. 16: classification of rapid tooling techniques [26].	22
Figure 1. 17: example of silicon moulds [28].	23
Figure 1. 18: industrial example of epoxy moulds [31].	24
Figure 1. 19: metal spray process [32].	25
Figure 1. 20: process stages in electroforming.	25
Figure 1. 21: example of shell mould obtained by electrodeposition [34].	26
Figure 1. 22: Keltool process steps [35].	27
Figure 1. 23: industrial application of resin tools [43].	28
Figure 1. 24: example of injection mould insert made by STL technology [46].	29
Figure 1. 25: commercial example of hydroforming die made by FDM [47].	30
Figure 1. 26: example of laminated tools with integrated cooling channels [44].	31
Figure 1. 27: schematization of the objective of this research thesis.	33
Figure 2. 1: scheme of a monomer and polymer chain.	37
Figure 2. 2: example of polymers tensile behaviour at different temperatures.	38
Figure 2. 3: torsional pendulum.	39
Figure 2. 4: schematizations of linear (a), pronged (b) and meshed (c) polymers [4].	39

Figure 2. 5: schematizations of amorphous (a), crystalline (b) and semi-crystalline (c) polymers structures [6].....	40
Figure 2. 6: schematizations of different types of monomers chain: static (a), alternated (b), segmented (c), grafted (d) [8].	40
Figure 2. 7: example of Thermoplastics (a) and Thermosets (b) materials.....	41
Figure 2. 8: typical mechanical behaviours of thermoplastics (a), reinforced thermoplastics (b) and thermosets materials (c).	42
Figure 2. 9: experimental tensile specimen of Necuron 1300 (red), Necuron 1050 (light green), Necuron 1150 (dark green).....	44
Figure 2. 10: tensile tests machine MTS Alliance RT/100.	45
Figure 2. 11: extensometer used for measuring the displacement of the specimen during the tensile tests.....	45
Figure 2. 12: fracture sections of the Necuron 1050 (left) and Necuron 1150 (right). ..	46
Figure 2. 13: machine used for the compression tests.....	47
Figure 2. 14: extensometer used for compression tests.	47
Figure 2. 15: example of particular collapse phenomena observed during the compression tests for Necuron 1300 (a), 1150 (b) and 1050 (c).	47
Figure 2. 16: Necuron 1050 stress-strain curves resultant from the compression tests.....	49
Figure 2. 17: Necuron 1150 stress-strain curves resultant from the compression tests.....	50
Figure 2. 18: Necuron 1300 stress-strain curves resultant from the compression tests.....	50
Figure 2. 19: Rapid tools design zones.	51
Figure 2. 20: scheme of the compression simulation setup.	52
Figure 2. 21: general schematization of tetrahedral (a), tetrahedral quadratic (b), hexahedral (c) and hexahedral quadratic (d) elements.	53
Figure 2. 22: imposed displacement for the upper plate.	54
Figure 2. 23: Yield stress - plastic strain curves implemented in the compression tests simulations.....	55
Figure 2. 24: comparison of the resultant forces on the upper plate at the end of the experimental and simulated compression test for Necuron 1300.	55
Figure 2. 26: comparison of the resultant forces on the upper plate at the end of the experimental and simulated compression test for Necuron 1150.	56
Figure 2. 27: comparison of the resultant forces on the upper plate at the end of the experimental and simulated compression test for Necuron 1050.	57
Figure 3. 1: geometry of the component for case study 1, dimensions in mm (left) and 3D view (right).....	60
Figure 3. 2: geometrical dimensions of the SACMI PH150 press used for the experimental activities and particular of the rapid tools inside the press.	61

Figure 3. 3: external dimensions (left) and transversal middle section of the stamping die (right).....	62
Figure 3. 4: external dimensions (left) and transversal middle section of the blankholder (right).....	62
Figure 3. 5: external dimensions of the punch.....	62
Figure 3. 6: scheme of the designed plate implemented for the punch.	63
Figure 3. 7: scheme of the designed plate implemented for the blankholder.....	63
Figure 3. 8: scheme of the designed plate implemented for the die (sectioned).....	63
Figure 3. 9: scheme of the entire tool assembly and the stamping direction.	64
Figure 3. 10: milling machine used for making the experimental rapid tools (a) and definition of the finishing operation in the CAM module of Pro-e (b).	64
Figure 3. 11: milling operations of punch (a), die (b), blankholder (c) and finished tools (d).....	65
Figure 3. 12: resume of the economical comparison between metal and rapid tools solutions case 1.	66
Figure 3. 13: blankholder force profiles for experiment 1 to 5 of the experimental plan.	67
Figure 3. 14: repeatability of blankholder force profiles for correspondent experiments.....	68
Figure 3. 15: fractures zone on blank B4 (a) with a detailed view (b).....	68
Figure 3. 16: fractures zone on blank B12 (a) with a detailed view (b).....	69
Figure 3. 17: profiles measuring on the CMM machine (a), and details of the measuring path (b-c).....	69
Figure 3. 18: locations of the deviations between the experimental tests and the designed component (test case 1).	70
Figure 3. 19: distributions of the deviations between the experimental tests and designed component on the profile portion (test case 1).	70
Figure 3. 20: automatic tetra meshing process workflow in Visual Mesh 11 [9].	72
Figure 3. 21: transversal section of the stamping setup at the end of the stamping operation with highlight of the designed end stroke.	73
Figure 3. 22: example of refinement at level 4 [12].	74
Figure 3. 23: schemes of angle criterion (a) and geometrical criterion (b) implemented in PAM-STAMP 2g 2015.1 [12].	74
Figure 3. 24: Scheme of the simulation setup.	75
Figure 3. 25: AL1050-O hardening curve coming from the Krupkowsky constitutive law.....	76
Figure 3. 26: merged nodes at the interface between the rigid middle plate and deformable blankholder.....	77
Figure 3. 27: scheme of the nodes and elements with boundary conditions applied.	78
Figure 3. 28: scheme of the boundary condition applied on the blank in springback step.....	78

Figure 3. 29: FLD of the simulation of test 4-9 compared with experimental results.	80
Figure 3. 30: grid mesh applied on the aluminium blank (a), blank before the deformation (b), stamping result and results of the experimental plan with meshed blanks (d).	81
Figure 3. 31: comparison between simulated (a) and measured (b) engineering major strain maps, simulated (c) and measured (d) engineering minor strain maps for experiment 3.	82
Figure 3. 32: comparison between simulated (a) and measured (b) engineering major strain maps simulated (c) and measured (d) engineering minor strain maps for experiment 4.	82
Figure 3. 33: comparison between simulated (a) and measured (b) engineering major strain maps, simulated (c) and measured (d) engineering minor strain maps for experiment 5.	83
Figure 3. 34: distributions of the numerical error between the experimental tests and simulated components on the profile portion.	84
Figure 3. 35: errors between fem and experimental profile for experiments 3 and 10.	84
Figure 3. 36: experimental vs. fem errors; experimental vs. designed profile deviations.	85
Figure 3. 37: main steps of the DA compensation algorithm: stamping simulation (a), springback analysis (b), calculation of the springback field vector (c), generation of new geometrical tools setup (d).	86
Figure 3. 38: main steps of the FDM compensation algorithm: stamping simulation (a), evaluation of the reaction force acting on the punch (b), application of the reaction forces on mesh product (c), generation of new geometrical tools setup (d). .	87
Figure 3. 39: example of control surface approximating the product geometry [29].	88
Figure 3. 40: blank mesh at the end of springback analysis (left) and successive mesh refinement (right).	89
Figure 3. 41: computation of the new tool nodes position.	91
Figure 3. 42: flow chart of the tool compensation algorithm.	92
Figure 3. 43. δ -plot before compensation; isometric and top views, units in [mm]....	93
Figure 3. 44: major strain maps concentrations on the tools after the stamping simulation with non-compensated tools.	94
Figure 3. 45: minor strain maps concentrations on the tools after the stamping simulation with non-compensated tools.	94
Figure 3. 46: comparison between the compensated and not compensated tools shape, for test case 1.	95
Figure 3. 47: deviations between designed and optimized components after one iteration.	95
Figure 3. 48: FEM reaction force measured on the die before (iteration 0) and after (iteration 1) the compensation.	96

Figure 3. 49: FEM reaction force measured on the punch before (iteration 0) and after (iteration 1) the compensation.....	96
Figure 3. 50: norm of deviation vector vs. iteration.....	97
Figure 3. 51: geometry of the component for case study 2, dimensions in mm (left) and 3D view (right).....	98
Figure 3. 52: deformable tools setup of the test case 2 (left) and schematization of the stamping direction (right).....	99
Figure 3. 53: real view of the die (left) and main dimensions in mm (right).....	99
Figure 3. 54: real view of the blankholder (left) and main dimensions in mm (right).	100
Figure 3. 55: real view of the punch (left) and main dimensions in mm (right).	100
Figure 3. 56: milling operations performed for making the punch.....	101
Figure 3. 57: costs comparison between Miketool (polyurethane) and Zamak2 for making the die in the experimental case.	102
Figure 3. 58: configuration of the clamping tools for die locking (a) and the steel ring used for the blankholder (b).	103
Figure 3. 59: identification of the fracture zone at experiment 7.....	105
Figure 3. 60: distributions of the deviations between the experimental tests and designed component on the profile portion (test case 2).....	105
Figure 3. 61: locations of the deviations between the experimental tests and the designed component (test case 2).	106
Figure 3. 62: scheme of the simulation setup in 3D (upside) and sectioned view (downside).....	107
Figure 3. 63: stress-strain curve resultant form the single compression test performed ton Miketool 1440.....	108
Figure 3. 64: merged nodes at the interface between the punch and the base.	109
Figure 3. 65: scheme of the nodes and elements with boundary conditions applied.	109
Figure 3. 66: node-locking condition chosen by the isostatic PAM-STAMP locking algorithm.....	110
Figure 3. 67: fracture localization - experiment no. 7.....	111
Figure 3. 68: distributions of the numerical error between the experimental and simulated components on the profile portion of the case 2.....	112
Figure 3. 69: deviations comparison for experiment 2 and 3.....	112
Figure 3. 70: δ -plot before compensation; isometric and top views, units in [mm]..	113
Figure 3. 71: minor strain maps concentrations on the tools of the test case 2, after the stamping simulation with non-compensated tools.	114
Figure 3. 72: major strain maps concentrations on the tools of the test case 2, after the stamping simulation with non-compensated tools.	114
Figure 3. 73: comparison between the compensated and not compensated tools shape, for test case 2.	115

Figure 3. 74: deviations between designed and optimized components after one iteration.	115
Figure 3. 75: norm of deviation vector vs. iteration for test case no. 2	116
Figure 3. 76: FLD map of test case no.3 before compensation (a) and after compensation (b).....	116
Figure 3. 77: comparison of the punch upper profile before and after the compensation.	117
Figure 3. 78: General compensation algorithm.	117
Figure 3. 79: Hydraulic testing machine used in fatigue tests (a) and the cylindrical specimen enclosed within the compression plates (b).	119
Figure 3. 80: maximum compensation magnitude imposed by the algorithm.....	120
Figure 3. 81: Von Mises stress values for the die of the case 1, made by Necuron 1050.....	120
Figure 3. 82: Von Mises stress values for the punch of the case 1, made by Necuron 1300.....	121
Figure 3. 83: Von Mises stress values for the die of the case 2, made by Miketool 1440.....	121
Figure 3. 84: specimens deformations at the end of fatigue test performed at upper load level.	122
Figure 3. 85: Force vs Displacement diagram of compression fatigue cycles for Necuron 1150 at load level condition of 48 kN.	123
Figure 3. 86: Force vs Displacement diagram of compression fatigue cycles for Necuron 1050 at load level condition of 35 kN.	123
Figure 3. 87: Force vs Displacement diagram of compression fatigue cycles for Necuron 1300 at load level condition of 41 kN.	123
Figure 3. 88: Force vs Displacement diagram of compression fatigue cycles for Miketool 1440 at load level condition of 51 kN.....	124
Figure 3. 89: specimens deformations resultant at the end of fatigue test performed at mean load level.....	125
Figure 3. 90: Force vs Displacement diagram of compression fatigue cycles for Necuron 1300 at load level condition of 36 kN.	125
Figure 3. 91: Force vs Displacement diagram of compression fatigue cycles for Miketool 1440 at load level condition of 40 kN.....	125
Figure 3. 92: specimens deformations resultant at the end of fatigue test performed at lower load level.....	126
Figure 3. 93: Force vs Displacement diagram of compression fatigue cycles for Necuron 1300 at load level condition of 30 kN.	126
Figure 3. 94: Force vs Displacement diagram of compression fatigue cycles for Miketool 1440 at load level condition of 28 kN.....	127
Figure 4. 1: bending rapid die concept.	133
Figure 4. 2: comparison of the trend of the tools cost respect to the purchase quantities.	134

Figure 4. 3: metal punch P97.88.R08/C (a) used in the experimental activities with the geometrical dimensions (b).....	135
Figure 4. 4: metal die T80.R06.88/C (a) with geometrical dimensions (b).	136
Figure 4. 5: metal frame with nylon insert TN80-14-C (a) with geometrical dimensions of the insert (b).	136
Figure 4. 6: rapid die solution (a) with the geometrical dimensions (b) and the detail of the V-shape cavity of each insert made by Necuron 1050 (c), 1150 (d) and 1300 (e).	138
Figure 4. 7: detail of the MPG45 with the black locking plates (a) and rapid die with the Necuron 1050 insert inside the press brake (b).	138
Figure 4. 8: schematization of the rolling direction and the dimensions of the standard specimen.	139
Figure 4. 9: bend angle results grouped by tools technology.	142
Figure 4. 10: measured bend angle of experiments made by Fe37 with thickness 0.7 mm.	143
Figure 4. 11: measured bend angle of experiments made by Fe37Z with thickness 1 mm.	143
Figure 4. 12: measured bend angle of experiments made by Fe37 with thickness 0.8 mm.	144
Figure 4. 13: normal distribution of the residuals.	145
Figure 4. 14: distribution of the fitted vales versus residuals.	146
Figure 4. 15: interaction plot of the angle versus the rolling direction at different insert materials.	146
Figure 4. 16: interaction plot of the angle versus the thickness at different insert materials.	147
Figure 4. 17: example of aesthetical defects on a specimen bent with metal tool....	147
Figure 4. 18: example of aesthetical defects on a specimen bent with nylon insert (white) tool.	148
Figure 4. 19: specimen 32 bent with rubber tool with no defects.	148
Figure 4. 20: specimen 33 bent with drilled rubber tool with no defects.	148
Figure 4. 21: specimen 41 bent with die Necuron 1050 with no defects.	149
Figure 4. 22: specimen 51 bent with die Necuron 1150 with no defects.	149
Figure 4. 23: specimen 61 bent with die Necuron 1300 with no defects.	149
Figure 4. 24: comparison of the bending zone and the free zone of the Necuron 1050 insert.	150
Figure 4. 25: comparison of the bending zone and the free zone of the Necuron 1150 insert.	151
Figure 4. 26: comparison of the bending zone and the free zone of the Necuron 1300 insert.	151
Figure 4. 27: rubber (a) and rubber drilled (b) dies marked by the punch.	152
Figure 4. 28: nylon die after the experimental activities.	152

Figure 4. 29: trend of the measured bend angle in the repeatability test plan performed with the die insert of Necuron 1050.	153
Figure 4. 30: positioning of the Necuron 1150 (a) and nylon (b) inserts on the platform moved with micrometric slides (c) and the scheme of the measuring operation (d).....	155
Figure 4. 31: main dimensions of the metal tools: punch (a), die (b), metal framework for polyurethane and rubber inserts (c) and framework for nylon insert (d).....	155
Figure 4. 32: measured dimensions of the inserts made by Necuron 1050 (a), 1150 (b), 1300 (c), Rubber (d), drilled rubber (e) and Nylon (f).	156
Figure 4. 33: schematization of the simulations setup with metal tools (a), nylon die (b), rubber die (c), drilled rubber die (d) and Necuron die (e).....	157
Figure 4. 34: blank before (a) the waterjet cutting operation (b) and after (c).	158
Figure 4. 35: tensile specimen dimensions cited in the standard ASTM E8.	159
Figure 4. 36: references for the rolling direction of the tensile specimens.	160
Figure 4. 37: machine (a) and extensometer (b) used for tensile tests.....	160
Figure 4. 38: stress-strain curves resultant from the compression test.....	163
Figure 4. 39: compression stress-strain curves used for calculate the Mooney Rivlin coefficients in PAM-STAMP.....	164
Figure 4. 40: scheme of the compression simulation setup of rubber material.	164
Figure 4. 41. imposed displacement for the upper plate.	165
Figure 4. 42: comparison of the resultant forces on the upper plate at the end of the experimental and simulated compression test for Rubber shore 90A.....	165
Figure 4. 43: scheme of the boundary condition applied on the blank in springback step.....	167
Figure 4. 44: experimental (alfa_exp) and simulated (alfa_fem) comparison for specimen bent by rigid die.....	169
Figure 4. 45: experimental (alfa_exp) and simulated (alfa_fem) comparison for specimen bent by Necuron 1050 insert.	169
Figure 4. 46: experimental (alfa_exp) and simulated (alfa_fem) comparison for specimen bent by Necuron 1150 insert.....	169
Figure 4. 47: experimental (alfa_exp) and simulated (alfa_fem) comparison for specimen bent by Necuron 1300 insert.	170
Figure 4. 48: experimental (alfa_exp) and simulated (alfa_fem) comparison for specimen bent by Nylon insert.....	170
Figure 4. 49: experimental (alfa_exp) and simulated (alfa_fem) comparison for specimen bent by Rubber insert.....	170
Figure 4. 50: experimental (alfa_exp) and simulated (alfa_fem) comparison for specimen bent by drilled Rubber insert.	171
Figure 4. 51: stress map (GPa) of the Necuron 1050 insert at the end of bending operation for specimen Fe37Z.	171
Figure 4. 52: stress map (GPa) of the Necuron 1150 insert at the end of bending operation for specimen Fe37Z.	172

Figure 4. 53: stress map (GPa) of the Necuron 1300 insert at the end of bending operation for specimen Fe37Z.	172
Figure 4. 54: example of the rubber flow inside the metal frame cavity when high sheet metal deformation are performed [15]......	172
Figure 4. 55: displacement map (mm) of the Necuron 1050 insert at the end of bending operation for specimen Fe37Z.	173
Figure 4. 56: displacement map (mm) of the Necuron 1150 insert at the end of bending operation for specimen Fe37Z.	173
Figure 4. 57: displacement map (mm) of the Necuron 1300 insert at the end of bending operation for specimen Fe37Z.	174
Figure 4. 58: stress (GPa) (a) and displacement (mm) (b) maps of the Nylon insert at the end of bending operation for specimen Fe37Z.	174
Figure 4. 59: stress (GPa) (a) and displacement (mm) (b) maps of the Rubber inserts at the end of bending operation for specimen Fe37Z.	175
Figure 5. 1: tube section.	180
Figure 5. 2: case study tools setup (exploded view).	181
Figure 5. 3: Scheme of the tube bending simulation setup.....	181
Figure 5. 4: Rst37-2 hardening curve calculated with the Krupkowsky's constitutive law.....	182
Figure 5. 5: velocity profile applied at the rotational axis of the bend die.	183
Figure 5. 6: elements where the rotational kinematics along the z-axis has been applied.....	183
Figure 5. 7: Locking condition applied on the nodes of the mandrel.....	184
Figure 5. 8: locked nodes belonging to the rear surface of the pressure die.	184
Figure 5. 9: description of the zone on the tube surface.	186
Figure 5. 10: comparison of the extrados thickness profiles between the rigid and deformable cases.	186
Figure 5. 11: Enlarged view of the mandrel at the initial state and during the bending process.....	187
Figure 5. 12: comparison of the intrados thickness profiles between the rigid and deformable cases.	187
Figure 5. 13: FLD diagram of the bent tube in the deformable (a) and rigid (b) cases.	188
Figure 5. 14: distance analysis between the tube bended with rigid tools and the one bended with deformable tools.....	188
Figure 5. 15: schematization of the section at 45° (a) and comparison between the simulated tubes section with the nominal one.....	189
Figure 5. 16: Von Mises stress maps on the pressure die (a), clamp die 1 (b), clam die 2 (c), mandrel (d) and bend die (e).	190
Figure 5. 17: reinforced bed die.	191

Figure 5. 18: Von Mises stress map on the reinforced bend die obtained from the rotary draw bending simulation model with deformable tools.....	192
Figure 5. 19: rubber mandrel.	192
Figure 5. 20: tube FLD diagram of the simulation with rubber mandrel.....	193
Figure 5. 21: rubber membrane (a) dimensions (b).	193
Figure 5. 22: Major stress measured on the tube section along the plane XY.....	194
Figure 5. 23: application of the internal pressure of 120 MPa (a) and schematization of the internal surface modelled with shell elements.....	194
Figure 5. 24: FLD diagram of the tube bent with the pressurized rubber membrane.	195
Figure 5. 25: comparison of the thickness distribution on the tube intrados for rigid, deformable and rubber membrane cases.	195
Figure 5. 26: comparison of the thickness distribution on the tube extrados for rigid, deformable and rubber membrane cases.	196
Figure A- 1: Stress strain curve obtained from tensile tests on specimen Necuron 1050 – T1.	203
Figure A- 2: Stress strain curve obtained from tensile tests on specimen Necuron 1050 – T2.	204
Figure A- 3: Stress strain curve obtained from tensile tests on specimen Necuron 1050 – T3.	205
Figure A- 4: Stress strain curve obtained from tensile tests on specimen Necuron 1150 – T1.	206
Figure A- 5: Stress strain curve obtained from tensile tests on specimen Necuron 1150 – T2.	207
Figure A- 6: Stress strain curve obtained from tensile tests on specimen Necuron 1150 – T3.	208
Figure A- 7: Stress strain curve obtained from tensile tests on specimen Necuron 1300 – T1.	209
Figure A- 8: Stress strain curve obtained from tensile tests on specimen Necuron 1300 – T2.	210
Figure A- 9: Stress strain curve obtained from tensile tests on specimen Necuron 1300 – T3.	211
Figure A- 10: Stress strain curve obtained from compression tests on specimen Necuron 1050 – C1.	212
Figure A- 11: Stress strain curve obtained from compression tests on specimen Necuron 1050 – C2.	213
Figure A- 12: Stress strain curve obtained from compression tests on specimen Necuron 1050 – C2.	214
Figure A- 13: Stress strain curve obtained from compression tests on specimen Necuron 1050 – C4.	215
Figure A- 14: Stress strain curve obtained from compression tests on specimen Necuron 1050 – C5.	216

Figure A- 15: Stress strain curve obtained from compression tests on specimen Necuron 1150 – C1.....	217
Figure A- 16: Stress strain curve obtained from compression tests on specimen Necuron 1150 – C2.....	218
Figure A- 17: Stress strain curve obtained from compression tests on specimen Necuron 1150 – C3.....	219
Figure A- 18: Stress strain curve obtained from compression tests on specimen Necuron 1150 – C4.....	220
Figure A- 19: Stress strain curve obtained from compression tests on specimen Necuron 1150 – C5.....	221
Figure A- 20: Stress strain curve obtained from compression tests on specimen Necuron 1300 – C1.....	222
Figure A- 21: Stress strain curve obtained from compression tests on specimen Necuron 1300 – C2.....	223
Figure A- 22: Stress strain curve obtained from compression tests on specimen Necuron 1300 – C3.....	224
Figure A- 23: Stress strain curve obtained from compression tests on specimen Necuron 1300 – C4.....	225
Figure A- 24: Stress strain curve obtained from compression tests on specimen Necuron 1300 – C5.....	226
Figure B- 1: schematization of the punctual profile offset operation.	227
Figure B- 2: result of the variable offset of the blank profile for the test case 1.....	229
Figure B- 3: result of the variable offset of the blank profile for the test case.....	229
Figure C- 1: Stress strain curve obtained from the tensile test for specimen 1 made by FE37 thickness 0.7 mm.	231
Figure C- 2: Stress strain curve obtained from the tensile test for specimen 2 made by FE37 thickness 0.7 mm.	232
Figure C- 3: Stress strain curve obtained from the tensile test for specimen 3 made by FE37 thickness 0.7 mm.	233
Figure C- 4: Stress strain curve obtained from the tensile test for specimen 4 made by FE37 thickness 0.7 mm.	234
Figure C- 5: Stress strain curve obtained from the tensile test for specimen 5 made by FE37 thickness 0.7 mm.	235
Figure C- 6: Stress strain curve obtained from the tensile test for specimen 6 made by FE37 thickness 0.7 mm.	236
Figure C- 7: Stress strain curve obtained from the tensile test for specimen 7 made by FE37Z thickness 1 mm.	237
Figure C- 8: Stress strain curve obtained from the tensile test for specimen 8 made by FE37Z thickness 1 mm.	238
Figure C- 9: Stress strain curve obtained from the tensile test for specimen 9 made by FE37Z thickness 1 mm.	239

Figure C- 10: Stress strain curve obtained from the tensile test for specimen 10 made by FE37 thickness 0.8 mm. 240

Figure C- 11: Stress strain curve obtained from the tensile test for specimen 11 made by FE37 thickness 0.8 mm. 241

Figure C- 12: Stress strain curve obtained from the tensile test for specimen 12 made by FE37 thickness 0.8 mm. 242

Figure C- 13: Stress strain curve obtained from the tensile test for specimen 13 made by Al thickness 1 mm. 243

Figure C- 14: Stress strain curve obtained from the tensile test for specimen 14 made by Al thickness 1 mm. 244

Figure C- 15: normal distribution of the residuals. 247

Figure C- 16: distribution of the fitted vales versus residuals. 248

List of tables

Table 1. 1: main characteristics of bending methods [15].	8
Table 1. 2: summary of the advantages and disadvantages described above.	19
Table 1. 3: Hydroforming pressures recommended for FDM tools materials.	30
Table 1. 4: cost comparison between traditional and FDM tools manufacturing methods [48].	30
Table 1. 5: resume of the rapid tooling technologies obtained from the analysis of the state of the art.	32
Table 2. 1: tensile specimen geometry and dimensions [10].	44
Table 2. 2: measurements of the transversal section of the tensile specimens.	45
Table 2. 3: material properties resultant from the performed tensile tests.	46
Table 2. 4: dimensions of the specimens used in the compression tests.	48
Table 2. 5: material properties resultant from the performed compression tests.	49
Table 2. 6: mechanical properties found on the materials datasheets.	51
Table 2. 7: elements and nodes quantities for each compression simulation.	53
Table 2. 8: elastic materials properties used in the simulation model of the compression tests.	54
Table 3. 1: technical specification of the press involved in the experimental activities.	61
Table 3. 2: economical comparison between metal and rapid tools solution for case 1.	65
Table 3. 3: experimental plan of case 1.	67
Table 3. 4: number of elements and nodes used for meshing the tools.	73
Table 3. 5: material properties of the polyurethane tools and aluminium blank.	75
Table 3. 6: resume of the complete boundary conditions imposed in the simulation setup.	79
Table 3. 7: simulation interaction matrix between tools (master) and blank (slave).	79
Table 3. 8: experimental plan with meshed blanks.	81
Table 3. 9: time needed for 1 iteration.	97
Table 3. 10: RMS values obtained after one iteration by changing the λ values.	97
Table 3. 11: price of the polyurethane standard blocks.	101
Table 3. 12: standard price of the Zamak 2 alloy.	101
Table 3. 13: list of the cost given by the company.	102
Table 3. 14: technical data of the press used in the experimental activities of the test case 2.	103
Table 3. 15: experimental plan of case 2.	104

Table 3. 16: number of elements and nodes used for meshing the tools.	107
Table 3. 17: material properties of the polyurethane tools and aluminium blank. .	108
Table 3. 18: list of the complete boundary conditions imposed in the FEM setup of the case 2.	110
Table 3. 19: simulation interaction matrix between tools (master) and blank (slave).	111
Table 3. 20: time needed for 1 iteration	116
Table 3. 21: fatigue tests experimental plan.....	121
Table 4. 1: manufacturing costs of the die used in the experimental activities.....	132
Table 4. 2: cost unit and available standard dimensions for Necuron boards.	133
Table 4. 3: cost of each rough insert with dimensions of 30x30x420.	134
Table 4. 4: manufacturing operations data and total costs of the Necuron inserts.	134
Table 4. 5: metal frame MPG45 (a) and rubber inserts dimensions (b), (c) and the assembly of the rubber dies (d) and (e).	137
Table 4. 6: tensile material properties of the bending dies used in the experimental activities.....	138
Table 4. 7: technical data of the press break involved in the experimental activities.	139
Table 4. 8: available combinations of the specimen in terms of material, thickness, rolling direction and quantity	139
Table 4. 9: experimental results in terms of final bend angle.....	141
Table 4. 10: experimental results of the specimen bended with Necuron inserts. ..	144
Table 4. 11: analysis of variance coming from the regression analysis.	145
Table 4. 12: results of the repeatability test plan.....	153
Table 4. 13: number of elements and nodes used for meshing the object of the simulations.	157
Table 4. 14: material properties of the Nylon insert.	158
Table 4. 15: process parameters of the waterjet operation.....	159
Table 4. 16: material properties resultant from the tensile tests.	160
Table 4. 17: calculation of the anisotropy r_0 , r_{45} and r_{90} coefficients.....	162
Table 4. 18: material properties of the rubber shore 90 used in the simulation.....	164
Table 4. 19: number of elements and nodes used for meshing the object in the compression simulation.....	164
Table 4. 20: resume of the complete boundary conditions imposed in the simulation setup.....	166
Table 4. 21: master and slave contact relations.....	167
Table 4. 22: simulation results and deviations with the experimental values of blanks bend angle.....	168
Table 5. 1: number of elements and nodes used for meshing the tools.	182

Table 5. 2: material properties of the tube.....	183
Table 5. 3: master and slave contact relations.....	184
Table 5. 4: resume of the complete boundary conditions imposed in the tube bending simulation setup.	185
Table A- 1: tensile mechanical properties of Necuron 1050 - T1.....	203
Table A- 2: tensile mechanical properties of Necuron 1050 - T2.....	204
Table A- 3: tensile mechanical properties of Necuron 1050 - T3.....	205
Table A- 4: tensile mechanical properties of Necuron 1150 - T1.....	206
Table A- 5: tensile mechanical properties of Necuron 1150 - T2.....	207
Table A- 6: tensile mechanical properties of Necuron 1150 - T3.....	208
Table A- 7: tensile mechanical properties of Necuron 1300 - T1.....	209
Table A- 8: tensile mechanical properties of Necuron 1300 - T2.....	210
Table A- 9: tensile mechanical properties of Necuron 1300 - T3.....	211
Table A- 10: compression mechanical properties of Necuron 1050 – C1.....	212
Table A- 11: compression mechanical properties of Necuron 1050 – C2.....	213
Table A- 12: compression mechanical properties of Necuron 1050 – C2.....	214
Table A- 13: compression mechanical properties of Necuron 1050 – C4.....	215
Table A- 14: compression mechanical properties of Necuron 1050 – C5.....	216
Table A- 15: compression mechanical properties of Necuron 1150 – C1.....	217
Table A- 16: compression mechanical properties of Necuron 1150 – C2.....	218
Table A- 17: compression mechanical properties of Necuron 1150 – C3.....	219
Table A- 18: compression mechanical properties of Necuron 1150 – C4.....	220
Table A- 19: compression mechanical properties of Necuron 1150 – C5.....	221
Table A- 20: compression mechanical properties of Necuron 1300 – C1.....	222
Table A- 21: compression mechanical properties of Necuron 1300 – C2.....	223
Table A- 22: compression mechanical properties of Necuron 1300 – C3.....	224
Table A- 23: compression mechanical properties of Necuron 1300 – C4.....	225
Table A- 24: compression mechanical properties of Necuron 1300 – C5.....	226
Table C- 1: tensile properties of specimen 1 made by FE37 thickness 0.7 mm.	231
Table C- 2: tensile properties of specimen 2 made by FE37 thickness 0.7 mm.	232
Table C- 3: tensile properties of specimen 3 made by FE37 thickness 0.7 mm.	233
Table C- 4: tensile properties of specimen 4 made by FE37 thickness 0.7 mm.	234
Table C- 5: tensile properties of specimen 5 made by FE37 thickness 0.7 mm.	235
Table C- 6: tensile properties of specimen 6 made by FE37 thickness 0.7 mm.	236
Table C- 7: tensile properties of specimen 7 made by FE37Z thickness 1 mm.	237
Table C- 8: tensile properties of specimen 8 made by FE37Z thickness 1 mm.	238

Table C- 9: tensile properties of specimen 9 made by FE37Z thickness 1 mm. 239
Table C- 10: tensile properties of specimen 11 made by FE37 thickness 0.8 mm. .. 240
Table C- 11: tensile properties of specimen 11 made by FE37 thickness 0.8 mm. .. 241
Table C- 12: tensile properties of specimen 12 made by FE37 thickness 0.8 mm. .. 242
Table C- 13: tensile properties of specimen 13 made by Al thickness 1 mm. 243
Table C- 14: tensile properties of specimen 14 made by Al thickness 1 mm. 244
Table C- 15: data extracted from experimental plan..... 246
Table C- 16: analysis of variance coming from the regression analysis..... 247

Abstract

In the sheet metal forming industry the rigid metallic tools setup are the most common configurations used to plastically deform blanks or tubes (i.e. deep drawing and rotary draw bending), especially in the big batches productions. The use of metal rigid tools setup ensures robust process performances in terms of repeatability of the final tolerances of the components, thanks also to their high wear resistance. Furthermore, the numerous information available in scientific and industrial literature, in terms of design guidelines and numerical modelling, speed up all the initial phases of the process design. If the rigid tools could represent the best solution in terms of process accuracy and reduced time developments, the main disadvantage of the rigid metal tools can be researched on the elevated cost of the manufacturing operations, like milling or thermal treatments, which have a great impact on the total costs of the process especially in small-medium industrial productions.

In order to reduce the tooling costs, especially for small batches productions, rubber or flexible tools, with general purpose shape, have been coupled together with one rigid metal tool, die or punch (i.e. flexforming and rubber pad forming), in order to enforce repeatable geometry of the stamped parts. The use of a general-purpose rubber tool coupled with a metal one allows reducing the tooling costs around the 50% with respect to a total rigid metal tools configuration, because only the total rigid metal tool must be manufactured each time new product must be stamped. Esthetical defects, like scratches on the component surface, are generally avoided thank to intrinsic auto-lubricating properties of the rubbers materials. If these advantages make the rubber tools as an attractive solution for the industrial production scenario, it should be noted that the rubber tools are not suitable for hot-forming processes (typical used in automotive industry), because at temperature approximatively of 80°C the mechanical behaviour of the rubber material tends to degenerate. Furthermore, the production rate of the processes based on rubber tools is very low, because elevated strain rates reduce the rubber tools life. The concept time phase of a process with rubber tools is normally very long because very few information and guidelines about design methodologies and numerical modelling are available in scientific and industrial literature, maybe due to their low diffusion in the industrial scenario. The behaviour of the rubber tools is not easy to be predicted, because the simulation models of a rubber forming process often need to be validated with experiments, which require a lot of resources in term of time and costs.

From the considerations made above, it follows that the rubber tools setup can be suitable for small batches production, especially when small precision and components with simple features are manufactured.

Resuming the considerations made above, the rigid and deformable tools seem to be opposite solutions in terms of achievable production volume, final accuracy in terms of tolerances on the stamped parts, production costs and design time. These opposite characteristics suggest that another solution could be investigated in order to reach

the best compromise in terms of time and costs, especially in case middle production volume and restricted interval of tolerances are required.

Since from the advent of rapid prototyping technologies, the rapid tools method has always been used in the production of prototypal tools setup, made by polymers, intended for the manufacture of pre-series products.

Over the years, the polymer materials have been subjected to a lot of attention from the applied research, especially with the tremendous growth of additive manufacturing technologies observed in the last few years. The development of reinforced plastic materials with high performances gave a reborn attention on rapid tooling technologies as a possible cost-efficient and innovative solution for the improvement of the traditional sheet metal forming processes

The main objective of this doctoral thesis is to investigate potentiality of rapid tools, made by different polyurethane materials (pure and reinforced with sand or with glass fiber), in three representative cold sheet metal forming processes, in order to formalize some guidelines based on direct experiences grown up by the collaboration of research laboratories and industries.

In the first chapter of this thesis a general introduction about the rigid and rubber tools setups has been presented in detail with the analysis of the cold sheet metal forming processes most diffused in the companies encounter during the period of this doctoral research. The analysis of the sheet metal forming processes with metal and rubber tools allowed to identify the advantages and disadvantages of these two macro categories of tools setup intended to outline the necessity of the investigation of new tools setup solution. This new solution has been identified in the rapid tools by the presentation of an investigation of possible innovative materials suitable for tooling purpose. After the identification of the rapid tools as a possible alternative solution to the traditional tools setup, the state of the art and the description of the technologies able to manufacture them has been presented.

In the second chapter a review of polymer materials has been performed in order to define their classification and the attended mechanical behaviour. Afterwards, the complete description of the performed tensile and compression tests, need for the characterization of the materials used in the case studies, has been described. After the characterization of the materials, the simulations of the compression tests have been performed in order to tests the capability of the FEM software PAM-STAMP in predicting the deformation of the characterized polyurethane materials.

In the third chapter, the application of the rapid tools setup has been studied in sheet metal stamping process. Two case studies with different shapes, have been analysed experimentally, by the execution of experiments, and numerically, by the development of simulation models able to predict the final geometry of the stamped components. A compensation algorithm has been presented, together with a small state of the art of possible compensation methodologies, in order to correct the geometrical errors obtainable from the use of the rapid tools in the stamping process. Finally, fatigue tests on the polyurethane materials used in the experiments have been conducted, in order to evaluate the possible tools life at similar conditions of the stamping tests performed in the two case studies.

In the fourth chapter, the application of the rapid tools in the sheet metal air bending process has been presented. A modular bending die with polyurethane inserts has

been designed and compared with other traditional commercial die configurations made by meta, nylon and rubber. A big experimental plan has been designed and conducted in order to evaluate and compare the performances of the rapid tools with respect to the commercial solutions. Afterward, a numerical simulation model able to predict the process results has been presented for analysing the stress and strain maps on the rapid tools in order to evaluate the tools life, according with the tests performed in the previous chapter, and possible improvements for future developments.

In the fifth chapter, a possible rapid tools implementation has been presented for tube rotary draw bending process. A simulation model with a polyurethane tools setup will be compared with a simulation model implemented and validated by the author in the thesis presented during the bachelor degree. The FEM model has been used for improve the polyurethane tools setup with some prototypal proposal which can be taken in account in the future developments.

In the conclusions section, all the achieved results, maturated experiences and possible future developments will be resumed.

Chapter 1

State of the art

1.1 Introduction

The sheet and tube metal forming processes have been subjected to continuous improvements from the research activities (especially in the last few years with the advent of the additive manufacturing technologies) in terms of order and number of sequential operations, process parameters optimization, initial shape of the components, tools compensation and the development of new kind of deformation processes.

Traditionally, in sheet metal forming the stamping operation is the reference process, where a blank with standard shape, as a rectangle or circle, undergoes a transformation into a component with a complex feature.

In the conventional deep drawing and stamping processes, a tooling setup made of a die, a punch and a blankholder is traditionally used. Afterwards other rigid tools, like drawbeads, have been introduced in order to avoid the wrinkling defects on the final component.

The introduction of multi-step stamping process, with intermediate annealing steps, allows making component with complex features.

Over the years, many “new” process solutions have been implemented in the metal forming field in order to reduce the time and costs of the operations or for manufacturing particular features like undercuts. These solutions are known as Hydroforming and Gas-forming processes, which involve the action of a fluid in pressure for forming components with the features cited before, which are largely used in automotive and motorcycle industries [1].

Later, many different types of flexible sheet metal forming processes have been developed in the industry, in order to improve the process, and especially in order to compress the tooling production times and costs. Single point and double point incremental forming processes [2] have been invented and are continuously being developed to this purpose. As another cost saving option, one or more of the metal tools are replaced with a rubber membrane. The Guerin process makes use of a movable thick rubber pad pressed against a die ([3]-[4]) or punch ([5]-[6]). The Marform process is a variant of the Guerin, using an active blankholder [7]. In flexforming with a fluid cell, a rubber diaphragm is pressurized by a fluid or by a bladder [8]. In deep drawing

flexforming, a movable punch is used, too [9]. In multi-point stretch forming [10], stretch forming clamps are used with the sheet bent over a flexible die made by a raster of metallic movable pins. Most of these applications have been developed and are largely used in the aerospace industry, due to their low tooling cost, which is very convenient in the production of small batches.

Normally, these processes involve using a metallic tool (punch or die) and a counter-rubber-die with "general purpose" shape, due to the high deformation capacity of the elastomeric material, e.g. a membrane or a cushion.

In the last few years, the tremendous growth of additive manufacturing technologies is changing completely the way of thinking about functional parts and designing them. At the same time, a reborn attention is being given to Rapid Tooling technologies [11], which offer cost-efficient and innovative solutions for improving the sheet metal forming processes.

In this chapter these alternative sheet metal forming solutions will be presented in order to describe the advantages and disadvantages of each solution. Then, three macro-categories of processes will be defined: rigid tools based, deformable tools based and the rapid tools based. These macro-categories will allow to define a new definition of "Rapid Tools". The new definition of Rapid Tools will be based no more on the specific production time and costs of the particular tool, but on the selection of the best solution (Rigid, Deformable or Rapid) for the specific process, in order to define the new category named "Smart Tools".

1.2 Rigid Tools Processes

In this paragraph a brief description of the forming processes which use rigid tools will be done in order to underline the advantages and disadvantages in using this kind of tools for metal forming processes.

The process analysed will be: deep drawing, tube bending and air bending process. The description of these processes will be useful because, in the following paragraph, similar processes which use deformable tools will be presented as a comparison.

The description of the deformation mechanism of the blank during the process will be omitted because it has been largely discussed in several works along the years ([12]-[13]).

1.2.1 Deep drawing

1.2.1.1 Description of the tools setup

Deep drawing is a sheet metal forming process in which a sheet metal blank is radially drawn into a forming die by the mechanical action of a punch [14]. The process is considered "deep" drawing when the depth of the drawn part exceeds its diameter.

In a deep drawing process, a blank is subjected to a pressure from a preformed punch. The action of this tools forces the blank to overlap on the die wall. The material flow of the blank is controlled by the blankholder, which act a force on the free boundary of the blank unconstrained from the punch and die (Figure 1. 1).

Initially the blank is stretched under the action of the blankholder force which press it lightly. When the blank wins the stretch pressure it slides along the punch action.

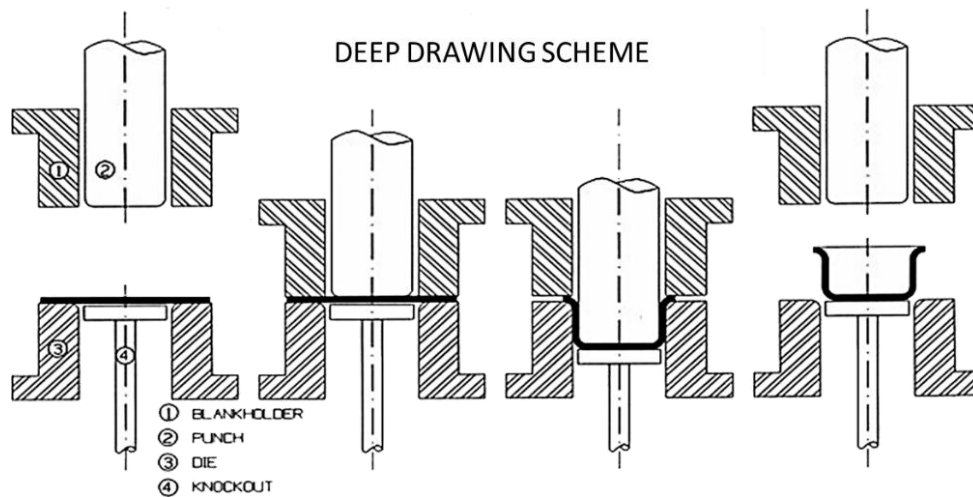


Figure 1. 1: Scheme of traditional deep drawing process.

The blankholder force must be sufficient to control the sliding of the blank during the whole process in order to avoid wrinkling defects. So the blankholder should apply the maximum forces allowed from the material strength limits.

In case of non-axisymmetric complex components, the sliding of the blank is not easy to be controlled so another kind of tools, called drawbeads, must be introduced. The purpose of the drawbeads is to slow down the sliding of the blank in the zone with straight edge characterized by big curvature radius (Figure 1. 2).

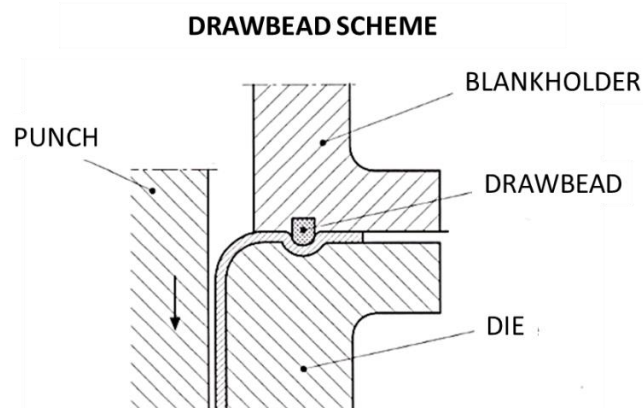


Figure 1. 2: schematic example of drawbead.

1.2.1.2 Process parameters

The described process tools setup seems to be very simple but usually is very difficult to define correct values of process parameters like the lubrication and blankholder forces. The generalization of the correct values of the process parameters is very difficult to be defined because the variety of components and features obtained by sheet metal forming processes are infinite. For this reason, in this paragraph, the definition of the process parameters will be described for axisymmetric components. Generally, the blankholder force is the most important parameter in a stamping process because most of the defects on the stamped components are due to incorrect values of this process parameter. The pressure of the blankholder should be enough to allow the sliding of the material along the boundary of the blank outside the action of the punch. The values of the blankholder force can influence the final results of the

process in terms of wrinkles defects, in case of low force values, or rupture of the component, in case of too high force values.

An empirical equation is generally used in order to evaluate the initial value of the blankholder force defined as:

$$P = \frac{\pi}{4} (D_{ext}^2 - d^2) \cdot p \quad (1.1)$$

where P is the blankholder force expressed in Kg, D_{ext} and d are the external diameter of a sheet metal disk and the diameter of the cylindrical die respectively and p is the specific pressure expressed in kg/cm², which values are defined in [13].

The lubrication of the blank is very important to simplify the sliding during the process. The lubrication allows the blanks to contrast the effect of the tangential forces due to the friction between the die and punch walls. The magnitude of the friction coefficient in a stamping process is very difficult to be measured. In the industrial production the definition of the friction is obtained experimentally by the application of special oil or grease which allows the best sliding of the blank during the process, without the insurgence of defects.

1.2.2 Tube bending

The tube bending process is a general definition of all processes which generate a bent tubular profile starting by a rectilinear one. The usual bent profile is characterized by a convex surface (extrados) longer than the opposite concave surface (intrados). The most common bending tube processes used in the industrial production are:

- Rotary draw bending
- Compression bending
- Roll bending
- Push Bending

Each method has specific advantages and limitation related to the angle and to the type of curve achievable. In Table 1. 1 the characteristics of each method has been resumed.

Method	Curvature types	Maximum angle
Rotary Draw	Single, multiple, compound	Up to 180°
Compression Ram and press Manual	Single Series of different bend angles Single, compound, helical	Less than 180° Up to 165° 360°
Roll	Circular, spiral, helical	360°
Push bending	Single	Less and equal 90°

Table 1. 1: main characteristics of bending methods [15].

The selection of the most appropriate bending method is related to:

- 1 Request quality of the results
- 2 Time production
- 3 Geometrical parameters of components like the outer diameter (D), wall thickness (t) and curvature radius (R).

The combined application of the two nomograms shown in Figure 1. 3 and Figure 1. 4 allows to find the most suitable method to achieve the objective cited before.

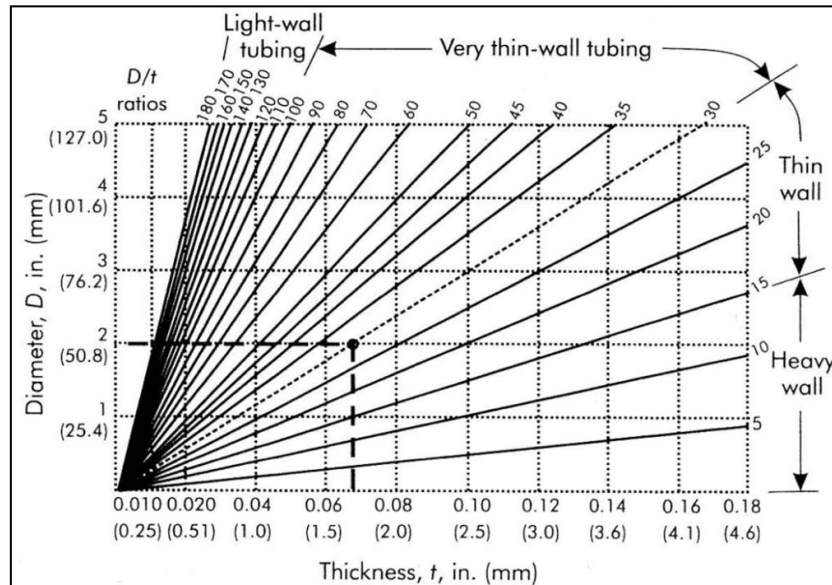
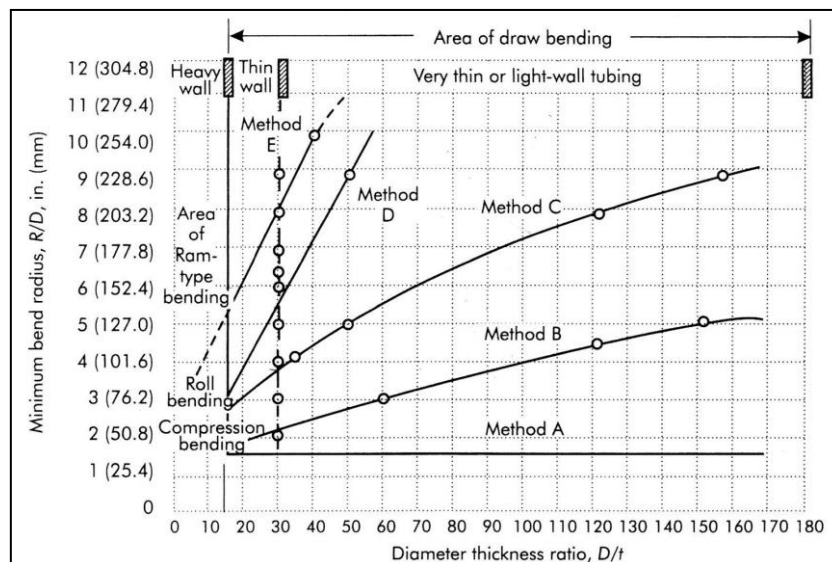
Figure 1. 3: nomogram used for evaluate the ratio D/t .

Figure 1. 4: nomogram used for choosing the best curvature method.

Each method is characterized by a specific mechanism and tools setup, which will be briefly described below (Figure 1. 5):

- **Rotary draw bending:** this process is one of the most complex ones. It is composed by a very large number of tools like: rotary die, pressure die, wiper die, clamp die, internal plug (usually coupled by a series of spheres) and booster. All of the cited tools have a specific role during the process. The rotary die is coupled to the clamp die for locking the tube during the bending process; the pressure die moves externally in simultaneous along the tube axis in order to control the material flow on the tube extrados, instead the wiper die is fixed during the process and control the phenomenon of the wrinkle generation. Further information about this process can be found in [15] and [16].

- **Compression bending:** the tools setup is quite similar to the previous process described but, in this case, the die is fixed and a rotary slide substitutes the clamp die. So the component is blocked on the die and the rotary slide rolls up the tube on one end. On the other end the tube is locked in order to avoid the undesired movements and controlling the process.
- **Roll bending:** this is the most economical and efficient process used for bending very complex profile with big curvature radius, like four times the diameter of the tube. The component is arranged, generally, between three rolls, two lower rolls and one upper. This tools setup allows to obtain also bent profile with variable radius [17]. Generally, the three rolls are placed at the same horizontal or vertical plane in pyramidal way.
- **Push bending:** the process is very different to the ones described before. It is a mix between a forming and bending process. It does not require a specific bending machine because it uses the same stamping presses used for metal forming. The component is locked inside two preformed dies (upper and lower dies). The bending operation is given by a punch which pushes the tube inside the curved dies shape. The curvature of the tube is controlled externally by the contact with the dies walls, internally by the contact of a curved plug. This kind of process is largely used in the oil and gas industry in order to produce very thick hydraulic pipes.

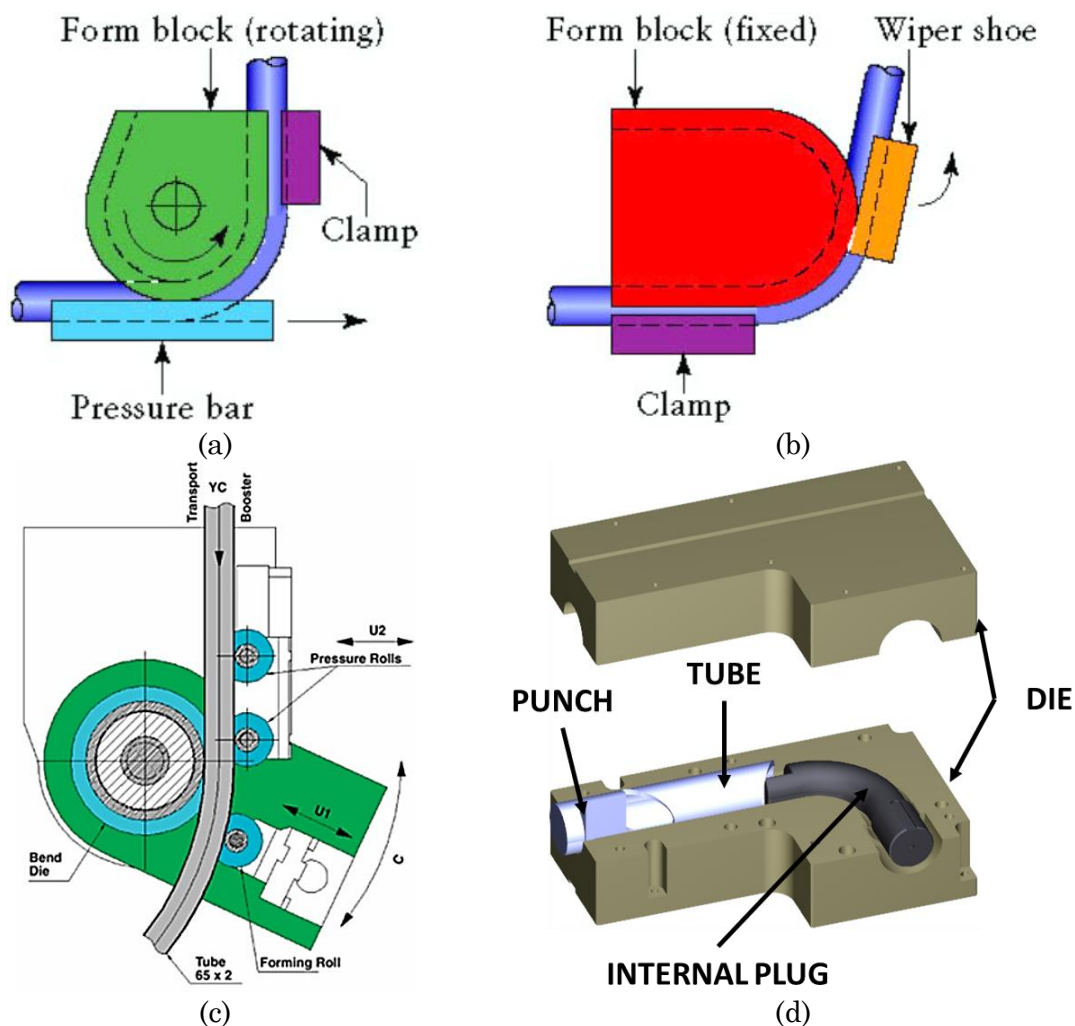


Figure 1. 5: schemes of the described tube bending processes: rotary draw (a), compression (b), roll (c) and push (d) bending.

1.2.3 Air bending

The air bending process is apparently the simplest technology in term of the tooling setup, with respect to the ones described before.

The tools setup is composed by a preformed V die and one punch. The name of “air” bending comes from the sheet metal forming mechanism on which the process is based. Differently from the bottoming process where the sheet is bent between the die and the punch until the tools closure, the “air” process is based on a three points bending of the sheet; so the ending of process does not depend on the tools closure but on a defined punch stroke (Figure 1. 6). After the bending phase, the component is subjected to the springback mechanism which influences the final angle of the component. Furthermore, another important parameter which is fundamental for the production of a multi-bent profile is the bend deduction (BD) defined as the elongation of the fibers of the component at the end of the process. So, after the choice of the best bending tools, the only parameters to manage is the punch stroke in order to obtain the desired final angle and BD. There is a lot of literature about the description of the air bending process and the algorithm to predict the resulting angle and BD ([18]-[21]), but until today there is not an industrial solution which allows to predict the final results of the process with sufficient precision without any initial trials.

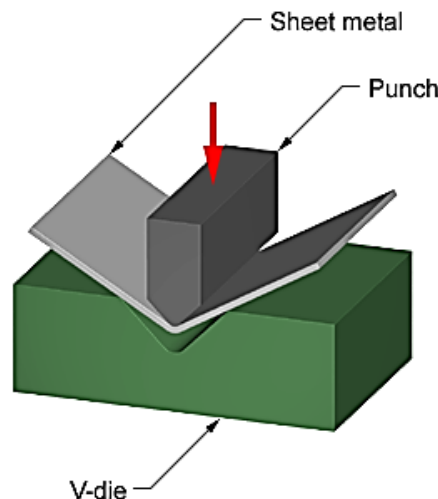


Figure 1. 6: scheme of the air bending process.

1.2.4 Rigid tools: Advantages and disadvantages

The process descriptions made above may suggest the advantages related regarding using rigid tools. One of the main advantages is related to the huge knowledge available from literature and from industrial experiences collected over the years. Generally, the rigid metal tools are made by a stiffer material than the one subjected to deformation, especially in the processes which involve the deformation of a thick component. So the stiffness of the tools allows to neglect the dimensional defects related to the tools deformation. From the considerations made above, it could be possible to state that designing a stamping tools setup is easy to make, especially if the information available in the literature are coupled with the current advanced numerical simulation technologies, but some remarks and considerations about rigid metal tools should be made, in order to understand the reason why other technologies which involve deformable or rapid tools have been implemented.

Using metal tools means that they must be produced through previous milling operations. A milling operation for producing a metal tool is a very expensive and time

costly phase which can last for a lot of hours especially for very big automotive stamping dies. Furthermore, after the milling phase a thermal treatment of the tools is required in order to reduce the residual stresses coming from the previous phase. Generally, the thermal treatment requires a lot of minutes (hours in some cases) for being carried out.

The considerations made above allow understanding that the cost items related to the making of rigid metal tools cannot be neglected in an economic evaluation of a production process. It must be reminded that each tools setup is dedicated for one type of components, so the rigid metal tools cannot be suitable for flexible or personalized productions.

In a flexible production a lot of tools setup should be required, so the costs are multiplied for the typology of the produced components; moreover, due to the intrinsic high weight of the tools, the changing tools setup operations are very slow because they should be executed by a fork lift machine for the safety of the operators.

In conclusion, if on one hand the rigid tools represent the best solution in terms of the repeatability and quality of the manufactured product, at the same time they are not always an efficient choice in terms of the process management. These characteristics should be taken in account in a research of the best compromise between quality and costs in the design of a production process.

1.3 Deformable tools processes

The processes described in the previous paragraphs are largely used in the industrial production because they are suitable for high rate productions especially for the repeatability of the results.

In the aeronautical or supercar sectors, smaller productions are required; for this reason processes which involve deformable tools (or fluid in pressure) have been implemented.

Often, these processes involve using a metallic tool (punch or die) and a counter-rubber-die with "general purpose" shape, due to the high deformation capacity of the elastomeric material, e.g. a membrane or a cushion. For this reason, this processes are very convenient in terms of tooling cost especially for the production of small batches. In the following paragraphs the processes which involve deformable and fluid in pressure tools will be described in order to gather more information about the advantages and disadvantages in using this kind of tools.

1.3.1 Fluid based processes

In the hydroforming process a fluid in pressure is used to form a blank or tube component, for this reason two macro categories can be defined Sheet-Hydroforming (SHF) and Tube-Hydroforming (THF). Usually these processes are applied for structural parts of cars, medical instruments or household hardware where the shape of the components are very complex and high performance of the product are required. In sheet hydroforming (SHF) there are bladder forming (where there is a bladder that contains the fluid; no liquid contacts the sheet) and hydroforming where the fluid contacts the sheet (no bladder). Where bladder is used the forming process change name in Flexforming. In the Sheet hydroforming, fluid can act as a punch or a die. In case of fluid die the rigid punch and the blankholder are used in order to control the sliding of the blank. In this case, the process can be also called Aquadraw (Figure 1.7a).

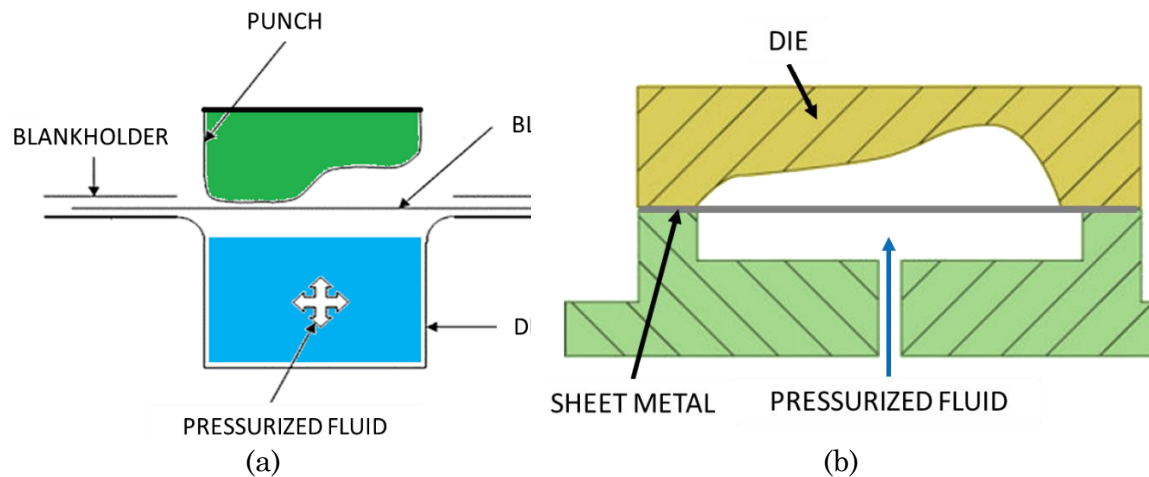


Figure 1. 7: scheme of aquadraw (a) and Hydroforming process (b).

Following the scheme represented in Figure 1. 7a, the Aquadraw process seems to be very close to the stamping process, because the sheet is deep drawn to form over the punch, against a counter-pressure in the pressure pot generated by a pressurizing fluid. The pressurized fluid can be with passive control, with a relief valve or with active control by an external pump.

In Sheet Hydroforming with rigid die, the fluid acts as a punch and the sheet is pressed against a female die. During the process, the blankholder can control the sliding of the blank but in most case, where an economical press machine is used, the blankholder is replaced by the plate of the press where the fluid outcomes.

Tool design for sheet hydroforming is similar to regular stamping; the achievable minimum radius on the part depends on the available maximum fluid pressure. Generally, in the Hydroforming or Aquadraw processes, the rigid tools are designed for the specific part to be made instead the fluid tools is common for all parts.

A different version to the Hydroforming process is used for high dimension parts with small drawing ratio due to the required pressure. Flexforming is the name of such method which involves a pressurized rubber bladder and a half tool, usually a die, for manufacture a sheet metal component.

The sheet metal blank is forced to assume the shape of the rigid tool half by a flexible diaphragm pressurized by a high-pressure fluid (Figure 1. 8).

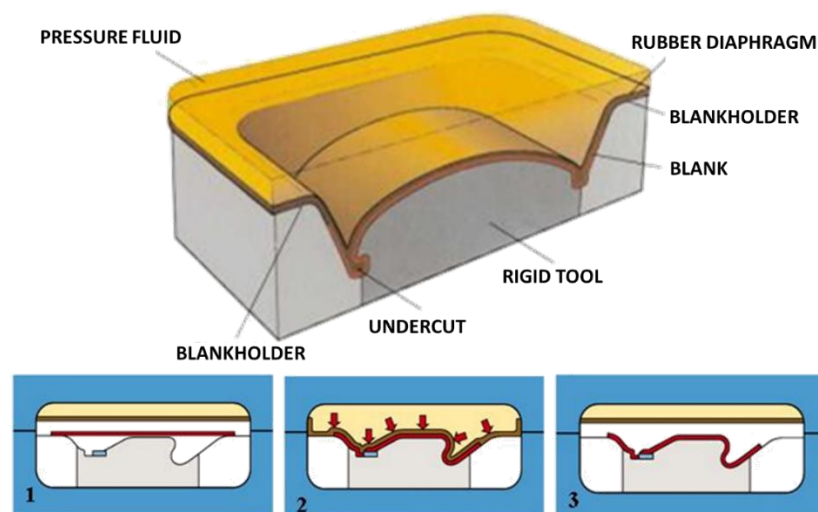


Figure 1. 8: scheme of the flexforming process.

The blank is positioned on the single rigid tool half, which is placed on the press table; the table is moved into the press frame, where the other tool half, a flexible diaphragm with oil back up, is located. The oil is pumped into the press above the diaphragm and forces it to wrap the blank around the rigid tool half.

The high and uniform forming pressure ensures close tolerances and makes undercuts and trimming

possible. After decompression of the pressure fluid, the diaphragm returns to its initial upper position, leaving the formed part on the single rigid tool half to be removed after the press table is moved out of the press frame.

Generally, the blank-holder is not present and the blank is held by the flexible diaphragm, which is pressurized by the overhanging fluid; so that the material flow depends only on the pressure value and it results in a less controllable process, which requires dies and punches careful design and optimized selection of initial blank dimensions.

The minimal concave curvature radii attainable depends on blank material and thickness t and on the maximal forming pressure. Moreover, its value is limited by the presence of the flexible diaphragm, which sometimes, to resist to the high pressure value, has higher thickness than the blank; the circumstance makes it difficult to penetrate in small cavities. Another Flexforming characteristic is the possibility to integrate in the forming process, a trimming operation, which is feasible because of the presence of the rubber diaphragm: when the metal begins to tear during trimming, the diaphragm continues to seal off the pressure fluid and maintains the high pressure required to complete the trimming operation.

Other fluid based metal forming methods can be found in literature for each specific usage, like Tube Hydroforming process [22]; but the objective of this introduction is only to provide a general impression about the processes, which involve deformable tools in order to better describe the general advantages and disadvantages related on the implementation of this kind of tools.

1.3.2 Rubber pad forming

The rubber pad forming process is employed in the manufacture of components for aeronautical, motorsport or military applications.

Like the previous processes, also the rubber pad forming involves only one rigid tools (similar to a traditional stamping tool) but, instead of fluid, a very thick rubber cushion is used.

The rubber cushion carries out a constant pressure on the entire surface of the sheet metal. Thanks to the incompressibility of the material, during the closure of the stamping press, the rubber forces the blank assuming the shape of the preformed rigid tool.

The entity of the sheet metal deformation is larger with respect to traditional stamping processes, because the distribution of the stamping pressure is distributed over all directions. For this reason, the rubber pad forming process is very useful for flexible productions of small batches of products.

The main processes which use rubber cushion are the Guerin and Marform process.

1.3.2.1 Guerin process

The Guerin process takes its name from his inventor Henry Guerin which, during the '30 years, he comprehended that using a rubber pad could reduce at 50% the work manufacturing of the stamping tools.

The rubber pad is closed inside a rigid container in order to prevent the leakage of the rubber material in the lateral directions. The rigid container is locked on the upper plate of the stamping press. During the closure of the process, the container pushes the rubber on the sheet metal by forcing it assuming the shape of the rigid punch (Figure 1. 9).

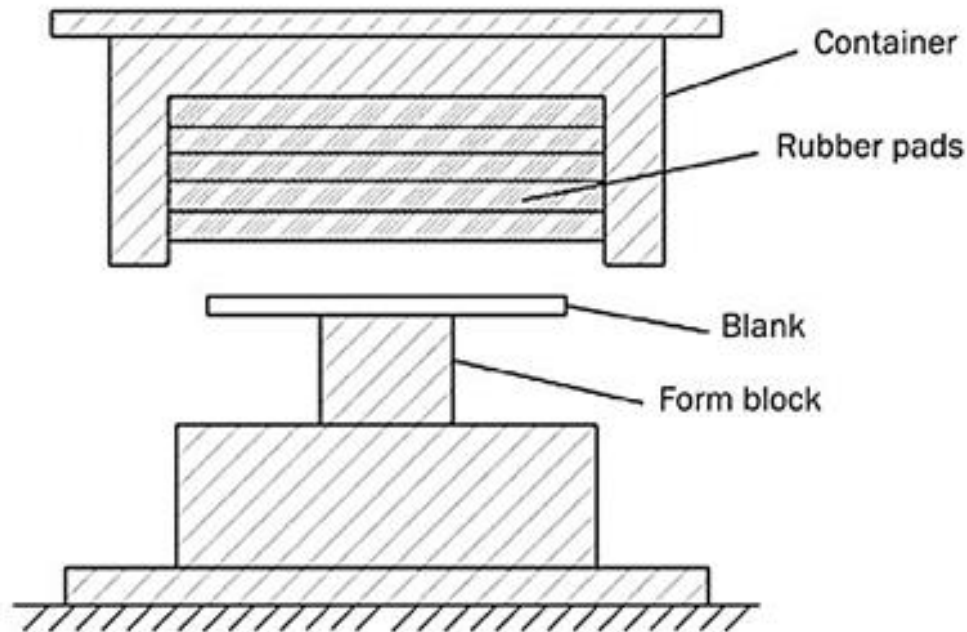


Figure 1. 9: scheme of Guerin process.

The typology of the products which can be produced by Guerin process is closed to limited deep and flanged components. The limitation is due to the low compression strength of the rubber material which does not avoid the wrinkling defects.

Generally, the rubber pad can be stressed until 100 MPa, so it demonstrates that every hydraulic press could be used for Guerin process, but it is always better to compare the nominal tonnage of the used press.

The rubber cushion can be built by a single component or multi-layered one with different stiffness.

Normally the stiffer layer (50-75 Shore A) is used for the deformation and it is three times deeper than the needed deep-drawing depth. So if the component is 50 mm deep, the height of the rubber cushion is between 150-250 mm. For very deeper components, more rubber layers can be involved, but the wearing of the deformable tool will be reduced.

The usefulness in using a rubber cushion is related to the working surface of the rubber pad which can be easily restored by rotating upside-down the cushion or quickly substituted. For reducing the wearing of the rubber pad, a thin membrane is applied between the rubber pad and the blank to be deformed. The container of the rubber pad is made up by steel walls 20-30 mm thick. The rigid tool usually is made by steel or cast iron, only in very particular cases, with very easy components can be made by wood, plastic or mild steel. The deformable tool's life can be increased by reducing the stamping depth or increasing the curvature radius of the stamped component when allowed. Some feasible typical shapes by Guerin process are presented in Figure 1. 10. Another application of the Guerin process will be described in the following chapter for sheet metal bending process (Figure 1. 11).

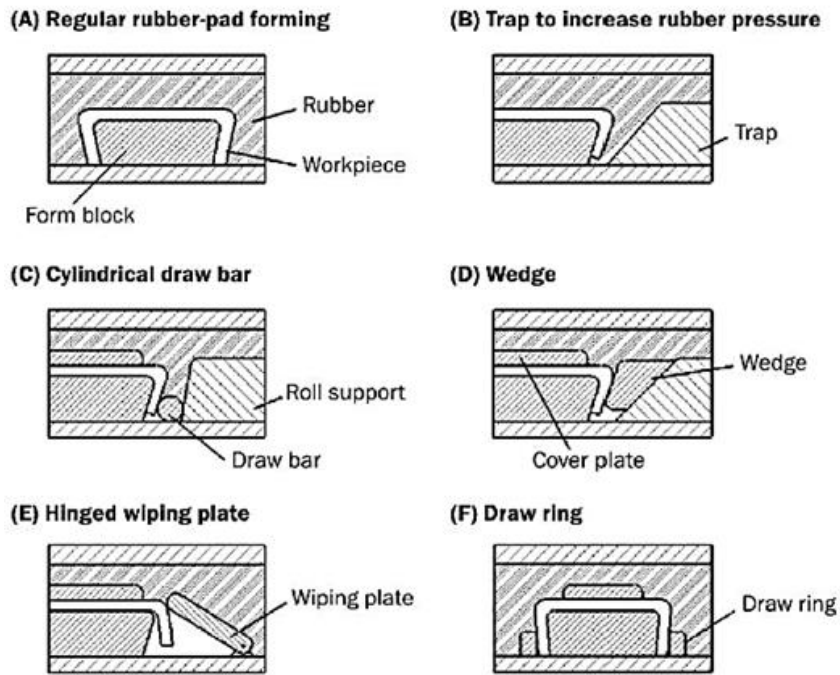


Figure 1. 10: typical shape realized by Guerin process.

The Guerin process is usually used in U and V bending. In 1986 Vankatesh and Goh made a statistical study where they found the correlation between the Limit Drawing Radius (LDR) and the process parameters like R_p (punch radius), H (shore of the rubber) and Th (sheet metal thickness):

$$LDR = 0.995 - 0.00125 * R_p + 0.0005 * H + 0.100 * Th \tag{1.2}$$

The equation shows that the LDR values increases at increasing of the sheet metal thickness and rubber hardness by reducing the punch radius ([6], [23]-[24]).

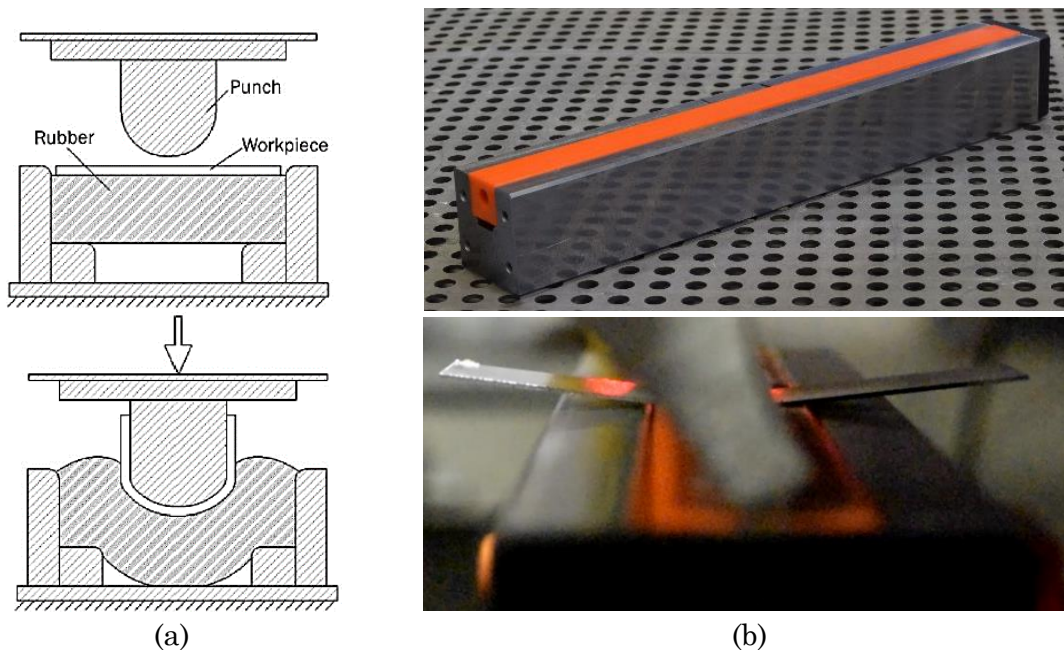


Figure 1. 11: scheme (a) and practical example of Guerin process (b).

1.3.2.2 Marform process

The Marform process, similar to the previous one, has been developed for using deformable tools made by rubber. This process is used for making deep drawn component without wrinkles. Also for this method, it can be made components with vertical walls or undercuts (Figure 1. 12).

Differently by the Guerin process, the Marform process involves a blankholder controlled in pressure by a seal ring. As shown in Figure 1. 12, during the descent of the container, the blank is held between the blankholder and the rubber cushion. The pressure monitoring on the blankholder allows to control the sliding of the blank in order to avoid the wrinkles defects. As in the Guering process, the rubber behaviour forces the blank to assume the shape of the punch. The general values of the blankholder pressure is between 35 and 100 MPa. Thanks to the deformation of the rubber die, the sliding of the blank is assisted during the process by reducing the risk of fracture of the blank.

Similar to the Guerin process, the thickness of the rubber pad is 2 times more than the depth of the component. The rubber pad can be covered by thin membrane in order to reduce the wearing.

The Marform process allows to produce deeper components but it is slower than the Guerin once [23]-[24].

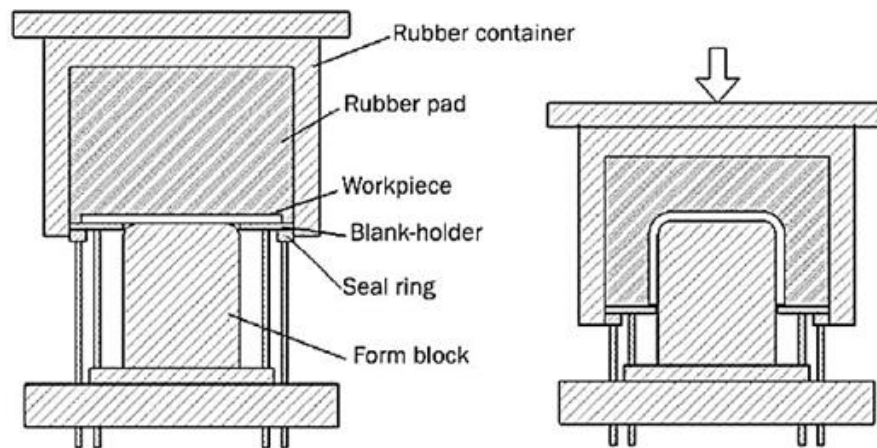


Figure 1. 12: scheme of the Marform process.

1.3.3 Deformable tools: Advantages and disadvantages

Over the years, other metal forming processes which use deformable tools have been developed, most of them can be compared to the Flexforming process like the Verson-Hydroform, ASEA Quintus Fluid Cell, Verson-Wheelon and other are similar to a classical bulge test like the Bulging Punch process. Every process which use rubber tools share the same advantages and disadvantages.

Generally, they involve only one dedicated tool and one general purpose shaped, this characteristic allows reducing approximatively at the 50% the costs related to the tools manufacturing. The rigid tools, in some cases can be manufactured with cheaper material than metal. The time related to the tools setup is reduced because only one tool must be changed. The same rigid tool can be used for stamping different material with different thickness. Furthermore, using a rubber pad allows to neglect the errors related to a wrong tools positioning, which is one of the large source of dimensional errors in a traditional stamping process, usually solved by using auto-centred tools. The aesthetical defects (e.g. scratches due to the elevated friction between the component and tools surfaces) usually obtained with rigid stamping tools, are avoided

in rubber pad forming processes, and the lubrication is not needed thank to intrinsic auto-lubricating properties of the rubbers materials involved in this processes.

From the consideration made above, the rubber based processes seem to be the best solution to apply in the industrial production, but a lot of disadvantages can be found in using rubber tools.

The rubber pad can be subjected to a fracture after a lot of cycles, if the stamped component has cutting edges. Too elevated values of pressure can reduce the wearing of the rubber due to high compression and to the sliding of the material. Reducing the pressure means less precision of the features obtained from the calibration phase. The production rate is very low, for this reason this processes are usually involved in low batch productions. The rubber tools cannot be used at high temperature, because at approximatively 80°C they tend to reduce their mechanical characteristics.

Furthermore, the behaviour of a deformable tool and the process results are not easy to predict, so there is not enough literature which explain how correctly design a deformable tool. In most cases virtual instruments, like Finite Element simulations of the process are required in order to have the order of magnitudes of the error obtained, but they are very complicated to be developed in order to manage correctly the interactions between the deformable tools, blank and rigid tools.

In the further chapters some solutions will be proposed in order to solve most of the disadvantages described in this paragraph.

1.4 Choice of the tools materials

In the previous paragraphs an overview of the “traditional” sheet metal forming processes has been made. The overview underline that the choice of the tools material can affect process results not only in terms of the tolerances or aesthetical defects on the final component, but also in term of global management of the process in terms of time and costs.

The results in terms of interval of tolerances on the final component can be well predicted in most cases for sheet metal processes based on rigid tools with the aid of: process design guidelines available in literature, empirical models, simulation models, compensation algorithms etc. A metal tool is normally considered infinitely rigid respect to the sheet metal; for this reason, the behaviour of rigid tools is easy to be predicted due the intrinsic non-deformable behaviour. Instead, the results of a process based on deformable are very hard to be predicted with high accuracy because the tool material behaviour (generally rubber) is difficult to be described and modelled. All of These considerations suggest that the consequently design time is lower for rigid tools than for deformable tools.

The rigid tools are generally manufactured by milling operations and thermal treatments; moreover, they have dedicated shape for each sheet metal formed component. The deformable tools are normally produced by extrusion or casting processes due to their basic general purpose shape (e.g. membrane, standard blocks) which allows manufacturing sheet metal components with different shapes. These characteristics make guess that the manufacturing time and costs are higher for the rigid tools than the deformable ones. At the same time, the rubber tools can manufacture sheet metal components with different shapes, thanks to their deformable behaviour; for this reason, the rubber tools can be involved in flexible productions where many different small batches are produced. On the contrary the rigid behaviour of the metal tools confers higher life cycle with respect to rubber tools. Furthermore the rubber tools cannot resist to high temperature (more than 150 degree) without undergoing to degradation due to their low fusion temperature; for

this reason, they cannot be used in hot sheet metal forming processes, as opposed to metal tools which have higher fusion temperature.

The considerations found in literature and made above for the different tools setup can be resumed in Table 1. 2.

The overview in Table 1. 2 demonstrates that the two solutions are so distant and opposed to each other. These opposite characteristics show that a middle solution is required in phase of the initial process planning in order to enlarge the possibilities of choices and to reach the best compromise in terms of time and costs of the process.

Characteristics	Rigid Tools	Deformable Tools
Interval of tolerances on the final component	Strict	Large
Design time	Low	High
Manufacture time	Very High	Very low
Manufacture costs	Very high	Very low
Flexible productions	Not possible	Possible
Tools life	Very high	Very low
Hot forming	Possible	Not possible

Table 1. 2: summary of the advantages and disadvantages described above.

From these considerations an investigation has been made about the tools materials which could substitute the traditional ones used in the processes described above.

The first comparison has been made by searching the material which minimizes the energy needed for being worked by machining operation [MJ/m^3] and the price [$\text{€}/\text{m}^3$]. The unit of m^3 has been chosen because the densities of the analysed materials are different so a Volume unit is more suitable for a fair comparison.

The choice of the best compromise can be made by analysing the Pareto Front which is the domain of the dominant solutions in a set of possible solutions [25].

In the right low zone of the Pareto Front (Figure 1. 13) there are the traditional metals used for stamping tools manufacturing.

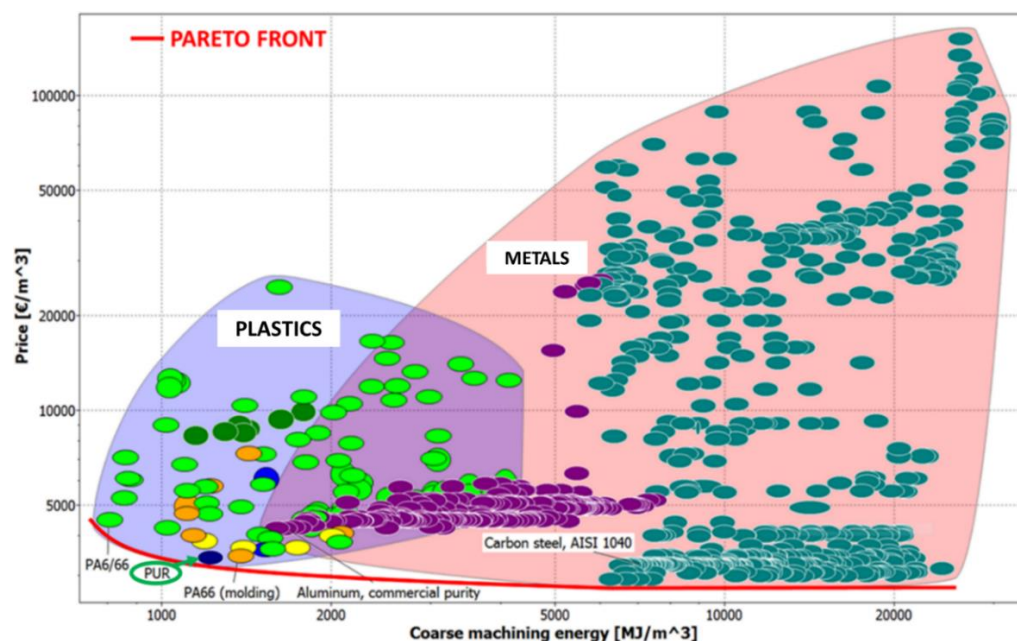


Figure 1. 13: minimization of Machining Energy and Price of for the materials used in tools manufacturing.

The metals have very low price than plastic materials, but the required machining energy is higher because the metals are harder. Instead, the plastics, like PA6/66, have a comparable price but very low values of machining energy required due to the intrinsic ductility of the materials. The rigid polyurethane material (PUR) and the polyamide (PA66) are the middle zone of the Pareto Front so they seem to be the best compromise between the price of the material and the required machining energy. The aluminium alloys are outside the Pareto Front, so they seem not suitable for tools especially when manufacturing and purchase costs are compared. The elastomers (like rubber) cannot be included in the comparison in Figure 1. 13 because they cannot be machined due to the high intrinsic elongation behaviour.

Another comparison can be performed between the yield strength (elastic limit) and the Fatigue Cycles which could help during the design phase of the tools setup. From an FEM (Finite Element Model) simulation of the stamping process it is possible to evaluate the order of magnitude of the maximum Von Mises stress on the tools so, from this value, it is possible to choose which material can resist to these stresses. The fatigue cycles can give an idea about the dimension of the batch which can be manufactured and the evaluation of the maintenance time interval of the tools.

The comparison in Figure 1. 14 seems to have a positive linear trend, so it could be easy to choose the metal (green points) as the best solutions and the elastomer as the worst ones.

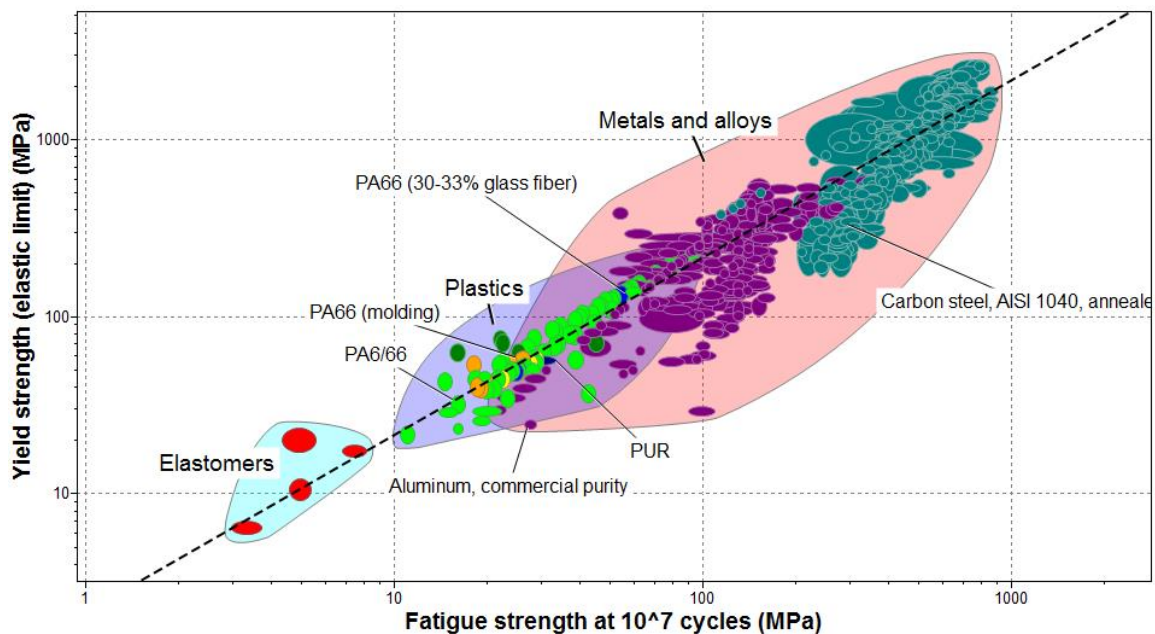


Figure 1. 14: comparison between Yield strength and Fatigue Strength

In this graph it is possible to demonstrate the consideration made at the beginning of this paragraph. The metal and the elastomers are the upper and lower limits of the line and the plastic materials seem to be the solution in the middle. The Polyurethane and Polyamide (PA66) represent the solutions in the middle, which are more convenient by the economic point of view (Figure 1. 13). In the Figure 1. 14, also the PA66 reinforced with glass fiber has been highlighted in order to demonstrate that a hybrid solution between plastics and metals is possible only if the composite materials are involved. Unfortunately, it is well known that these kind of materials are used only for making aeronautical and motorsport components due to their high purchase and manufacturing costs.

The last comparison which could be made is between the Young Modulus and Poisson's ratio. These physical characteristics give us an idea about the stiffness and the compressibility behaviour of the materials. Higher Young's modulus means stiffness and higher Poisson's ratio means incompressibility. High stiffness is typical for the metal alloys, instead incompressibility behaviours is typical elastomer (Figure 1. 15). The comparison in Figure 1. 15 demonstrates again that the universe of the metals and elastomers are completely opposed. The plastic materials confirm again the middle position with respect to the other two domains. They are more rigid respect to the elastomers but more incompressible respect to the metals alloys.

All the comparisons made above show that plastic materials could be very interesting to be involved in tooling applications because they are economically convenient with respect to the traditional metal alloys and their behaviour could be suitable for most stamping applications.

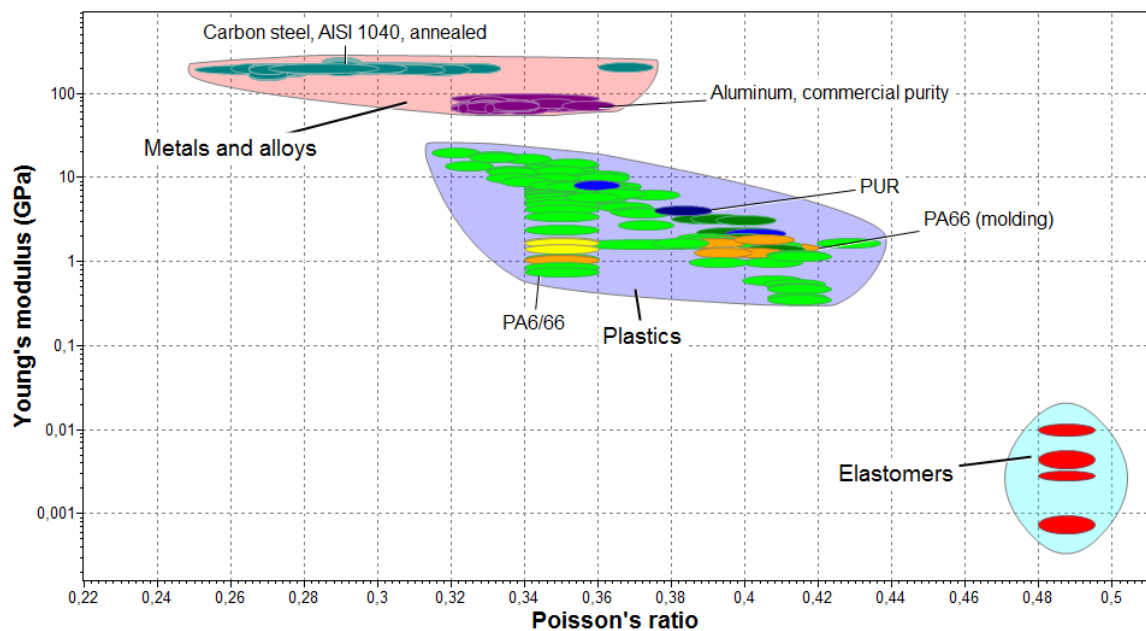


Figure 1. 15: comparison between Young's modulus and Poisson's ratio.

In the next chapters some case studies about tools made by plastics will be described in order to describe their behaviour in an industrial stamping operation. Also an experimental compensation algorithm will be proposed in order to simplify the design phase of them. At the end, a hybrid solution on air bending process will be proposed to demonstrate that the evolution of the traditional tooling setup could be found in the rapid tools.

1.5 Rapid tools

The personalization of the products is becoming a very important feature for the modern industry. The high request of new and modern technological products from the marketplace reduces drastically the products life cycles. This is the example of the mobile industry, which every six months release a new model with new features. The frenetic production of large series of different personalized components makes the traditional productions techniques too expensive in terms of manufacturing time and costs. In order to be more competitive, the development of rapid and economical methods are always required.

In the field of sheet metal forming, the rapid tooling technique was classified as a rapid prototyping method able to produce tools for prototypal production series with small amount of time and costs [26]. Along the years, the Rapid Tooling technique became an independent prototyping technology with its classification of different methodologies.

The classification of the Rapid Tooling methodologies developed over the years usually is not clear and the border of each class is not well defined. Despite this, the two main groups identifiable from the production methods are the direct and the indirect Rapid Tools. Then the indirect Rapid Tools can be divided in soft and hard tools (Figure 1.16).

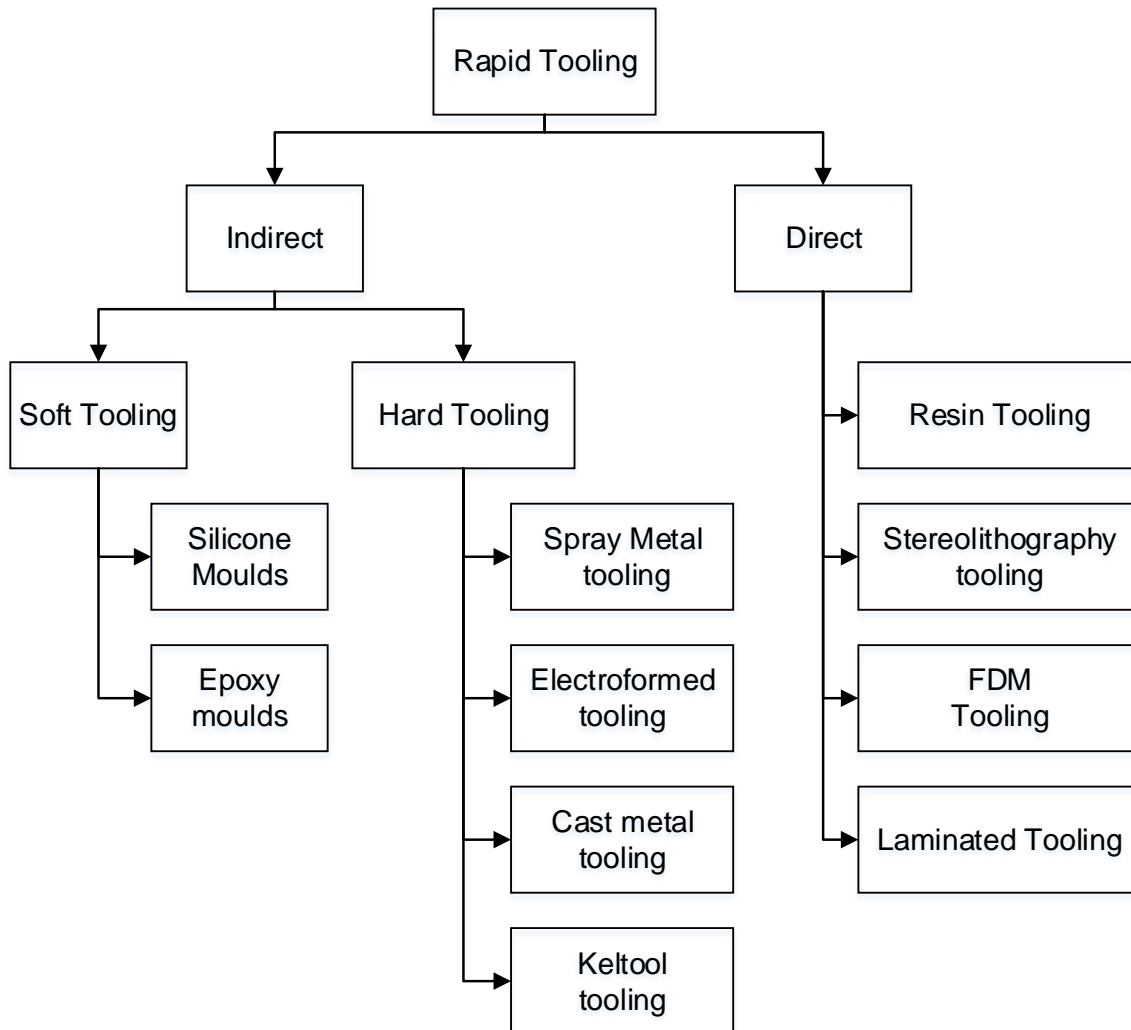


Figure 1.16: classification of rapid tooling techniques [26].

1.5.1 Indirect tooling

The indirect tooling techniques come before the diffusion of the rapid prototyping machines [27], they generate an initial rough component, which will be worked by successive operations.

1.5.1.1 Soft Tooling: silicon moulds

The silicon moulds allow to reduce drastically the management costs related to the purchase of material, manpower and production costs; it can be used to produce wax patterns and plastic or low-melting-point metal parts [26].

The main advantages of these moulds are: the thermal and chemical strength, reduced shrinkage, high flexibility and wear resistant, ease to be manufactured by casting processes.

The process used to make these tools is the RTV (Room Temperature Vulcanizing). The process starts by a prototypal master pattern where the separation plane and the casting channel are identified. Then everything is moved inside a foundry mould where the resin is drained at atmosphere pressure. Then the residual gases are removed from the mould and everything is moved into a furnace for the final hardening step. By this process is possible to make flexible moulds characterized by very low friction coefficient, which allows making very complex components [26]-[27]. The silicon moulds are limited to low pressures, low volume and low temperature production processes. A popular application is in vacuum casting of prototypal polyurethane components.

Silicon mould method provides fast, inexpensive moulds, excellent part cosmetics, and the option of using multiple materials.

The life of silicon moulds is closed around 50 parts with a gradual deterioration of surface quality.

Another benefit of silicone rubber tooling is the negative draft (undercuts) that can be achieved due to the flexibility of the mould material.

Another application is in spin casting. In the spin casting liquid metal or plastic is poured inside a central feed channel and the silicon mould is rotated in order to fill the liquid inside all cavities. The life of the silicon mould for this application is around 100-300 cycles. The implementation of silicon moulds has been investigated in stamping process also [28]. The author performed experimental activity by comparing different tools setup made entirely by silicon rubber, polyamide (PA) and a mixed tools setup made by aluminium and silicon rubber. The experimental results shown that soft materials can be used for flexible forming but it is hard to set the process due to their low durability.

In addition, has been demonstrated that tools setup made by semi-rigid plastics can achieve better results in terms of die durability and spring back.



Figure 1. 17: example of silicon moulds [29].

1.5.1.2 Soft Tooling: epoxy moulds

The epoxy moulds are often used for making small batches of functional component by injection moulding. One of the main advantages of using epoxy resin is to produce very big tools with very small investment. As revealed in advance, the low thermal conductivity and wear strength restricted their application in the injection moulding process.

Also this kind of moulds are generated by foundry process. The resin is poured in a mould with a positive master, made by Stereolithography (STL), inside and then cured inside a furnace. Runners, gates and air vent can be added to the master or can be machined after the casting. Generally, the life of epoxy mould is closed from 50 to 500 pieces, depending to the complexity of the components.

A similar approach has been found in a recent paper [29], where a rapid tools setup made by polymer concrete has been manufactured with epoxy mould method. Elevated risk of fracture on the tested solution has been found, but the research is still in progress.



Figure 1. 18: industrial example of epoxy moulds [31].

1.5.1.3 Hard tooling: spray metal tooling

Spray metal moulds are used generally in low pressure processes like rotational moulding and vacuum forming and usually in injection moulding. Other applications can be found in literature [32] for sheet metal forming application where the authors demonstrate that a polymeric tool setup covered by WC-FeCSiMn can be suitable for stamping sheet metal made by high-strength steels.

The process consists in spraying melted metal directly on the prototypal mould, where a release agent has been applied previously. The melted metal is obtained from a spraying arc system where the electrodes at the end fuses a metal wire. The fused metal particles will generate the superficial layer on the prototypal mould. The process is repeated until the required thickness of metal shell is obtained (0.5-5 mm). The properties of metal spray moulds depend on the metal used, its structure and the type of support of the metal shell.

The metal is often kirksite, a zinc-based alloy, although new techniques can successfully spray other metals, including steel.

The normal tool life is several hundred injection moulded parts. Very good results have been reported for nickel-spray tooling. The hardness of a nickel shell (Rockwell hardness Hc 50±58) provides excellent abrasion resistance and the tool life is adequate for high volume production [26].

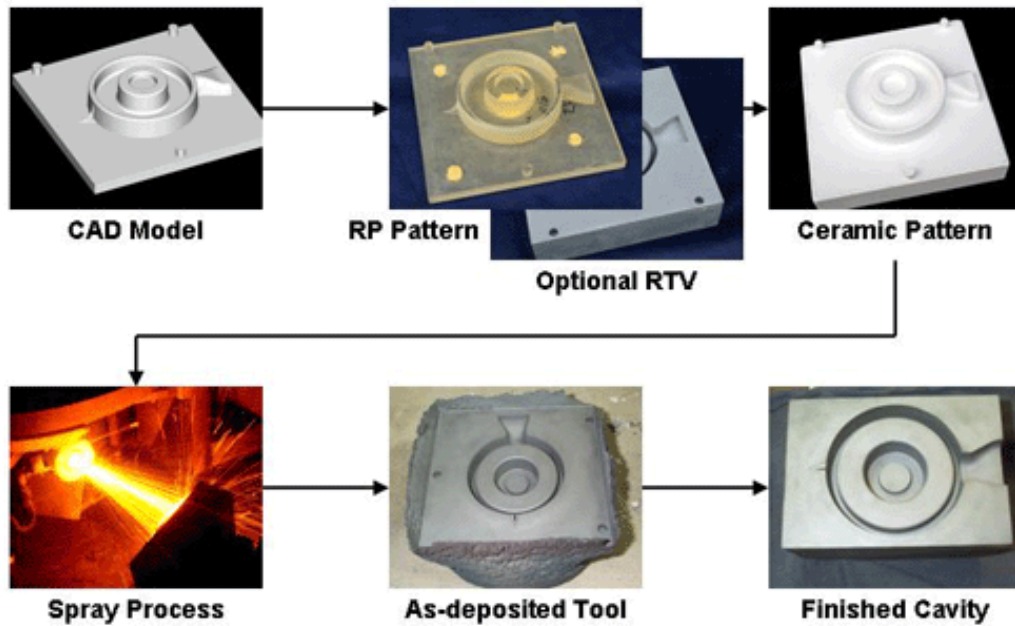


Figure 1. 19: metal spray process [33].

The mould-making process introduces little or no additional shrink, so the process is relatively accurate.

The disadvantages are that the mould has a limited life, and complex shapes and features may require adding metal inserts, increasing cost and production time.

1.5.1.4 Hard tooling: electroformed tooling

The electro-depositioning process is generally used to improve the characteristic of the surfaces by galvanic deposition of thin chrome or nickel layer. The same process can be used for covering a prototypal mould like the spraying process described before.

The method consists in covering a prototypal master with a conductive paint, then the component is immersed in a galvanic bath in order to deposit the metal layer. Thanks to the mechanical properties of the shell together with the excellent reproduction of the surface finish, the process is widespread within the aerospace industry. The main disadvantage is related to the time required to electroform the shell (about 2 weeks for 3 mm) [26]. For prototype applications the shell thickness can be reduced to 1 mm with rigidity of the tool provided by a good backing.

The metal shell can be involved in making of inserts for plastic moulds or stamping punches [27].

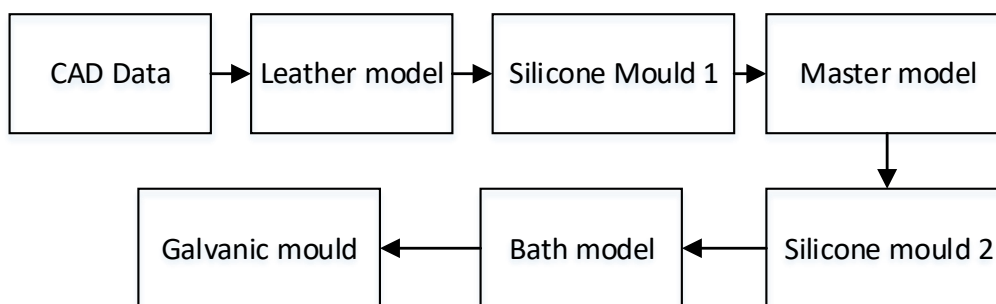


Figure 1. 20: process stages in electroforming.

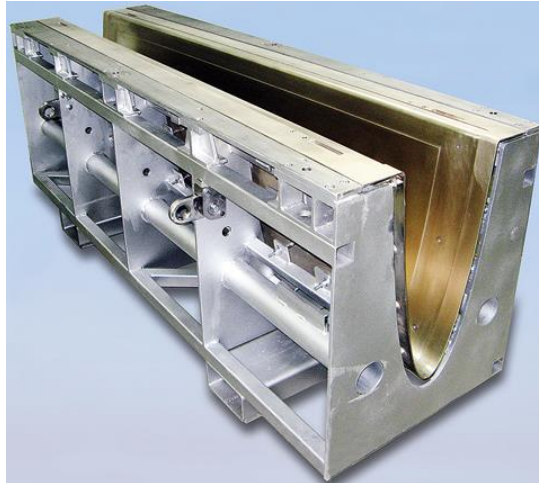


Figure 1. 21: example of shell mould obtained by electrodeposition [33].

1.5.1.5 Hard tooling: cast metal tooling

Tools used for injection moulding and die casting are manufactured by investment casting. The Rapid prototyping techniques, like 3D Printing are used for making the sacrificial model for the investment casting process [26]. The pattern for moulds and die can be generated in two ways. The first method consists in a CAD reverse engineering, starting by the solid model of the component by dividing it on the split line, defining the cavity shapes and adding the remainder of the tools cavity. So a prototypal mould can be made by using Rapid prototyping techniques and involved as a pattern in an investment casting process. Otherwise, starting by the positive prototypal component, a resin cast mould can be made and used as pattern in a sand casting of the metal mould. In both cases following machining operations are needed in order to improve the surfaces quality.

The tools can be cast in aluminium or zinc for prototypal purposes (100-500 pieces) or by steel for high production volume.

1.5.1.6 Hard tooling: KelTool tooling

The 3D Keltool process allows producing metal tools starting by a component made by rapid prototyping techniques. 3D Keltool is a powder metal process used to make injection-mould inserts

and other durable tooling from master patterns.

The process can be divided in four main steps:

- Starting by the CAD solid model of the component, a master pattern is generated by Stereolithography. The produced model is generally called "Master Pattern" because the 3D Keltool process uses it as patterns to produce silicone rubber transfer moulds.
- The master pattern made by STL technology is covered with the epoxy resin in order to generate the "Transfer Mould".
- The "Transfer Mould" is filled with a mixed solution composed by 70% of tool steel powder and tungsten carbide powder, and 30% epoxy binder which is used to bring the two powders together. At the end, the product (green part) is de-moulded and put into a hydrogen-reduction furnace for sintering at 100°C. During the sintering the epoxy binder is burned-off and the resultant part (brown part) will be composed by steel and tungsten carbide, and 30% void (air).

- As final step, the brown part is filled with copper in order to obtain a final part composed by 70% of tool steel powder and tool steel powder, tungsten carbide powder, and 30% of copper.

The hardness of the resultant tool insert is Rc 35-55. Keltool inserts made of tool steel should survive for at least one million shots [26]. The process is best suited for small parts [35].

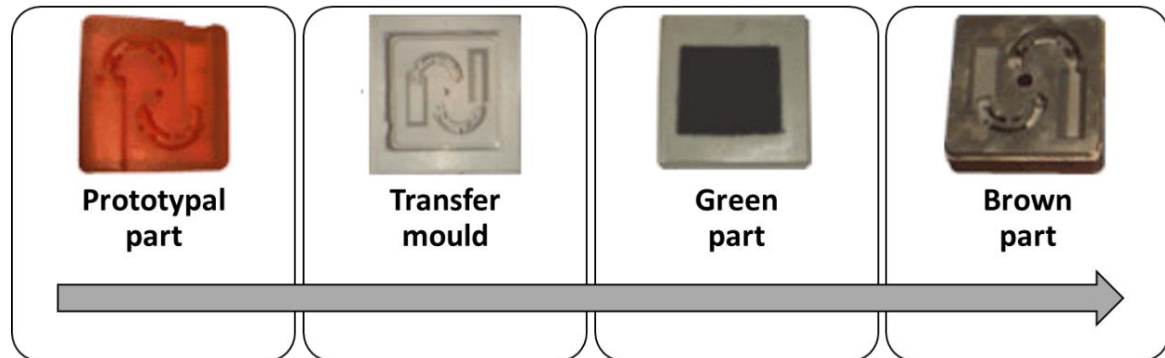


Figure 1. 22: Keltool process steps [35].

1.5.2 Direct tooling

All the indirect methods described before involve making a master pattern by rapid prototyping techniques for generating the final tool. The making of a master pattern introduces one step more in a general tool manufacturing process. This extra step introduces intrinsically errors or inaccuracies on the final tool.

The direct tooling techniques allow to build the tools setup suitable for production without the need of a master pattern. The main advantage in direct tooling methods is related on the better controlling of the inaccuracies. Most of the direct rapid tools are made by rapid tools technologies like Stereolithigraphy (STL), Fused Deposition Modelling (FDM), Laminate Object Manufacturing (LOM). There is also the possibility to generate rapid tools through traditional technology like milling (see paragraph 1.5.2.1) or machining.

The examples of the components achievable by these methods are: tools insert for injection moulding, stamping tools made by polyurethane resins, shells for investment casting process, cores for sand casting process.

The main objective of this Doctoral Thesis is related to the study of some industrial cases which involves direct rapid tools in order to generate a sort of guidelines useful for the design of this particular solutions.

1.5.2.1 Resin tools

This technique has been employed in injection of wax patterns for investment casting. Thanks to their characteristic related to the temperature of glass transition of 80°C which is higher than the wax melting point (50-55 °C). The usual injection pressure is 3.5 MPa. The material involved in this techniques are polyurethane or polycarbonate. It has been demonstrated that manufacturing resin tools is 60% faster than Zamak tools [36]. In automotive industry, due to the size of the external panel components, casting dies are not advantageous in terms of time and cost of preparation. In [37] a polymer-metal carcass die method has been studied in order to manufacture huge stamping tools with 40% less lead time and 33% less investment in respect to the traditional cast iron die production method.



Figure 1. 23: industrial application of resin tools [43].

Other application can be found in stamping processes where the polyurethane direct tools substitutes the entire stamping tools setup. They are made by direct milling operation from a polyurethane bar. The polyurethane tools can be used directly in a usual stamping press machine without needing of adjustments. They are industrially used for making demo components or producing small batches [37]-[41]. In deep drawing of pure copper foils, the resin tools have been coupled with Nylon 66 auxiliary sheet in order to prevent wrinkling effect. In that case the clearance between the punch and die was set to be approximately 84.4% of the total thickness of the auxiliary sheet and foil blank. The Nylon 66 auxiliary sheet was subjected to ironing during deep drawing and the foil blank was subjected to strong compression in the thickness direction in the wall of the foil cup as well as at the flanges of the die shoulder, due to the action of the punch, Nylon 66 auxiliary sheet and PTFE die [42].

1.5.2.2 Stereolithography tooling

In the indirect tooling methods, the Stereolithography (STL) process was involved for making the master pattern.

The STL is based on the concept of the photopolymerization process. In the photopolymerization process a liquid photosensitive polymer is solidified under the action of the ultraviolet radiations.

The ultraviolet beam is focused onto the surface of the liquid photopolymer by forming a single layer of the desired 3D object. Then an elevator platform moves along the vertical direction, by a distance equal to the thickness of a single layer of the design, in order to allow the beam to be directed on the successive layer. The process is repeated for each layer (slicing) of the design until the 3D object is complete.

Designs are then immersed in a chemical bath in order to remove any excess resin and cured in an ultraviolet oven.

The Stereolithography techniques allows to produce directly usable tool, it is also possible to inject polymer into SL cavities and produce usable parts. The parts are similar to those created with traditional metal tooling.

Currently only polymers with lower melting points are being moulded. A drawback of the SL tooling process is that the tools are susceptible to failure after producing only a small number of parts. Tools produced by Stereolithography can make over 500 parts [44].

The thermal properties of Stereolithography materials, notably the low thermal conductivity, have often been stated as a vulnerability of this process. The mould wear mainly depends on the individual polymer used, furthermore appropriate choices in mould design and process variables can reduce the risk of failure.

Also consider that the thermal characteristics of SL moulds have an influence on the morphological structure of the parts. In some polymers, this may lead to a difference in the morphology of parts from SL tools as compared to those from metal tools. Such morphological differences can affect the shrink and mechanical properties of the moulded part [45].

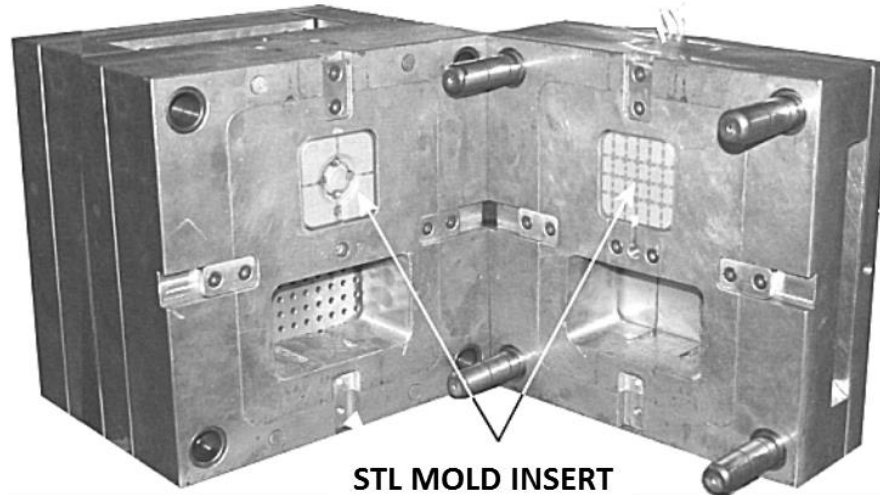


Figure 1. 24: example of injection mould insert made by STL technology [46].

1.5.2.3 FDM tooling

Like the STL process, also the FDM (Fused deposition modelling) is an additive manufacturing technology suitable for modelling, prototyping and production applications.

The first step of the FDM technology consist in the mathematical slicing of the STL solid model and the orientation of it. The orientation of the model is necessary for finding the setup of the supports needed for locking the cantilever protrusions of a component.

After the initial setup, the process consists in the filaments deposition of melted thermoplastic material from a movable extruder. The extruder follows a tool path made by CAM (Computer Aided Manufacturing) software. It builds the component layer by layer along the vertical direction similar to the STL method described before. The orientations design of the plastic filaments, as for the composite materials, depend to the structural applications of the final component. The supports are made by a secondary extruder in order to be easily removed at the end of the process.

A lot of material are available for FDM technology such as Acrylonitrile Butadiene Styrene ABS, Polylactic acid PLA, Polycarbonate PC, Polyamide PA, Polystyrene PS, lignin, rubber and many others.

The FDM technology allows to produce dies for process like Blow moulding and Hydroforming. FDM tools can help companies move from tool design to production in as little as a week. This manufacturing process allows reducing the cost for die production by 50% to 70% and reduces lead-time by 60% to 80% **Errore. L'origine riferimento non è stata trovata.** In Hydroforming application can be found in **Errore. L'origine riferimento non è stata trovata.**, where the company manufactured FDM tool for forming aluminium alloys, stainless steels, titanium and nickel-based super alloys such as Inconel. Sheet thicknesses that have been formed successfully range from 0.41 mm to 2.54 mm. After 600 of cycles the tools shown no signs of wear. The tools made by FDM are lighter than traditional metal tools, so the safety of the tool handlers and machine operators is generally improved. The efficiency

of the hydroforming process is improved also for the natural lubricity of the FDM materials. The recommended hydroforming pressure for FDM tools are listed in Table 1. 3. Economical comparisons have been briefly reported from industrial experience in Table 1. 4.

Material	Pressure range
Acrylonitrile butadiene styrene (ABS-M30)	Up to 20 MPa
Polycarbonate (PC)	20 MPa to 55 MPa
ULTEM 9085	Up to 69 MPa

Table 1. 3: Hydroforming pressures recommended for FDM tools materials.

Method	Cost	Time
CNC machining	1400 €	5 days
FDM	420 €	1 days
Savings	980 € (70%)	4 days (80%)

Table 1. 4: cost comparison between traditional and FDM tools manufacturing methods [47].

Other application can be found in automotive industry for sheet metal stamping process [49]. In the study dimensional conformance analyses have been carried out for DC04 and S355MC components formed by FDM dies. The author demonstrate that FDM tools are suitable for stamping DC04 components in terms of dimension tolerances within 100 parts. Instead S355MC components are harder than DC04 so using FDM is not convenient in term of tolerance range. A very recent interesting approach has been found in [50] where a robot has been used for manufacturing a die by FDM process and a second robot has been involved in sheet incremental forming operation. The achieved results demonstrated the evidence of the general feasibility of the used approach.



Figure 1. 25: commercial example of hydroforming die made by FDM [48].

1.5.2.4 Laminated Tooling

Another alternative method for manufacturing tools cavities is Laminated Tooling. It employees the similar principle of the LOM process where layers of metal sheet are cut in order to replicate slices through CAD model. The profiles are manufactured by water jet or laser cutting processes.

In order to produce the forming tool, the CAD model should have the same form of the required cavity. A stack of laminates can be made for reproducing the original CAD model by cutting all the layers of the cavity in sheet metal steel. In order to avoid complex post-process cutter path planning, either clamping or diffusion bonding are used for generating the pseudo-solid cavity in hardened tool steel. In this process,

thick laminates of 1 mm are usually involved so the surface of the tools must be machined by a finishing operation.

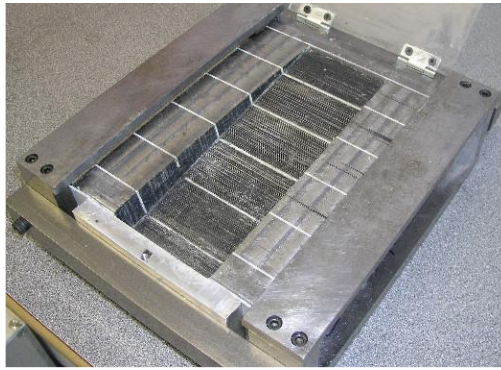


Figure 1. 26: example of laminated tools with integrated cooling channels [44].

Laminated tools are involved in a lot of moulding techniques like press tools, blow moulding, injection moulding and vacuum forming. Application in stamping processes can be found in [51] where the study of very large stamped component has been performed. The research is now pushing the laminate tools in pressure die casting also.

The tools life can be related to the material used for the initial sheets which could be hardened after the cutting and lamination operations. The complexity of the achievable die shape is limited to the thickness of the layers. The advantage in using laminated tooling is the possibility in changing the design of the tool by replacing the laminates. If needed the cooling channel can be also easily incorporated inside the tools [44].

1.6 Conclusion

In this chapter, I demonstrated that a lot of tool setup solutions for sheet metal forming processes are available in the literature and as industrial cases.

The traditional solutions composed by rigid tool setup are largely used in most industrial cases especially for high volume productions. The rigid tool solutions are supported by a very large quantity of literature publications, which define the guidelines for an optimized tools manufacturing and process design. On the contrary the deformable tools are very complex to be managed in terms of design operations and are suitable for very small production volume. There are a lot of publications which support the advantages of the deformable tools and a lot of case studies but the industrial diffusion is limited to very particular sectors like motorsport, aeronautical or military.

Considering these two macro categories of tooling setup described (rigid tools and deformable ones), there is the necessity to develop solutions for middle volume productions, easily to be designed and managed in term of time and costs. A possible solution can be found in rapid tooling methods, which allow producing tools with reduced investment of time and costs with respect to rigid tools solutions. The methods described in the previous paragraphs show that a lot of literature is available about the concept of the rapid tools, but very few design methods or design guidelines have been developed [28], [36] and [49].

The definition of rapid tooling method refers to rapid production of parts that function as a tool as opposed to being a prototype or a functional part [52]. But in most of

described methods it is very difficult to assume that the entire production process is more rapid than a traditional way to manufacture a rigid tool setup. If on one hand the manufacturing process is faster, the design phase can be very long, especially when no design guidelines are available.

In Table 1. 5 the main characteristics of the described rapid tooling (RT) technologies has been presented. Considering the maximization of the tool life ($t_r \geq 10.000$ components), in order to manufacture more components as possible, the minimization of the development time ($D_t < 1$ week), the resin tooling method is the best compromise between all the available tooling technologies suitable for sheet metal forming processes.

Rapid Tooling Technology	Tools materials	Development time (D_t)	Manufacturing Processes	Worked materials	Tool Life (T_r)
Silicon moulds	Silicon resins	3 to 4 weeks	Injection moulding, Vacuum casting, Spin casting	wax	100 to 300
Epoxy moulds	Epoxy resins (aluminium filled)	3 to 4 weeks	Injection moulding, sheet metal forming	Plastics, wax, aluminium	50 to 500
Spray metal	Tin-zinc, steel (sprayed), nickel	1 to 2 weeks	Injection moulding, vacuum forming, rotational moulding, sheet metal forming	Plastics, wax, steel, aluminium	1.000 to 10.000
Electroformed	Steel, Nickel, aluminium, copper	>3 weeks	Injection moulding, Sheet metal forming , Hydroforming	Plastics, steel, aluminium	>5.000
Cast metal	Aluminium, steel	>2 weeks	Investment cast, injection moulding	Plastics	>2.000
Keltools	70% Steel and 30% copper	>2 weeks	Injection moulding	Plastics	>1.000.000
Resin	Polyurethane resins	<1 week	Injection moulding, Sheet metal forming	Plastics, steel, aluminium	>10.000
STL	Epoxy resins, polystyrene, acrylate	<1 week	Injection moulding	Plastics, wax	200 to 2.000
FDM	ABS (infiltrated epoxy or aluminium)	<1 week	Injection moulding, Hydroforming, Sheet metal forming	Wax, steel, aluminium	600
Laminated	Paper, wood, steel, plastics	>2 weeks	Injection moulding, Sheet metal forming	Wax, aluminium, steel	>2000

Table 1. 5: resume of the rapid tooling technologies obtained from the analysis of the state of the art.

In Figure 1. 27, the schematization of the objective of this doctoral thesis has been shown by representing the qualitative positioning of the three tools setup solutions described above with respect to the production batch quantity and the developing time. In the paragraphs 1.4, it has been described that the rigid tools setups allow producing bigger production batches with respect to the deformable ones. If the developing time is considered as a sum of design time and manufacturing time, the rigid tools and deformable tools can be positioned at the same level; because the rigid tools can be designed in reduced time with respect to deformable ones, but the manufacturing time is higher for the reasons largely explained in paragraph 1.4.

As described in paragraph 1.5, the production batch volume made by the rapid tools can be positioned in the middle between the deformable and rigid tools setups, but the developing time is higher with respect to the other two tool setup solutions (rigid and deformable). If the manufacturing time is smaller (depending by the rapid tools methodology chosen), the design time is very high because very few guidelines and information about their performances are available in literature.

As resumed in the Figure 1. 27, the main objective of this thesis is to reduce the developing time of the rapid tools by defining some guidelines for the design of a reliable tools setup with resin rapid tools method.

This objective will be reached by presenting 4 case studies, which will be compared with the traditional rigid tools solutions in order to determine a new definition “smart tools”. This definition will characterize the best compromise of tools setup in terms of time and costs saving in manufacturing and design phases.

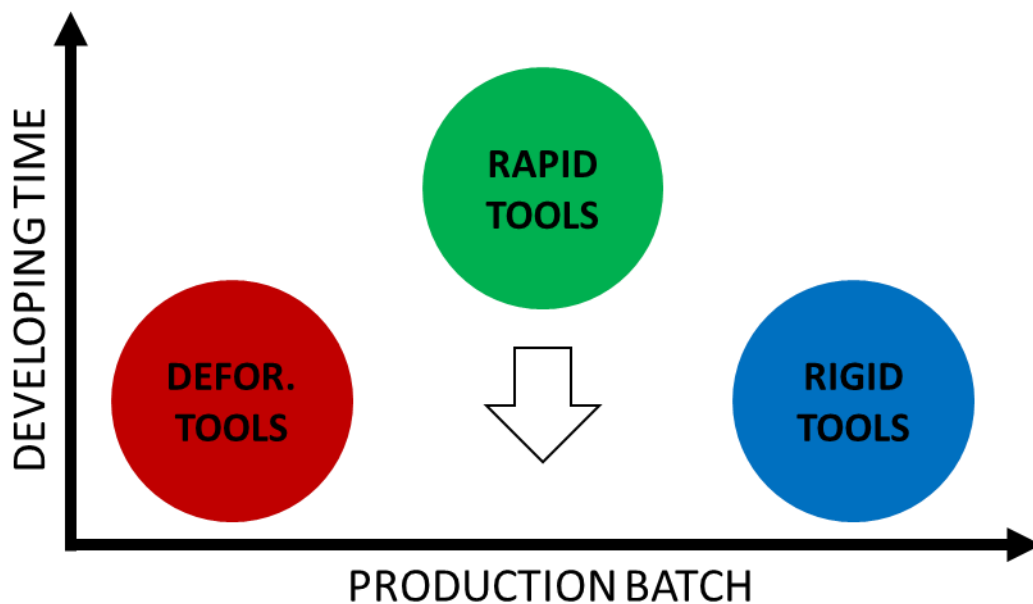


Figure 1. 27: schematization of the objective of this research thesis.

1.7 References

- [1] Iorio, L., Maspero, E., & Strano, M. (2014). Hydroforming of locally heat treated tubes. *Journal of Manufacturing Processes*, 16(2), 157-165.
- [2] Malhotra R, Cao J, Ren F, Kiridena V, Cedric Xia ZZ, Reddy NV. Improvement of Geometric Accuracy in Incremental Forming by Using a Squeezing Toolpath Strategy with Two Forming Tools. *ASME. J. Manuf. Sci. Eng.* 2011;133(6):061019-061019-10. doi:10.1115/1.4005179.
- [3] Del Prete A, Papadia G, Manisi B. Computer Aided Modelling of Rubber Pad Forming Process. *Key Engineering Materials*. 2011 Mar; 473:637–644.
- [4] Son C-Y, Jeon Y-P, Kim Y-T, Kang C-G. Evaluation of the formability of a bipolar plate manufactured from aluminum alloy Al 1050 using the rubber pad forming process. *Proceedings of the Institution of Mechanical Engineers, Part B: Journal of Engineering Manufacture*. 2012 Jan 30;226(5):909–918.
- [5] Ramezani M, Ripin ZM, Ahmad R. Sheet metal forming with the aid of flexible punch, numerical approach and experimental validation. *CIRP Journal of Manufacturing Science and Technology*. 2010 Jan;3(3):196–203.
- [6] Giuseppe Sala. A numerical and experimental approach to optimise sheet stamping technologies: part II - aluminium alloys rubber-forming. *Materials and Design*. 2001; 22:299–315.
- [7] Ramezani M, Ripin ZM. Analysis of deep drawing of sheet metal using the Marform process. *The International Journal of Advanced Manufacturing Technology*. 2011; 59(5-8):491–505.
- [8] Strano M. Optimization under uncertainty of sheet-metal-forming processes by the finite element method. *Proceedings of the Institution of Mechanical Engineers, Part B: Journal of Engineering Manufacture*. 2006; 220(8):1305–1315.
- [9] Vollertsen F, Breede R, Beckman M. Process layout and forming results from deep drawing using pressurized membranes. *Proceedings of the Institution of Mechanical Engineers, Part B: Journal of Engineering Manufacture*. 2001 Jan 1;215(7):977–990.
- [10] Cai Z-Y, Wang S-H, Xu X-D, Li M-Z. Numerical simulation for the multi-point stretch forming process of sheet metal. *Journal of Materials Processing Technology*. 2009;209(1):396–407.
- [11] Chua CheeKai, Leong KahFai, Liu Zhong Hong, *Rapid Tooling Manufacturing, Handbook of Manufacturing Engineering and Technology*, Springer, 2014, p. 1-22.
- [12] Rossi M., 1979, “Stampaggio a freddo delle lamiere”, Hoepli, Milano.
- [13] Santochi M., Giusti F., 2012, “Tecnologia Meccanica e studi di fabbricazione”, Casa Editrice Ambrosiana.
- [14] DIN 8584-3: Manufacturing Processes Forming Under Combination of Tensile and Compression Conditions - Part 3: Deep Drawing; Classification, Subdivision, Terms and Definitions
- [15] A. Mentella, *Metodi di Progettazione Avanzata per la Curvatura di Tubi a Controllo Numerico*, 2009. Doctoral Thesis at Università di Cassino.
- [16] L. Iorio, *Curvatura Di Tubi A Sezione Non Circolare: Analisi Fem E Sperimentale*, 2009. Bachelor Thesis at Università di Cassino.
- [17] M. Strano, L. Carrino, R. Gemignani. *CNC Tube bending with variable radius*. Montecatini: AITeM, 2008.
- [18] D.-K. Leu, «A simplified approach for evaluating bendability and springback in plastic bending of anisotropic sheet metals» *Journal of Material Processing Technology*, n. 66, pp. 9-17, 1997.
- [19] L. J. De Vin, «Curvature prediction in air bending of metal sheet» *Journal of Material Processing Technology*, n. 100, pp. 257-261, 2000.

- [20] K. S. R. Elkins, «Non-Iterative Control of Small-Radius Bend Angle» *Journal of Manufacturing Processes*, vol. 1, n. 1, pp. 18-30, 1999.
- [21] H. N. N. A. T. Kim, «Prediction of Bend Allowance and Springback in Air Bending» *Journal of Manufacturing Science and Engineering*, vol. 129, pp. 342-351, Aprile 2007.
- [22] M. Monno, B. Previtali, M. Strano (2012). *Tecnologia meccanica. Le lavorazioni non convenzionali*. p. 1-508, ISBN: 9788825173772, Città Studi Edizioni.
- [23] Maziar Ramezani, Zaidi Mohd Ripin, 2012, “Rubber-pad Forming Process – Technology and Applications”, Woodhead Publishing.
- [24] Di Orville D. Lascoe, 1998, “Handbook of Fabrication Processes”, International, ASM, pp. 53-56.
- [25] IORIO, Lorenzo, et al. Application of the Kalai-Smorodinsky approach in multi-objective optimization of metal forming processes. *International Journal of Material Forming*, 2016, 1-12.
- [26] A Rosochowski, A Matuszak, Rapid tooling: the state of the art, *Journal of Materials Processing Technology*, Volume 106, Issues 1–3, 31 October 2000, Pages 191-198, ISSN 0924-0136, [http://dx.doi.org/10.1016/S0924-0136\(00\)00613-0](http://dx.doi.org/10.1016/S0924-0136(00)00613-0).
- [27] Gatto A., Iuliano L., 1998, “Prototipazione rapida: La tecnologia per la competizione globale”, *Tecniche Nuove*, Milano.
- [28] QUADRINI, Fabrizio; SANTO, Loredana; SQUEO, Erica Anna. Flexible forming of thin aluminum alloy sheets. *International Journal of Modern Manufacturing Technologies*, 2010, 2.1: 79-84.
- [29] Silicone Molds - <http://www.rapidmade.com/pattern-and-tool-making-silicone-casting-molding-thermoforming/> accessed on 13/01/2018.
- [30] Guillaume C., Mousavi A., Brosius A., Hybrid Deep Drawing Tool for Lubricant Free Deep Drawing, *ESAFORM* 2017.
- [31] Epoxy molds - <http://www.ineo.es/servicios/colada-al-vacio> accessed on 13/01/2018.
- [32] J. Witulski, M. Trompeter, A.E. Tekkaya, M. Kleiner, High wear resistant deep drawing tools made of coated polymers, *CIRP Annals - Manufacturing Technology*, Volume 60, Issue 1, 2011, Pages 311-314, ISSN 0007-8506, <http://dx.doi.org/10.1016/j.cirp.2011.03.149>.
- [33] Spray Metal Tooling - https://commons.wikimedia.org/wiki/File:Sprayed_Metal_Tooling_processing_steps.gif accessed on 13/01/2018.
- [34] Electroformed Tools - <https://fi-sch.de/en/galvanisation/> accessed on 05/07/2017
- [35] Keltool Process - http://www.3dsystems.ru/products/productiontooling/3dkeltool/products_3dkel_howitworks.asp.htm accessed on 13/01/2018.
- [36] H. Müller, J. Sladojevic, Rapid tooling approaches for small lot production of sheet-metal parts, *Journal of Materials Processing Technology*, Volume 115, Issue 1, 22 August 2001, Pages 97-103, ISSN 0924-0136, [http://dx.doi.org/10.1016/S0924-0136\(01\)00749-X](http://dx.doi.org/10.1016/S0924-0136(01)00749-X).
- [37] Durgun, İ., Altinel, S.A., Sakin, A., Aybaraz, E., Polat, E., (2013), “Prototype Tooling of Sheet Metal Components of Car Body”, 7 International Conference and Exhibition on Design and Production of Machines and Dies / Molds, Antalya
- [38] A. Donghi, Studio di un processo di stampaggio mediante utensili deformabili, Master Thesis at Politecnico di Milano.
- [39] IORIO, Lorenzo, et al. Design of Deformable Tools for Sheet Metal Forming. *Journal of Manufacturing Science and Engineering*, 2016, 138.9: 094701.
- [40] IORIO, Lorenzo; STRANO, Matteo; MONNO, Michele. Development of a Die Compensation Algorithm for Sheet Metal Stamping with Deformable Tools. In: *ASME 2015 International Manufacturing Science and Engineering Conference*. American Society of Mechanical Engineers, 2015. p. V001T02A089-V001T02A089.

- [41] Mário Pinto, Abel D. Santos, Pedro Teixeira, P.J. Bolt, Study on the usability and robustness of polymer and wood materials for tooling in sheet metal forming, *Journal of Materials Processing Technology*, Volume 202, Issues 1–3, 20 June 2008, Pages 47-53, ISSN 0924-0136,
- [42] Yasuo Marumo, Hiroyuki Saiki, Liqun Ruan, Influence of resin dies and resin auxiliary sheets on deep drawability of metal foil, *Journal of Materials Processing Technology*, Volumes 162–163, 15 May 2005, Pages 530-533, ISSN 0924-0136.
- [43] A. Donghi, Realizzazione di un riflettore tramite un processo di stampaggio e di idroformatura, Bachelor Thesis at Politecnico di Milano.
- [44] HAGUE, R. J. M.; REEVES, P. E. Rapid prototyping, tooling and manufacturing. iSmithers Rapra Publishing, 2000.
- [45] Wohlers: Wohlers Report 2006: Rapid prototyping tooling and manufacturing state of the industry, Annual Worldwide Progress Report (Wohlers, Fort Collins 2006).
- [46] BEAL, V. E.; AHRENS, C. H.; WENDHAUSEN, P. A. The use of stereolithography rapid tools in the manufacturing of metal powder injection molding parts. *Journal of the Brazilian Society of Mechanical Sciences and Engineering*, 2004, 26.1: 40-46.
- [47] FDM tool costs - http://usglobalimages.stratasys.com/Main/Files/Application%20Briefs_AB/AB_FDM_MetalHydroforming.pdf?v=635850936681624518 accessed on 13/01/2018.
- [48] FDM Tooling - <http://www.stratasys.com/solutions/additive-manufacturing/tooling/metal-hydroforming> accessed on 13/01/2018.
- [49] Ismail Durgun , (2015),"Sheet metal forming using FDM rapid prototype tool", *Rapid Prototyping Journal*, Vol. 21 Iss 4 pp. 412 – 422.
- [50] Rieger M., Storkle D.D., Thyssen L., Kuhlenkotter B., Robot-Based Additive Manufacturing for Flexible Die-Modelling in Incremental Sheet Forming, ESAFORM 2017.
- [51] Juraj Hudák, Rapid Tooling for Production of Stamping Dies Components, *Transfer inovácií*, Vol. 24 pp 111-114.
- [52] CHUA, Chee Kai; LEONG, Kah Fai; LIU, Zhong Hong. Rapid Tooling in Manufacturing. In: *Handbook of Manufacturing Engineering and Technology*. Springer London, 2015. p. 2525-2549.

Chapter 2

Polymeric materials

2.1 Introduction

The polymeric materials, better known as plastic materials or polymeric resins, are substances composed by big organic molecules obtained from chemical bonds of monomers chain (Figure 2. 1).

Some polymers such as cellulose or natural rubber can be found in nature; other polymers like celluloid and Bakelite are industrially manufactured since 1870.

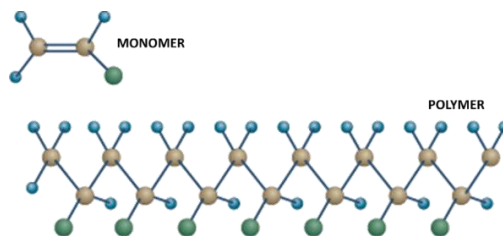


Figure 2. 1: scheme of a monomer and polymer chain.

The main characteristics of the polymers can be resumed as follows:

- Remarkable chemical inertness
- Low Yield strength
- High elongation at break
- Poor resistance at high temperature; very few polymers can be used at 250 °C
- Poor solubility in solvents solutions, except in case of similar chemical composition
- Poor thermal conductivity
- High thermal expansion coefficient

The mechanical properties such as yield strength, rupture strength and hardness are very modest, if compared to the metal materials. The tensile properties depend strongly to the temperature. [1]

The Yield stress can vary from 10 MPa (polyethylene) to 90 MPa (epoxy resins). In mechanical engineering applications, the following behaviours are generally investigated:

- *Flexural behaviour*: used for calculate the flexural Young's modulus by a three points bending test
- *Deflection load at high temperature*: this test evaluates the deflection entity and load at increasing temperatures
- *Impact strength*: the failure energy is evaluated in relation with the specimen section [J/cm²]. Through this test it is possible to evaluate if the material is ductile or brittle. The test can be executed at different temperatures.
- *Tensile test*: a standardized specimen is put in traction by tensile machine. This kind of test is the most used in engineering applications, especially when FEM simulations are made.
- *Compression test*: it is close to the tensile test. A cylindrical standard specimen is put in compression for evaluating the Young's elastic module and the load curve.

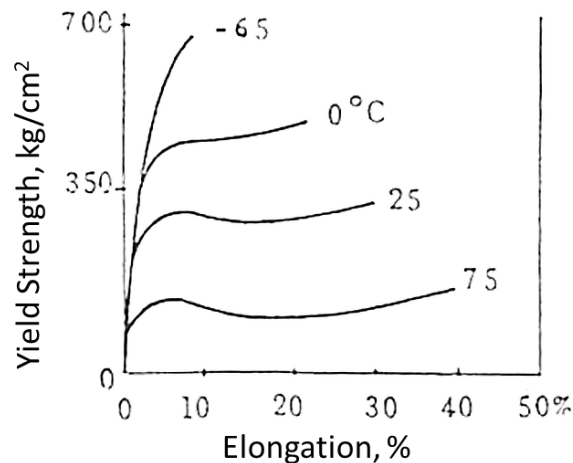


Figure 2. 2: example of polymers tensile behaviour at different temperatures.

Other dynamics characteristics can be obtained by a torsional pendulum at free oscillation (Figure 2. 3). The measure of the amplitude oscillations establishes the dynamic elastic torsion module, and the measurement of the amplitude variations determines the damping material. The execution of this test at different temperature allows to obtain the glass or crystalline transition temperatures and the thermal interval where the analysed material can be defined as brittle, strong, viscous [2]. From the shapes of the obtained curves it is possible to distinguish the amorphous thermoplastic materials, elastomeric and thermoset materials.

The electrical conductivity of the polymers is generally very low. In the recent years poly-acetylene mixed with iodine has been manufactured in order to having a material with the same electrical conductivity of the copper but more light weighted.

Most polymeric materials can be easily formed in injection moulding processes, worked in milling operations, joined, glued ore welded.

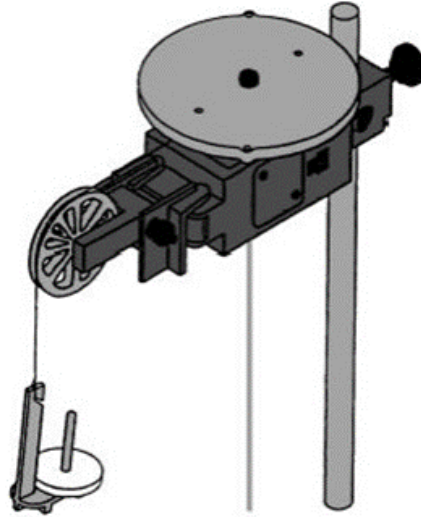


Figure 2. 3: torsional pendulum.

2.2 Classification

The polymers can be classified by taking in account the concatenation and the dislocation in the space [3]:

- *Linear polymers*: the macromolecules are enveloped along a specified direction (Figure 2. 4a).
- *Pronged polymers*: the macromolecules are enveloped along multiple directions (Figure 2. 4b).
- *Meshed polymers*: a set of macromolecules is mutually linked by transversal intermolecular chemical bond in order to make a three-dimensional solid reticulum (Figure 2. 4c).

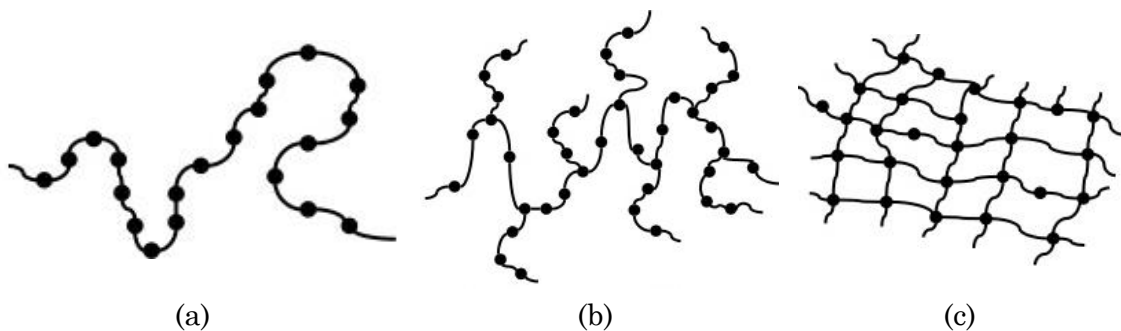


Figure 2. 4: schematizations of linear (a), pronged (b) and meshed (c) polymers **Errore. L'origine riferimento non è stata trovata.**

If the structure of the solid molecule is considered, the classification of polymers can be made as follows [4]:

- *Amorphous polymers*: they are characterized by a homogeneous and messy molecular structure. Every molecular chain is linked with others at several points in order to make a rigid structure (Figure 2. 5a).
- *Crystalline polymers*: the molecules are ordered in crystalline substructures in an amorphous matrix (Figure 2. 5b).

- *Semi-crystalline polymers*: composed by a mixed and heterogeneous amorphous and crystalline structures (Figure 2. 5c).

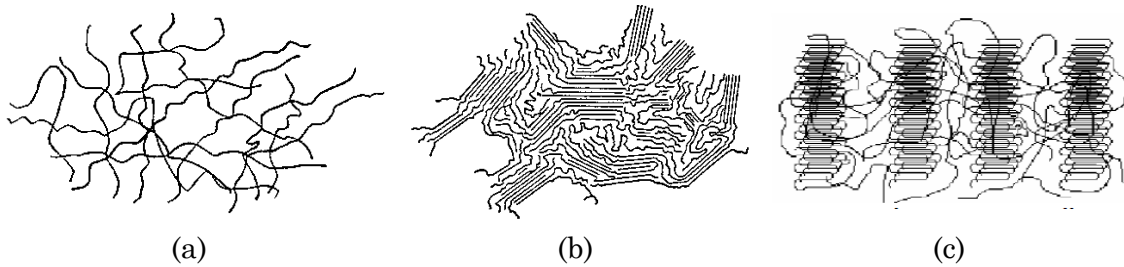


Figure 2. 5: schematizations of amorphous (a), crystalline (b) and semi-crystalline (c) polymers structures [6].

The polymers can be classified also by considering the disposition of the monomers chain [7]:

- *Homopolymers*: there is the repetition of the same monomer along the chain
- *Copolymers*: the chains are composed by the repetition of two or more monomers. The copolymers can be divided in:
 - *Static*: the sequence of the repeated monomers is random (Figure 2. 6a).
 - *Alternated*: the sequence of repeated monomers is regular (Figure 2. 6b).
 - *Segmented*: batches of monomers are repeated sequentially (Figure 2. 6c).
 - *Grafted*: the chains of different monomers are intersected to the main chain composed by a single type of monomer (Figure 2. 6d).

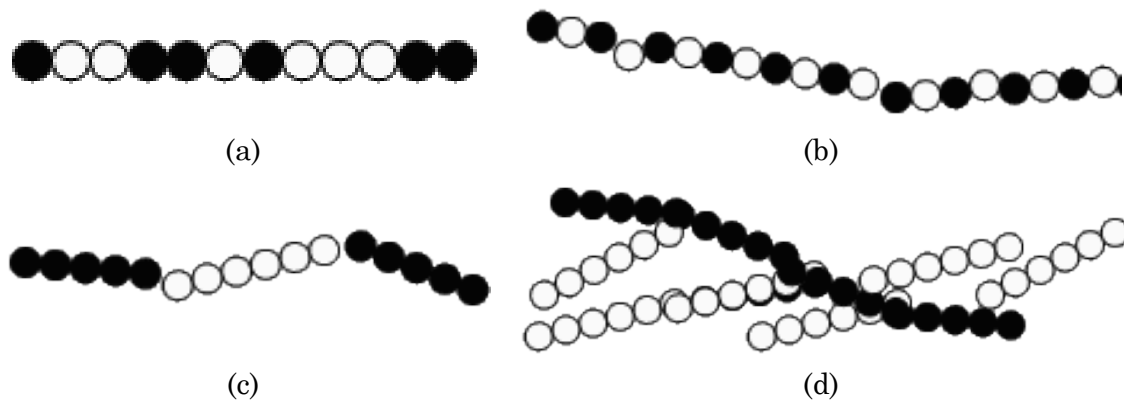


Figure 2. 6: schematizations of different types of monomers chain: static (a), alternated (b), segmented (c), grafted (d) [8].

The polymers can be also classified by considering the primary and secondary chemical bonds type:

- *Fibers*: the polymers chains are linear and oriented along a unique direction. They are very strong and offer good stability along the main fiber direction.
- *Elastomers*: composed by long and thin molecules which use to align themselves when are stretched and to come back to original shape when the

solicitation is ended. The elasticity is very high from 300% to 600%. In order to be very elastic, a lot of transversal chemical bonds are introduced inside the three-dimensional structure (vulcanization). The vulcanization is an irreversible operation; it is not possible to change the polymer structure by a thermal operation.

- *Plastics*: are synthetic polymers with an elevated molecular weight. They are stiff and hard at ambient temperature, when heated they can be modelled a lot of times [3].

Finally, if the thermal behaviour is considered, the polymers can be divided as [9]:

- *Thermoplastics*: the chains are linked together with Van der Waals forces and hydrogen chemical bonds. If heated, the chemical bonds separate themselves and the material melts. The glass transition and forming temperatures must be well defined in order to deform the material in a production process (Figure 2. 7a).
- *Thermosets*: the meshed structure prevents the separation of the chain at high temperature. If heated, the thermosets materials tend to burn instead of melt [10]. After the initial forming step, the thermosets materials cannot be easily deformed and, if heated, they become more stiff due to the meshed structure (Figure 2. 7b).



Figure 2. 7: example of Thermoplastics (a) and Thermosets (b) materials.

The macromolecules of the commercial polymers are frequently combined with additives in order to improve their structural properties or for reducing their price.

The most used additives are divided as follow:

- *Plasticizers*: they are organic and reduce the attractive forces between the chains of the thermoplastic polymers like the polyvinyl chloride (PVC). They improve the flexibility and the softness of the components.
- *Reinforcements*: they increase the tensile and flexural strength, the wearing and high temperature resistance. Generally, the reinforcements can be constituted by particles, plates, long or short fibers, homogeneously distributed in the polymeric matrix or concentrated in the most solicited zones of a component. The most used are the carbon and glass fibers, which are usually

mixed in polyamide or polypropylene matrix. The reinforcements increase the price of the polymer materials within [20-30] %.

- *Drug-loads*: usually they are constituted by poor materials like kaolin, talcum, marmalade and wood powders. They are usually added to thermoset materials in order to improve the thermal resistance, toughness and tensile strength.
- *Antioxidant*: they are added for improving the stability to the atmospheric agents by contrasting the deterioration due to the contact with the oxygen. The substances are based on lead chloride or calcium and zinc soaps in order to absorb the ultraviolet radiations and to improve the thermal resistance at high temperatures.
- *Lubrificants*: they are used for improving the workability and for reducing the friction and the contact heating.
- *Colorants*: they are used for aesthetical functionalities. The pigments are inorganic oxides like TiO_2 , Fe_2O_3 , ZnO , which are opaque, stable at the light, and warm.

Considering the typology of the polymers and the additives described, many parameters should be taken in consideration, like: loads to be carried, operating temperature environment, surface finish, material, manufacturing and disposal costs. Concerning the mechanical aspects, during the design phase should be taken in account the different behaviours, which can be found in the category of the polymeric materials (Figure 2. 8).

In Figure 2. 8 typical mechanical behaviours of different polymeric materials are shown. The thermoplastic materials tends to have a mechanical response with a gradual yielding behaviour (Figure 2. 8a); instead, if reinforced, they present a brittle fracture response (Figure 2. 8a). The thermoset materials show an initial phase with elastic behaviour (OA zone), then there is a transition phase where a stable plastic deformation is observed (AB zone), finally the material tends to have an instable behaviour with the decay of material properties. In the graphs in Figure 2. 8 the first rule for designing polymeric tools is given. The point A defines the elastic behaviour limit, which must be strongly taken in consideration in a process simulation phase.

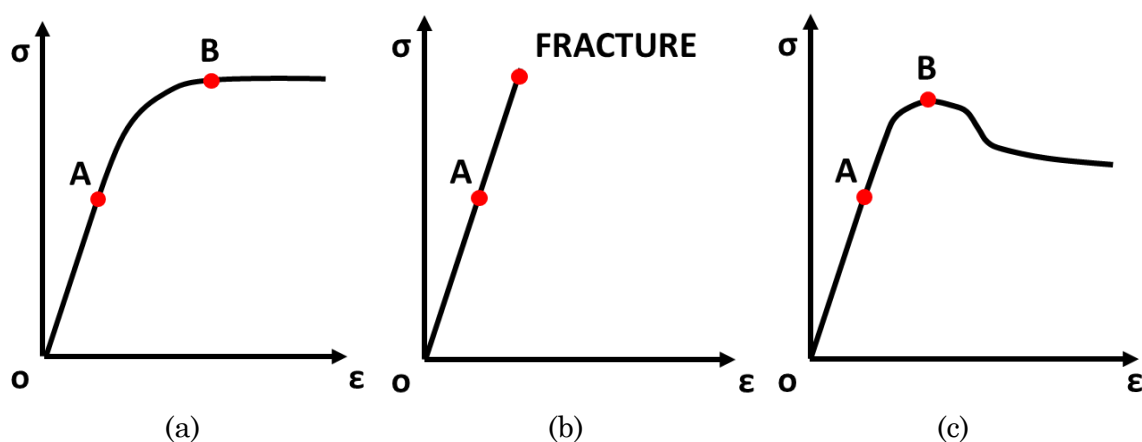


Figure 2. 8: typical mechanical behaviours of thermoplastics (a), reinforced thermoplastics (b) and thermosets materials (c).

Usually in the cold sheet metal forming processes the influence of the temperature is minimal except for severe deformations or high the friction. It is important to mention that the mechanical properties of the polymeric materials tend to deteriorate if the temperature increases; instead, when the temperature decrease under the zero degree, the Young's modulus increases and the final elongation decreases. Considering these described aspects, the *creep* phenomena should be taken in consideration when the designed component should resist to prolonged loads. The polymeric materials subjected to constant loads tend to increase to gradually their elongation until the reaching of fracture also at low loads. This might be the case of sheet metal forming processes where reinforced polymeric materials are more suitable.

2.3 Material tests

The polyurethane (PUR) materials are included in the domain of the polymers. Generally, the polyurethanes are characterized by high compression strength, good machinability, wear resistance and low humidity absorption. These properties confer good dimensional stability and make polyurethane suitable for industrial applications like: insulation, roles, protection covers, gears, bearing, sheet metal forming tools. The classification made above demonstrates that the mechanical characteristics of the polymers can be different due to the additives included by the manufacturer. For this reason, mechanical tests have been performed for the polyurethane materials used in this doctoral thesis.

In this chapter, the mechanical characterization of the commercial polyurethanes Necuron 1050, Necuron 1150 and Necuron 1300 will be presented. For the mechanical tensile and compression tests, the standards ASTM D638-02a [11] and D695-02a [11] have been followed.

2.3.1 Tensile tests

The specimens needed for the tensile tests have been made in MUSP Laboratory of Piacenza by following the standard ASTM D638-02a [11] for plastic materials. The geometry of the specimens have been obtained by following the model Type III of the ASTM standard (Table 2. 1). A total of 9 specimens have been made, 3 of each material tested, for example three specimens have been shown in Figure 2. 9 for representing the different colour of the materials tested.

The tensile tests have been performed in Politecnico di Milano with the tensile machine MTS Alliance RT/100 (Figure 2. 10). The tensile machine needs as input the dimension of the transversal section of the specimen, so the section measurements have been performed before by using a micrometre (Table 2. 2) for each available specimen.

The tensile tests have been performed at velocity of 2 mm/min, as reported in the ASTM standard, and the displacement have been measured with the extensometer MTS 634.25F-54 (Figure 2. 11).

At the end of each tensile test a report has been generated containing the following information:

- Material Name

- Specimen number
- Peak Stress [MPa]
- Yield Stress [MPa]
- Young's Modulus [MPa]
- Strain at break
- Stress at break [MPa]
- Elongation [%]
- Deformation velocity [mm/min]

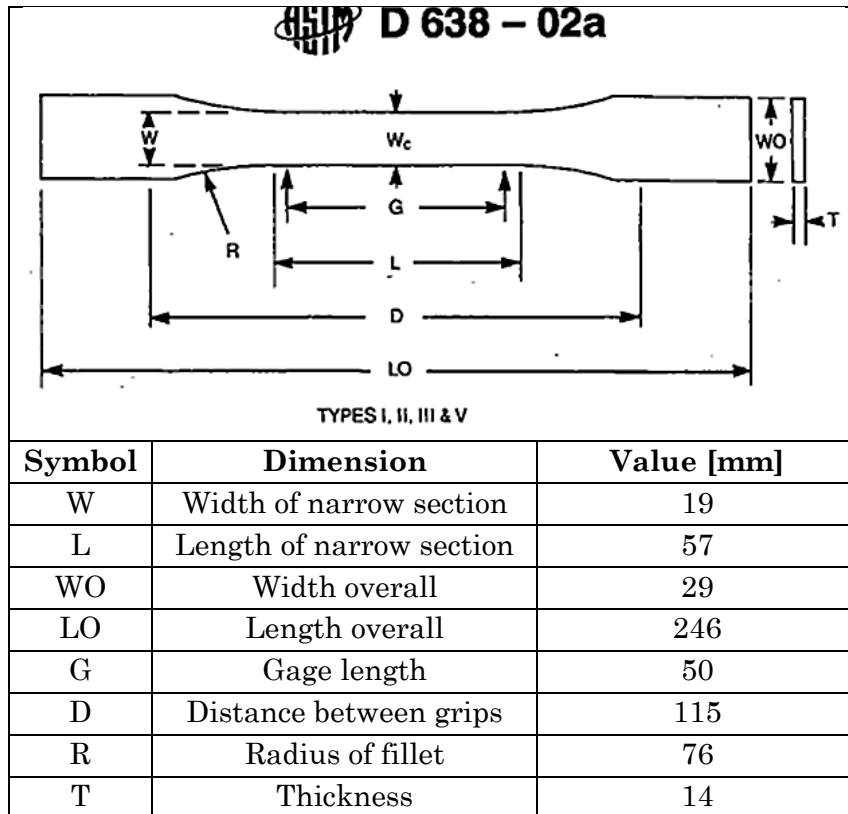


Table 2. 1: tensile specimen geometry and dimensions [10].



Figure 2. 9: experimental tensile specimen of Necuron 1300 (red), Necuron 1050 (light green), Necuron 1150 (dark green).



Figure 2. 10: tensile tests machine MTS Alliance RT/100.

Material	Specimen	W	T	Section
-	-	[mm]	[mm]	[mm ²]
Necuron 1050	1	18,95	14,04	266,12
	2	18,98	14,00	265,89
	3	18,97	14,01	265,94
Necuron 1150	1	18,97	14,13	268,04
	2	18,97	14,02	266,06
	3	18,99	14,06	267,15
Necuron 1300	1	19,04	14,00	266,67
	2	19,04	13,97	266,16
	3	18,97	14,00	265,73

Table 2. 2: measurements of the transversal section of the tensile specimens.



Figure 2. 11: extensometer used for measuring the displacement of the specimen during the tensile tests.

The results of the tensile tests for each specimen have been resumed, for brevity, in Table 2. 3. The complete data and the tensile curve for each specimen have been reported in the appendix. The order of magnitude of the obtained results in the tensile tests are in according with the reference [13] especially for the material Necuron 1300. From a qualitative point of view, it is possible to confirm that the Necuron 1300 and Necuron 1050 presents a more brittle fracture respect to Necuron 1150 which presents ductile fracture. These differences are related to the reinforcements included in Necuron 1300 and 1050 (which are loaded with glass spheres) respect to Necuron 1150, which is pure polyurethane.

Material	Specimen	Young's Modulus (E)	Yield Stress (R_s)	Peak Stress (R_m)	Elongation (A%)
-	-	[MPa]	[MPa]	[MPa]	[%]
Necuron 1050	1	2929	26	34	2.9
	2	3413	31	40	2.3
	3	3400	33	40	2.6
Necuron 1150	1	2875	43	62	16.4
	2	2918	43	63	11.4
	3	2952	42	63	16.6
Necuron 1300	1	2752	37	49	15.1
	2	2783	38	49	11.0
	3	2747	37	50	10.1

Table 2. 3: material properties resultant from the performed tensile tests.

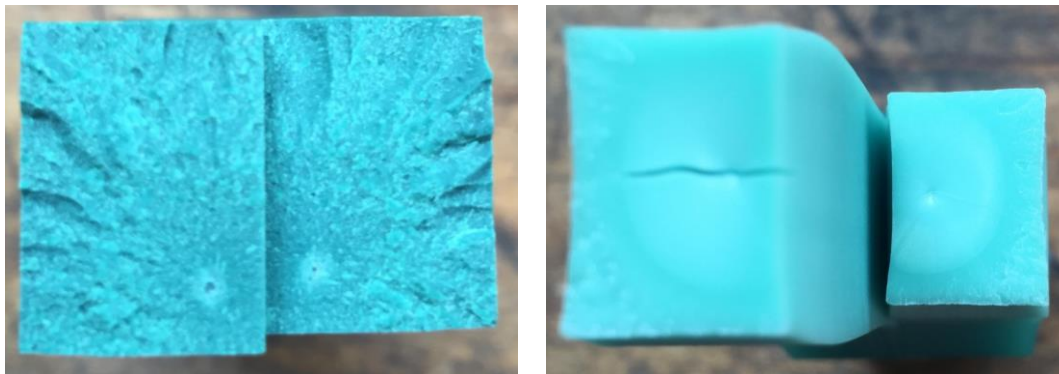


Figure 2. 12: fracture sections of the Necuron 1050 (left) and Necuron 1150 (right).

2.3.2 Compression tests

The manufacturing processes studied in this thesis are sheet metal stamping and bending, tube push-bending and rotary draw bending. In these kind of processes, the tools are subjected mainly to compression stresses; furthermore, the FEM software used for the simulations does not allow to define the compression and tensile behaviour separately. The tools must be designed considering the elastic field of the

material, for this reason, it should be checked if the material chosen has similar Young's modulus for tensile and compression load conditions. From these considerations, compression tests have been performed on 15 specimens (five for each material considered). The compression tests have been performed in Politecnico di Milano with MTS Alliance RF/150 compression test machine coupled with the MTS 634.12F-24 extensometer for the evaluation of the deformations.



Figure 2. 13: machine used for the compression tests.



Figure 2. 14: extensometer used for compression tests.

The tests have been performed at velocity of 1.3 mm/min as suggested from ASTM standard [12]. Not all tests have been conducted until the onset of fracture because some specimens shown asymmetrical collapse phenomena (Figure 2. 15) during the compression and only one test fail during the execution due to premature brittle fracture.

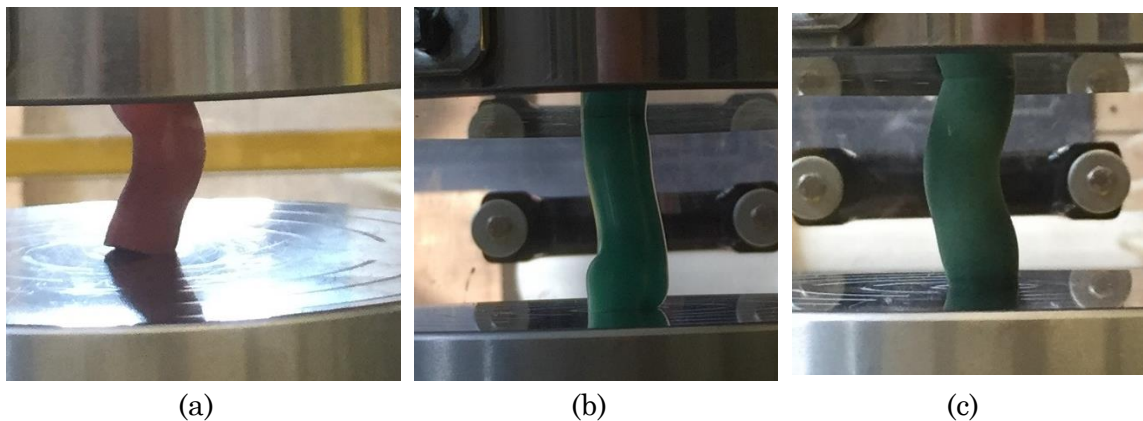


Figure 2. 15: example of particular collapse phenomena observed during the compression tests for Necuron 1300 (a), 1150 (b) and 1050 (c).

These phenomena show how the behaviour of the polymeric material can be unpredictable without a correct preliminary testing phase.

The main objective of the compression tests was the evaluation of the Young's Modulus and the peak stress values. For this reason, the specimen must have slenderness ratio at least equal to 16:1.

The slenderness ratio is defined as:

$$\lambda = l/\rho \quad (2.1)$$

where l is the height of the specimen and ρ is the radius of gyration calculated at the moment of Inertia of the transversal area of the specimen, defined for circular section as:

$$I_x = I_y = \frac{\pi d^4}{64} \quad (2.2)$$

where d is the diameter of the specimen. In Table 2. 4 the dimensions in terms of diameter and height, of the compression specimen is reported. The results of the compression tests are resumed in Table 2. 5 for the numerical values and in Figure 2. 16, Figure 2. 17 and Figure 2. 18 for the resultant stress-strain curves. The complete results are reported in the appendix.

Material	Specimen	d	h	Section
-	-	[mm]	[mm]	[mm ²]
Necuron 1050	1	12.70	48.08	126.68
	2	12.71	48.04	126.68
	3	12.72	48.05	126.87
	4	12.72	47.97	126.68
	5	12.72	48.03	126.68
Necuron 1150	1	12.71	48.11	126.67
	2	12.71	48.17	126.67
	3	12.71	47.99	126.67
	4	12.71	48.06	126.67
	5	12.71	48.10	126.67
Necuron 1300	1	12.71	47.98	126.67
	2	12.70	48.03	126.67
	3	12.70	48.07	126.67
	4	12.70	47.98	126.67
	5	12.71	47.98	126.67

Table 2. 4: dimensions of the specimens used in the compression tests.

Material	Specimen	Young's Modulus (E)	Yield Stress (R _s)	Peak Stress (R _m)
-	-	[MPa]	[MPa]	[MPa]
Necuron 1050	1	2907	50	61
	2	3174	45	67
	3	2898	51	61
	4	3422	35	61
	5	3037	54	68
Necuron 1150	1	2747	77	86
	2	2587	80	86
	3	2847	74	86
	4	3104	58	86
	5	2387	81	83
Necuron 1300	1	2810	61	73
	2	2794	66	79
	3	2565	68	70
	4	2607	68	74
	5	2543	69	71

Table 2. 5: material properties resultant from the performed compression tests.

As reported in [12] the compression yield point is defined as: “the first point on the stress-strain diagram at which an increase in strain occurs without an increase in stress.”. The compression tests have been performed with a testing machine suitable for metals. For this reason, the “Yield Stress” indicated in Table 2. 5 corresponds to the stress value at 0.2% of strain normally calculated for metals, which is lower than the compression yield point (peak stress in Table 2. 5) calculated for plastic materials.

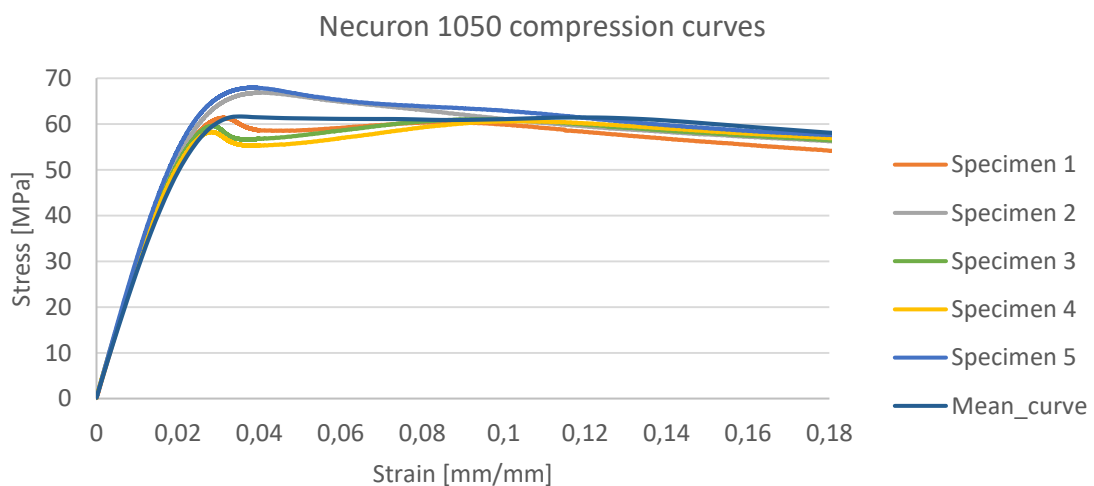


Figure 2. 16: Necuron 1050 stress-strain curves resultant from the compression tests.

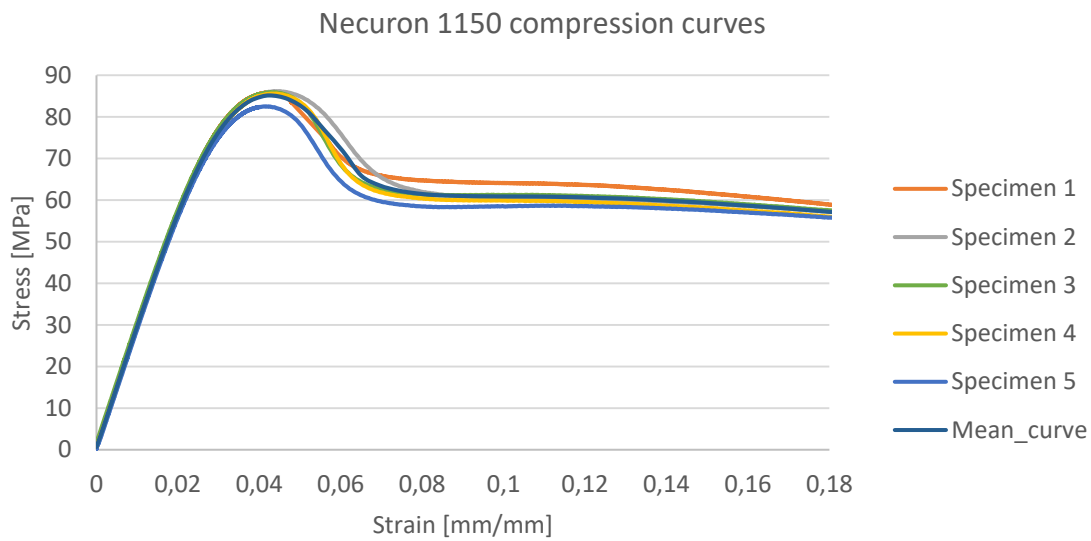


Figure 2. 17: Necuron 1150 stress-strain curves resultant from the compression tests.

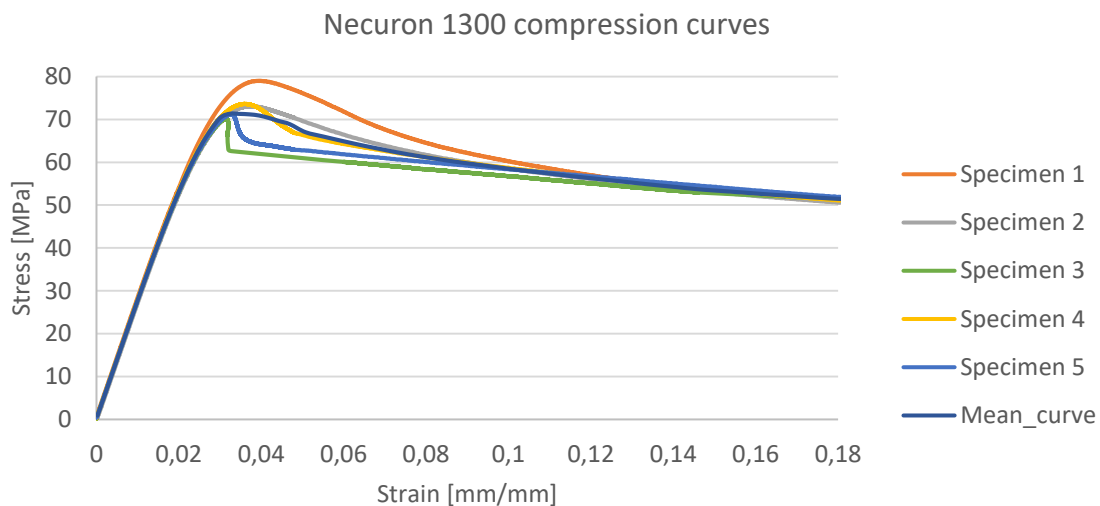


Figure 2. 18: Necuron 1300 stress-strain curves resultant from the compression tests.

Considering these values, three intervals can be defined on the compression stress-strain curve for designing a rapid tool suitable for sheet metal forming processes (Figure 2. 19):

1. *Safe zone*: the material behaviour is purely elastic where the expected tool life should be at the maximum value;
2. *Unstable zone*: the material behaviour is elasto-plastic, so for increasing compression stress values very small permanent deformations could appear;
3. *Failure zone*: for stress and strain values over the peak stress condition the material behaviour is very unstable and fracture or undesired deformations could appear.

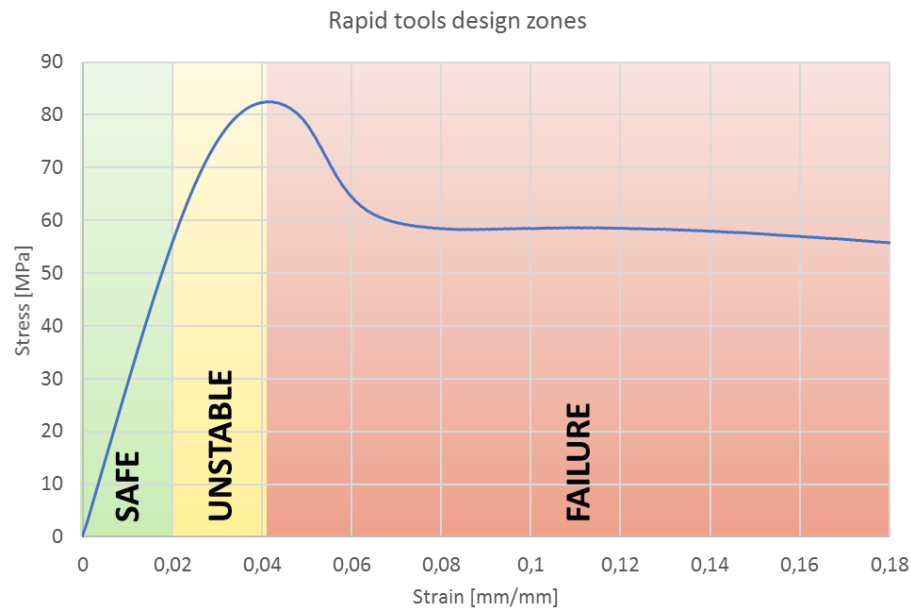


Figure 2. 19: Rapid tools design zones.

The results obtained from the performed compression tests demonstrate that the material behaviour is stable for low values of deformations, instead the compression yield point tends to have a large variability. For a brief comparison, the data sheet provided by the manufacturer are shown in Table 2. 6.

Fatigue tests have been also performed, but the description of them will be presented in chapter 3.

Characteristic	Value		
Material	Necuron	Necuron	Necuron
Colour	light green	dark green	red
Shore D	82	80	80
Density	1.2 g/cm ³	1.20 g/cm ³	1.15 g/cm ³
Compression	82 N/mm ²	83 N/mm ²	87 N/mm ²
Flexural strength	81 N/mm ²	104 N/mm ²	92 N/mm ²

Table 2. 6: mechanical properties found on the materials datasheets.

2.4 FEM simulation of the compression test

In the next chapters, the analysis of process which involves polyurethane tools will be presented. The analysis has been carried out experimentally and numerically. The numerical approach consisted in the generation of FEM model able to describe the process results in reliable way and in the development of solutions able to solve or optimize the obtained results.

The FEM simulations have been carried out by the explicit commercial software PAM-STAMP 2015.1 coupled with Visual Mesh module included in the suite Visual Environment 11, both developed by ESI group.

Before the development of the FEM model of the analysed processes, the simulations of the compression tests have been carried out for all the material involved in the tests described above. The simulation of the compression test is needed for evaluate if the software is able to describe correctly the tools material behaviour. Furthermore, a comparison with different elements formulation has been carried out in order to evaluate which one could be preferable for describing the material behaviour in terms of precision and simulation time costs.

2.4.1 Geometry and boundary conditions

The simulated specimen has been reduced to a quarter of cylinder, due to the geometrical double symmetry. The radius of the specimen is 6.35 mm and the height is 48 mm. The cylinder of the compression machine in contact with the specimen (Figure 2. 13), have been reduced to rigid 2D plates. The geometry of the model has been schematized in Figure 2. 20.

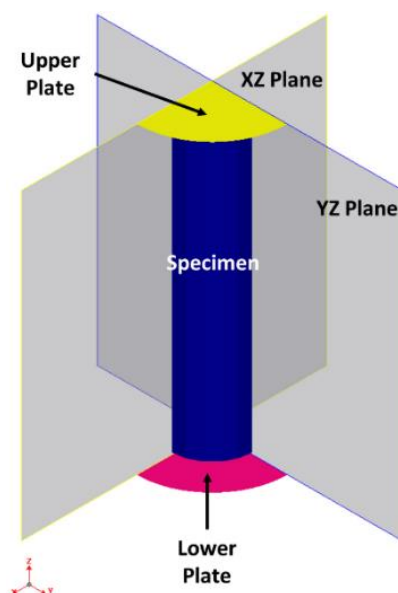


Figure 2. 20: scheme of the compression simulation setup.

The rigid upper and lower plate have been modelled by shell elements with thickness of 0.5 mm for improving the contact compatibility with the solid elements of the specimen.

The specimen has been modelled with 4 different solid elements configurations (Figure 2. 21):

1. Tetrahedral: 4 nodes
2. Tetrahedral quadratic: 10 nodes
3. Hexahedral: 8 nodes
4. Hexahedral quadratic: 20 nodes

All the solid elements configurations have been modelled with Uniform integration rule and Flanagan-Belytschko Stiffness hourglass control algorithm [14].

In the Table 2. 7, the quantities of elements and nodes has been resumed for each carried simulation.

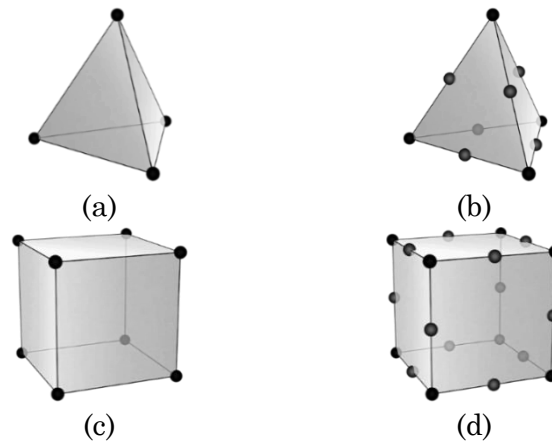


Figure 2. 21: general schematization of tetrahedral (a), tetrahedral quadratic (b), hexahedral (c) and hexahedral quadratic (d) elements.

Simulation setup	Object	Behaviour	Elements	Nodes
All setups	Upper plate	Rigid	17	15
	Lower plate	Rigid	17	15
Tetra	Specimen	Deformable	1704	481
Tetra-quad	Specimen	Deformable	1704	2946
Hexa	Specimen	Deformable	1680	2254
Hexa-quad	Specimen	Deformable	1680	8382

Table 2. 7: elements and nodes quantities for each compression simulation.

All the displacements of the lower plate have been locked, instead the upper plate has been imposed a displacement of 10 mm, as shown in Figure 2. 22. The simulation time is 3 order of magnitude lower than the real one, in order to reduce the calculation time and the inertia effects. Furthermore, the material formulation is independent to the strain rate, so the velocity of the simulation is not influent on the final results.

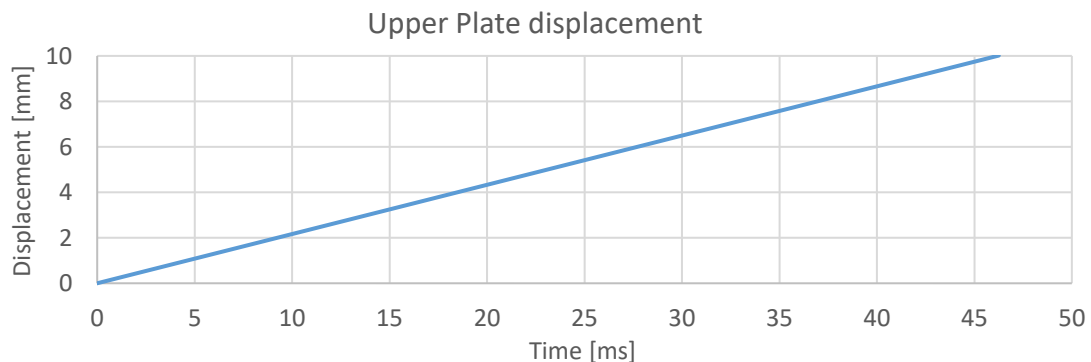


Figure 2. 22: imposed displacement for the upper plate.

The Accurate algorithm has been chosen for modelling the contact between the rigid plates and the deformable specimen, by imposing a friction of 0.24 very close to the value found in [15].

The Accurate contact avoids the penetration between the nodes and elements. During the simulation, the nodes are kept on the surface of the elements in order to allow the software calculating the contact forces precisely. This contact type is specifically developed for stamping process because it respects the tools geometry.

2.4.2 Material properties

The simulations of the compression tests have been generated by replicating one compression test for each material. The experiment 4, 2 and 5 have been chosen for Necuron 1300, 1150 and 1050 respectively because no particular collapse phenomena have been observed during tests. In Table 2. 8 the material properties corresponding to the elastic behaviour for each chosen test are resumed.

Material	Compression test	Density	Young's Modulus	Poisson coeff.
-	-	[Kg/mm ³]	[GPa]	-
Necuron 1300	4	1.15*10 ⁻⁶	2.607	0.34
Necuron 1150	2	1.2*10 ⁻⁶	2.587	0.34
Necuron 1050	5	1.2*10 ⁻⁶	3.037	0.34

Table 2. 8: elastic materials properties used in the simulation model of the compression tests.

The plastic behaviour of the tested material has been modelled by using the Yield stress-plastic strain curve obtained directly from the compression tests (Figure 2. 23).

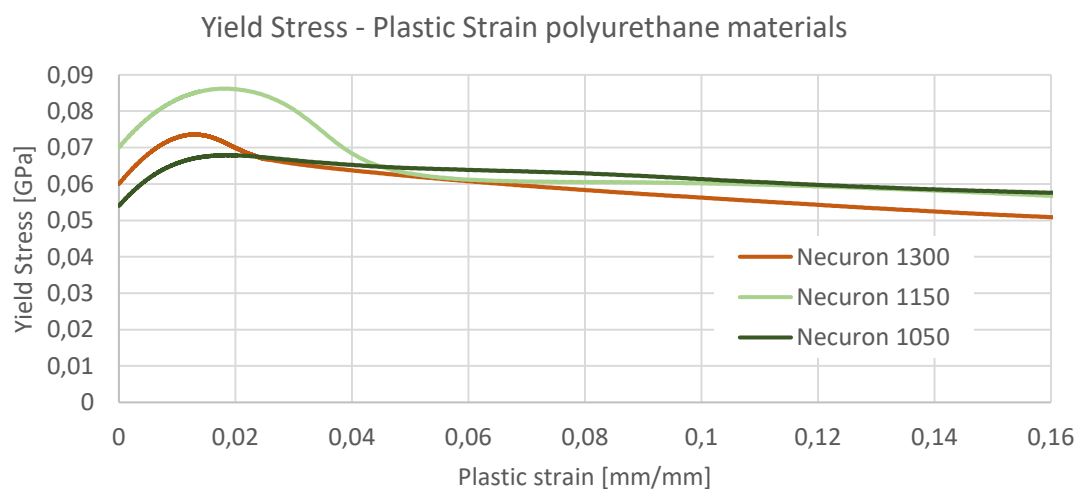


Figure 2. 23: Yield stress - plastic strain curves implemented in the compression tests simulations.

2.4.3 Simulations results

As described before, 4 types of elements have been analysed for the simulation of the compression tests. The first results obtained from the Necuron 1300 demonstrate that the FEM software does not make difference between the linear or quadratic formulation of the elements as shown in the Figure 2. 24.

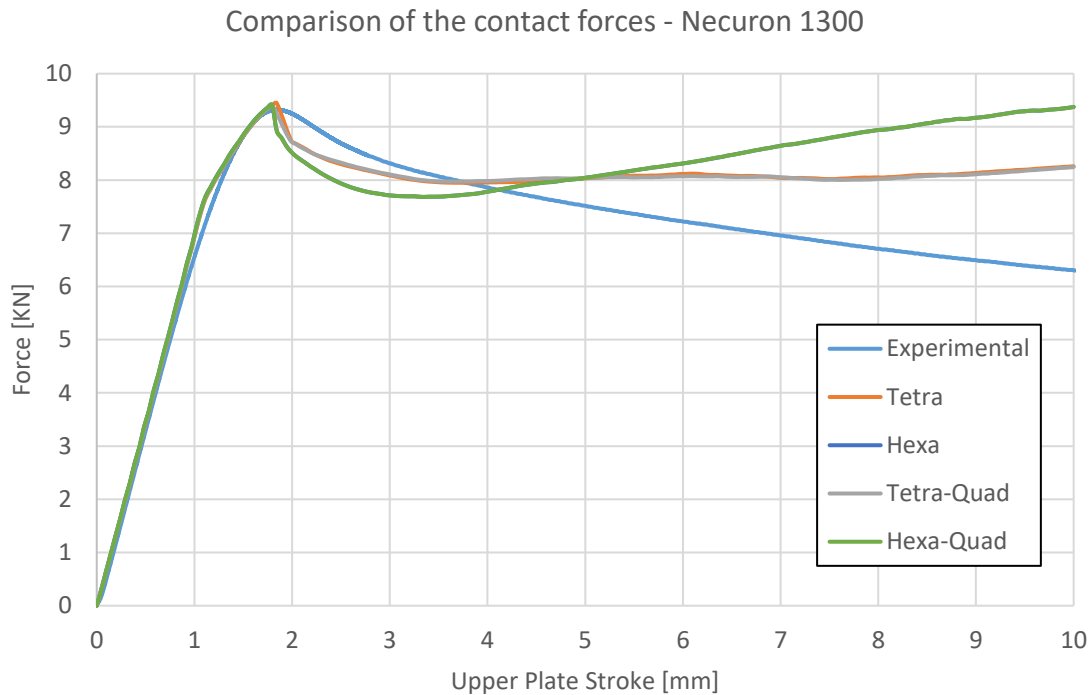


Figure 2. 24: comparison of the resultant forces on the upper plate at the end of the experimental and simulated compression test for Necuron 1300.

In Figure 2. 24 comparison between the experimental and numerical forces for Necuron 1300 is presented. The curve of the linear formulations and the quadratic ones are equal and overlapped, this result suggests that the used FEM software does not implement the quadratic formulation for solid elements.

As described in the previous paragraph the application field of this material should be restricted in the elastic behaviour in order to improve the tools life. From this consideration and from the results in Figure 2. 24, both solution of Tetrahedral and Hexahedral elements are able to describe the elastic behaviour of the analysed polyurethane material at the same way. In term of the simulation time, the hexahedral formulation needs 0.08 hours (5 minutes) respect to the 0.06 hours (4 minutes) needed for the tetrahedral one; this difference of 1 minute seems apparently very small, but if scaled to bigger models which require hours for being computed, this time difference will obviously increase.

For the materials Necuron 1150 and Necuron 1050, only the linear elements (tetrahedral and hexahedral) formulations have been investigated due the results obtained during the investigation of the Necuron 1300. Also for these two materials the elastic behaviour is well described by the FEM software.

Finally, it can be demonstrated that both elements formulations, tetrahedral and hexahedral one, are able to describe the behaviour of the considered polyurethane materials. The tetrahedral solution needs less time to be computed respect to hexahedral one. It should be noted that the two configurations have similar number of elements but very different amount of nodes. In the explicit FEM models this condition is fundamental for the computation time. At least it should be considered that the meshing operation with only hexahedral elements is not always possible, especially for very complex tools shape. For this reasons the tetrahedral solution will be applied chosen for the models presented in the next chapters.

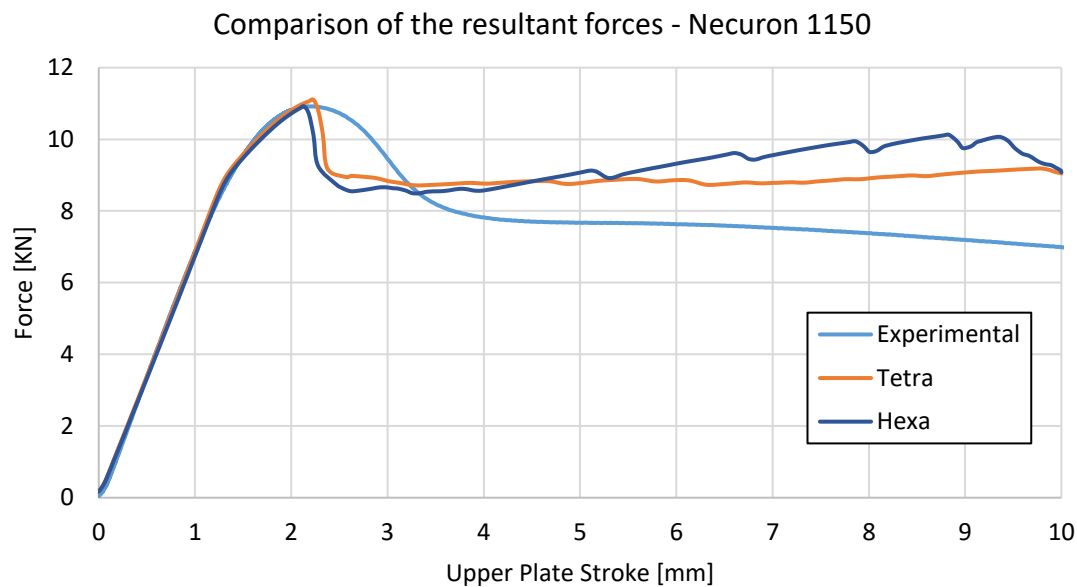


Figure 2. 25: comparison of the resultant forces on the upper plate at the end of the experimental and simulated compression test for Necuron 1150.

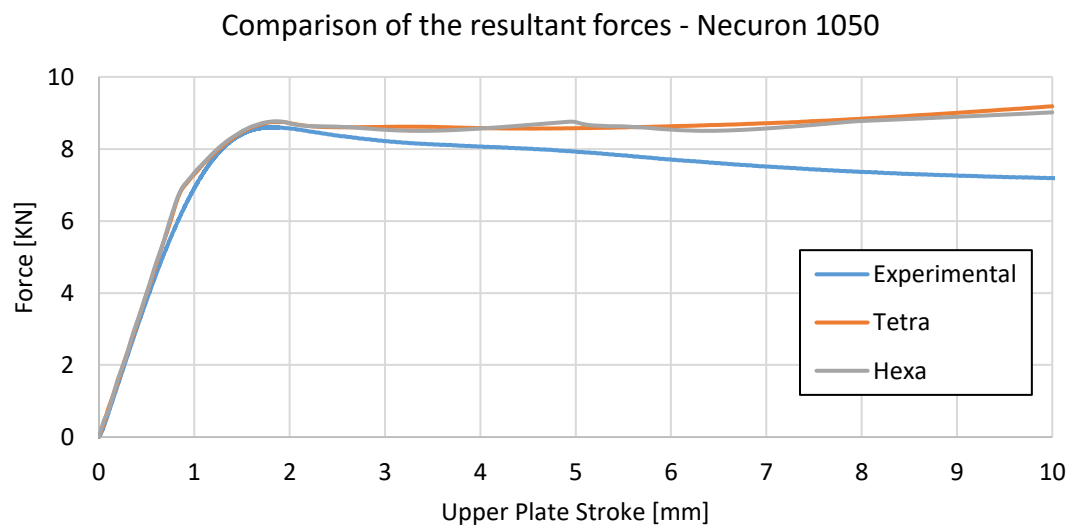


Figure 2. 26: comparison of the resultant forces on the upper plate at the end of the experimental and simulated compression test for Necuron 1050.

2.5 References

- [1] Ehrenstein, G.W., *Polymeric Materials: Structure, Properties, Applications*, Hanser Publishers, 2001.
- [2] TURI, Edith (ed.). *Thermal characterization of polymeric materials*. Elsevier, 2012.
- [3] Bertolini L., Bolzoni F., Cabrini M., Pedferri P., 2007, “Tecnologia dei materiali: ceramici, polimeri e composti”, Milano: Città Studi.
- [4] Polymers chains - <https://www.slideshare.net/roy98/3-polimeri-bt-2012> accessed on 13/01/2018.
- [5] Brückner S., 2007, “Scienza e tecnologia dei materiali polimerici”, Napoli: Edises.
- [6] Polymers structures - <http://www.textoscientificos.com/polimeros/estructura> accessed on 13/01/2018.
- [7] J. Roesler, 2007, “Mechanical Behaviour of Engineering Materials – Metals, Ceramics, Polymers and Composites”, Springer.
- [8] Monomers chains - http://puraquimicahd.blogspot.it/2012_04_01_archive.html accessed on 13/01/2018.
- [9] M. Guaita, F. Ciardelli, F.P. La Mantia, E. Pedemonte. *Fondamenti di Scienza dei Polimeri*. Pacini, 1998.
- [10] ROSU, Dan, et al. Thermal degradation of thermosetting blends. In: *Thermal Degradation of Polymer Blends, Composites and Nanocomposites*. Springer International Publishing, 2015. p. 17-49.
- [11] ASTM, D. 638-02a. Standard test method for tensile properties of plastics. New York. 2003.
- [12] ASTM, D695–02a. Standard Test Method for Compression Properties of Rigid Plastics, American Society for Testing and Materials, 2002.
- [13] MARSAVINA, Liviu, et al. Experimental Determination and comparison of some mechanical properties of commercial polymers. *Materiale plastice*, 2010, 47: 85-89.
- [14] Pam-Stamp 2015.1 Userguide.
- [15] COLTON, J. S.; PARK, Y. Sheet metal forming using polymer composite rapid prototype tooling. *Journal of engineering materials and technology*, 2003, 125.July: 247-255.
- [16] A. Colombo, Stampaggio Massivo: Studi Tribologici E Ottimizzazione Multi-obiettivo, master thesis at Politecnico di Milano 18/12/2014.

Chapter 3

Rapid tools in stamping process

3.1 Introduction

In the previous chapters, general overviews about sheet metal forming processes and rapid tools have been presented. The mechanical behaviour of the polymer materials, of which rapid tools are made, has been also described.

Rapid tools have been already treated in the literature from the experimental point of view as a prototypal solution [1], but also as a suitable setup for the manufacture of small batches [2]-[3]. They have been also compared with the corresponding rigid metal tools solution in [4]-[5], where the economic advantages related to the rapid tools costs, compared with the quality of obtained results make the rapid tools solution an attractive one for the industrial scenario. One common drawback underlined in the literature is connected to the need of a very accurate design phase, because the deformation of the rapid tools during the stamping process is not always easy to predict.

The objective of this chapter is to present the application of rapid tools in sheet metal stamping process by analysing two case studies developed for this doctoral thesis. Both test cases have been studied experimentally and numerically. These two activities allowed understanding directly the advantages and disadvantages of the rapid tools described in the previous chapters. The experimental activities consisted initially in the implementation of experimental plans where a lot of parts have been stamped by the two different tools setup at different process parameters. The stamped components have been measured geometrically in order to allow the validation of the FEM model. The numerical simulations underlined the main defect of this kind of tools setup, which is related to the geometrical deviations of the final component with respect to the designed one. This “defect” will be discussed deeply in this chapter and will be solved by the development of a compensation algorithm, which will be applied in both case studies. The results coming from the experimental and numerical activities on the test cases allowed the implementation of fatigue tests on the rapid tools material in order to have some indication about their expected lifetime. The fatigue tests results return very interesting information about the applicability of these kind of tools in stamping processes, which are very useful in industrial applications.

3.2 Case study 1: simple component

3.2.1 Experimental setup

The first case study consists in a sheet metal stamping process with rapid tools of a simple component. Therefore, the geometry of the component (Figure 3. 1) consists in features easy to be obtained by stamping. The component shown in Figure 3. 1 is symmetrical along the longitudinal direction with maximum stamping depth of 34 mm, constant wall inclination of 20° , minimum radius of 10 mm, round corners of 38 mm and thickness of 2 mm.

This component contains many of typical feature obtainable in stamping except the reverse deep draw feature, which will be implemented in the second case study.

Starting by the designed component, the geometries of the rapid tools have been obtained by using directly the internal and external surfaces of it.

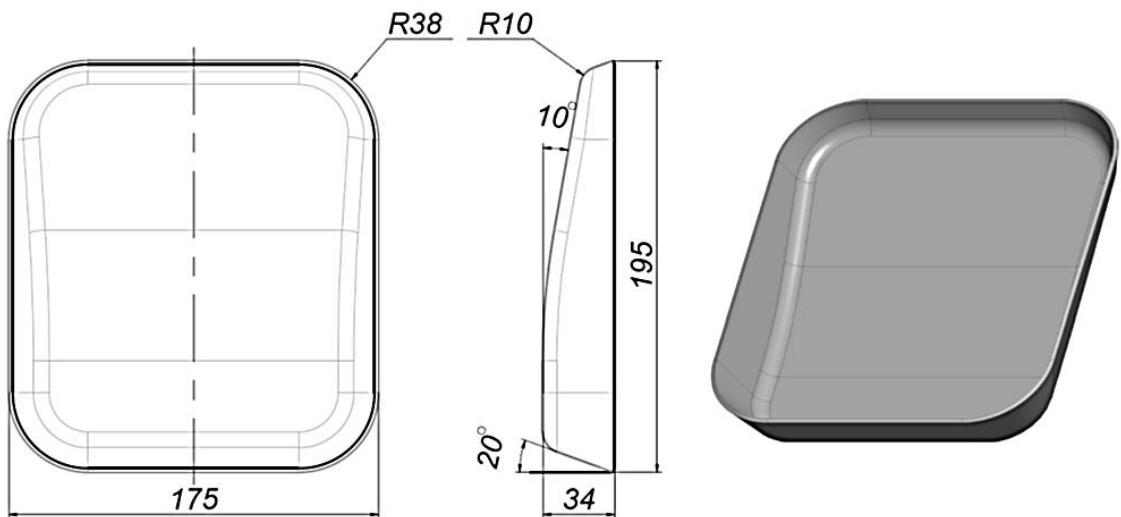


Figure 3. 1: geometry of the component for case study 1, dimensions in mm (left) and 3D view (right).

The hydraulic press machine involved in the experimental activities is a SACMI PH150 (Figure 3. 2), which has been reprogrammed for stamping operation. The characteristics of the press are resumed in Table 3. 1. The hydraulic press has been designed as a general purpose press, so supporting plates have been designed for coupling the stamping tools inside the press.

The external dimensions of the stamping tools (Figure 3. 3, Figure 3. 4 and Figure 3. 5) have been reduced, with respect to a normal tools setup, in order to be introduced in the hydraulic press available in the experimental laboratory.

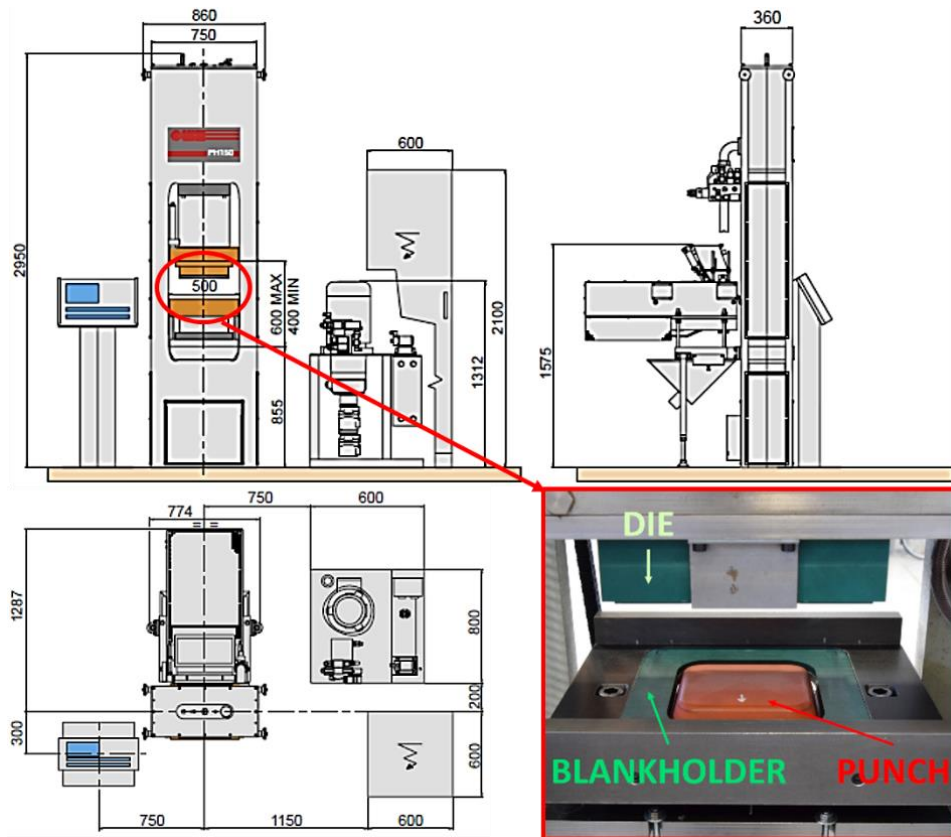


Figure 3. 2: geometrical dimensions of the SACMI PH150 press used for the experimental activities and particular of the rapid tools inside the press.

SACMI PH150 Press Specification	
Clearance between columns	500 mm
Plunger max stroke	200 mm
Max pressing force (upper plate)	1500 kN
Max ejector power (middle plate)	78.5 kN
Installed motor power	15 kW
Die heating	5 kW
Oil quantity for hydraulic system	100 l
Oil cooling water	16 l/min
Net weight	2.5 kg

Table 3. 1: technical specification of the press involved in the experimental activities.

The punch coupling plate (Figure 3. 6) is composed by: 4 threaded holes for fixing the plate to the press machine, 2 through holes which allow the transition of the pistons which impose the reaction force to the blankholder during the stamping process, and 4 positioning supports designed for centring the punch and used as end-stroke for the process. The blankholder coupling plate (Figure 3. 7) can be assimilated to a container with 2 through flared holes used for joining the plate to the press pistons. In Figure 3. 8, the die has been sectioned in order to make visible 2 of 4 flared threaded holes. The

four supports make the die centred and locked to the plate because the press is a single action; for this reason, the die will descend on the blankholder upside-down, as shown in Figure 3. 9.

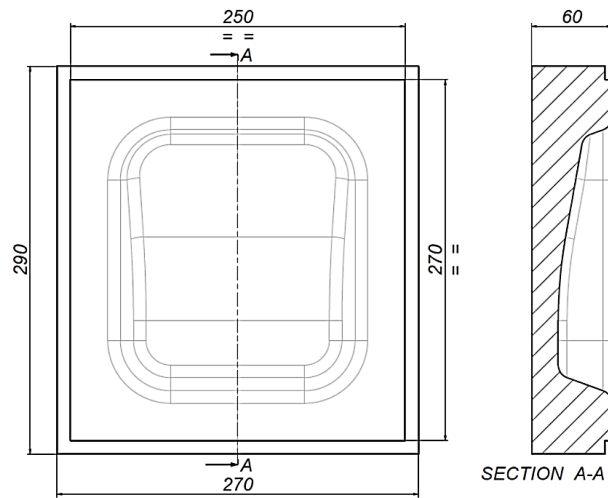


Figure 3. 3: external dimensions (left) and transversal middle section of the stamping die (right).

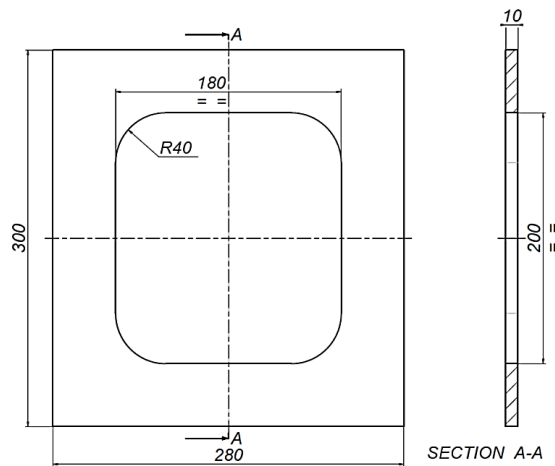


Figure 3. 4: external dimensions (left) and transversal middle section of the blankholder (right).

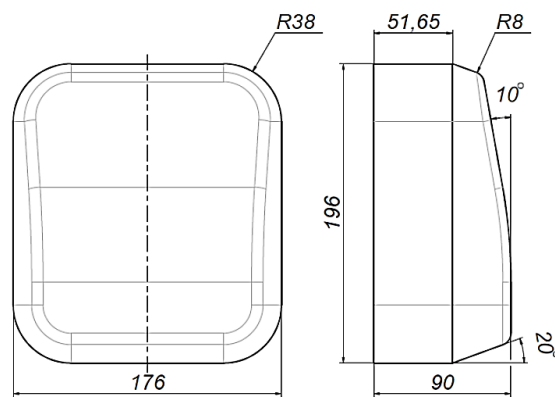


Figure 3. 5: external dimensions of the punch.

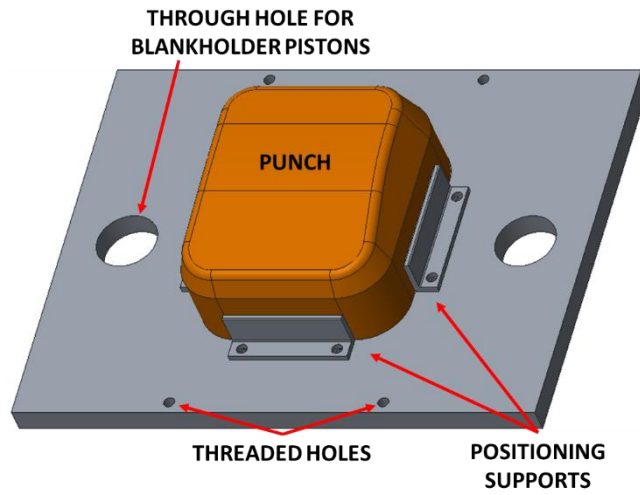


Figure 3. 6: scheme of the designed plate implemented for the punch.

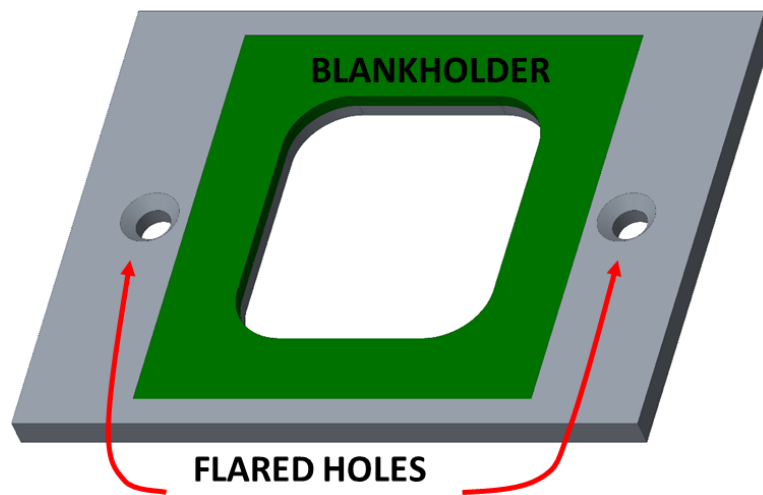


Figure 3. 7: scheme of the designed plate implemented for the blankholder.

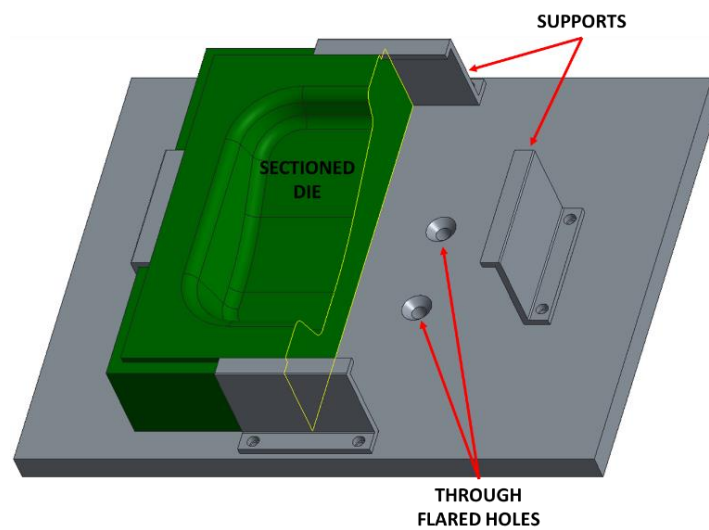


Figure 3. 8: scheme of the designed plate implemented for the die (sectioned).

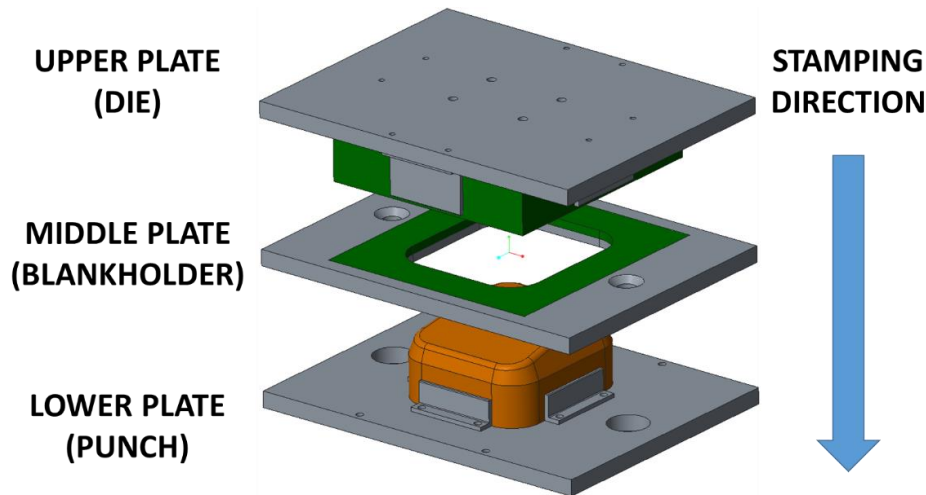


Figure 3. 9: scheme of the entire tool assembly and the stamping direction.

The rapid tools have been manufactured internally by using the milling machine of the laboratory Jotech Jobs 020 (Figure 3. 10a). The part program has been implemented with the CAM (Computer Aided Manufacturing) module of the PTC-Creo 3.0 software (Figure 3. 10b). The milling operation (Figure 3. 11) has been divided in two steps:

1. **Coarse machining:** where the cutting depth has been imposed 5 mm with a feed rate of 7500 mm/round, due to the very high ductility of the material.
2. **Finishing:** the cutting depth has been imposed 0.5 mm and 5000 mm/round as feed rate, in order to obtain an accurate finished surface.

After the milling operations an economical comparison has been done in order to evaluate directly the benefits in terms of total cost, compared to a traditional metal solution. The cost comparison presented in Table 3. 2 is related to the manufacture of the tools setup shown previously in Figure 3. 3, Figure 3. 4 and Figure 3. 5.

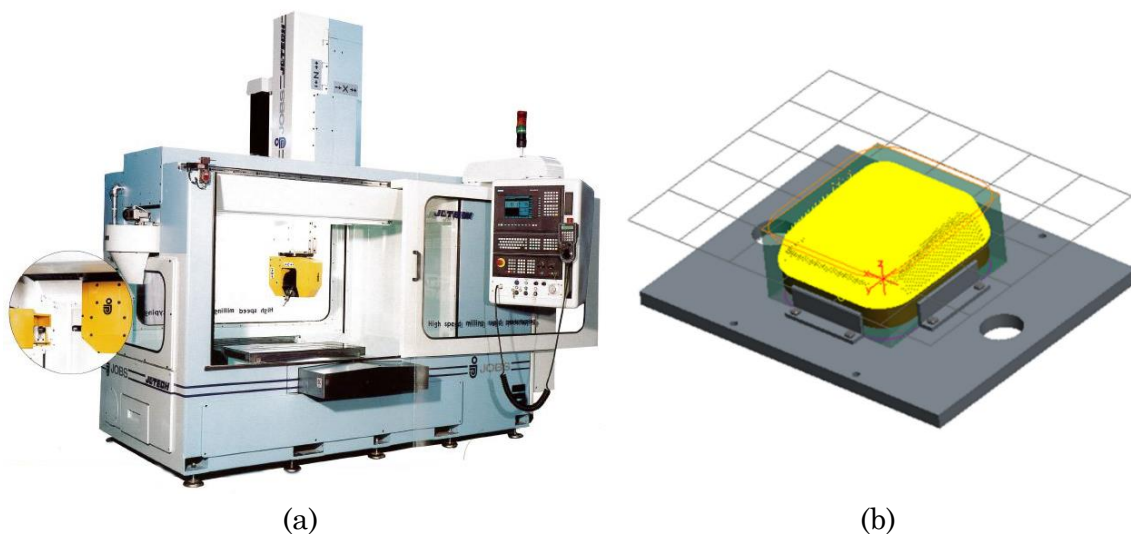


Figure 3. 10: milling machine used for making the experimental rapid tools (a) and definition of the finishing operation in the CAM module of Pro-e (b).

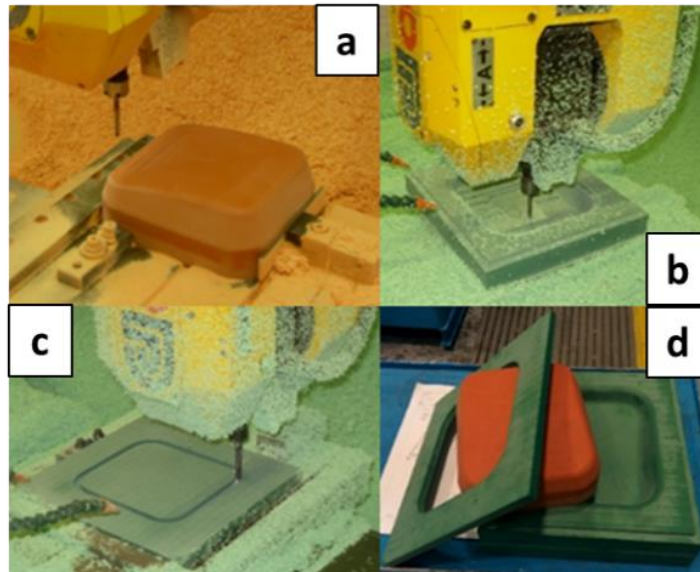


Figure 3. 11: milling operations of punch (a), die (b), blankholder (c) and finished tools (d).

Characteristics	Unit	Solutions		
		Metal Tools	Rapid Tools	
Material	-	Steel C40	Necuron 1300	Necuron 1050
Price	€/m ³	9360	8100	6000
MRR	cm ³ /min	35	150	
Die rough vol.	m ³	6.72E-03	-	6.72E-03
Blankholder rough vol.	m ³	1.86E-03	-	1.86E-03
Punch rough vol.	m ³	3.60E-03	3.60E-03	-
Die final vol.	m ³	3.59E-03	-	3.59E-03
Blankholder final vol.	m ³	4.94E-04	-	4.94E-04
Punch final vol.	m ³	2.68E-03	2.68E-03	-
Die removed vol.	m ³	3.13E-03	-	3.13E-03
Blankholder removed vol.	m ³	1.37E-03	-	1.37E-03
Punch removed vol.	m ³	9.20E-04	9.20E-04	-
Total removed vol.	m ³	5.41E-03	9.20E-04	4.49E-03
Milling time	min	154.70	6.13	29.97
Die material cost	€	62.90	-	40.32
Blankholder material cost	€	17.41	-	11.16
Punch material cost	€	33.70	29.16	-
Total material cost		114.00	29.16	51.48
Milling cost unit	€/h	40		
Milling cost	€	6188.04	245.26	1198.62
Thermal Treatment	€	630.20	-	-
Total cost	€	6302.05	274.42	1250.10

Table 3. 2: economical comparison between metal and rapid tools solution for case 1.

The purchase price of the material has been evaluated in €/m³ because the density of the considered materials is different with a factor of 7, moreover in milling operation it is easier making calculation in m³ of material removed. The material removal rate has been calculated using the equation suggested by SANDVIK [6]. The final volume of the tools has been obtained directly from the CAD software. The manufacturing cost unit has been approximated as equal for both solutions, but it should be considered higher for the metal solution, due to the higher hardness with respect to the polyurethane.

The resume of the economical comparison, presented in Figure 3. 12, demonstrates that the rapid tools solution is 4.5 times cheaper than the metal one. Furthermore, despite the rapid tools solution does not need thermal treatment, the main cost difference is related to the cost of the milling operation which corresponds to the 90% of the total cost of the tools setup.

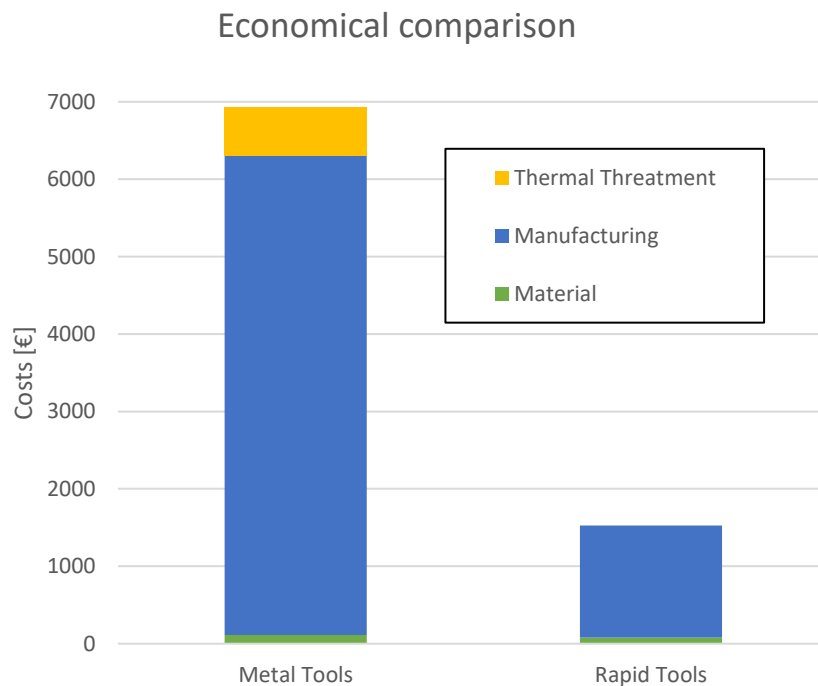


Figure 3. 12: resume of the economical comparison between metal and rapid tools solutions case 1.

3.2.2 Experimental plan and results

The experimental activities consisted in the execution of stamping operations with rapid tools setup of blanks at different values of blankholder force [7]-[8]. The material chosen for the test case is Al1050, annealed, with 2 mm wall thickness. The dimensions of the rectangular blank are 250x270 mm. As described before, the deformable tooling setup (Figure 3. 9) is composed by the die, the blankholder (green tools) and the punch (orange tool). The polyurethane materials chosen for testing the deformable tools are: Necuron 1050 for the die and blankholder; Necuron 1300 for the punch. The material properties will be discussed in the FEM modelling section. Figure

3. 9 shows the direction of the stamping process. The steps of the stamping process performed in the experimental activities can be summarized as follows:

1. **Holding:** the blank is placed on the blankholder and then the die moves downward for holding it;
2. **Stamping:** the die pushes down the blank and the blankholder on the punch; in this step the blankholder applies a force towards the stamping direction, for controlling the draw-in of the blank during the stamping operation in order to prevent the onset of wrinkling.
3. **Springback:** the tools are released and the blank tends to return to the initial state due to the residual stresses generated by the stamping operation.

While the die moves downward with a controlled displacement, the punch is fixed and the blankholder opposes a reaction force BHF. An experimental plan has been designed with 5 variable levels of the blankholder force. Each level has been replicated twice (Table 3. 3). The die velocity, the reaction force on the die and the blankholder force have been measured with a sampling frequency of 100 Hz.

The value presented in Table 3. 3 corresponds to the mean values of the blankholder force profiles registered from the numerical control of the press machine. In Figure 3. 13 the profile of the blankholder force for the first 5 experiment is shown.

Experiment no.	Mean BHF (kN)	Blank_code
1	38	B7
2	40	B11
3	22	B6
4	46	B4
5	30	B8
6	38	B9
7	30	B10
8	40	B14
9	46	B12
10	22	B13

Table 3. 3: experimental plan of case 1.

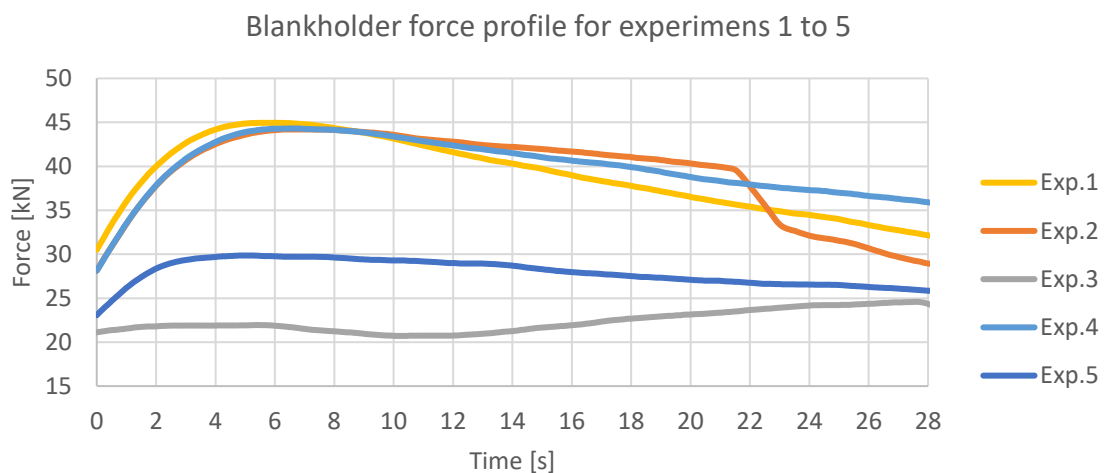


Figure 3. 13: blankholder force profiles for experiment 1 to 5 of the experimental plan.

In Figure 3. 14, the BHF profiles for replicated experiments no. 3 and 10 (minimum level of BHF) and for replicated experiments 4 and 9 (maximum BFH) are shown. The graphs indicate that there is a very good reproducibility of the tests, at least with respect to forces.

The plan has been designed in order to determine which level of maximum blankholder force could determine failure of the parts (by either wrinkling or fracture) OR failure of the tools (by fracture or plasticization). The plan was also meant to produce different degrees of errors of the stamped vs. the designed part.

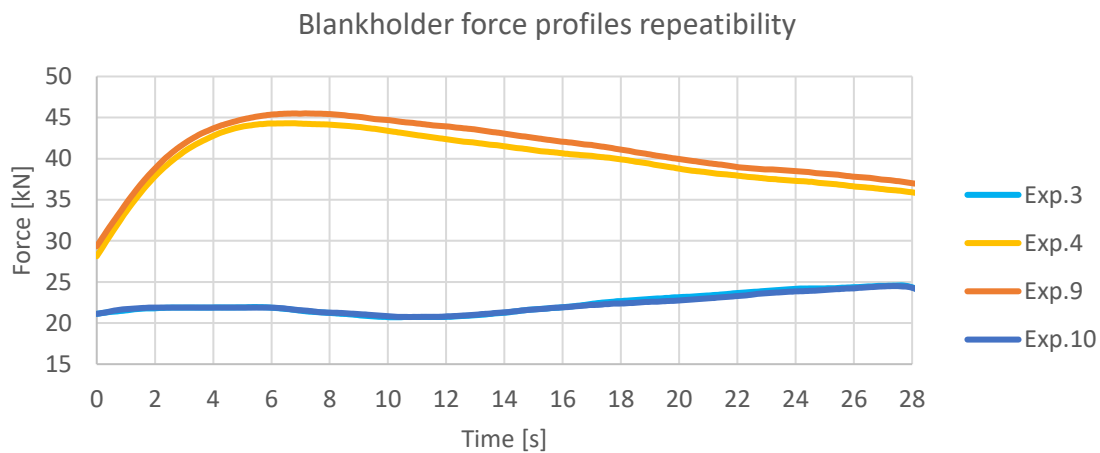


Figure 3. 14: repeatability of blankholder force profiles for correspondent experiments.

The experimental results showed that no macroscopic wrinkling occurred along the wall of the component at any level of BHF. The parts at experiments no. 4-9 failed by fracture (Figure 3. 15 and Figure 3. 16), hence the safe limit to fracture for BHF_{max} was assessed at 40 kN.

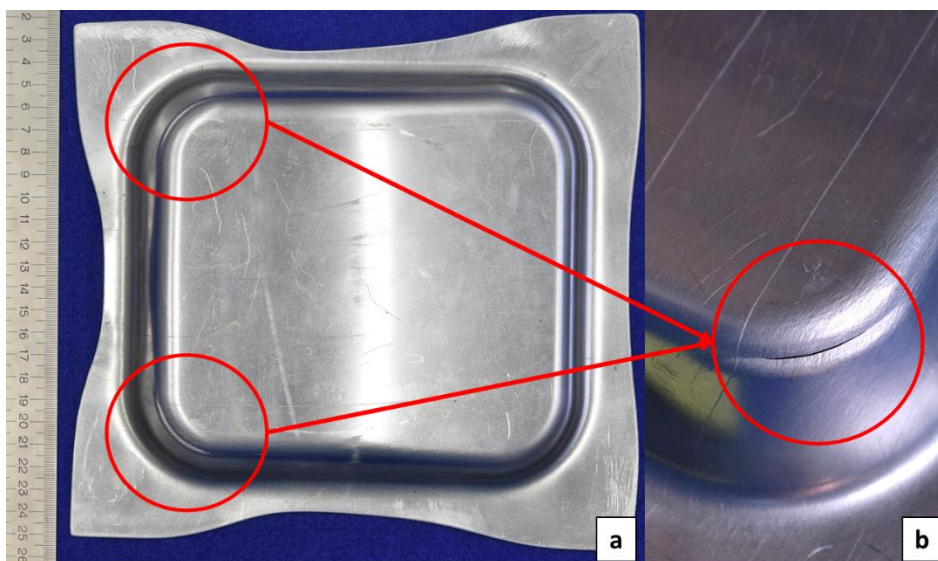


Figure 3. 15: fractures zone on blank B4 (a) with a detailed view (b).

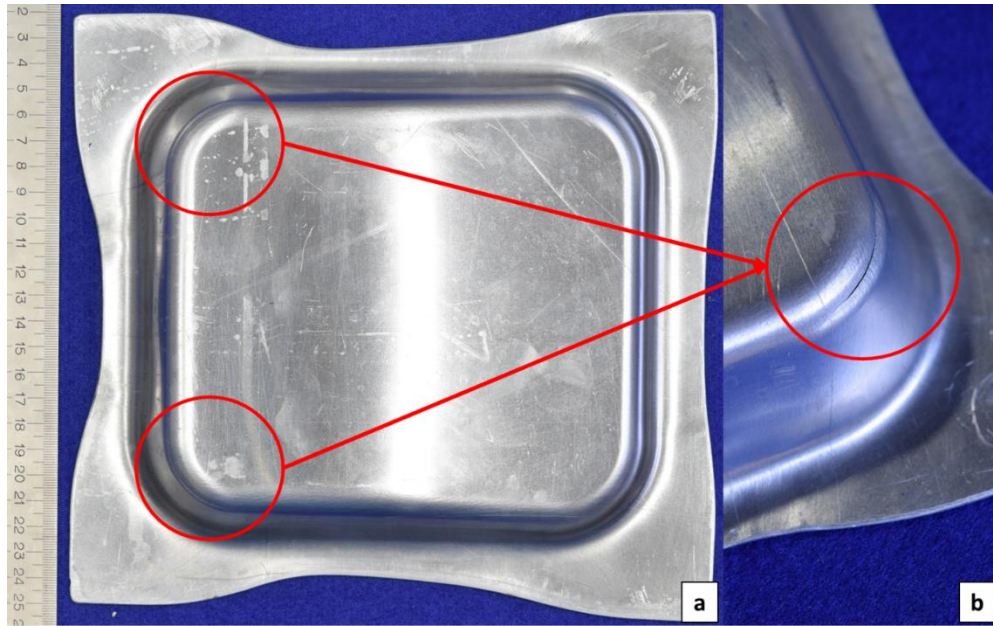


Figure 3. 16: fractures zone on blank B12 (a) with a detailed view (b).

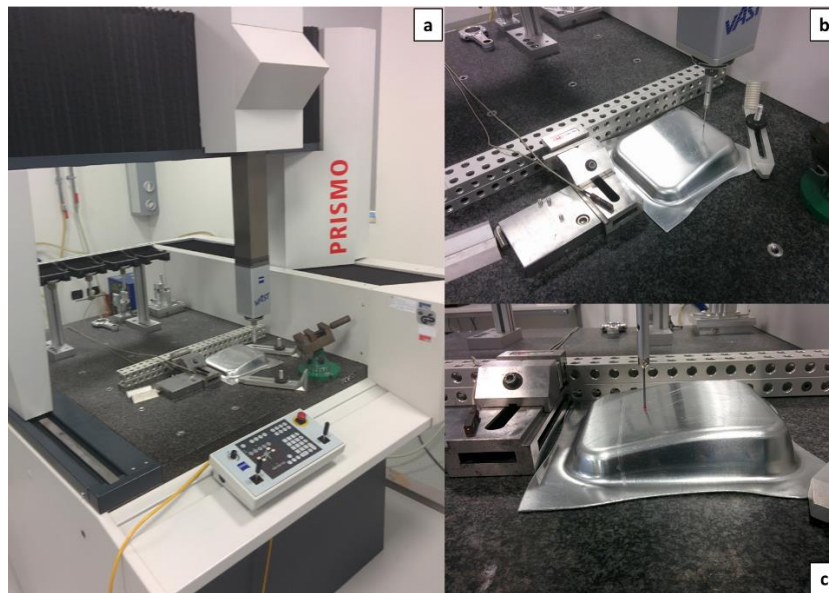


Figure 3. 17: profiles measuring on the CMM machine (a), and details of the measuring path (b-c).

All stamped parts have been measured with a Zeiss Prismo 5 VAST MPS HTG Coordinate Measuring Machine (CMM), obtaining their profile at the symmetry plane (Figure 3. 17).

Very large deviations have been found between the experimental components and the designed one presented in Figure 3. 1. Possible causes of these deviations can be conferred to springback effects but also largely to the deformation of the tools during the process, due to the low stiffness of the material highlighted also during the mechanical tests described in chapter 2.

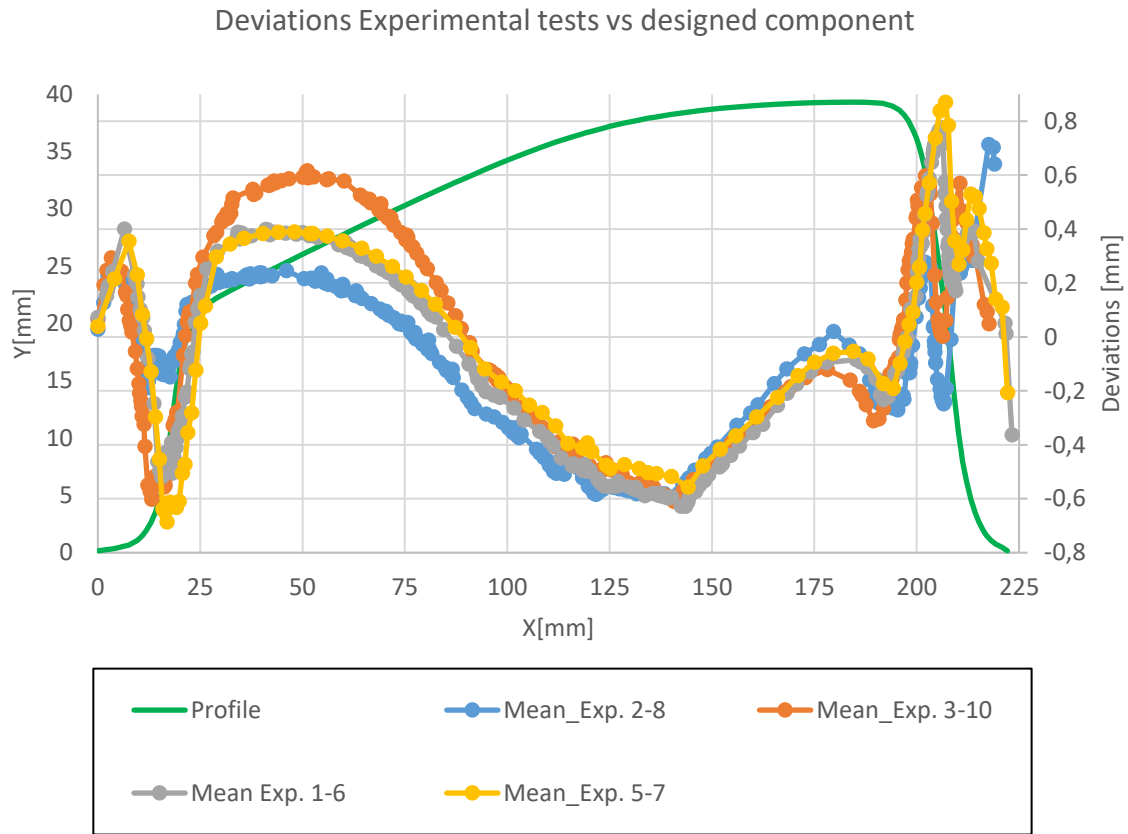


Figure 3. 18: locations of the deviations between the experimental tests and the designed component (test case 1).

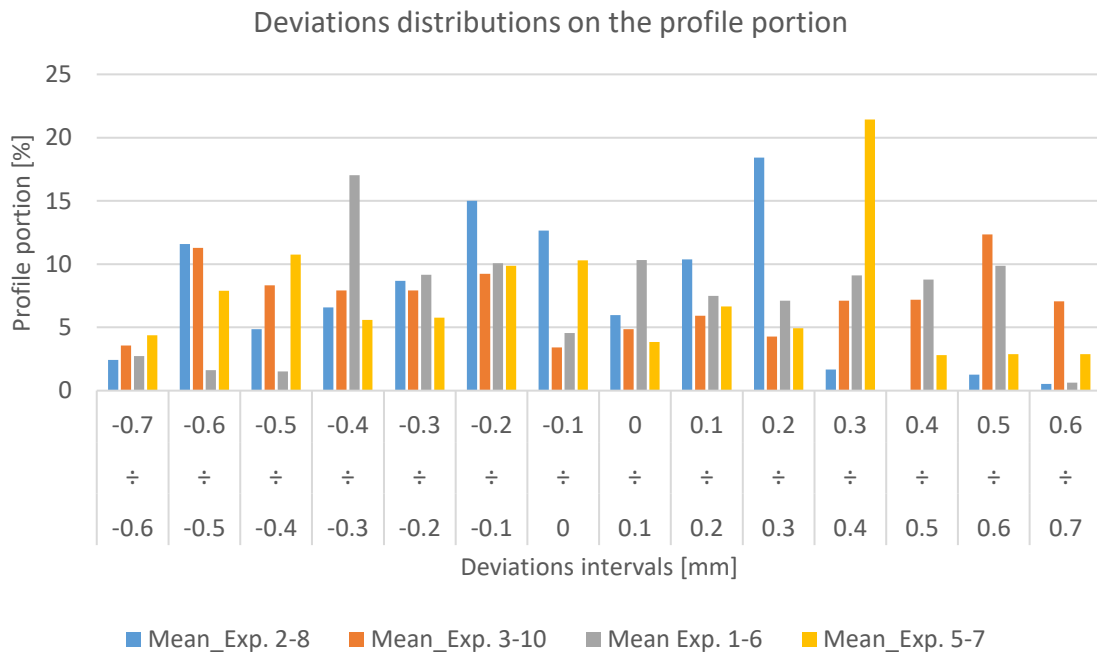


Figure 3. 19: distributions of the deviations between the experimental tests and designed component on the profile portion (test case 1).

In Figure 3. 18 and Figure 3. 19, the trend and the distributions of the deviations, between the experimental and designed component, are presented. The experimental deviations have been presented as mean values of the corresponding experiment in order to be shown clearly. The geometrical deviations present similar trends, and the largest geometrical errors can be observed with a value of BHF 22 kN (experiments 3-10). On the other hand, the smallest values of stress on the plastic tools is obviously expected at the minimum possible values of blankholding constraints. Plastic tools that are less stressed during the stamping process will have a longer expected life and will eventually be more cost efficient. In spite of the economic advantage presented in the paragraph 3.2.2, very large geometrical errors within [-0.7; +0.7] mm have been found due to springback and tools deformation effects. Therefore, the necessity of the implementation of a tool shape compensation approach has been highlighted and demonstrated. The compensation algorithm presented in the following paragraph will allow reducing the geometrical errors within tolerance, while still keeping the BHF value at a low level, in order to have the best compromise solution between tools life and dimensional quality results.

3.2.3 FEM model

3.2.3.1 Mesh and geometry

The FEM model has been implemented with the commercial code PAM-STAMP 2G V2015.1, which allows defining the rectangular geometry of the blank directly in the graphical unit interface in a parametric way.

The stamping process simulation will need to evaluate the deformation of the blank and the tools at the same time [9], in order to obtain the similar profile of the experimental blanks. For this reason and for the results obtained from the simulation of the compression tests presented in chapter 2, the mesh of the polyurethane tools has been generated with four-node tetrahedral solid elements. The solid mesh of the plastic tools has been created with VisualMesh 11 by using an integrated automatic tetra mesh algorithm. Fundamental steps of the process are: to repair CAD models, when necessary, assembly volumes by detecting overlapping zones and connecting them, split at intersections of volumes, generate good quality skin triangular mesh and fill the volumes with tetra mesh using the skin mesh [10]. The workflow of the automatic tetra mesh algorithm operates with the following procedure (Figure 3. 20):

1. **Collect inputs:** all the curves, points and coincident surfaces present in the model are deleted. Also, all the neighbouring surfaces lying within the stitch tolerance are stitched together. The tolerance value to identify the coincident surfaces will be a little higher than the stitch tolerance which is specified through process parameter table. The user can also choose:
 - a. *The element size.* If necessary, multi element size can be also chosen in order to generate bigger elements in the zones of the component with less concentrations of complex feature (ex. small radius, curvature changes).
 - b. *The topology simplification level,* which simplifies the surfaces of the component. Small edges and sharp corners are removed during

simplification of topology. The simplification avoids small element creation with small internal angles.

- c. *Boundary layer*. It assures that a layer of interior nodes will be generated inside a thin-walled region even if the surface mesh at this location has no interior nodes connecting the boundary edges.
2. **Repair bad geometry**: removes surface overlaps and small intersecting fins, punches holes when cylinders touch surface of volume and fills gaps.
3. **Stitch Volumes (Assembly)**: assembles the stitched surfaces, which have overlapping surfaces between them, and creates a single volume.
4. **Simplify Surfaces**: the topology faces is simplified according with the level chosen at first step.
5. **Generate 2D Mesh**: Creates skin triangular mesh on the cleaned topology faces. Different meshing schemes are tried for the complex faces, to generate high quality mesh and to avoid mesh failure.
6. **Check & Correct 2D Mesh**: Checks the skin mesh problems such as intersections and cracks present in the model and corrects (if present) automatically.
7. **Generate 3D Mesh**: the tetra mesh is generated according with the boundary layer method selected in the first step. The validation of the generated mesh is performed with the following parameters, which values can be chosen by the user (in this case the default values have been used):
 - a. **Tetra Aspect Ratio**: Ratio of the Maximum edge length and Minimum edge length.
 - b. **Tetra Radii Ratio**: Ratio of the radii of the inscribed sphere and circumscribed sphere of the tetrahedron.
 - c. **Tetra Min Face Angle**: Minimum value of all face internal angles.
8. **Check 3D Mesh**: at the end, a complete report about the quality of the obtained mesh is generated.

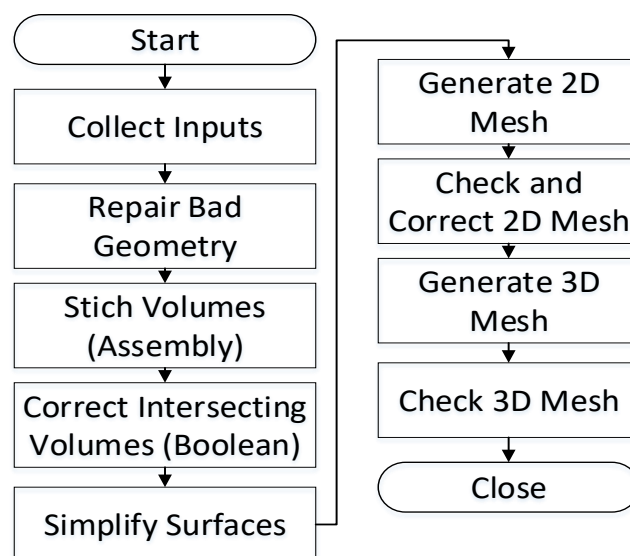


Figure 3. 20: automatic tetra meshing process workflow in Visual Mesh 11 [9].

By default in PAM-STAMP, the tetrahedral elements are composed by 4 nodes, with trilinear interpolation polynomials (element C⁰). Each node has three degrees of freedom in translation and no degree of freedom in rotation, with only 1 integration point in the element. The chosen hourglass control is Flanagan-Belytschko viscous based on shape vectors. An artificial bulk viscosity is computed whenever a solid element is undergoing compression and is added to the pressure. This viscosity permits the formation of shock waves and damps out numerical oscillations, the default values have been chosen as 1.2 for quadratic and 0.06 for linear, because preliminary tests have been performed with no relevant influence on the final geometrical results on the blank profile. The solid hourglass viscosity coefficient prevents vibrations in zero energy (hourglass) modes, as for the previous coefficient, the default value 0.1 has been chosen.

During the experimental activities, the exact displacement of the die could not be obtained with an accuracy of 0.1 mm, equal to the order of magnitude of the deviation errors found in Figure 3. 18. For this reason, during the design phase of the tools setup, mechanical end strokes for the blankholder have been generated (Figure 3. 21). This design solution allowed defining the stop criteria of the simulation with a higher order of magnitude respect to the evaluated experimental deviations.

In order to simulate the end-strokes effect, the middle plate and the upper surface of the end strokes have been also introduced in the simulation model as rigid tools composed by 2D elements, similar method can be found in [11].

The number of elements and the number of nodes for each deformable and rigid tools are shown in Table 3. 4.

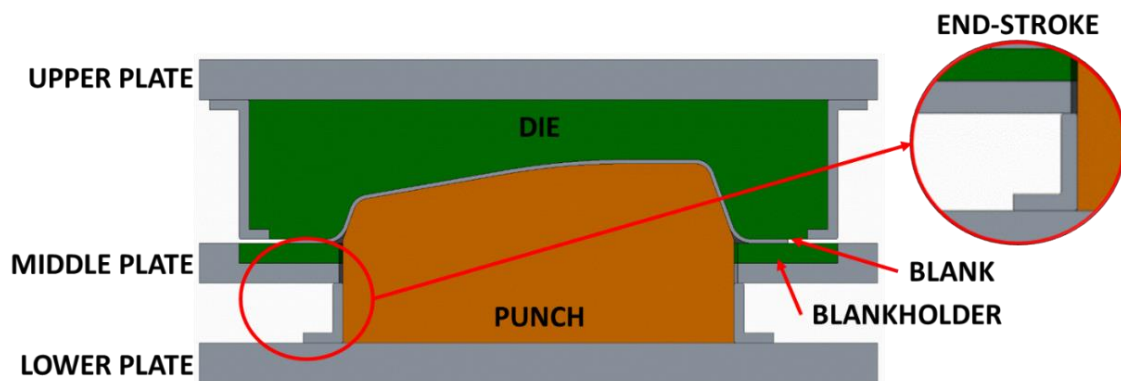


Figure 3. 21: transversal section of the stamping setup at the end of the stamping operation with highlight of the designed end stroke.

Tool	N. elements	N. nodes
Die	177083	34568
Blankholder	12260	3524
Punch	194665	36647
Middle plate	16460	2745
End strokes	439	117

Table 3. 4: number of elements and nodes used for meshing the tools.

The dimensions of the rectangular blank are 125x270 mm, due to the symmetry, and the surface area of each initial element is 345 mm² with a total number of 98 initial elements. The shell elements chosen for the blank have 4 nodes with three degrees of freedom in translation and three degrees of freedom in rotation and bi-linear interpolation polynomials. The thickness integration rule, which defines the distribution of the integration points across the thickness, and the weight of each point, is Gauss formulation where the weight is different and the distribution is done to improve the quality of the results. Five integration points have been imposed along the thickness in order to achieve good quality of the results [12]. The shell elements formulation is Belytschko-Tsay, which is based on the concept of uniform reduced integration and normally used in FEM simulation of plastic deformation. The Hourglass control, chosen for the blank elements, is based on the elastic modulus, which adds stiffness to elements. The anti-drilling is imposed by default by adding penalty on z-rotation.

Refinement will be also applied to the blank in order to split each quadrangular element into four smaller quadrangular shells, by an automatic refinement algorithm. The adaptive refinement algorithm will split, when required, the elements for 5 times. For clarification, an example of division at level 4 is shown in Figure 3. 22.

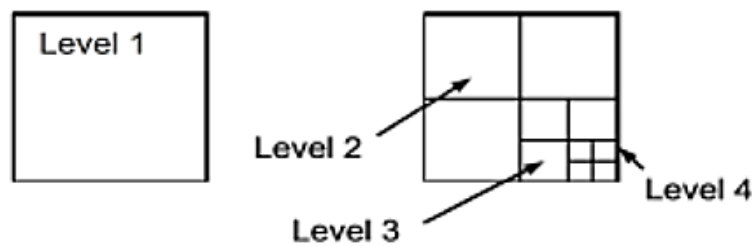


Figure 3. 22: example of refinement at level 4 [12].

Pam-Stamp 2g 2015.1 uses two refinement criteria for determining when an element should be refined: the angle and the geometrical criterions [12]. In the angle criterion (Figure 3. 23a), useful for the detection of wrinkling, the solver refines an element when the variation of the angle between its normal and that of one of its neighbours exceeds a limit angle whose default value is 10°. Instead, with the geometrical criterion (Figure 3. 23b), the solver adapts the density of the mesh to the local curvature of the tools close to the blank.

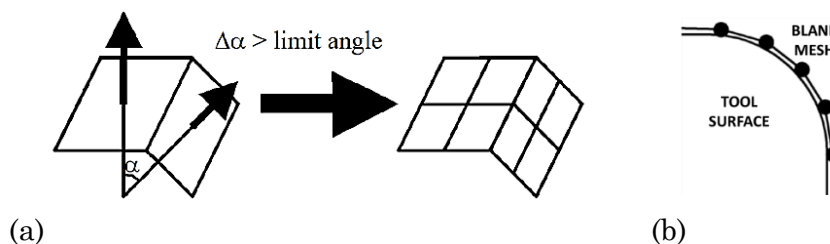


Figure 3. 23: schemes of angle criterion (a) and geometrical criterion (b) implemented in PAM-STAMP 2g 2015.1 [12].

The geometrical criterion triggers blank refinement before errors due to a too coarse mesh appear. It enables a more accurate simulation of the stress field. However, the angle criterion only acts once the error is detected. The scheme of the geometrical simulation setup is presented in Figure 3. 24 in order to resume schematically all the objects involved in the model.

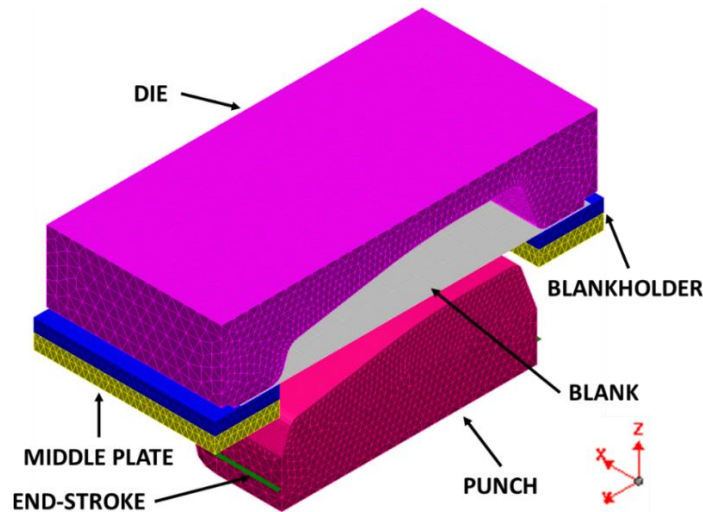


Figure 3. 24: Scheme of the simulation setup.

3.2.3.2 Material properties

The tensile test data of the blank have been retrieved in the “CES EduPack” material database, since the Al 1050 is a very common material. The FEM software used for this research calculates the effective stress in a symmetrical way with respect to mean tensile and compression states of stress. In other words, a unique Young’s modulus for tension and compression can be defined. The compression and tensile tests described in chapter 2 demonstrate that the compression and tensile Young’s are very similar for the polyurethane materials involved in the experimental activities. In Table 3. 5, the material properties of the blank and tools material are resumed.

Material	Young Modulus (E)	Yield Stress (R _s)	Peak Stress (R _m)	Elongation (A%)	Poisson (ν)	Density (ρ)
	[MPa]	[MPa]	[MPa]	[%]		[g/cm ³]
Al1050 (blank)	72000	33	76	35	0.335	2.73
Necuron 1300 (punch)	2664	66	61.8	-	0.340	1.15
Necuron 1050 (die, blankholder)	3088	47	73.2	-	0.340	1.20

Table 3. 5: material properties of the polyurethane tools and aluminium blank.

The elasto-plastic material properties of the polyurethane materials shown in Table 3. 5, have been calculated as a mean of the values obtained in the compression stress. The mean plastic stress-strain curves of the polyurethane materials have been already

presented in chapter 2. The density has been obtained from the datasheet of the materials, already presented in chapter 2, and the Poisson's coefficient value has been found in literature [13] - [15] where FEM models of sheet metal forming processes involved similar polyurethane materials.

The blank material has been modelled as elastic-plastic with the Krupkowsky constitutive law:

$$\sigma = K \cdot (\varepsilon_0 + \varepsilon_p)^n \quad (3.1)$$

The coefficient n , K and ε_0 of the Krupkowsky law have been calculated from the inverse equations 3.2, 3.3 and 3.4. The correspondent hardening curve is presented in figure.

$$\varepsilon_0 = \ln\left(1 + \frac{R_s}{E}\right) = 0.0005 \quad (3.2)$$

$$n = \frac{\ln[R_m \cdot (1 + A\%) - \ln(R_s \cdot e^{\varepsilon_0})]}{\ln[\ln(1 + A\%)] - \ln(\varepsilon_0)} = 0.175 \quad (3.3)$$

$$K = R_s \cdot \frac{e^{\varepsilon_0}}{\varepsilon_0^n} = 126.7 \text{ MPa} \quad (3.4)$$

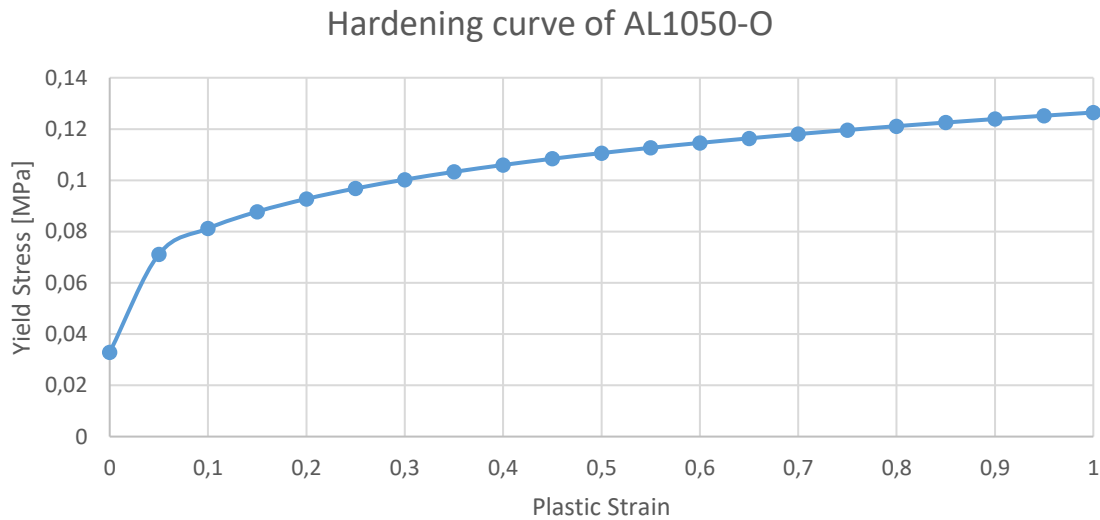


Figure 3. 25: AL1050-O hardening curve coming from the Krupkowsky constitutive law.

3.2.3.3 Boundary conditions

The simulation starts at the end of the holding stage in which the blank is held between the die and the blankholder (Figure 3. 24). Then the die moves down with a constant velocity, calculated from the data acquired during the experimental activity. The blankholder applies the experimentally measured BHF (Figure 3. 13), in order to control the draw-in of the blank.

The contact algorithm between the objects is defined by accurate algorithm described in chapter 2, taking into account a Coulomb friction coefficient of 0.25 [13] - [15], in

order to better simulate the interaction between polyurethane and aluminium materials condition.

The contact between the middle plate and the blankholder has been modelled by designing the same mesh on the surface of the two objects (rigid 2D middle plate and deformable solid blankholder) and, successively, merging the correspondent nodes at the interface (Figure 3. 26). This solution lock all the relative displacement between the blankholder and the middle plate, additionally, it represents a work-around solution for applying the force boundary condition on a surface of deformable solid object in PAM-STAMP.

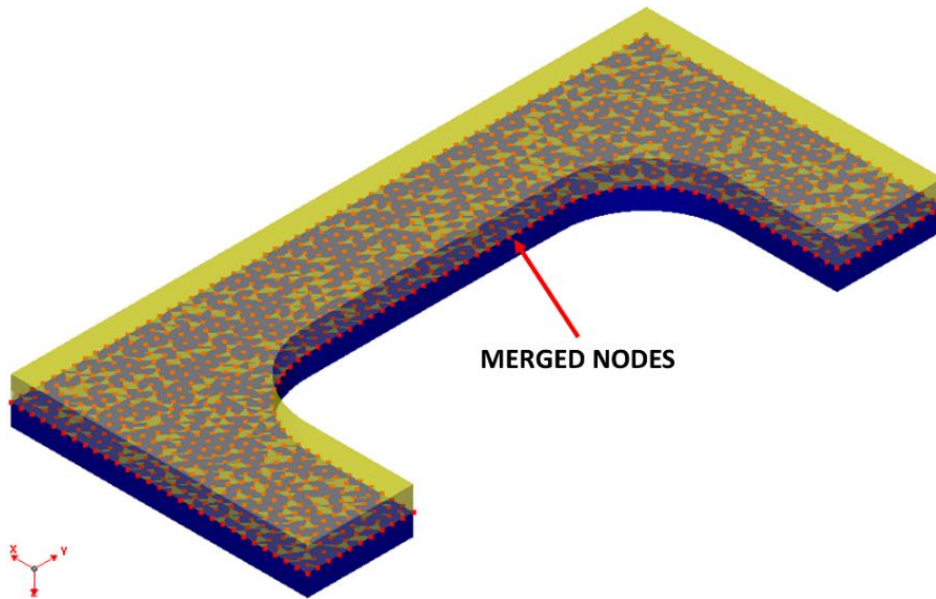


Figure 3. 26: merged nodes at the interface between the rigid middle plate and deformable blankholder.

As shown in Figure 3. 9, the plastic tools are enclosed within metal plates, which act as connecting elements to the press and as casings for the tools. In order to correctly simulate the effect of these plates on the deformable tools shown in Figure 3. 9 (green and orange tools), proper boundary conditions have been applied only on specific nodes.

For the die, a given velocity is applied on the upper and on some lateral nodes, in order to simulate the effect of the upper plate and supports shown in Figure 3. 8; a fixed displacement is applied on the lower and some lateral nodes of the punch, for obtaining the effect of the lower plate and positioning supports described in Figure 3. 6. A schematization of the boundary conditions of the entire model is presented in Figure 3. 27. For the die, a given velocity is applied on the upper and on some lateral nodes, in order to simulate the effect of the upper plate and supports shown in Figure 3. 8; a fixed displacement is applied on the lower and some lateral nodes of the punch, for obtaining the effect of the lower plate and positioning supports described in Figure 3. 6. A schematization of the boundary conditions of the entire model is presented in Figure 3. 27.

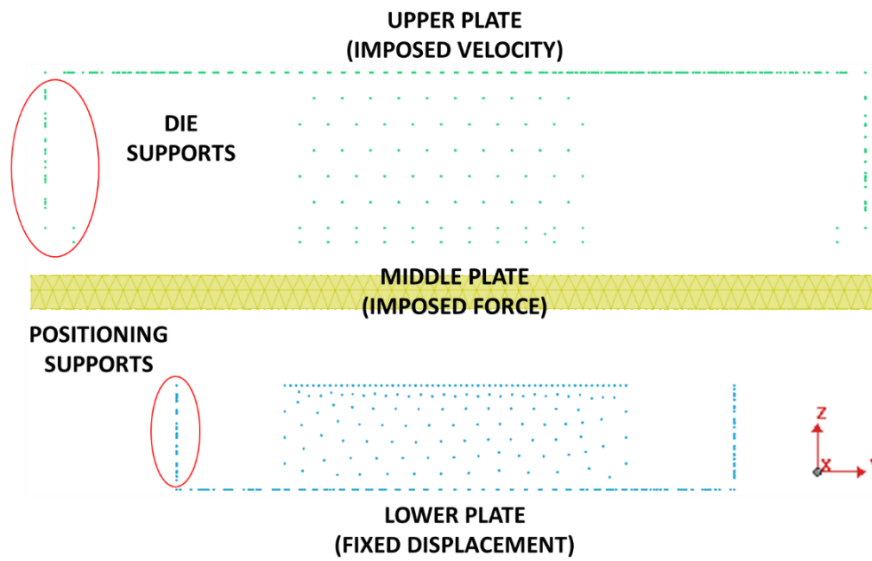


Figure 3. 27: scheme of the nodes and elements with boundary conditions applied.

The springback analysis has been run with the “Advanced Implicit” algorithm, implemented in the FEM software, by removing three degrees of freedom at two nodal locations on the stamped component, due to the symmetry (Figure 3. 28).

In Advanced Implicit formulation, the mechanical equation is solved on the final configuration of the previous increment, which is known (Update Lagrange method), while in implicit calculations it is solved on the current configuration, which is unknown (Quasi-Euler method). Updated Lagrange is usually more stable than Quasi-Eulerian method because it is easier to compute a tangent matrix, which is fully consistent with Residual Forces. In advanced implicit simulation, a set of non-linear equations is solved by using either the Newton - Raphson method (as in Implicit) or the Arc-length method [12], both used to convergence criteria on Force and displacement. For clarification, the resume of the boundary conditions and the interaction matrix of the simulation are presented in Table 3. 6 and Table 3. 7.

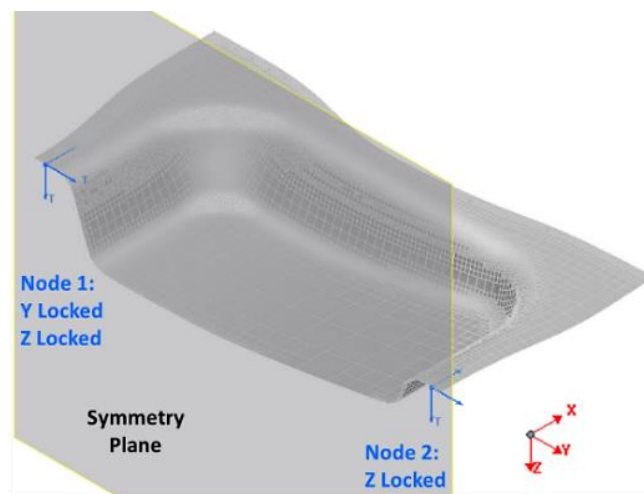


Figure 3. 28: scheme of the boundary condition applied on the blank in springback step.

Stage	Object	Rigid Body	Cartesian kinematic	Refinement	Springback	Boundary conditions
Stamping	Blank			Level 5		
	Die (nodes)		Locked translations: X, Y Locked rotations: X, Y, Z Imposed velocity: -Z			
	Punch (nodes)		Locked translations: X, Y, Z Locked rotations: X, Y, Z			
	Middle plate	Simplified	Locked translations: X, Y Locked rotations: X, Y, Z Imposed Force: Z (factor 0.5)			
	End Strokes	Simplified	Locked translations: X, Y, Z Locked rotations: X, Y, Z			
Springback	Blank				Advanced Implicit	Node 1: TY and TZ locked Node 2: TZ locked

Table 3. 6: resume of the complete boundary conditions imposed in the simulation setup.

Master \ Slave	Blank
Die	Accurate algorithm with friction 0.25
Blankholder	Accurate algorithm with friction 0.25
Punch	Accurate algorithm with friction 0.25

Table 3. 7: simulation interaction matrix between tools (master) and blank (slave).

3.2.3.4 Validation

In this paragraph, the validation of the FEM model will be presented by comparing the experimental values of the stamping process with polyurethane tools. As described before, 10 experiments have been performed where 5 levels of blankholder force have been replicated 2 times. The signals of the blankholder forces have been registered by a sampling frequency of 100 Hz. In Figure 3. 14, the repeatability of the registered

signal is robust for experiment with the same blankholder force level. For this reason, only 5 simulation have been conducted, due to the determinist behaviour of the FEM calculation.

As a first way for validating the accuracy of the simulations, the experiment no. 4 and 9 are very useful, where the maximum force is applied on the blankholder. In the real tests, fracture occurred at this high level of draw-in restraint (Figure 3. 15). Fortunately, the experiment and the simulation show the same location of the blank fracture localized at the deepest corners of the component (Figure 3. 29). No other simulation had occurrence of fracture.

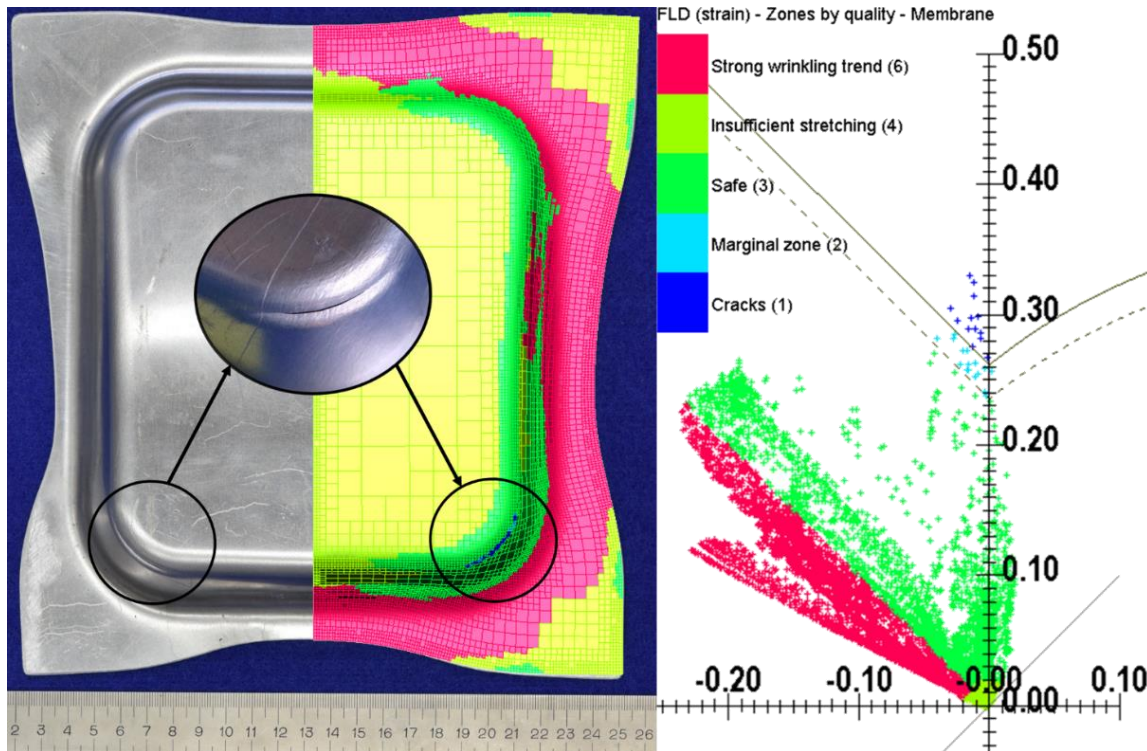


Figure 3. 29: FLD of the simulation of test 4-9 compared with experimental results.

The validation of the FLD map has been done by comparing the strain measured experimentally and the simulated ones. The experimental engineering major and minor strain have been measured with AutoGrid® 3D measuring system made by ViALUX [16]. The AutoGrid® 3D measuring system allows to evaluate the engineering strain on a stamped component previously meshed with a grid pattern (Figure 3. 30a). The meshing operation has been performed with chemical processes in collaboration with ViALUX. The 3D measuring system evaluates the deformation of the grid pattern on the stamped component and calculates the correspondent deformation in term of engineering strain maps. A smaller experimental plan, respect to the previous one described in Table 3. 3, has been performed in order to measure the strain maps at different blankholder force levels. The second experimental plan consist in 5 experiments at three BHF levels (minimum, maximum and mean), with 3 repetitions at mean level (Table 3. 8).

Experiment no.	Mean BHF (kN)	Blank_code
1	30	G01
2	30	G02
3	38	G03
4	30	G04
5	22	G05

Table 3. 8: experimental plan with meshed blanks.

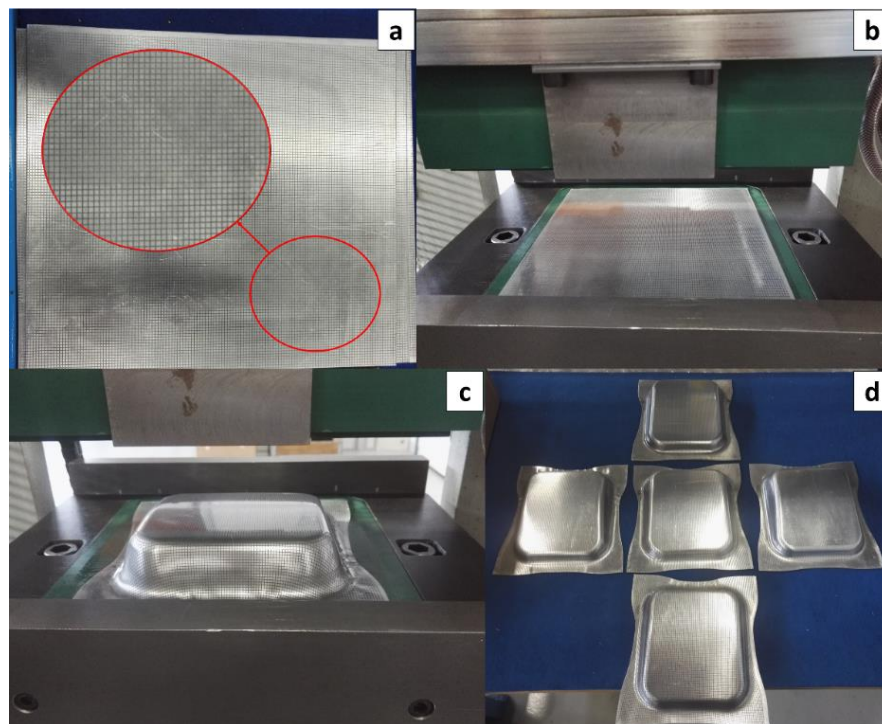


Figure 3. 30: grid mesh applied on the aluminium blank (a), blank before the deformation (b), stamping result and results of the experimental plan with meshed blanks (d).

The comparison between the FEM and AutoGrid® strain maps are shown in Figure 3. 31, Figure 3. 32 and Figure 3. 33. The strain values of the three experimental repetitions made at 30 kN does not change significantly, so only the results of the experiment 4 have been presented. The measured and simulated maps for the major strain compare very well, the two ranges are very close and the color maps are also very similar. As the only clear difference, the AutoGrid® measurements exhibit some localized spots of small negative values (pictured in dark blue), which are probably due to a small measurement error, also some elements of the mesh are missed during the acquisition phase. As for the minor strain maps, they are also very similar, although the FEM is not able to catch some small wrinkling at the flange, where the minimum negative values (pictured in dark blue) have been optically measured.

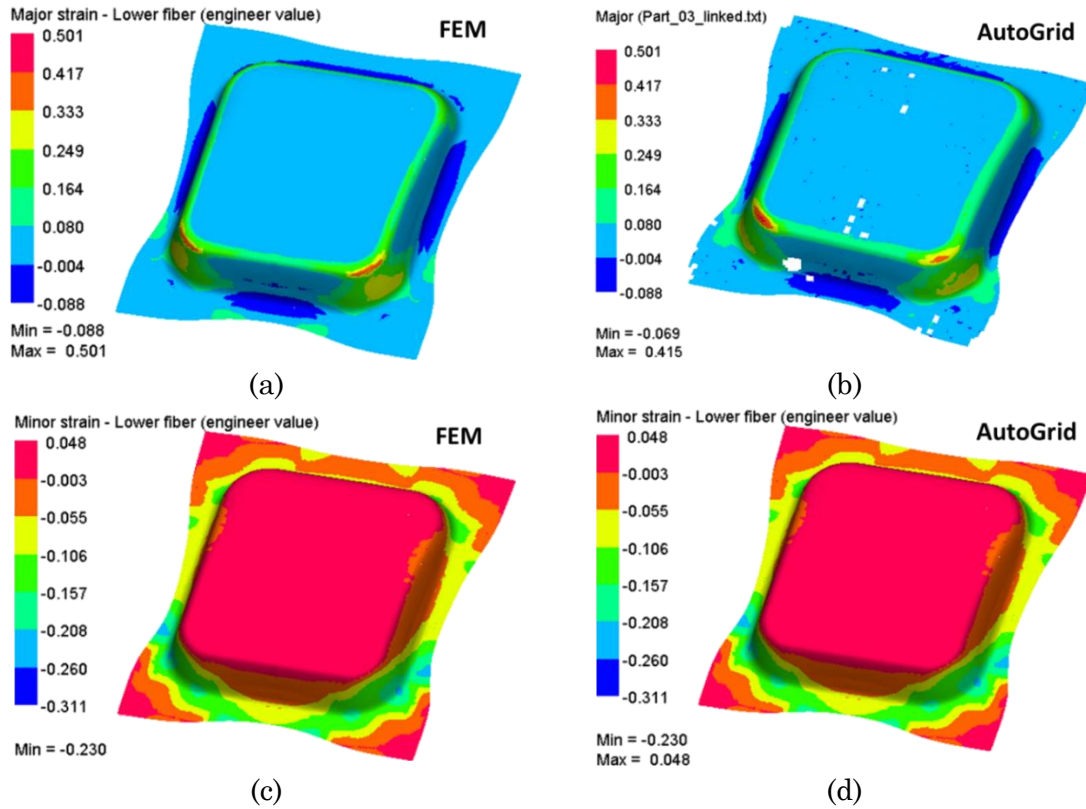


Figure 3. 31: comparison between simulated (a) and measured (b) engineering major strain maps, simulated (c) and measured (d) engineering minor strain maps for experiment 3.

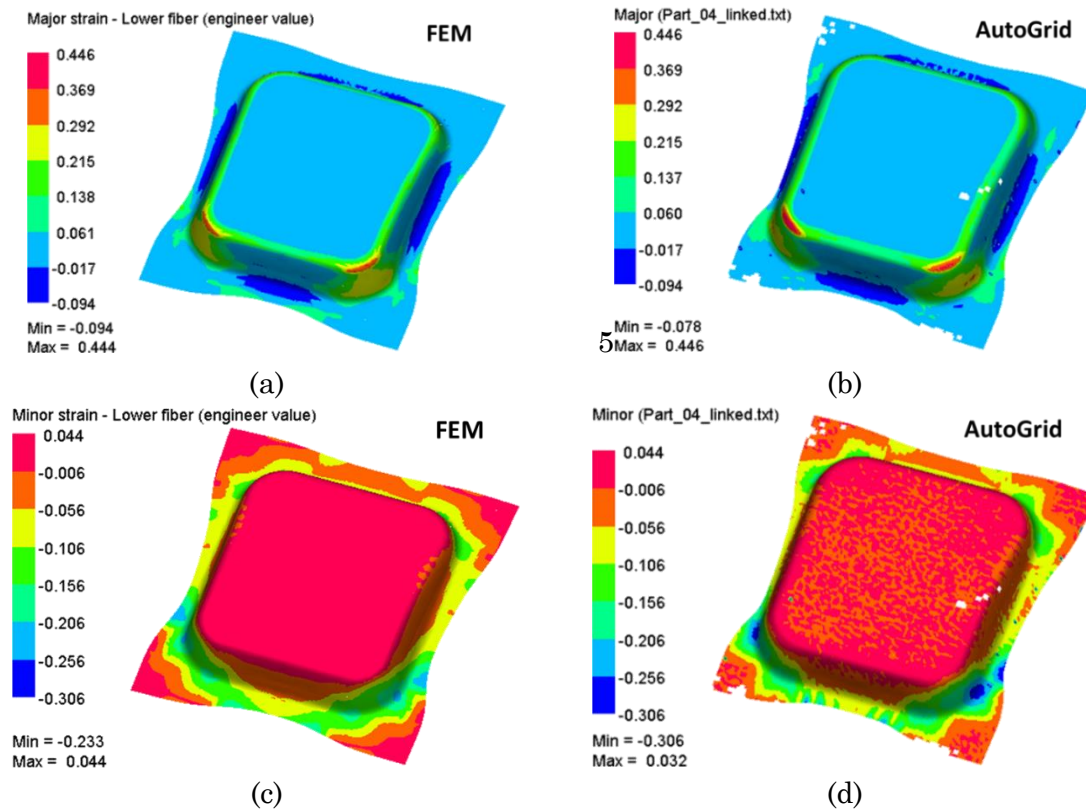


Figure 3. 32: comparison between simulated (a) and measured (b) engineering major strain maps simulated (c) and measured (d) engineering minor strain maps for experiment 4.

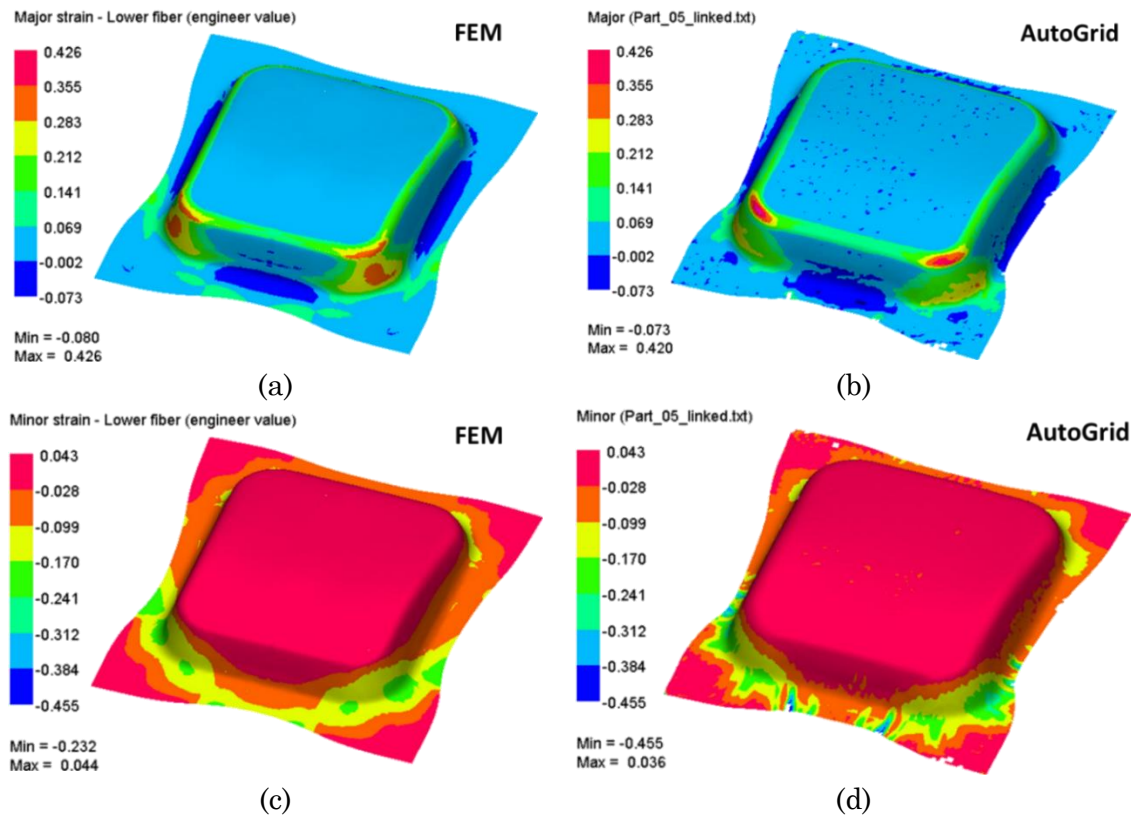


Figure 3. 33: comparison between simulated (a) and measured (b) engineering major strain maps, simulated (c) and measured (d) engineering minor strain maps for experiment 5.

As shown before, all stamped components have been measured with the Zeiss CMM in order to obtain the profiles along the symmetry plane, to be compared with the FEM simulation. In Figure 3. 34 the deviations distribution of the simulated components and the experimental ones are presented.

The range of the distributions of the “numerical error” is 50% smaller than the experimental one (Figure 3. 19). The numerical error seems apparently large, because it should be one order of magnitude smaller with respect to the experimental one; but it should be noted that the obtained error values are similar with the typical values obtained in numerical models where rigid tools are simulated [17]-[19].

The numerical error on the profiles of experiment no. 3 and 10 are presented in Figure 3. 35 The error between the experimental and numerical profiles are included in the range $[-0.46; +0.25]$ for part 3 and $[-0.40; +0.38]$ for part 10. 81.96 % of the deviation values are included within the interval of $[-0.25; +0.25]$; the mean of the deviations is -0.01 mm. In absolute terms, smaller error values can be observed close to the locations of the 2 FEM mesh nodes which have been locked in the simulation of springback (see Figure 3. 28).

As stated in the previous section, experiments no. 3-10 (mean blankholder force equal to 22 kN) form the most interesting test case, because of the low level of stresses on the tools and the corresponding large geometrical deviations between the stamped and the designed geometries. For this reason the deviations between the stamped components and the simulated one have been studied deeper than the others simulated cases (Figure 3. 35).

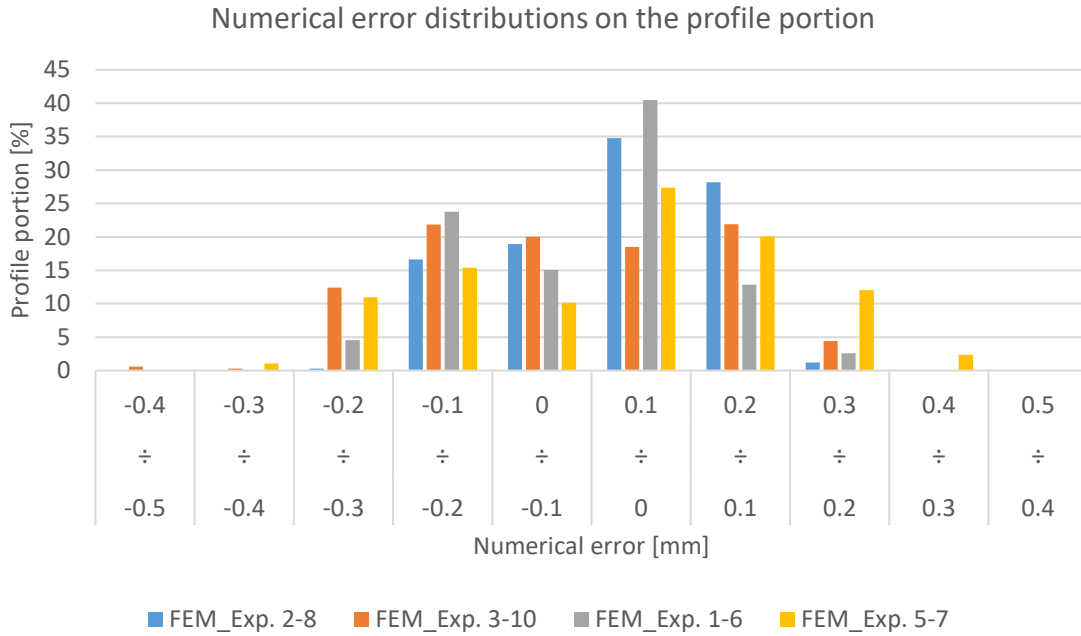


Figure 3. 34: distributions of the numerical error between the experimental tests and simulated components on the profile portion.

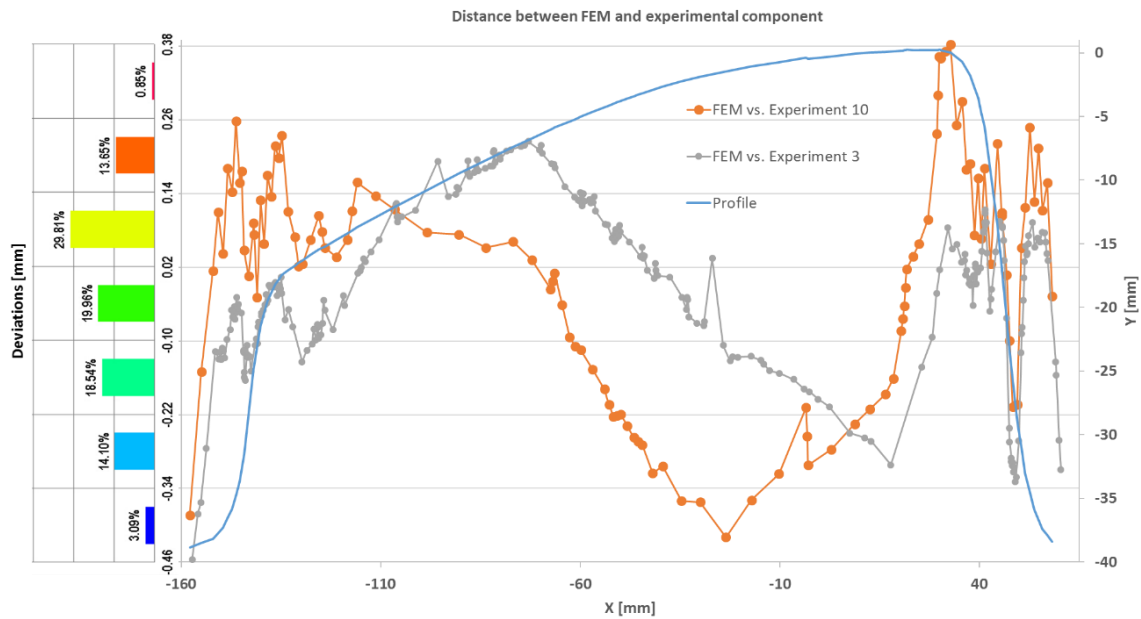


Figure 3. 35: errors between fem and experimental profile for experiments 3 and 10.

In Figure 3. 36, the range of the error between FEM and experiments (curves with triangles) is smaller than the deviations measured between the experimental and designed profile (curves with circles). In other words, the simulations seem to be accurate enough to allow for an improvement (through die shape compensation) of the stamped geometry.

In conclusion, the good results obtained from the comparisons of profiles and the fracture localization allow to consider the FEM model sufficiently accurate to model the stamping process with polyurethane tools. In the next paragraph, the validated FEM model will be used coupled to the compensation algorithm, developed for this doctoral thesis, for reducing the geometrical errors found in the experimental phase.

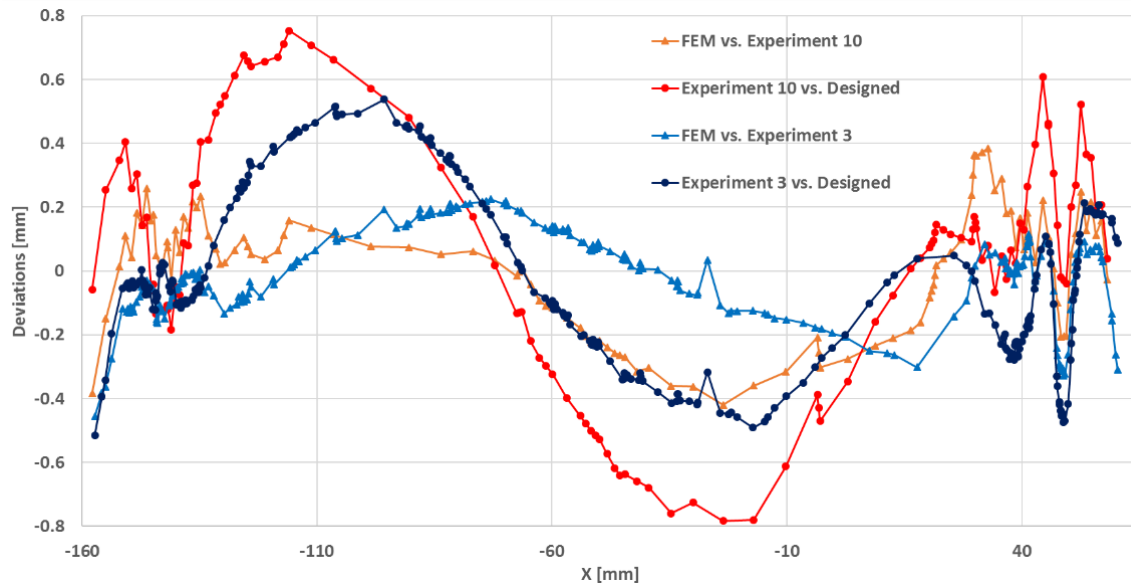


Figure 3.36: experimental vs. fem errors; experimental vs. designed profile deviations.

3.2.4 Compensation algorithm

3.2.4.1 Main compensation algorithm methods

The use of flexible tools as a true industrialised technique is limited, as emphasized during the experimental and numerical activities, by two main drawbacks: 1) the final geometry of the formed part is difficult to predict, because of the elastic deflection of the tools; 2) polymeric punches and dies are subject to early wearing and failure mechanisms, if compared to classic metal tools and, therefore, intended for single parts or very small batches. A study has been conducted for increasing the performance of the Rapid Tools made of coated polymers, by reinforcing the surface with a hard coating obtained by indirect spraying. The research work of J. Witulski et al. [17] demonstrates that reinforced Rapid Tools can be applied in small and medium batch productions of high strength materials.

One purpose of this doctoral thesis is to face the first issue, i.e. to solve the geometrical predictability problem, by using CAE in combination with a compensation technique. The approach is to predict the actual deformation of the tools and to determine their compensation in case the part falls outside the initial design tolerances.

The scientific literature on numerical die compensation methods is wide. Some of the more recent and relevant works in this field will be now cited.

The most frequently used methods for die compensation are the displacement adjustment (DA), the Force Descriptor Method (FDM) and the surface controlled overbending (SCO).

The displacement adjustment is probably the most effective method (Figure 3. 37); the tools nodes are displaced in the opposite direction of the blank springback [21]. This methodology is largely used in metal-forming processes where rigid metal tools are involved. The objective of the displacement adjustment method is the reduction of the springback amount. For this reason, the reference geometry is usually the deformed blank obtained at the end of stamping simulation ($\overline{blank}_{stamp_0}$). After the stamping simulation, a springback analysis is carried out and then the displacement of the blank (\overline{blank}_{sp_0}) can be calculated directly. The nodal displacements provide the “springback vector field”, a discrete field, defined on the nodes of the reference mesh only, discrete field, defined on the nodes of the reference mesh only:

$$\overline{sp}_{field} = \overline{blank}_{stamp_0} - \overline{blank}_{sp_0} \quad (3.5)$$

where \overline{sp}_{field} is the vectorial difference of the coordinates between the blank meshes end of stamping and springback analysis.

A proposition for a compensated product geometry is now calculated by displacing the nodes with a shape modification field.

After the compensation. A new FEM simulation is carried out with the optimized tools setup. The new springback mesh result (\overline{blank}_{sp_1}) is compared with the blank mesh coming from the initial stamping analysis ($\overline{blank}_{stamp_0}$).

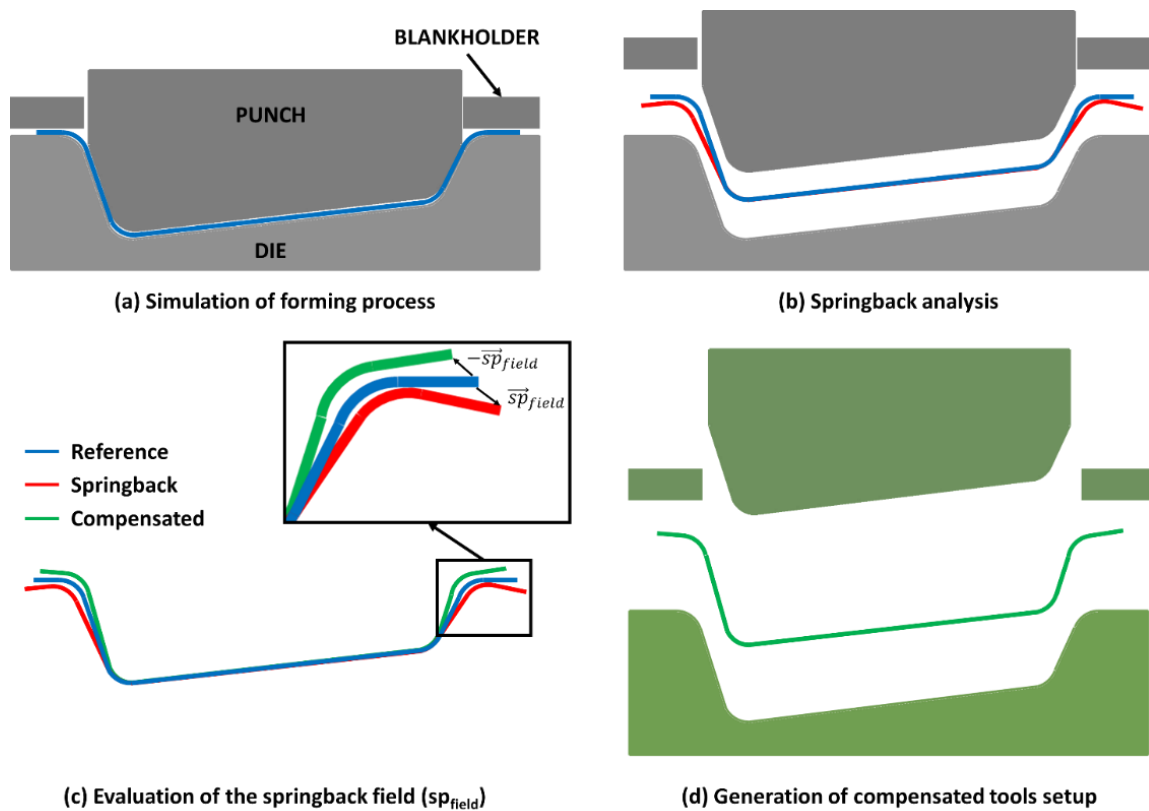


Figure 3. 37: main steps of the DA compensation algorithm: stamping simulation (a), springback analysis (b), calculation of the springback field vector (c), generation of new geometrical tools setup (d).

This comparison is done between two different simulations, for this reason calculating a “springback deformation field” is no more possible, but only a “shape deformation field” [22]. This operation is very difficult to carry out and it introduces some errors related to the continuous interpolation and extrapolation of complex 3D shape modification function. Another way is to apply directly a nodal displacement by calculating the deviations between the correspondent nodes of the blank ($\overrightarrow{blank}_{sp,1}$) and the initial stamped blank ($\overrightarrow{blank}_{stamp,0}$). This means that no remeshing can be possible or, alternatively, any new mesh must be remapped with reference to the mesh of the designed part. For this reason, the DA method is frequently used for simple 2D forming cases [23], where a small number of nodes must be mapped or remeshing is not even required.

The Force Descriptor Method proposed by Karafillis and Boyce [24] is an iterative method based on the evaluation of the internal forces of the component (Figure 3. 38). After the first stamping analysis, the contact forces (tractions) acting on the punch are ‘measured’ from the stamping simulation results result. The measure of the compensation is done in a separate FE calculation where the resulting force field (f) is applied to the blank geometry. The idea behind this is that at the end of stamping analysis, when the tools are closed, the blank retains its shape due to action of the force field (f).

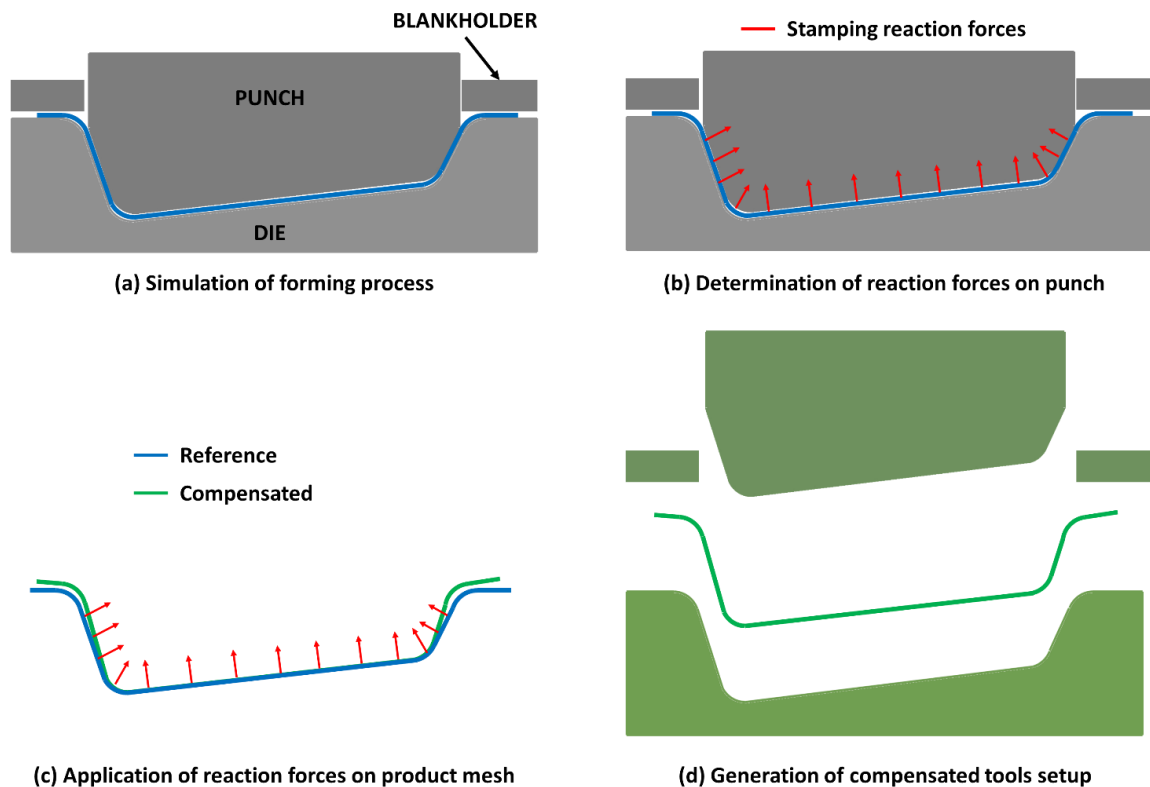


Figure 3. 38: main steps of the FDM compensation algorithm: stamping simulation (a), evaluation of the reaction force acting on the punch (b), application of the reaction forces on mesh product (c), generation of new geometrical tools setup (d).

When the tools are removed, it is assumed that the blank springs back under the action of that field. Therefore, the application of the force-field to the reference geometry can generate the compensated geometry, assuming that the deformation due to springback is compensated. It is assumed that residual stresses do not influence the elastic behaviour. This kind of algorithm suffers from lack of convergence, especially in symmetric cases or limit values of springback [25]-[26].

Another compensation method is called “surface controlled overbending”, which performs the calculation directly on the tools CAD. The basic idea behind the control surface algorithm is that a flexible surface can be generated for approximating the blank geometry before and after the springback (Figure 3. 39). The compensation between these two simplified surface can be easily performed by “displacement adjustment” method (already described before) directly on the CAD model instead of the mesh. This method is used to modify the shape of the tools directly but, again, the calculation complexity makes the method inaccurate on a surface with complex shape function [27]-[28].

All of the compensation methods found in literature have been developed for reducing the springback of the blank in a stamping process, because the rigid tools setup is used. In case of rapid tools, the compensation should be carried out by taking in account the springback of the blank, but also the deformability of the tools. In the next paragraph, a compensation algorithm suitable for stamping process with rapid tools will be presented.

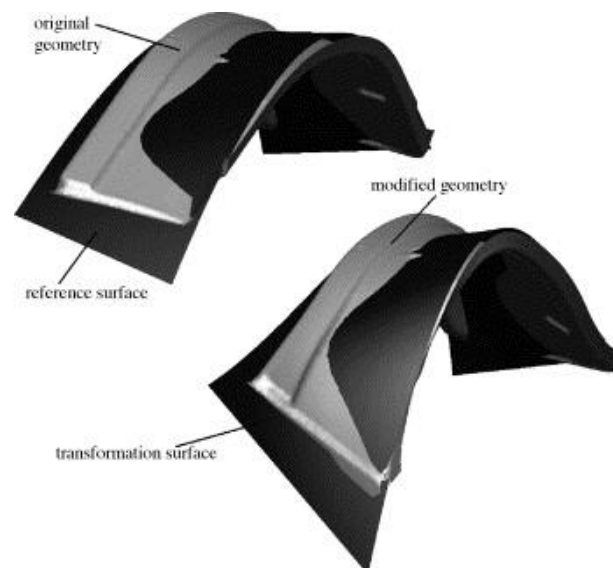


Figure 3. 39: example of control surface approximating the product geometry [29].

3.2.4.2 Description of the compensation algorithm

The purpose of this chapter is to describe the compensation algorithm developed in this doctoral research thesis, which will allow to determine the tools compensation in case the part (coming from a stamping analysis with deformable tools) falls outside the initial design tolerances. The proposed algorithm is inspired by the DA method, but improves the distance calculation by evaluating the normal distance from the tools

node to the interpolated blank surfaces. Unlike the standard DA, there is no need to keep track of predetermined couples of nodes. The calculation of the normal distance will solve the main disadvantage of the DA algorithm, allowing the applicability of the method also for 3D complex components. The present algorithm is an evolution of the preliminary results already presented in [30].

The main response variables in a stamping process with deformable tools should be the deviations between the geometry of the real *stamped* component and the *designed* one.

These deviations, shown in the previous paragraphs, are due mostly to the deformations of the rapid tools during the process and partly to unpredicted springback after the stamping process.

The deviations of the features registered at the end of the process can be reduced with an iterative compensation algorithm. The developed algorithm suggests the compensation to be applied on the rapid tools, in order to obtain the minimization of the deviations. The compensation algorithm iteratively runs the following two main steps:

1. **STEP I. FEM simulation:** the user prepares and runs a stamping simulation, followed by a springback simulation stage and a refinement stage (Figure 3. 40). The refinement stage can be put at the end of the simulation, in order to do not impact on the computing cost. In this stage, the meshes of the simulated component and the designed one are both regenerated with shell elements of approximately uniform side length. In the FEM model presented in paragraph 3.2.3 uniform level 5 of refinement has been chosen after the springback stage. The final mesh refinement stage is very useful for performing simpler and more accurate computations at the next step II. Geometrically, the meshes are built with shell elements which represent the middle surface of the part, i.e. half of the thickness should be added in the normal direction in order to model the actual outer or inner surface of the part. As a first guess, in the first iteration of the algorithm, the deformable tools can be built by offsetting the designed part by half of the initial sheet thickness.

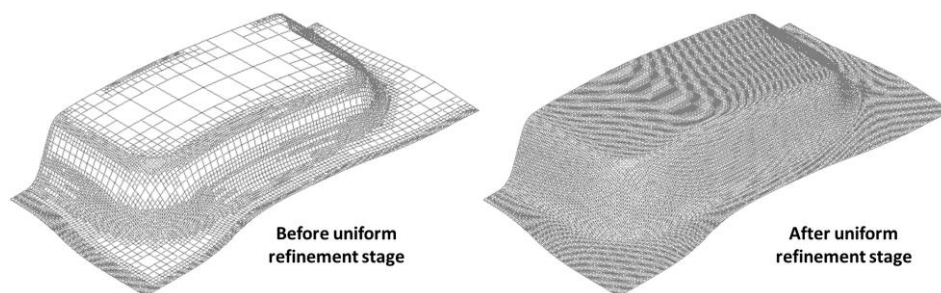


Figure 3. 40: blank mesh at the end of springback analysis (left) and successive mesh refinement (right).

2. **STEP II. Compensation:** the proposed algorithm has been coded within C++, on Linux platform, and is completely automatic. The routine requires the following inputs:

- a. the refined shell mesh with triangular elements of the simulated and the designed part, in order to construct the parametric surface functions. The triangular mesh can be obtained easily with a manual elements splitting operation after the refinement stage.
- b. the outer contour of the simulated part, which defines the domain of the compensation
- c. the mesh of the tools in composed by solid elements or by shell elements (only the external shell). The algorithm is able to distinguish the external point of the tools by imposing a calculation distance limit. If the calculation distance limit, between a generic tool node and the blank surface, is over the half nominal thickness of the blank plus 10%, the node can be considered as an internal node. In order to optimizing the computing time cost, the external shell mesh can be extracted by using directly the function of Visual-Mesh 11.0 called "Extract from 3D mesh" [10]. In this case, a lower number of nodes will be imported inside the algorithm which will can be very useful in case of very large models.

The compensation algorithm has been developed to be compatible with the mesh formats of PAM-STAMP software, because the FEM simulations have been performed with it. For extending the compatibility with other FEM software, translator plug-ins should be developed in order to easily read the nodes and elements matrix of the exported meshes.

The compensation algorithm modifies the tool geometry according to the following 4 sub-steps:

II.1 Blanks mesh import and surface fitting: the meshes of simulated and designed components, made by triangular elements, are imported. The nodal Cartesian coordinates of both the meshes are converted into parametric coordinates, with the library implemented in [31], as:

$$\Sigma_s = \begin{cases} x_s = x_s(u, v) \\ y_s = y_s(u, v) \\ z_s = z_s(u, v) \end{cases}; \quad \Sigma_d = \begin{cases} x_d = x_d(u, v) \\ y_d = y_d(u, v) \\ z_d = z_d(u, v) \end{cases} \quad (3.6)$$

The algorithm used for the surface reconstruction is the Multilevel B-spline Approximation (MBA) [32]-[33]. Starting by the parametric coordinates, the algorithm reconstructs the surface with a recursive refinement of the B-spline knots depending on the level of desired accuracy (k). This fitting allows handling the designed and simulated objects not as numerical meshes with their nodes, but as analytical surfaces. Researches in literature suggests that a good value of the accuracy level can be set between 9 and 10, [32]. No analysis at different accuracy level have been performed, because it will be demonstrated that the algorithm can converge rapidly to a stable solution.

II.2 Tools and blank contour import: the mesh of the tools and the outer contour of the simulated component are imported. The blank contour defines the domain of the compensation.

II.3 Compensation: Figure 3. 41 shows a 2D graphical representation of the computed quantities. The distances δ_d and δ_s between the generic tool node $\vec{T}_0(x_{t0}, y_{t0}, z_{t0})$, and the two fitted surfaces are computed through the conjugate gradient minimization algorithm [31].

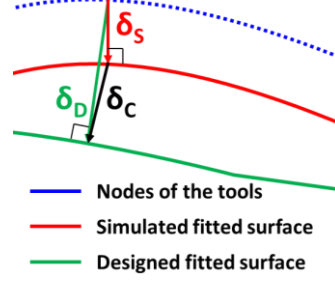


Figure 3. 41: computation of the new tool nodes position.

To be efficient the conjugate gradient algorithm needs a good starting point, in order to evaluate the domain of the tools node which will be involved in the compensation. Since the stamping direction of the current simulation is z , the xy plane is used as an initial guess. It is interesting to highlight that every main plane (xy , yz or xz) could be selected as initial guess, so there are no constraints related to the setup of the initial simulation. These distances are oriented in a 3D space, i.e. they are 3D vectors, with components in the Cartesian coordinates chosen for the simulation setup:

$$\vec{\delta}_s = [x_s, y_s, z_s] \quad (3.7)$$

$$\vec{\delta}_d = [x_d, y_d, z_d] \quad (3.8)$$

The deviation vector between the simulated and designed surfaces is defined as:

$$\vec{\delta}_c = (\vec{\delta}_d - \vec{\delta}_s) \quad (3.9)$$

In terms of coordinates:

$$\vec{\delta}_c = [x_{\delta c}, y_{\delta c}, z_{\delta c}] \quad (3.10)$$

The tool nodes are moved from the original position \vec{T}_0 by the quantity $\vec{\delta}_c$. The final position of the compensated tool node is defined as:

$$\vec{T}_c = \vec{T}_0 + \lambda \vec{\delta}_c \quad (3.11)$$

in terms of coordinates:

$$\vec{T}_c \begin{cases} x_{Tc} = x_{T0} + \lambda x_{\delta c} \\ y_{Tc} = y_{T0} + \lambda y_{\delta c} \\ z_{Tc} = z_{T0} + \lambda z_{\delta c} \end{cases} \quad (3.12)$$

Since the final tools shape is different from the initial one, the simulation of the subsequent iterations will give back different strain distribution on the stamped component, but also different springback behaviour and stresses distribution. In order to modify the compensation mechanism, the λ penalty coefficient can be tuned for controlling the strength of the compensation to be applied on the tools. Another method for influencing the quality of the compensation is by improving the quality of the tool mesh. In fact, the dimension of the \vec{T}_c vector is given by the number of nodes on the tool mesh. The effectiveness of the method partly depends on the tool mesh quality, especially in the zones where larger deviations are measured.

II.4 Exporting: step 3 must be repeated for both the punch and the die. The meshes of both compensated tools are exported, the FEM simulation is run again and the deviations, after compensation, are calculated again.

The algorithm can be applied iteratively, as shown in Figure 3. 42, and the whole procedure is repeated until convergence, i.e. until the deviations between the simulated and designed parts are within the tolerance interval chosen by the designer. Normally a tolerance interval between [0.1; -0.1] mm is acceptable for high precision stamped products.

In conclusion, the generation of this compensation procedure has been obtained by assembling different functions of pre-existing tools, as follow:

1. FEM simulations: PAM-STAMP explicit algorithm;
2. MBA algorithm for surface reconstruction from blanks meshes;
3. Go tools C++ libraries for compensation distances calculation.

The code of each single software tools (except for the FEM software) are freely available on internet [31], thanks to Geometry Group at SINTEF ICT, Department of Applied Mathematics for the development. Only the mesh import/export and the penalty method (equation 3.12) have been completely rewritten e recompiled together with the other software tools for generating a usable distribution of the compensation algorithm.

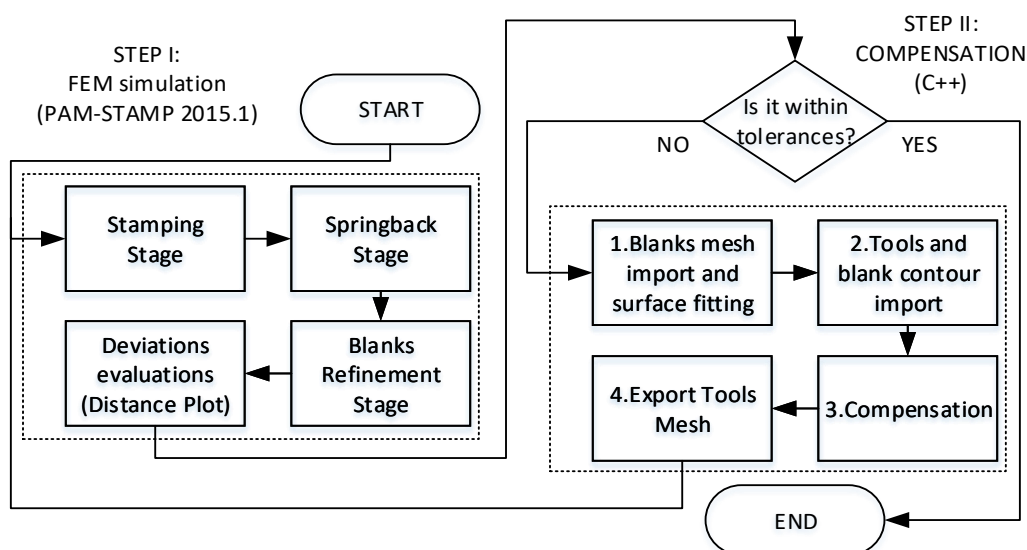


Figure 3. 42: flow chart of the tool compensation algorithm.

3.2.4.3 Application of the compensation algorithm on the case 1

The description of the compensation algorithm has been presented in the previous paragraph, in this section the results of the compensation algorithm will be presented for the case 1, performed by using as an input the results of the simulation of the test case made by experiments number 3 and 10, run with $BHF_{\max}=22$ kN (Table 3. 3).

The plot of the deviations between the simulated and designed components is shown in Figure 3. 43, for the whole part, including the flange. The results show that the simulated component deviates from its designed geometry in a range between $[-0.59; +0.71]$ mm, the distribution is very scattered and only 62.3% of the calculated deviations lay within the range of $[-0.22; +0.16]$. The deviation distribution is also compatible with the experimental distribution already discussed previously in Figure 3. 19. This distribution of geometrical errors (Figure 3. 43) is unacceptable for most engineering applications.

The maximum values of deviation are located on both the convex and concave corners. The locations of the main deviations correspond to a large deformation of both tools on the corner radii (Figure 3. 44 and Figure 3. 45). Not only the deviations on the four corners are large, but the error map in Figure 3. 43 shows some striations, which indicate the presence of a small wrinkling phenomenon.

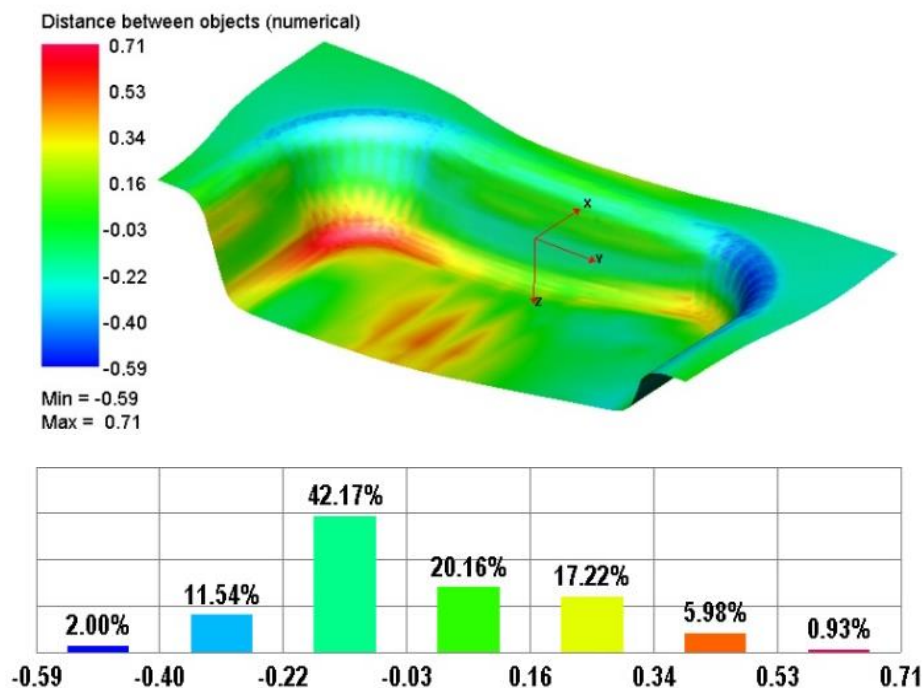


Figure 3. 43. δ -plot before compensation; isometric and top views, units in [mm].

The algorithm performed an automatic compensation of the tools geometry, with $\lambda=1$. As a result of the first compensation, the punch and die corners radii have been modified by the algorithm in order to reduce the deviations shown in Figure 3. 43. After the compensation, the range of the deviations between the designed and simulated components is drastically reduced.

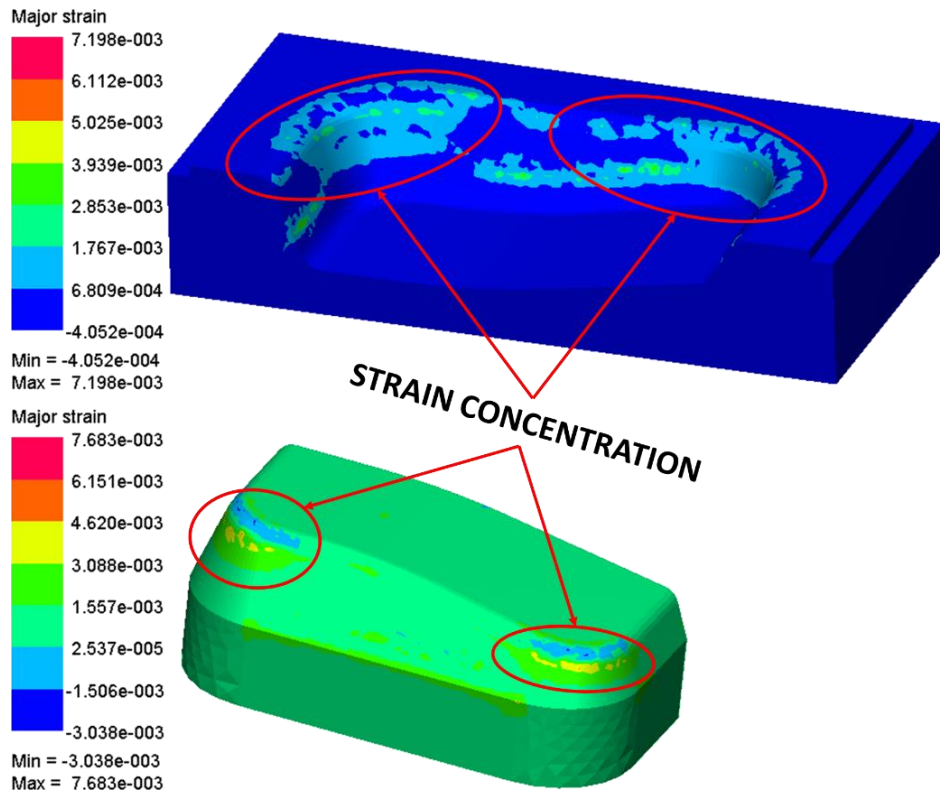


Figure 3. 44: major strain maps concentrations on the tools after the stamping simulation with non-compensated tools.

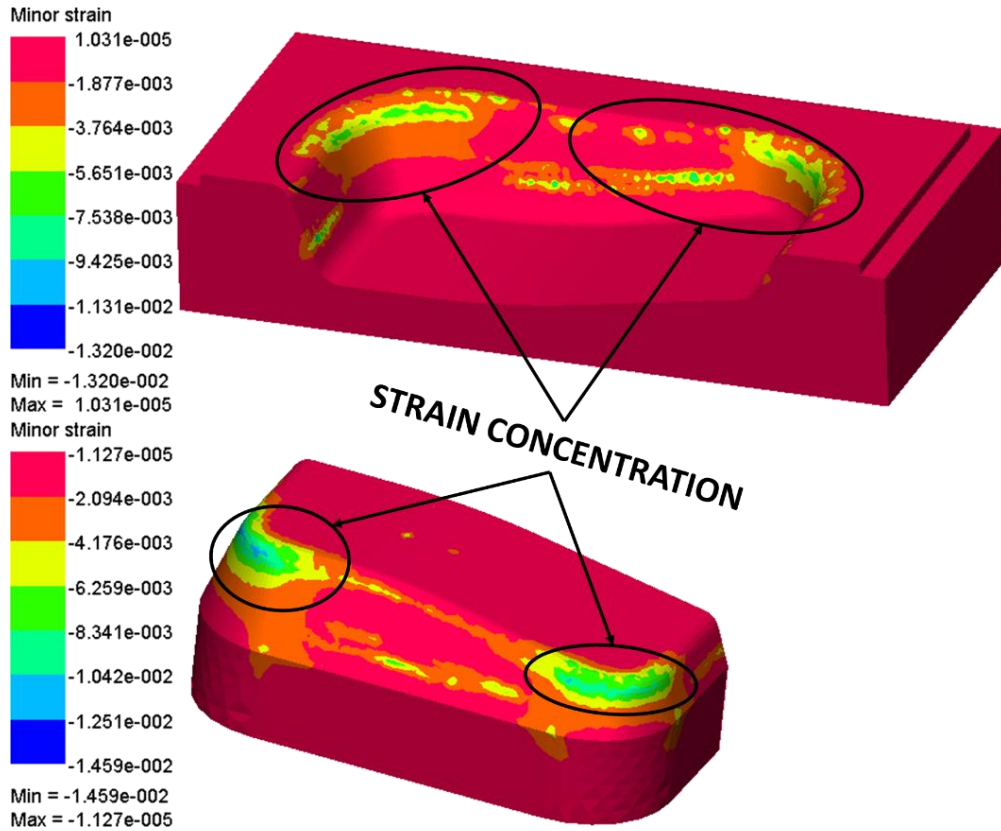


Figure 3. 45: minor strain maps concentrations on the tools after the stamping simulation with non-compensated tools.

In Figure 3. 47, the results of the first iteration are shown. The range of the deviations, Calculated in the normal direction, lays within the range $[-0.40; +0.40]$ Mm, in spite of the modifications made by the algorithm on the corner radii of the tools (Figure 3. 46).

This error range is still apparently large, but it must be noted that, unlike the view of Figure 3. 43 (obtained before compensation), Figure 3. 47 shows the larger deviations only in small regions located on the flange, i.e. out of the useful final workpiece. Furthermore, 97.5% of the surface is within the range of $[-0.15; +0.15]$ mm. The range obtained already after the first compensation is therefore totally acceptable, from an engineering point of view, for many industrial applications of interest.

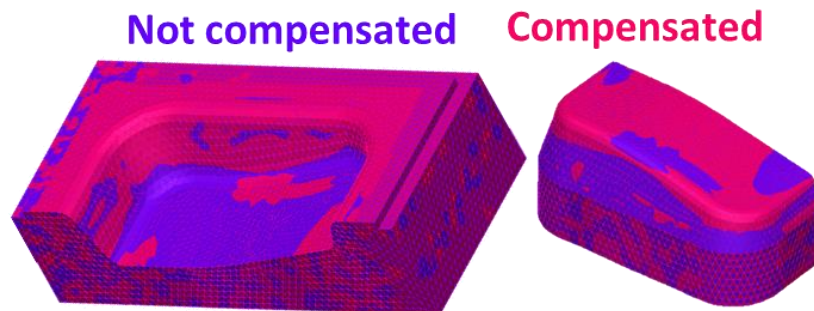


Figure 3. 46: comparison between the compensated and not compensated tools shape, for test case 1.

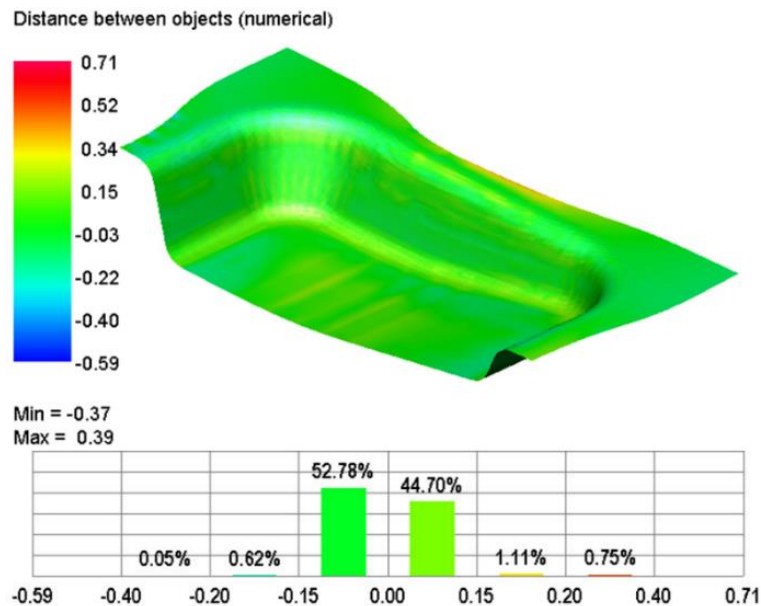


Figure 3. 47: deviations between designed and optimized components after one iteration.

The evidence of wrinkling in the compensated process is practically disappeared. The maximum measured reaction force on the die increases by only 0.05 percent after compensation. The maximum measured effective stress on the tools increases by 1 MPa on the punch and by 5 MPa on the die (Figure 3. 48, Figure 3. 49). This means

the proposed algorithm is able to reduce the geometrical errors with a negligible impact on the expected tool life.

If increasing the number of iterations, the quality of the obtained solutions does not significantly improve anymore. As Figure 3. 50 shows, the RMS values of the deviation vector decreases drastically after the first iteration and rapidly converges towards a stable solution. Within the first 4 iterations, the best result is obtained at the second one with very low benefit, on the engineering point of view, respect to the first iteration. As shown in Table 3. 9, the computation cost of the compensation algorithm is very paltry, because most of the time is taken by the simulation, which needs 3.17 h to converge.

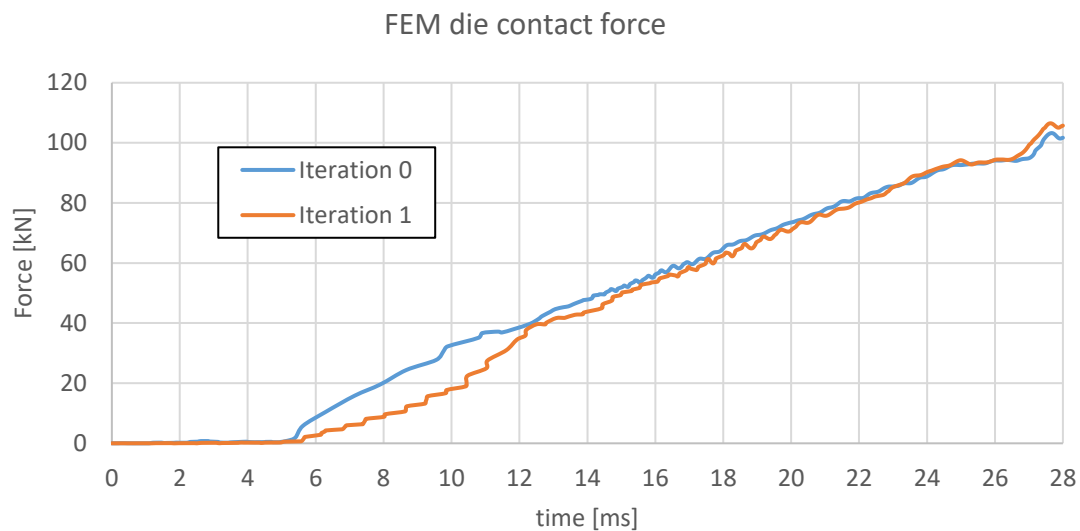


Figure 3. 48: FEM reaction force measured on the die before (iteration 0) and after (iteration 1) the compensation.

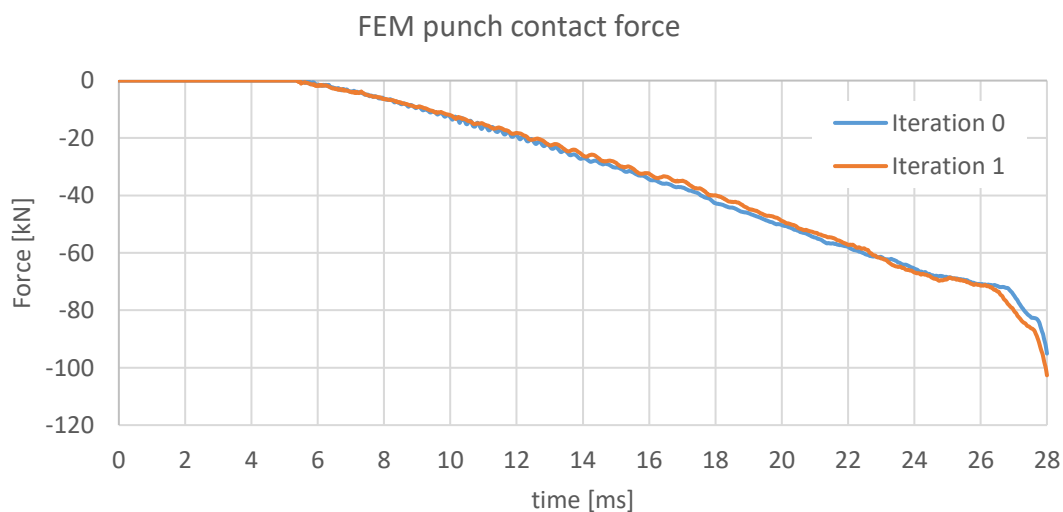


Figure 3. 49: FEM reaction force measured on the punch before (iteration 0) and after (iteration 1) the compensation.

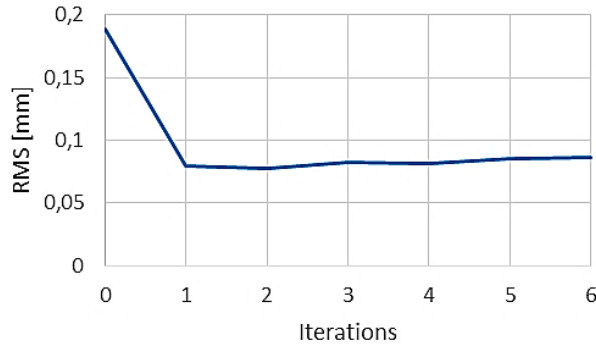


Figure 3. 50: norm of deviation vector vs. iteration.

Operation	Time needed
Simulation – 3 stages	11432 s
Reading blanks mesh	21.65 s
Parameterization	13.23 s
Compensation	90.48 s
Save tool mesh	0.07 s
Total	11557.43 s (3.21 h)

Table 3. 9: time needed for 1 iteration.

The calculation of the compensation \vec{T}_c is performed according to equation (3.11) which relies on a unique value of the parameter λ , which remains constant for the whole optimization and the correct λ -value is not known a priori, it can only be guessed. In the proposed example, we have $\lambda=1$. An investigation of the role of the penalty coefficient has been conducted by comparing the RMS values of the first iterations obtained by changing the λ values from 0.8 to 1.2; the obtained results are shown in Table 3. 10.

λ	RMS [mm]
0.80	0.090
1.00	0.079
1.20	0.073

Table 3. 10: RMS values obtained after one iteration by changing the λ values.

The RMS values in Table 3. 10 show that low values of penalty coefficient do not give back a complete compensation of the tools, so the RMS value is bigger. Instead, for λ -values larger than 1, the algorithm seems to improve its effectiveness. The over-compensation induced by larger penalty values not only corrects the deviations generated by the tools deformation, but also reduces the amount of the blank springback. This result is in agreement with the results found in literature where the penalty factor generally assumes values within [1.2; 1.3] in industrial applications, but it can also reach larger values within [1; 2.5], [22].

In conclusion, the case 1 has demonstrated, that an all-polymeric (deformable) tooling setup can be used for sheet metal forming applications. The deformation of the tools can be predicted via FEM and compensated, in order to reduce within acceptable limits the deviation of the part from its nominal shape.

The same FEM model setup and compensation algorithm will be used also for the second test case, which will be composed by a more complex part with a reverse drawing features. The second test case will allow to better validate the simulation setup but also to test the effectiveness of the compensation tools algorithm.

An FEM model for evaluating the deformations of sheet metal and polyurethane tools in a stamping process has been developed and validated.

3.3 Case study 2: complex industrial component

3.3.1 Experimental setup

In the previous section, the development and validation of an FEM model and compensation algorithm for designing a stamping process, which involves tools setup completely made by polyurethane, have been presented.

In this paragraph a second case study will be presented in order to test the effectiveness of the FEM model and compensation algorithm in a stamping process of component designed in collaboration with the company DALF S.r.l.

The test case (Figure 3. 51) is a stamped component with a double symmetry plane and some geometrical features which are predictably hard to be obtained in a stamping process with flexible tools. The constant radii (R6 in Figure 3. 51) are very small, i.e. difficult to be obtained in this kind of processes, because the deformable tools usually tend to slightly deform by compression in corner regions. The presence of the central, diamond shaped, depression, depth 5.5 mm, adds complexity to the overall geometry of the process.

The material chosen for the test case is Al1050, annealed, with 1.5 mm wall thickness. The reference geometry of the part given in Figure 3. 51, which will be called “designed geometry”, is the starting point for determining the geometry of the deformable tools.

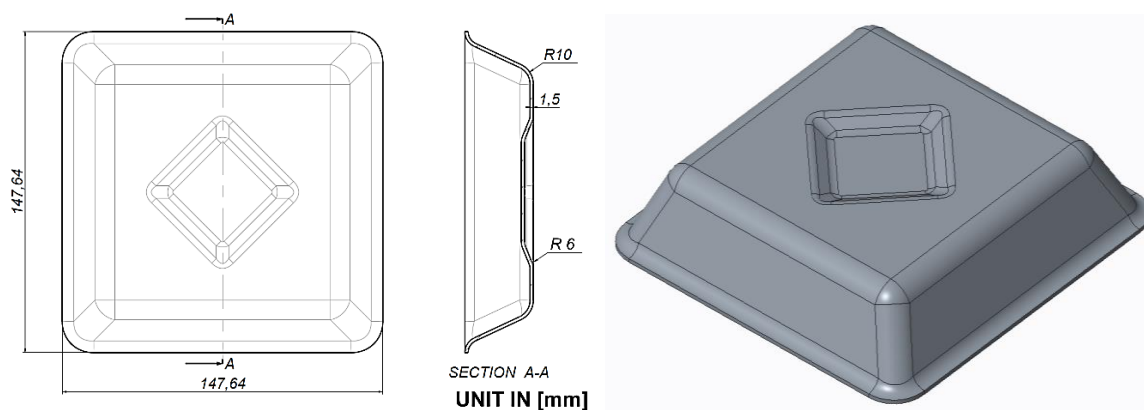


Figure 3. 51: geometry of the component for case study 2, dimensions in mm (left) and 3D view (right).

An initial guess geometry of the deformable tools is built as an offset of the surfaces of the test case part; the iterative compensation algorithm will suggest a modification of this initial geometry. The deformable tooling setup (Figure 3. 52) is made of a die (Figure 3. 53), a blankholder (Figure 3. 54) and a punch (Figure 3. 55).

The tools setup has been manufactured by milling operation with a 3 axis CNC machine (Figure 3. 56).

The base of punch (orange) has been generated by using the material milled to the centre part of the blank holder, in order to reduce the cost of the required resin.

As for the previous test case, an economical comparison has been made by comparing the making of the die made by Polyurethane or by Zamak 2 (Kirksite). The Zamak 2 is an alloy of Zinc, Copper and Alluminium which is a very low cost alloy generally used for making prototypal tools.

The resins used for the making the experimental tools are generally sold as blocks with standard dimensions.

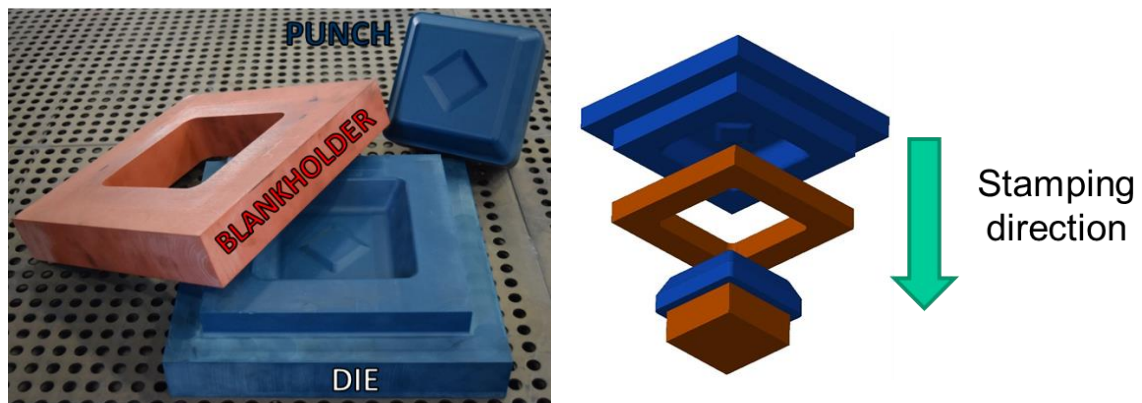


Figure 3. 52: deformable tools setup of the test case 2 (left) and schematization of the stamping direction (right).

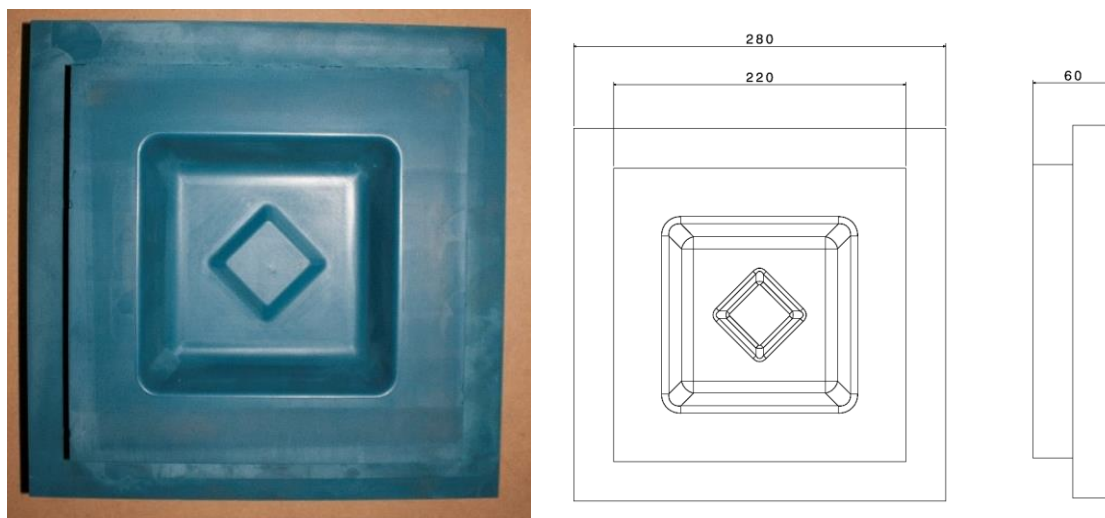


Figure 3. 53: real view of the die (left) and main dimensions in mm (right).

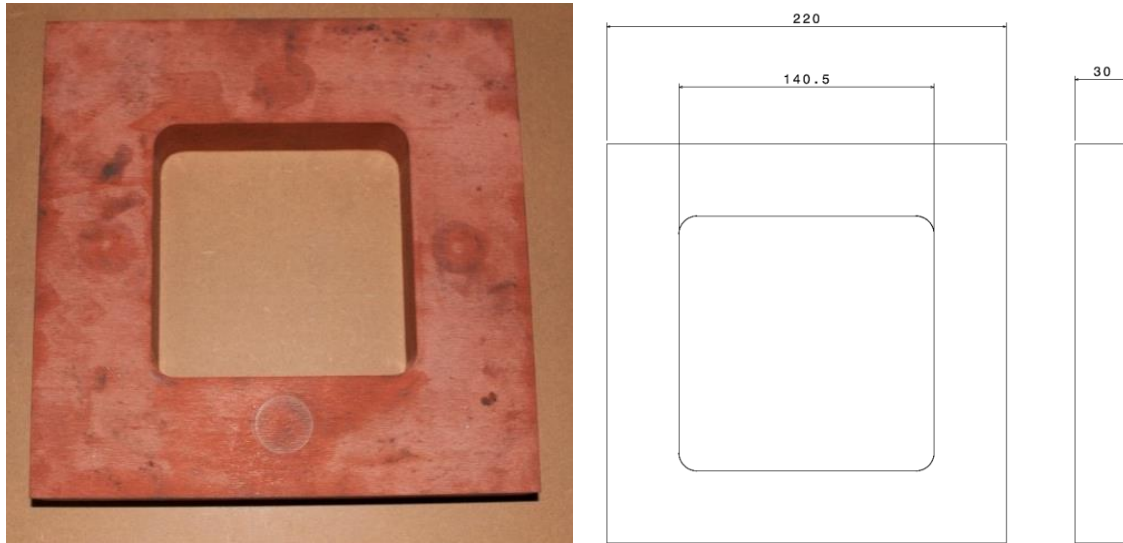


Figure 3. 54: real view of the blankholder (left) and main dimensions in mm (right).

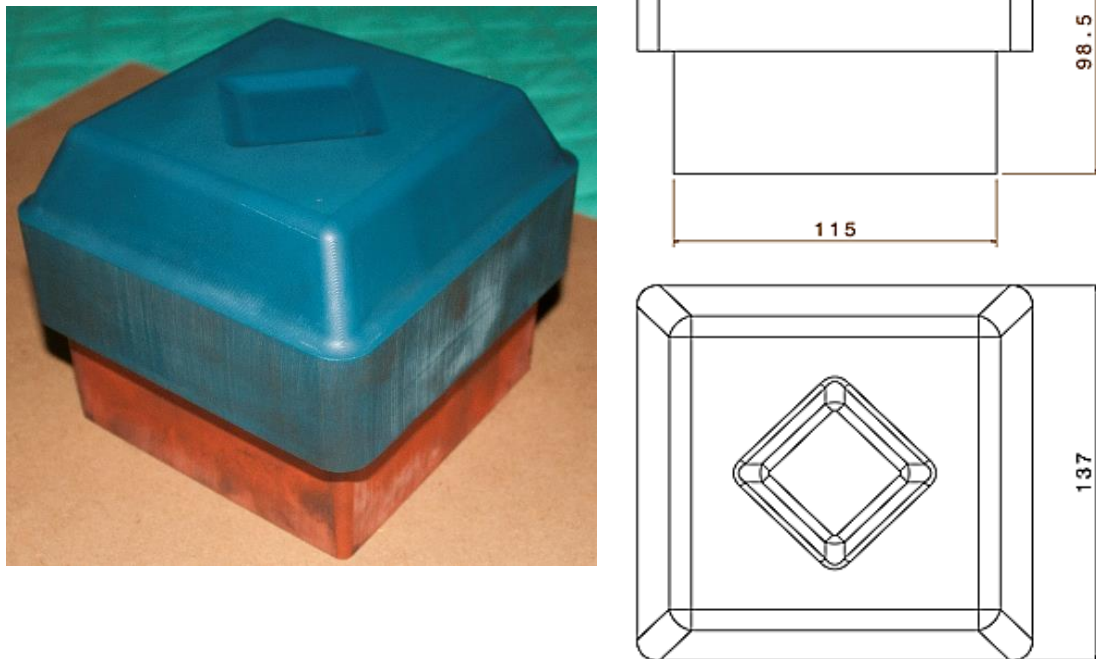


Figure 3. 55: real view of the punch (left) and main dimensions in mm (right).

In Table 3. 11 the commercial dimensions and the correspondent prices of the polyurethane blocks of the material involved in this test case are presented. From these data, it has been possible to evaluate the price on m^3 of the polyurethane material. Due to the different density of the Zamak 2, the selling procedure are different, so the correspondent costs are presented in Table 3. 12.



Figure 3. 56: milling operations performed for making the punch.

Material	Density [Kg/m ³]	Standard dim. [mm]	Price [€]	Volume [m ³]	Price at m ³ [€/m ³]	Price at Kg [€/Kg]
Necuron 1300	1150	1000x500x50	235	0.025	9400	8.17
	1150	1000x500x100	470	0.05	9400	8.17
Miketool 1440	1200	1000x500x50	280	0.025	11200	9.34
	1200	1000x500x100	560	0.05	11200	9.34

Table 3. 11: price of the polyurethane standard blocks.

Material	Density [Kg/m ³]	Price at m ³ [€/m ³]	Price at Kg [€/Kg]
Zamak 2	6800	39440	5.8

Table 3. 12: standard price of the Zamak 2 alloy.

In Table 3. 13, the resume of the costs given by the company has been presented where the material and manufacturing costs have been divided. From the point of view of the material cost, the polyurethane is 3 times expensive than the Zamak 2. It should be noted that Zamak 2 is a very economical alloy, normally used for very small production batches. Instead, if the manufacturing operations are considered, the cost of the polyurethane is quite lower than the Zamak 2. Indeed the manufacturing time needed for producing the die by milling Zamak 2 is 30h, instead the time needed for milling the polyurethane is 10 times lower.

It is also interesting to note that the different material costs are related also to the following conditions:

1. The die made by Zamak 2 can be smaller than the one made by polyurethane, due to the intrinsic material stiffness.
2. The polyurethane is sold in blocks with standard dimensions, so the milling operations generates a lot of wasted material very difficult to be re-used.

In conclusion, a quantitative comparison of the tools price in terms of total manufacturing and material costs has been presented in Figure 3. 57, in order to show the economic advantage related to the use of polyurethane tools.

A study about the evaluation of the tools life will be presented in the subsequent sections.

Cost	Polyurethane	Zamak 2
Material	790 €	260 €
Manufacture	200 €	1600 €
Total	990 €	1860 €

Table 3. 13: list of the cost given by the company.

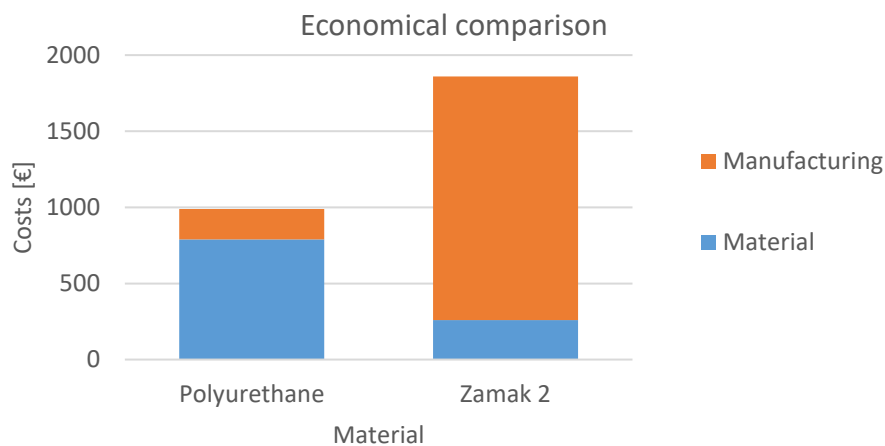



Figure 3. 57: costs comparison between Miketool (polyurethane) and Zamak2 for making the die in the experimental case.

The oleo-dynamic press machine involved in the experimental activities is a BULCOM ISC-100S (Table 3. 14). The main advantages of this kind of press machine is related to the high production rate respect to the mechanical ones, moreover the stroke, the pressure and the die velocity can be set.

The pressure pump is positioned on the upper side of the press. The pressure can control the velocity of the upper plate, therefore at maximum pressure correspond the minimum velocity and vice versa.

The BULCOM ISC-100S is a double action press, indeed on the lower plate there is an extractor which force can be controlled separately respect to the blankholder. In the experimental activities the double action has not been used due to the configuration of the process already presented in Figure 3. 52.



Description	Unit	Value
Max-Force	kN	980
Upper plate surface	mm	800 x 600
Lower plate surface	mm	1000 x 750
Max-span	mm	1000
Max-stroke	mm	600
Stamping velocity	mm/s	20 - 40
Blankholder Force	kN	392
Blankholder stroke	mm	250
Blankholder surface	mm	500 x 400
Max-Power	kW	22.4
Weight	Kg	12.000

Table 3. 14: technical data of the press used in the experimental activities of the test case 2.

The die has been locked to the upper plate with clamp tools (Figure 3. 58a); instead, the punch has been screwed on the lower plate with a rigid support. The blankholder laid on a rigid steel ring positioned on the pistons of the lower plate, in order to confer a uniform pressure over the blankholder surface during the process (Figure 3. 58b).

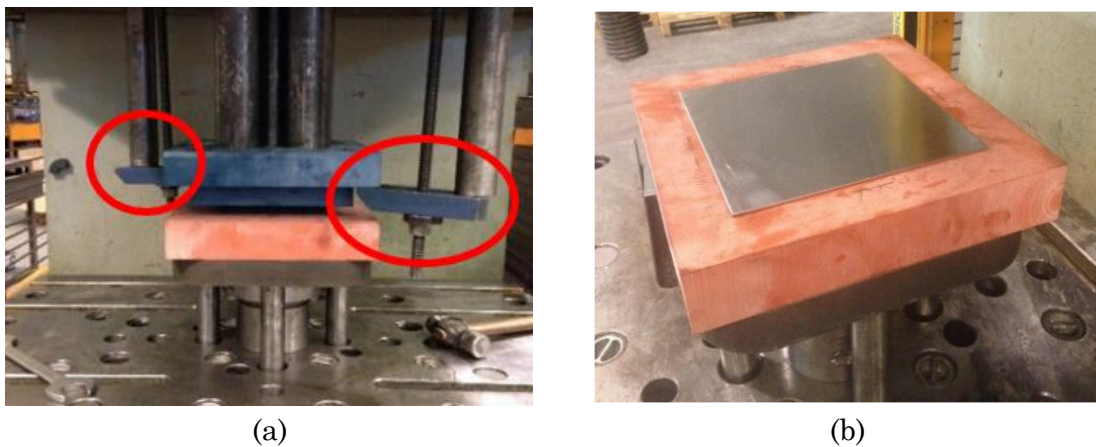


Figure 3. 58: configuration of the clamping tools for die locking (a) and the steel ring used for the blankholder (b).

3.3.2 Experimental plan and results

The experimental activities consisted in the execution of stamping operations with rapid tools setup of blanks at different values of blankholder force [34]. The material chosen for the test case is Al1050, annealed, with 1.5 mm wall thickness. The edge length of the square blank is 200 mm. As described before, the deformable tooling setup (Figure 3. 52) is composed by the die (blue tool), the blankholder (orange tools) and the punch (blue with based orange tool). The polyurethane materials chosen for testing the deformable tools are: Necuron 1300 for the blankholder and punch base; Miketool 1440 for the punch and the die.

The material properties will be discussed in the FEM modelling section. Figure 3. 52 shows the direction of the stamping process. The stamping process is made of three steps:

1. **Holding:** the blank is placed on the blankholder and then the die moves downward for holding it;
2. **Stamping:** the die pushes the blank against a fixed punch and against the blankholder with a maximum force of 980 kN; the maximum available reaction force of the blankholder is 392 kN.
3. **Springback:** the tools are released and both the tools and the blank recover the elastic deformation.

An experimental plan has been designed with variable levels of the blankholder force BHF, without replications (Table 3. 15). The plan is aiming at determining which level of maximum BHF could determine failure of the parts (by either wrinkling or fracture) or failure of the tools (by fracture or plasticization). It is also aimed at determining the influence of BHF on the geometrical accuracy of the obtained parts. The experimental activities have been performed with the aid of the hosting company, the industrial press did not allow the measuring of the blankholder profile.

The experimental results showed that no macroscopic wrinkling occurred at any level of BHF_{max} .

The part at experimental condition no. 7 failed by fracture, hence the safe limit to fracture for BHF_{max} was assessed at 24.5 kN (Figure 3. 59). All stamped parts have been measured with a Zeiss Prismo 5 VAST MPS HTG Coordinate Measuring Machine (CMM), obtaining their profile at the symmetry plane (Figure 3. 51).

The deviations interval between the experimental and the designed component (Figure 3. 60) is 50% smaller respect to the one discussed in paragraph 3.2.2.

Experiment no.	Maximum BHF [kN]
1	4.9
2	9.8
3	14.7
4	19.6
5	23.5
6	24.5
7	25.5

Table 3. 15: experimental plan of case 2.

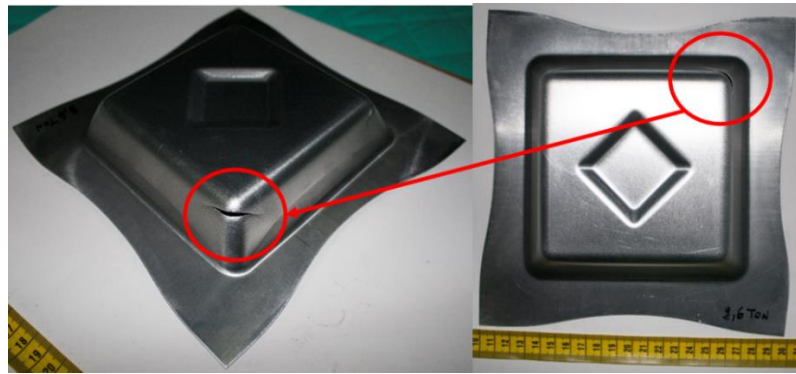


Figure 3. 59: identification of the fracture zone at experiment 7.

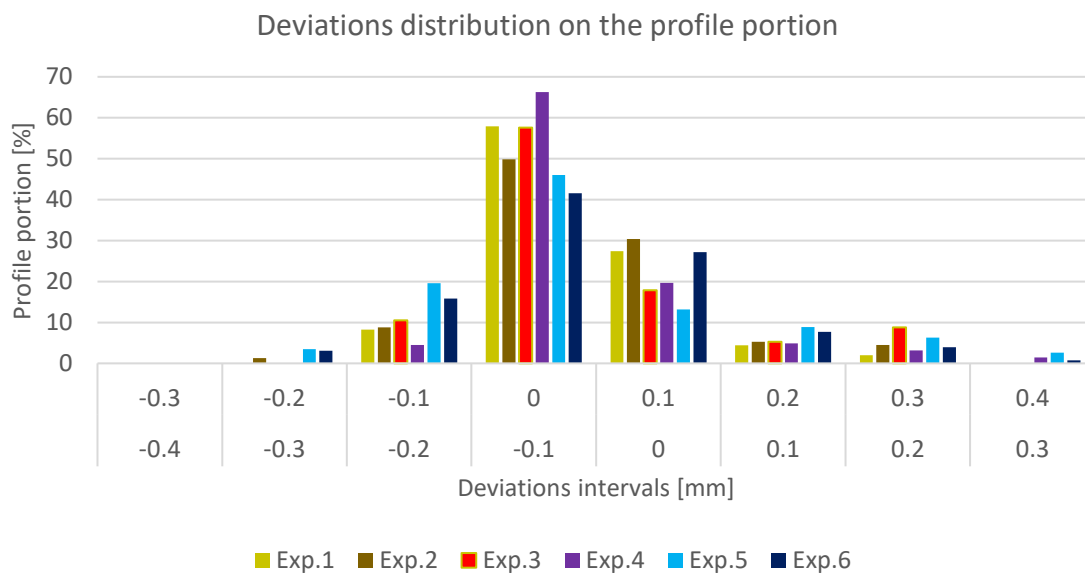


Figure 3. 60: distributions of the deviations between the experimental tests and designed component on the profile portion (test case 2).

The error profiles (Figure 3. 61) are not perfectly symmetrical around the centre of the chart because the clamping conditions of the blankholder were not perfectly symmetrical (Figure 3. 58a), hence different draw-in values have been allowed in different directions. Generally it can be observed that in the central region there the smaller amount of error, on the contrary larger errors can be registered on the corners. The low error in the central part is due to increased stretching, while the larger error on the corners is due to compression of the plastic die corners. From the deviations point of view, it is very difficult to define which experiment can be the best compromise. The experiment number 4 is the one with most percentage of the surface included in the interval within [-0.1; +0.1] (Figure 3. 60), but it is not really better than other profiles along the whole cross section. Indeed, this is the most interesting remark coming out of the comparison of the error profiles: there is not a single BHF

level able to generate an error, which is consistently smaller throughout the whole cross section.

In conclusion, the range of the errors measured on the component are smaller respect to the ones measured on the first test case. This result demonstrate the hypothesis made before, where more rigid polyurethane tools can assure smaller local deformations, which produce smaller deviations on the final component. Considering the main deviation interval, $[-0.2; +0.3]$ mm, obtained in this industrial case, it can be demonstrated that the rapid tools (if well designed) can be suitable for most of sheet metal stamping applications, where small-medium tolerances are required.

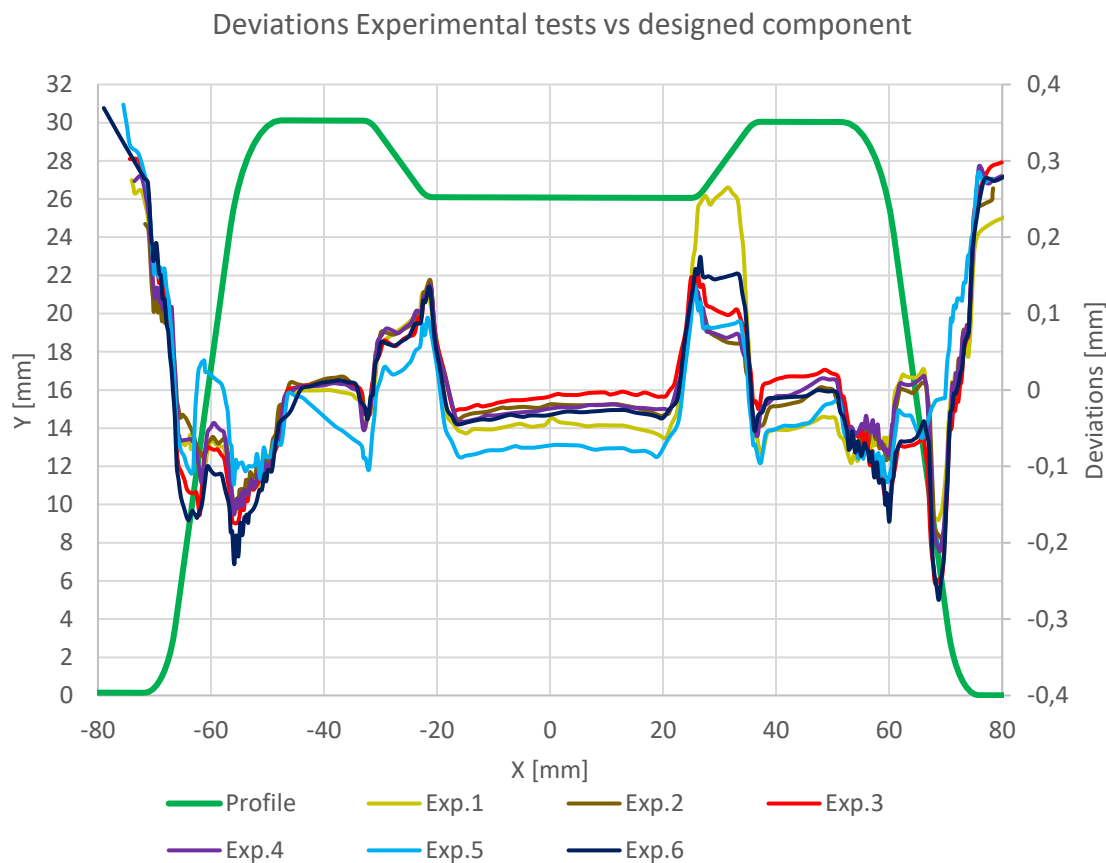


Figure 3. 61: locations of the deviations between the experimental tests and the designed component (test case 2).

3.3.3 FEM model

3.3.3.1 Mesh and geometry

The FEM model has been implemented with the commercial code PAM-STAMP 2G V2015.1.

In order to evaluate the deformation of the polyurethane tools, their mesh is made of four-node tetrahedral solid elements. The solid mesh of the plastic tools has been created with VisualMesh 11 by using the automatic meshing module described in paragraph 3.2.3.1.

The number of elements and the number of nodes for each tool is shown in Table 3. 16. As stressed before, a good discretization is important for the accuracy of the FEM simulation, but it is also very important for the application of the compensation algorithm described in the section 3.2.4.2.

The edge length of the squared blank is 200 mm and the surface area of each initial element is 400 mm² with a total number of 100 initial elements. Every refinement step splits 1 quadrangular element into 4 smaller quadrangular shells, by an automatic refinement algorithm. Each element can be split up to 5 times.

The scheme of the geometrical simulation setup is presented in Figure 3. 62 in order to resume schematically all the objects involved in the model. No symmetry has been used in order to simulate the effect of the clamping tools positioned along the diagonal of the entire setup (Figure 3. 58).

Tool	N. elements	N. nodes
Die	304291	58952
Blankholder	19898	4797
Punch	387548	71129
Punch Base	12064	2641

Table 3. 16: number of elements and nodes used for meshing the tools.

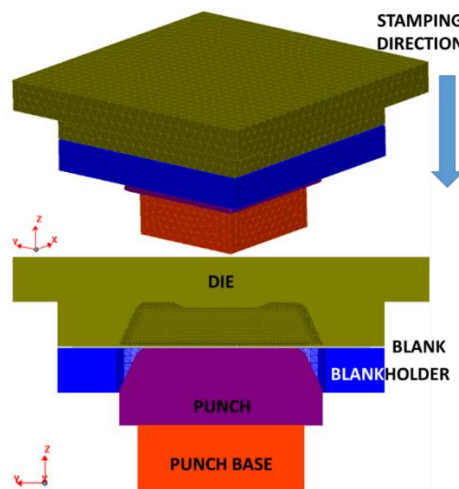


Figure 3. 62: scheme of the simulation setup in 3D (upside) and sectioned view (downside).

3.3.3.2 Material properties

As for the previous case, the tensile test data of the blank have been retrieved in the “CES EduPack” material database, since the Al 1050 is a very common material. The material properties of the Necuron 1300 have been obtained from the tests described in chapter 2. Also for the Miketool, due to the low availability of the material, a compression test has been performed where the corresponding stress-strain curve has been shown in Figure 3. 63. The resulting values for the elastic modulus and the Poisson coefficients are reported in Table 3. 17

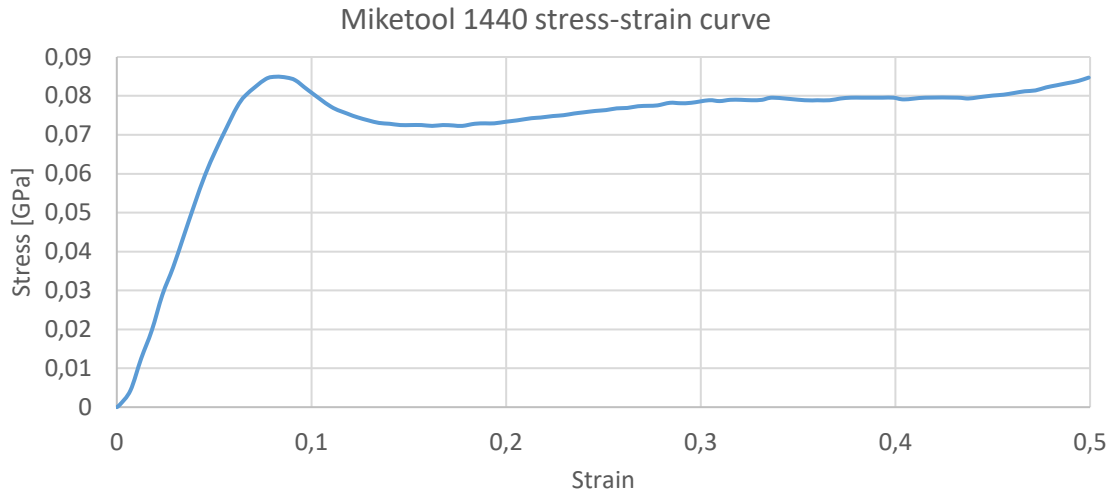


Figure 3. 63: stress-strain curve resultant form the single compression test performed ton Miketool 1440.

Material	Young Modulus [MPa]	Yield Stress [MPa]	Peak Stress [MPa]	Poisson coeff.	Density [g/cm ³]
Al1050 (blank)	72000		33	0.335	2.73
Necuron 1300 (blankholder and punch base)	2664	66	61.8	0.340	1.15
Miketool 1440 (die and punch)	2950	71	90	0.340	1.20

Table 3. 17: material properties of the polyurethane tools and aluminium blank.

The blank material has been modelled as elastic-plastic with the Krupkowsky constitutive law (equation 3.1), where the coefficient have been already presented in equations 3.2, 3.3 and 3.4 and the corresponding hardening curve has been shown in Figure 3. 25.

3.3.3.3 Boundary conditions

The simulation starts at the end of the holding stage in which the blank is held between the die and the blankholder (Figure 3. 62). Then the die moves down with an imposed displacement with constant velocity, imposed during the experimental activities. The blankholder applies the experimentally imposed BHF (Table 3. 15), in order to control the draw-in of the blank. The contact algorithm between the objects is defined by accurate algorithm described in chapter 2, taking into account a Coulomb friction coefficient of 0.25 [13] - [15], in order to better simulate the interaction between polyurethane and aluminium materials condition.

The contact between the punch (dark magenta) and the base (orange) has been modelled by merging the correspondent nodes at the interface (Figure 3. 64), because they have been glued during the manufacturing phase, in order to do not slip during the stamping stage.

As shown in Figure 3. 58, the plastic tools are enclosed within metal clamping tools which connect and lock the tools to the press machine. The position of the locking tools along the diagonal of the die does not allow the application of the symmetry to the FEM model. In order to correctly simulate the effect of each clamp on the deformable tools shown in Figure 3. 58, proper boundary conditions have been applied only on specific nodes and surfaces.

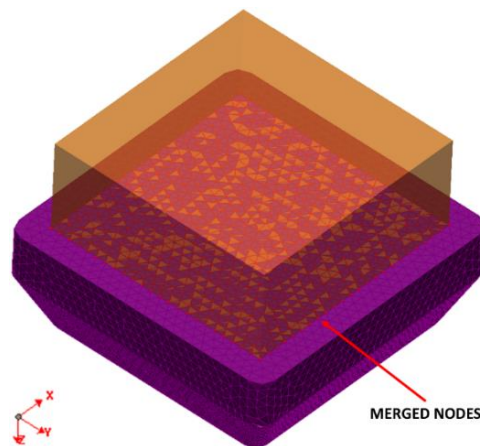


Figure 3. 64: merged nodes at the interface between the punch and the base.

For the die, an imposed displacement with constant velocity is applied on the upper and on some nodes corresponding to the clamping tools (Figure 3. 58). The BHF is applied on the lower surface, in order to simulate a uniform distribution of the pressure; finally, a fixed displacement is applied on the lower nodes of the punch base (Figure 3. 65).

The blankholder surface mesh has been obtained by extracting the external mesh surface by Visual Mesh 11.0 function.

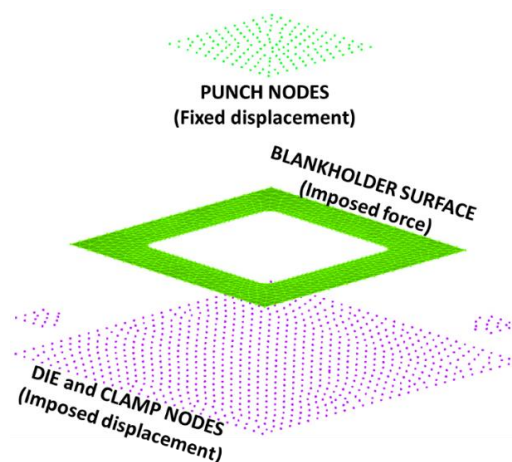


Figure 3. 65: scheme of the nodes and elements with boundary conditions applied.

Then the nodes of the extracted have been fused with the blankholder tetra mesh in order to impose the force as boundary condition. The springback simulation has been run by the FEM software with the “Advanced Implicit” algorithm. The locking of the blank’ nodes has been performed by the “isostatic locking” function included in PAM-STAMP, which allows to find automatically the best locking condition in springback analysis in case of models without symmetry (Figure 3. 66). As for the previous case, the boundary conditions and the contact matrix are resumed in Table 3. 18 and Table 3. 19.

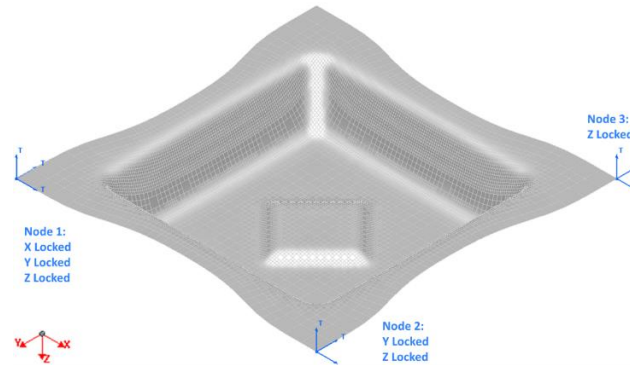


Figure 3. 66: node-locking condition chosen by the isostatic PAM-STAMP locking algorithm.

Stage	Object	Rigid Body	Cartesian kinematic	Refinement	Springback	Boundary conditions
Stamping	Blank			Level 5		
	Die/clamp (nodes)		Locked translations: X, Y Locked rotations: X, Y, Z Imposed velocity: -Z			
	Punch (nodes)		Locked translations: X, Y, Z Locked rotations: X, Y, Z			
	Blankholder surface	Simplified	Locked translations: X, Y Locked rotations: X, Y, Z Imposed Force: Z			
Springback	Blank				Advanced Implicit	Isostatic Locking

Table 3. 18: list of the complete boundary conditions imposed in the FEM setup of the case 2.

Master \ Slave	Blank
Die	Accurate algorithm with friction 0.2
Blankholder	Accurate algorithm with friction 0.2
Punch	Accurate algorithm with friction 0.2

Table 3. 19: simulation interaction matrix between tools (master) and blank (slave).

3.3.3.4 Validation

In this paragraph the FEM simulations results will be presented by comparing the obtained values with the experimental ones.

The failure zone detected at experiment 7 where the maximum force is applied on the blankholder has been compared in Figure 3. 67 with the simulation result. The experiment and the simulation show the same location of the blank fracture localized at the deepest corners of the component. No other simulations nor experimental case had occurrence of fracture. Both in simulations and in real tests, no macroscopic wrinkling was detected.

The experimental components have been measured along the section A-A (Figure 3. 51) in order to be compared with the designed component and the simulated ones. In Figure 3. 68 the numerical error distribution of the simulated components and the experimental ones are presented.

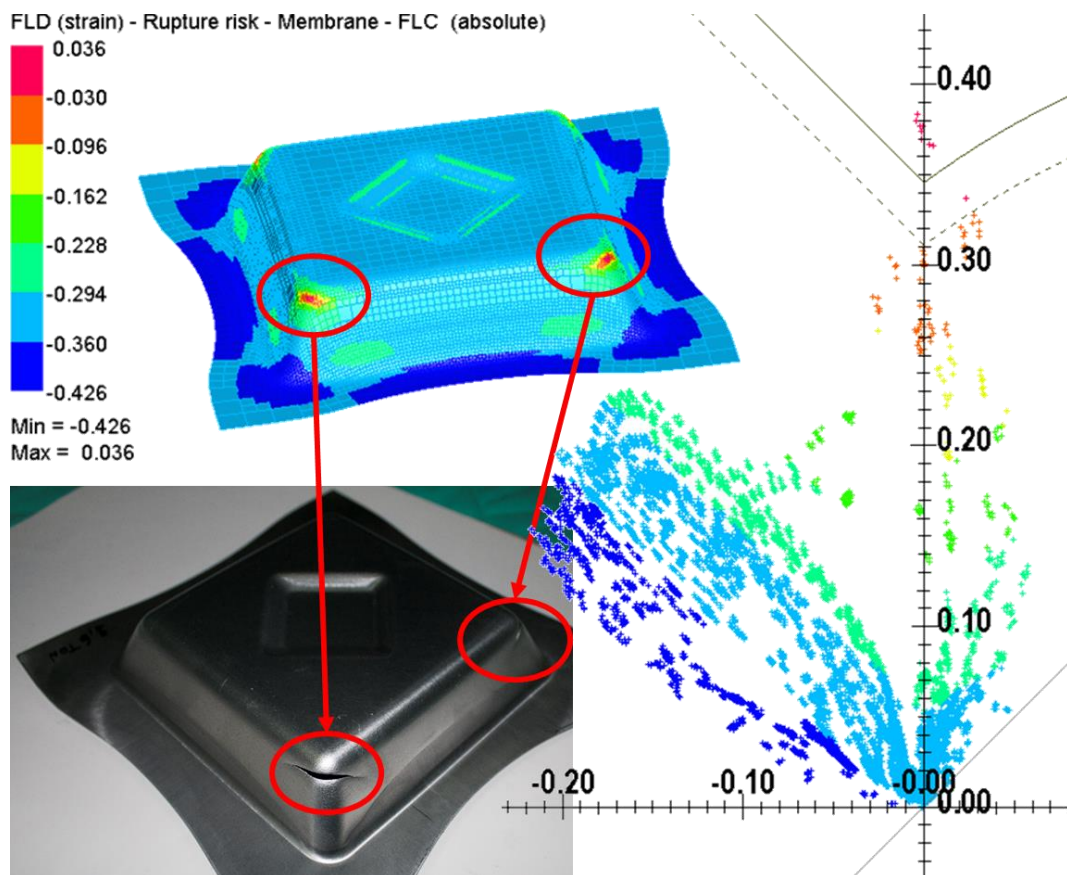


Figure 3. 67: fracture localization - experiment no. 7.

The Figure 3. 68 shows that large part of the deviations is included in the interval within [-0.2; +0.1]. This interval is smaller if compared with the results obtained for the previous case (Figure 3. 34), but it is very similar with the deviations distribution between the experimental and the designed already shown in Figure 3. 60. An interesting result can be observed in Figure 3. 69 where the error of the FEM profile with the experimental ones is compared with the deviations between the experimental and designed components.

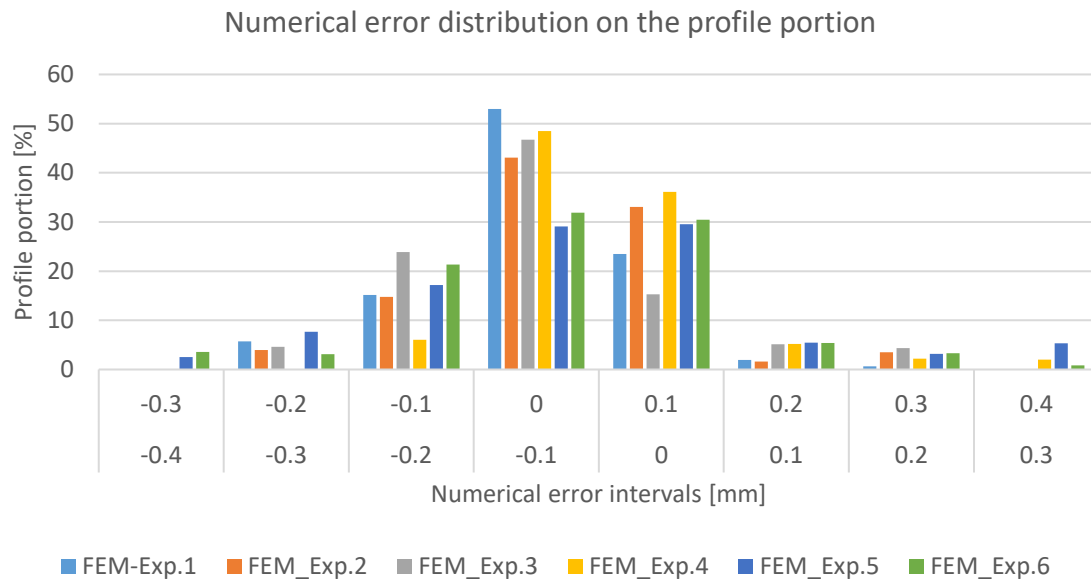


Figure 3. 68: distributions of the numerical error between the experimental and simulated components on the profile portion of the case 2.

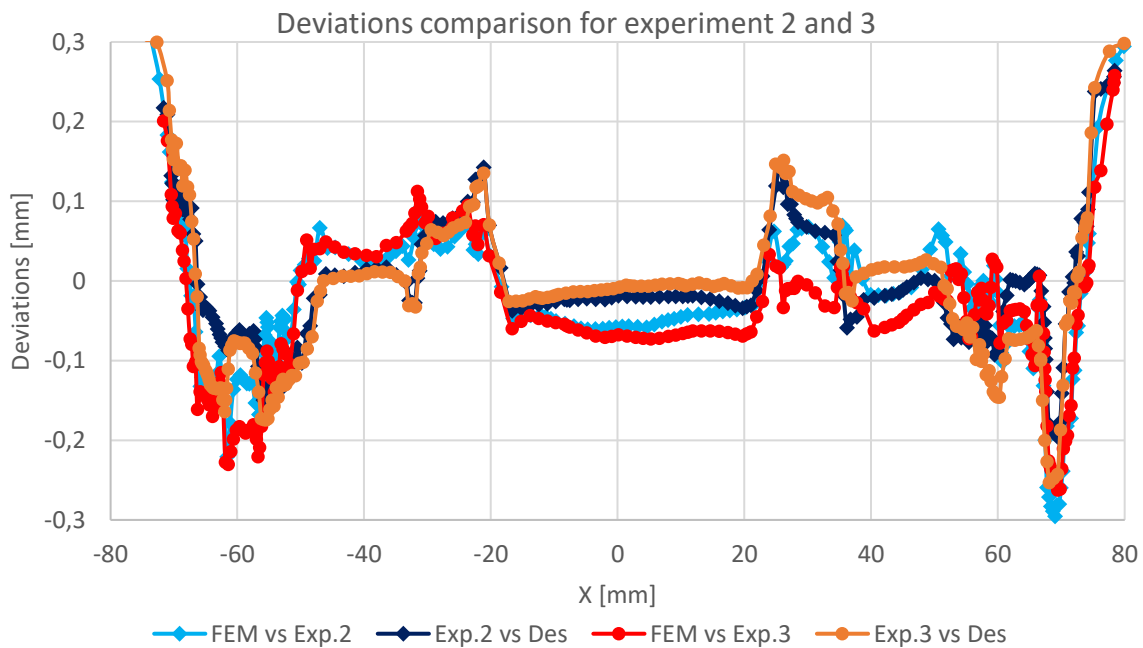


Figure 3. 69: deviations comparison for experiment 2 and 3.

In Figure 3. 69 the trends of the “numerical” and “experimental” deviations are presented for experiment 2 and 3 for clearness, but also because this two experiment will be chosen for the application of the compensation algorithm. In the compensation field, the main objective is the minimization of the deviations between two components. If the trends shown in Figure 3. 69 are similar the compensation algorithm will reduce the same deviations in the same direction, so the discrepancy between the nominal component and the real one will be reduced anyway.

The results obtained in the FEM simulations demonstrated that it is really difficult to reproduce a profile of a stamped component with polyurethane tools in a range within ± 0.1 mm. It should be noted again that the achieved results are in according with the typical results found in literature. [17]-[19].

3.3.3.5 Compensation algorithm results

In order to test the effectiveness of the algorithm in case of reverse drawing feature, the compensation algorithm described in paragraph 3.2.4.2 has been applied for the experiments 2 and 3, because the last one will show a reduced risk of fracture after the compensation that will be interesting to be discussed if compared with the experiment 2.

The experiment 2 has been run with BHF=9.8 kN. As for the previous test case, the tools have been simply built as an offset of the final designed part middle surface. The plot of the deviations between this simulated part and designed components is shown in Figure 3. 70, for the whole part, excluding the flange. The simulated component deviates considerably from its designed geometry in a range between $[-0.24; 0.44]$ mm and only 78.53% of the calculated deviations lays within the range of $[-0.14; 0.15]$. The maximum positive or negative values of deviation are located on both the convex and concave corners. This corresponds to a large deformation of both tools on the corner radii, as confirmed by the strain maps of the tools presented in Figure 3. 71 and Figure 3. 72.

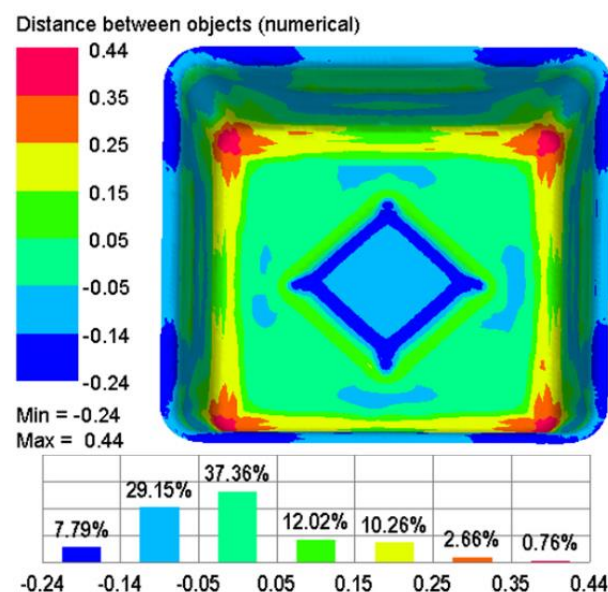


Figure 3. 70: δ -plot before compensation; isometric and top views, units in [mm].

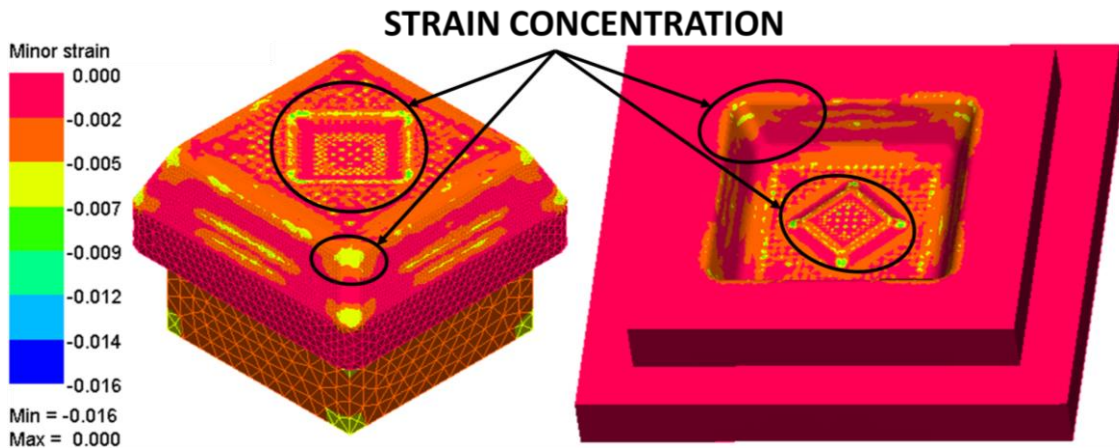


Figure 3. 71: minor strain maps concentrations on the tools of the test case 2, after the stamping simulation with non-compensated tools.

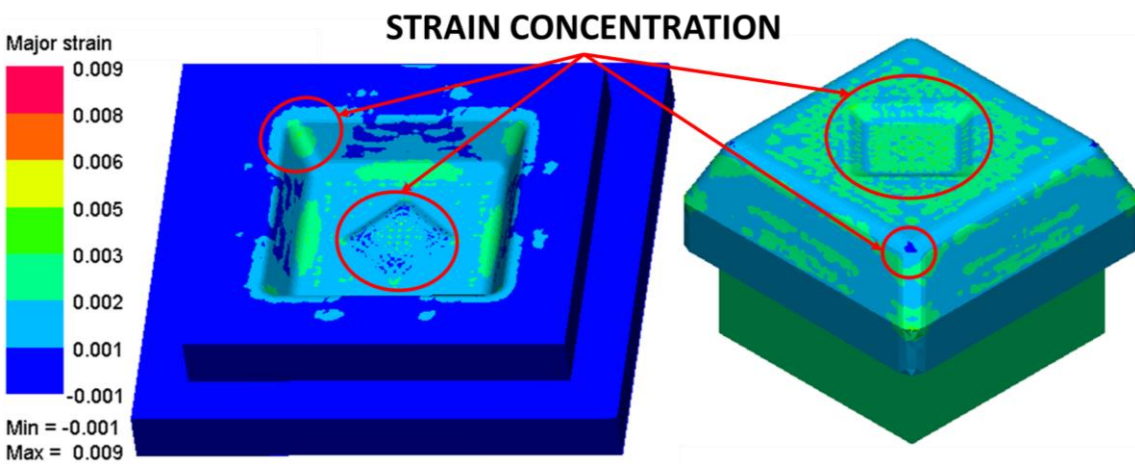


Figure 3. 72: major strain maps concentrations on the tools of the test case 2, after the stamping simulation with non-compensated tools.

The algorithm performed an automatic compensation of the tools geometry, with $\lambda=1$. As a result of the first compensation, the punch and die corners radii have been modified (Figure 3. 73) by the algorithm in order to reduce the deviations shown in Figure 3. 70.

As expected, the range of the deviations between the designed and simulated components is reduced after the compensation. In Figure 3. 74, the results of the first iteration are shown. The range of the deviations, calculated in the normal direction, lays within the range $[-0.22; 0.15]$ mm.

This error range is not much different from the one in Figure 3. 70 (obtained before compensation), but it must be noted that the 96.95% of the surface is within the range $[-0.12; 0.10]$ mm. Furthermore, the increase of calculated effective stress on the tools is limited to only 1 MPa on the punch and 7 MPa on the die. This means the proposed algorithm is able not only to reduce the geometrical errors but also to save the impact on the expected tool life.

The time required for 1 simulation (run with 8 processors) and for 1 tool compensation (with 1 processor) is summarized in Table 3. 20.

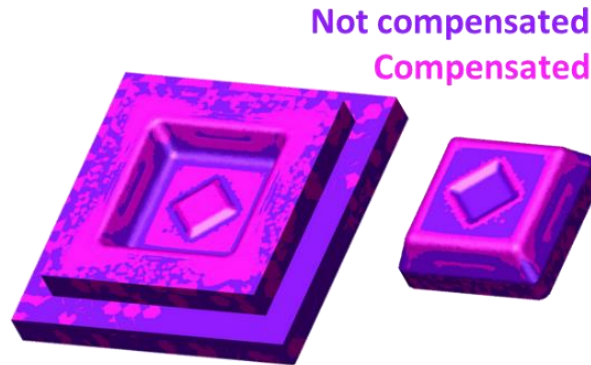


Figure 3. 73: comparison between the compensated and not compensated tools shape, for test case 2.

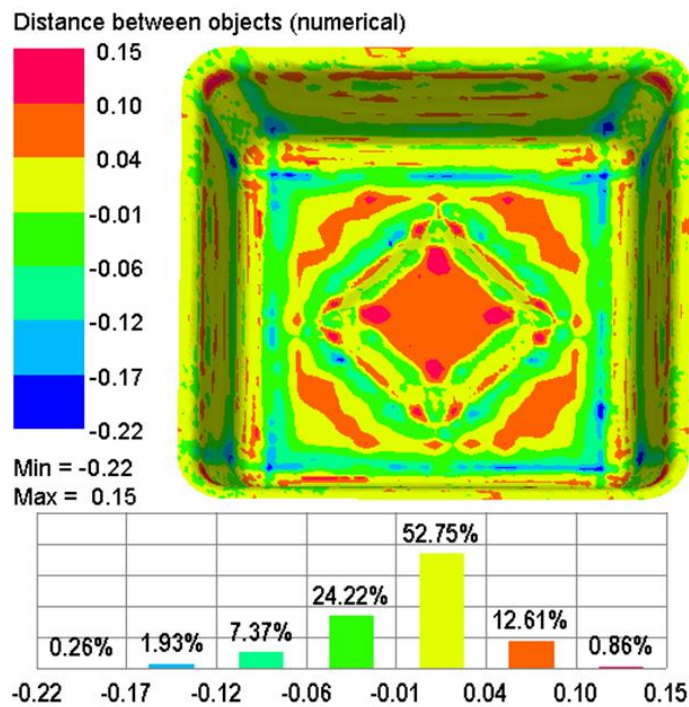


Figure 3. 74: deviations between designed and optimized components after one iteration.

The procedure described in Section 4 is iterative, it can be repeated with constant or variable values of the correction coefficient λ . In Figure 3. 75, the RMS value of the deviation vector is plotted vs. the number of iterations, with constant λ -value. The Figure 3. 75 shows that the RMS values of the deviation vector decreases drastically after the first iteration and rapidly converges towards a stable solution. A very similar trend had been observed also in the previous test case, and this indicates a typical behaviour of the proposed routine.

The compensation algorithm has been tested also for the experiment no. 3 which has been run with BHF=14.7 kN. The strain map, expressed in terms of distance from the FLD line, is shown in Figure 3. 76a.

Operation	Time needed
Simulation – 3 stages	4330 s
Reading blanks mesh	2 s
Parameterization	1 s
Compensation	60 s
Save tool mesh	0.1 s
Total	11557 s (1.23 h)

Table 3. 20: time needed for 1 iteration

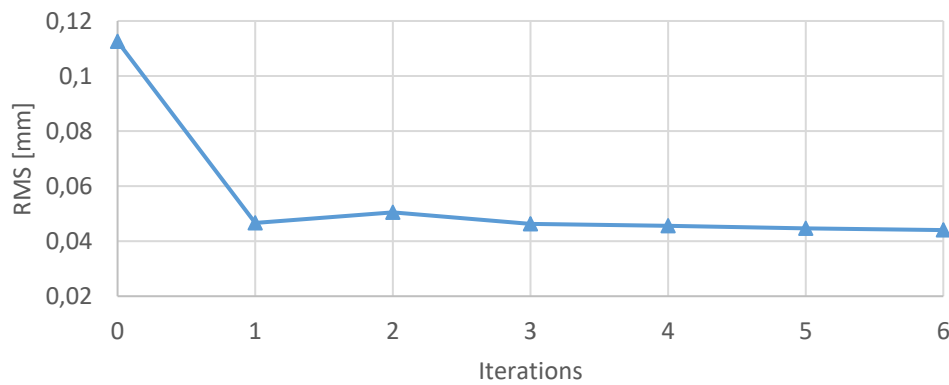


Figure 3. 75: norm of deviation vector vs. iteration for test case no. 2

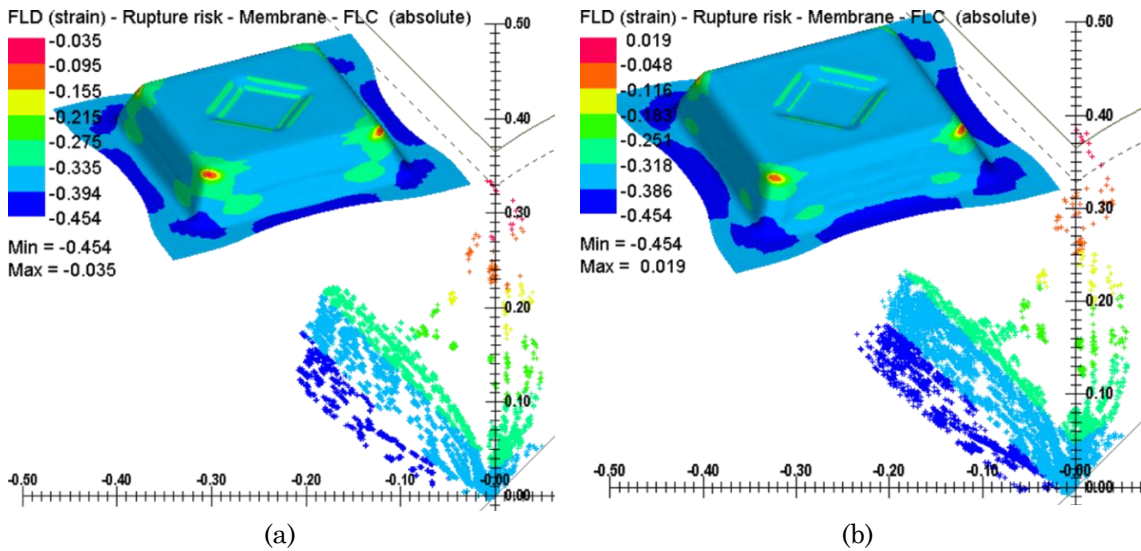


Figure 3. 76: FLD map of test case no.3 before compensation (a) and after compensation (b).

After the tool geometry compensation, the state of strain on the blank obviously changes, and the resulting FLD plot is shown in Figure 3. 76b, where larger risk of fracture is evident. In other words, in order to reduce the geometrical errors, the routine tends to increase the level of strain. This behaviour is typical since the algorithm changes the corner radii of the tools, this change increases the depth of the

stamping process, so lower level of force is needed in order to increase the sliding of the blank. In Figure 3. 77 the comparison of the upper part of the punch profile is presented in order to show the increment of the drawing depth after the compensation. Considering this result, the compensation procedure described in paragraph 3.2.4.2 can be framed in a more general algorithm, which involves the selection of the correct level of BHF and the evaluation of the risk of fracture. This general algorithm is summarised in Figure 3. 78. After the interval of tolerance condition, the fracture risk is an “obviously” condition to be checked before the conclusion of the algorithm. If the parte is within tolerance and safe, the algorithm can be closed, but if the part is within tolerance but fractured, the process parameters (like blankholder force) should be changed in order to make negative this last condition. Finally the process will result optimal in term of parameters and final shape of the component.

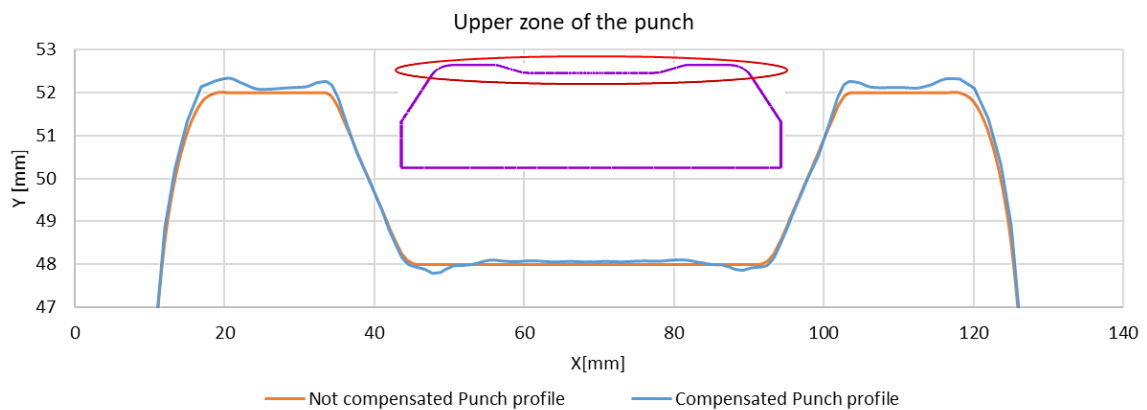


Figure 3. 77: comparison of the punch upper profile before and after the compensation.

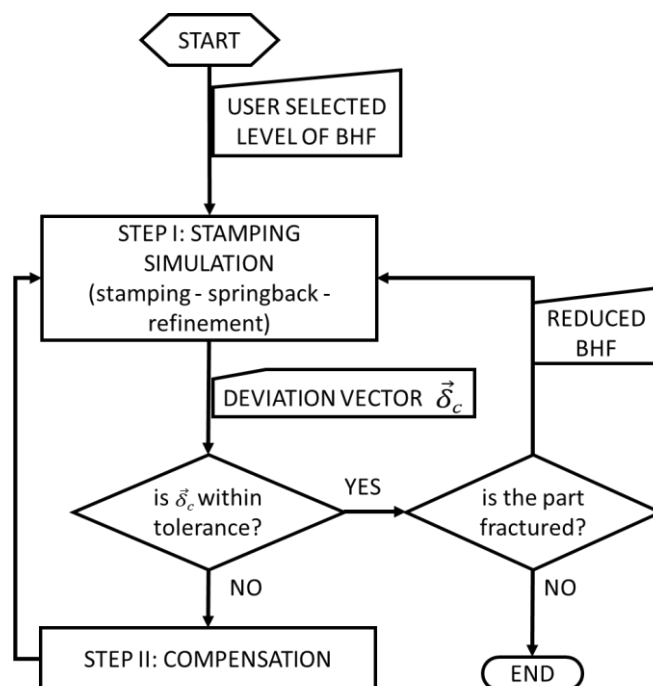


Figure 3. 78: General compensation algorithm.

As presented in this paragraph, the compensation algorithm is able to modify the tools shape also in a situation where the blank is made by complex features. The modification of the tools shape generates an increment of the final strain level on the blank with a possible increment of its risk of fracture. Then, the compensation procedure has been finally modified in order to take in account the risk of fracture of the blank. Similar approach has been used in [32], where the distribution of the contact pressure has been optimized by controlling the blankholder force. It has been also demonstrated that when the results of the compensation algorithm are far from the risk of fracture, the algorithm rapidly yields a satisfactory solution already after the first iteration.

In both test cases, the stress variation on the tools registered a negligible increment after the compensation, for this reason the tools life should not be modified respect to the uncompensated solution. It should be noted that no tools life estimation data are available in literature.

As a conclusion of the chapter about the stamping process with rapid tools, in the next paragraph, the expected tools life will be estimated with the implementation and description of fatigue tests, which simulates thousands stamping operations.

3.4 Tools life evaluation

3.4.1 Introduction

In this chapter the implementation of two test cases where polyurethane tools are involved in sheet metal stamping process have been presented.

The experimental activities shows that the tools are able to perform a stamping operation with good repeatability at fixed conditions. If correctly designed, the polyurethane tools can manufacture stamped component with very precise features within small interval of tolerances, as shown in case 2.

The numerical activities allowed to generate an FEM model able to predict the results of stamping process with polyurethane tools in a reliable way. The development of an FEM model of the stamping process with polyurethane tools is useful for predict the deformation of the tools during the process, which is the main cause, together with the springback effects, of the geometrical defect on the stamped component. The geometrical defects have been partially solved with the development of compensation algorithm which allows to modify the topology of the polyurethane tools, in order to reduce the error on the final components.

All of these activities allowed to solve one of the problems related in using rapid tools in stamping process: the difficulty related to tools design, due to the unpredictability of the results.

Another problem found during the analysis of the state of the art is related to poor information available in literature about the expected tools life.

Normally, it is very difficult to perform fatigue tests for evaluating the tools life in an industrial contest, because these activities requires long time and cost related to the production measurement of prototypal components.

For this doctoral thesis a fatigue test able to simulate a stamping process with polyurethane tools have been implemented.

3.4.2 Experimental setup and plan description

The fatigue test consist in compression tests repeated at frequency of 1 Hz [13]. The chosen frequency correspond a very high rate of production, which is very difficult to achieve also for automatic process chains. For this reason, all the obtained results can be considered in extreme conditions respect to the real use.

The machine used in the experimental test is an MTS 407 hydraulic press (Figure 3. 79a). The specimen is a cylindrical component with 30 mm of diameter and 30 mm of height (Figure 3. 79b).

The stopping criteria of the fatigue tests are:

- 1) The collapse of the specimen at defined load level.
- 2) The reaching of the maximum permanent deformation of 0.65 mm, because it corresponds to the maximum compensation magnitude imposed by the algorithm (Figure 3. 80). Reaching the value of maximum correction made by the compensation algorithm means that the stamped component will be drastically out of tolerance.
- 3) If no collapse or permanent deformation of 0.65 mm are registered, the other stopping criteria is the reaching of 10 thousand cycles, which correspond a small-medium industrial production batch.

The major economic advantages in using polyurethane tools are achieved in manufacturing of small-medium batches, because the costs of a traditional metal tools setup are very difficult to be covered without an increasing of component price.

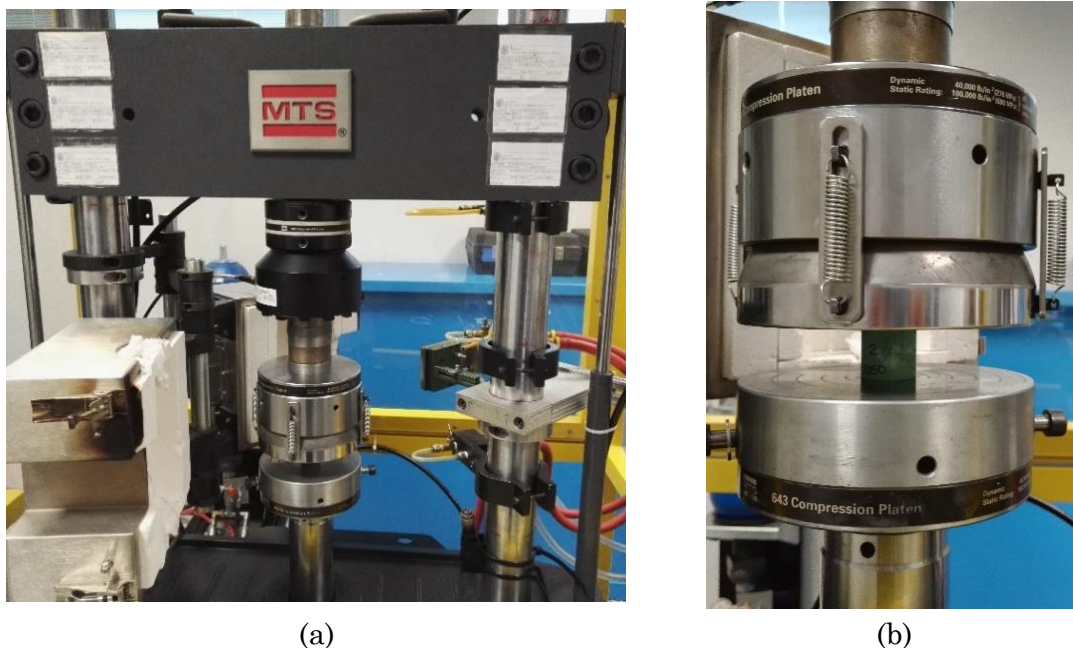


Figure 3. 79: Hydraulic testing machine used in fatigue tests (a) and the cylindrical specimen enclosed within the compression plates (b).

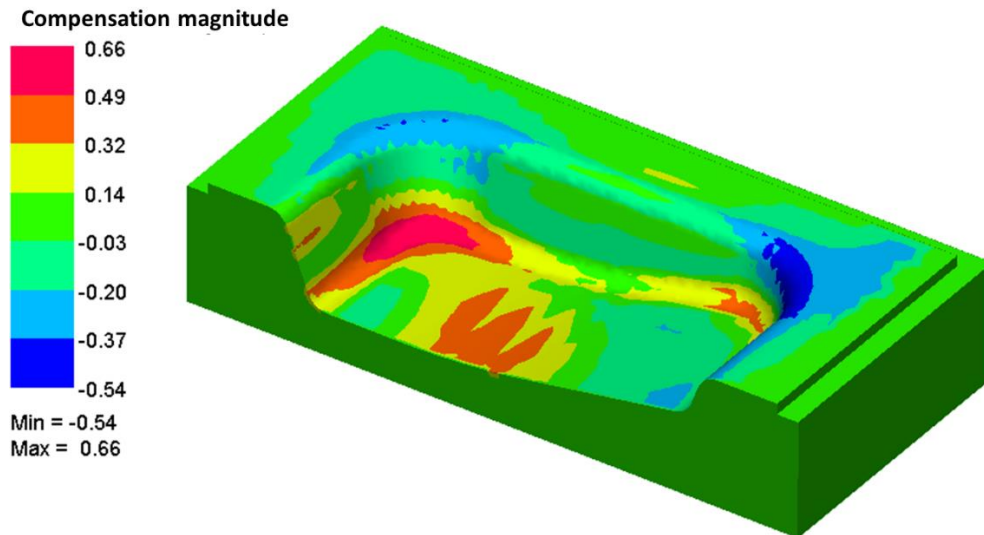


Figure 3. 80: maximum compensation magnitude imposed by the algorithm.

The tests have been performed by compressing the specimens at fixed levels of load and by measuring their height at interval of: 100, 200, 500, 1000 and then at intervals of 1000 cycles, until reaching one of the stop criteria.

The testing machine can be controlled by imposing an axial load expressed in kN. For this reason, the load levels have been chosen by these criterion:

1. **Lower level:** corresponds to the maximum Von Mises stress value obtained from the simulations of the stamping process. The Von Mises values have been extracted by the die and punch of test case 1, for Necuron 1050 (Figure 3. 81) and 1300 (Figure 3. 82) respectively, and from the die of test case 2 for Miketool 1440 (Figure 3. 83). The lower level for Necuron 1150 has been calculated as a mean of load values obtained by Necuron 1300 and 1050.
2. **Upper level:** has been calculated as 80% of the mean peak stress obtained by the performed compression tests described in chapter 2.
3. **Mean level:** is a mean between the upper and lower levels.

The calculated load levels have been resumed in Table 3. 21.

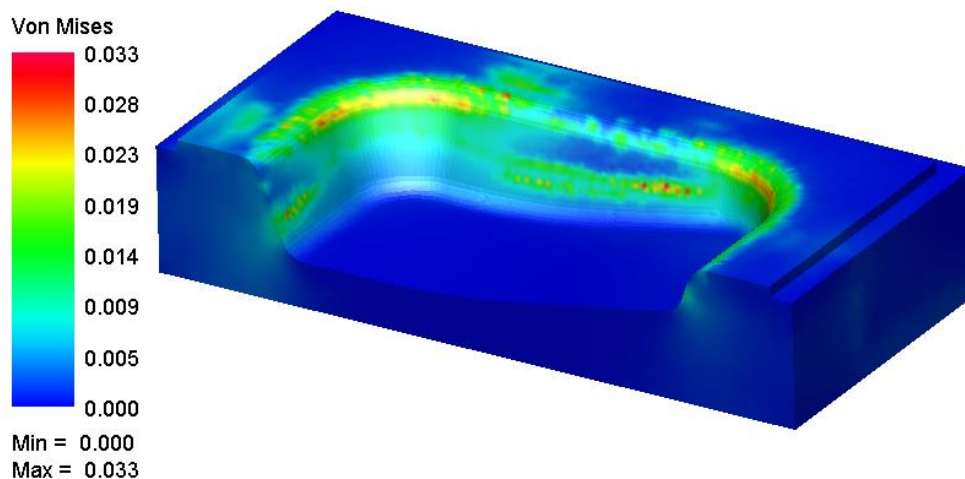


Figure 3. 81: Von Mises stress values for the die of the case 1, made by Necuron 1050.

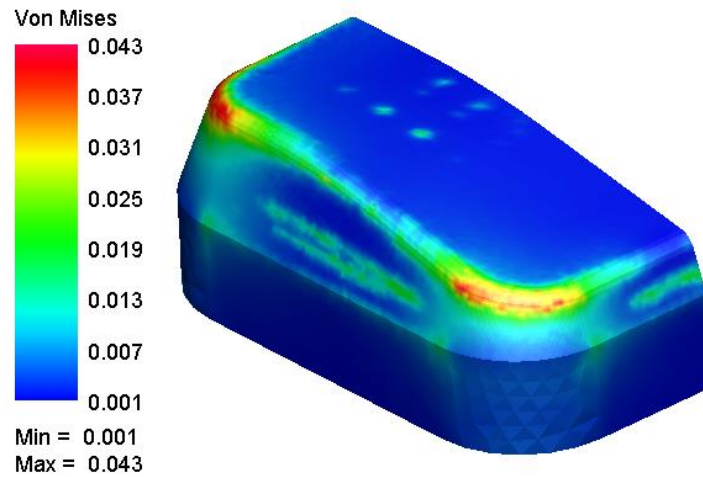


Figure 3. 82: Von Mises stress values for the punch of the case 1, made by Necuron 1300.

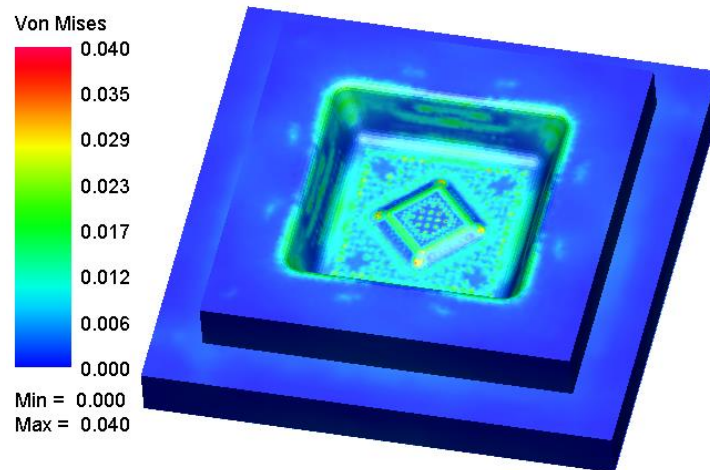


Figure 3. 83: Von Mises stress values for the die of the case 2, made by Miketool 1440.

Specimen data				Stress levels		Experimental load levels		
Material	Height	Diameter	Area	FEM Von Mises	Peak Stress	Lower level	Mean level	Upper level
-	[mm]	[mm]	[mm ²]	[MPa]	[MPa]	[kN]	[kN]	[kN]
Necuron 1300	30	30	707	43	73	30	36	41
Necuron 1050	30	30	707	33	62	23	29	35
Necuron 1150	30	30	707	38	85	27	38	48
Miketool 1440	45	30	707	40	90	28	40	51

Table 3. 21: fatigue tests experimental plan.

3.4.3 Experimental results

Considering the time needed for 1 fatigue test, 3 hours if no collapse is registered, the test at the upper load level (80% of the mean compression Peak stress) have been performed first in order to reduce the total testing time from 36 hours to 24. After the test of the upper level load, the two specimens (on total of 4) with the worst results have been chosen for testing the middle and lower levels.

All the specimens reached the collapse before the 10 000 cycles (Figure 3. 84) At maximum load level condition. The Necuron 1150, being collapsed at cycle 2263, proved to be the most resistant material between the tested ones. The graph in Figure 3. 85 shows the compression cycles (load and unload) at 48 kN maximal load until the reaching of permanent deformation limit of 0.65 mm. Initially the material has very low hysteresis, which increases rapidly when the permanent deformation reaches the value of 0.4 mm. Merging the data from Figure 3. 84 and Figure 3. 85, the material seems well resistant until 2000 cycles without relevant permanent deformation, after that limit, the Necuron 1150 becomes unstable with not negligible hysteresis effect.

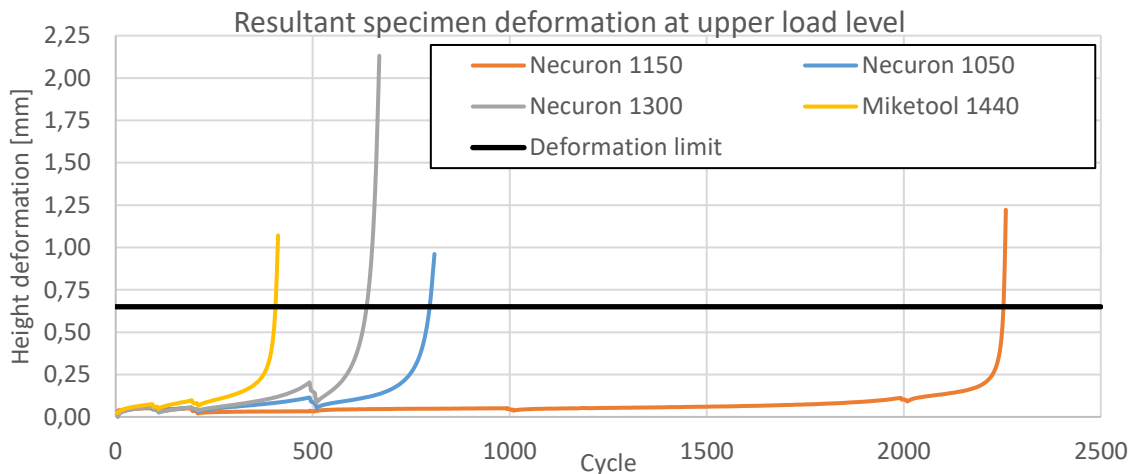


Figure 3. 84: specimens deformations at the end of fatigue test performed at upper load level.

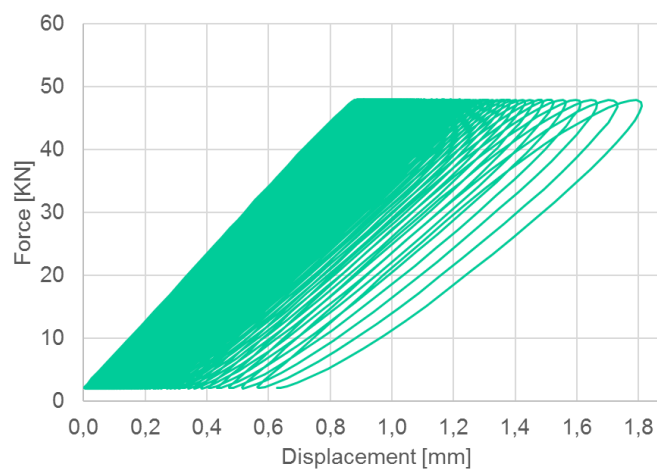


Figure 3. 85: Force vs Displacement diagram of compression fatigue cycles for Necuron 1150 at load level condition of 48 kN.

The Necuron 1050 showed very similar to Necuron 1300. It presented a collapse at cycle 813, respect to the 674 of the Necuron 1300. In Figure 3. 86 an increasing of the hysteresis effect can be observed near to permanent deformation of 0.5 mm, which is reached near to cycle 782. The Necuron 1300 tends to remain more stable in terms of hysteresis (Figure 3. 87), which seems to remain constant until the deformation limit of 0.65 mm, which is reached at cycle 633.

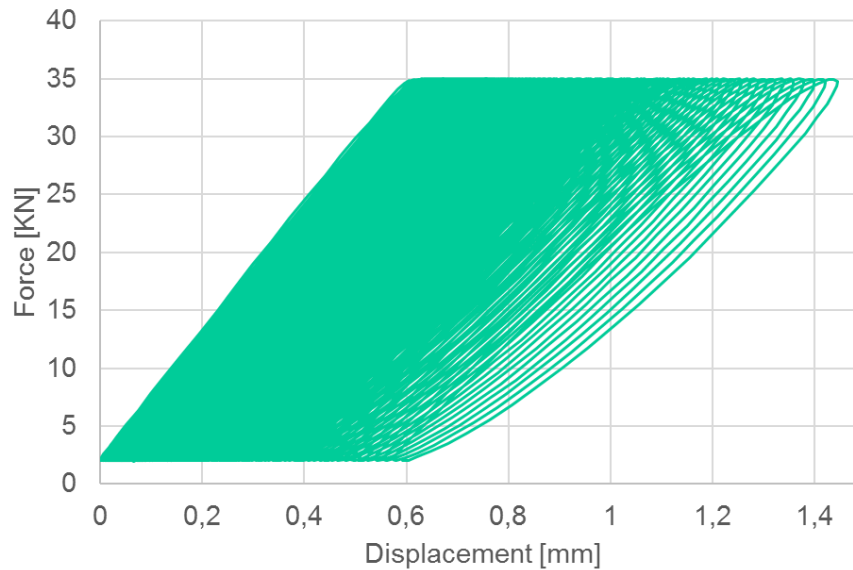


Figure 3. 86: Force vs Displacement diagram of compression fatigue cycles for Necuron 1050 at load level condition of 35 kN.

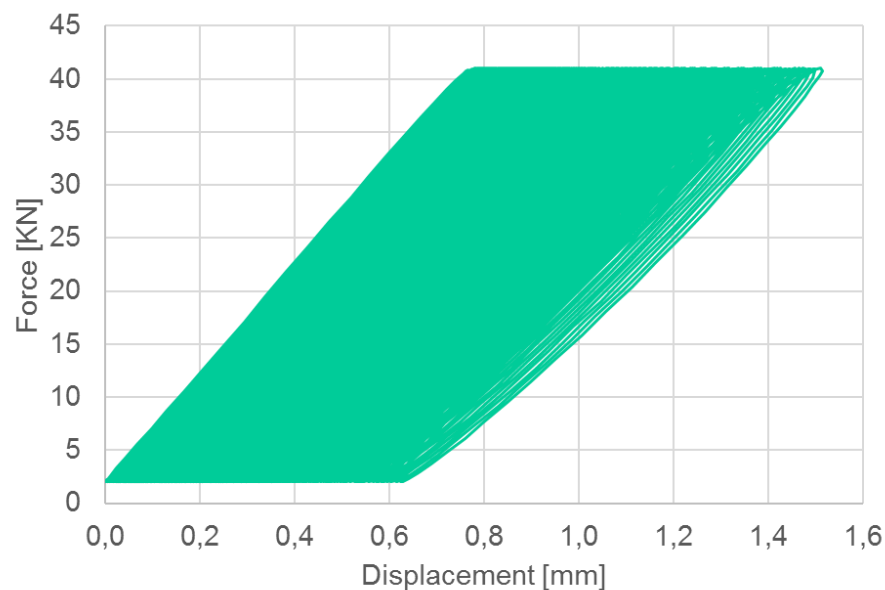


Figure 3. 87: Force vs Displacement diagram of compression fatigue cycles for Necuron 1300 at load level condition of 41 kN.

Finally, the Miketool 1440 presented the worst performances, since it collapsed at cycle 416, and reached the deformation limit at cycle 404. In Figure 3. 88, it can be observed that the hysteresis effect tends to be relevant near the deformation of 0.5 mm at cycle 400. Considering the slope of the load curves, the Miketool presented similar elasticity respect to Necuron 1150, indeed this two material are not reinforced as Necuron 1300 and 1050, which present similar elastic properties.

In conclusion, the Miketool and the Necuron 1300 have been chosen for being tested at mean and lower level. The results achieved in the upper level experimental condition are very interesting because the materials with the worst performances correspond with the most expensive (Necuron 1300) and the cheaper one (Miketool). Necuron 1300 is a reinforced material, which present elevated stiffness and more stable hysteresis condition respect to Miketool. If the performance of Necuron 1300 are lower respect Necuron 1050 and 1150, it should be noted that the density of Necuron 1300 is lower respect to the other resins (chapter 2). This quality can be fundamental for the design of lightweight components, but no for stamping tools applications where the tools weight is a secondary characteristic.

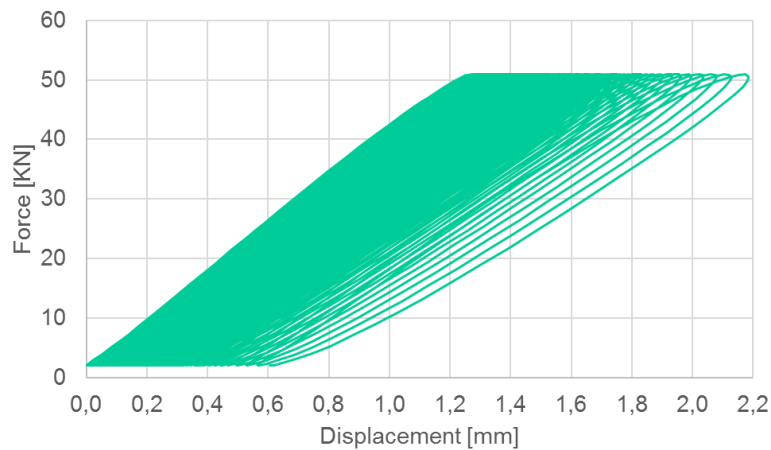


Figure 3. 88: Force vs Displacement diagram of compression fatigue cycles for Miketool 1440 at load level condition of 51 kN.

The results presented in Figure 3. 89 are related to the minimum deformation registered for fatigue tests at mean load level. Both materials, Necuron 1300 and Miketool 1440, did not collapse and did not achieve the deformation limit until 10000 cycle. As expected, The Necuron 1300 is more rigid respect to Miketool 1440. For this reason, in Figure 3. 89, it can be observed that the Necuron 1300 reaches a permanent deformation of 0.1 mm at 9000, after this limit the Necuron 1300 tends to deform fastly, even if no particular variation of the hysteresis effect can be observed in Figure 3. 90.

Thanks to the higher elasticity of the Miketool 1440, the specimen did not show relevant permanent deformations until 10000 mm, same results can be observed also for hysteresis effect in Figure 3. 91.

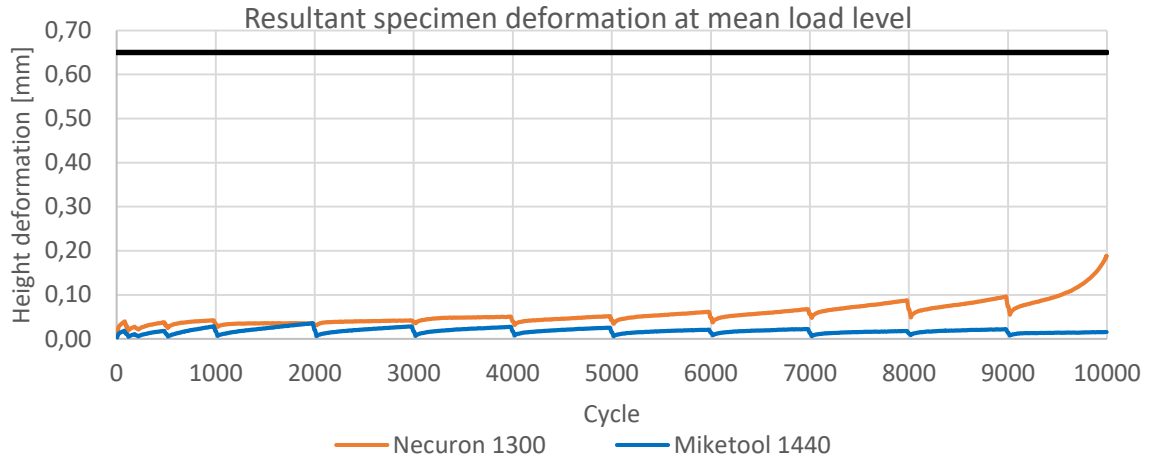


Figure 3. 89: specimens deformations resultant at the end of fatigue test performed at mean load level.

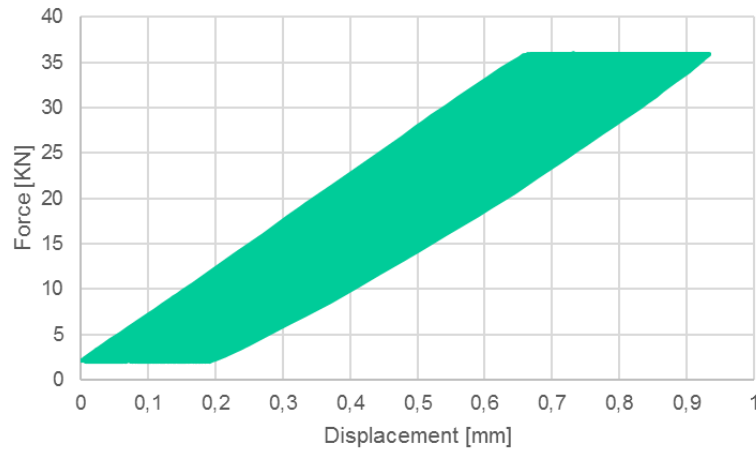


Figure 3. 90: Force vs Displacement diagram of compression fatigue cycles for Necuron 1300 at load level condition of 36 kN.

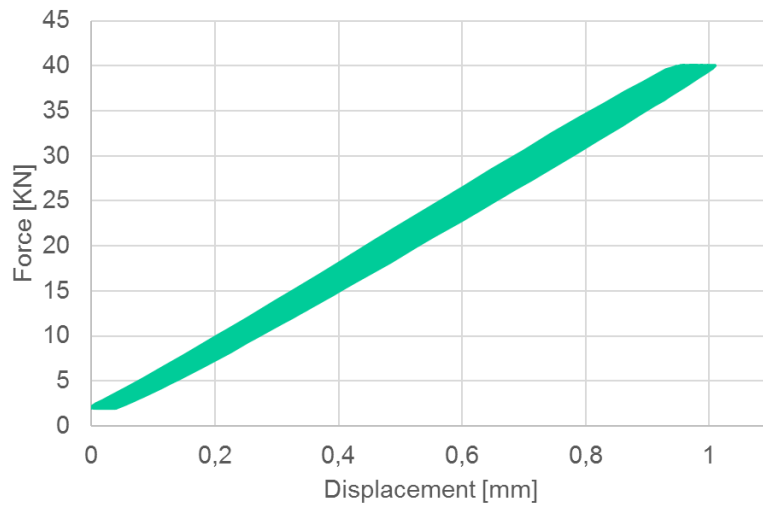


Figure 3. 91: Force vs Displacement diagram of compression fatigue cycles for Miketool 1440 at load level condition of 40 kN.

If for the mean load level no particular deformations have been registered, better results have been obtained for the lower load level (Figure 3. 92), where the maximum permanent deformations did not reach the value of 0.05 mm for all the performed cycles and, consequently, stability condition have been registered for hysteresis effect of both materials (Figure 3. 93 and Figure 3. 94).

Considering all the results obtained in the fatigue tests, the materials can reach without any problem until 10 000 cycles, if used in safe conditions in a range of loads until the 35 kN. The Necuron 1300 seem to be the less appropriate material for tooling applications, where high tools life is requested.

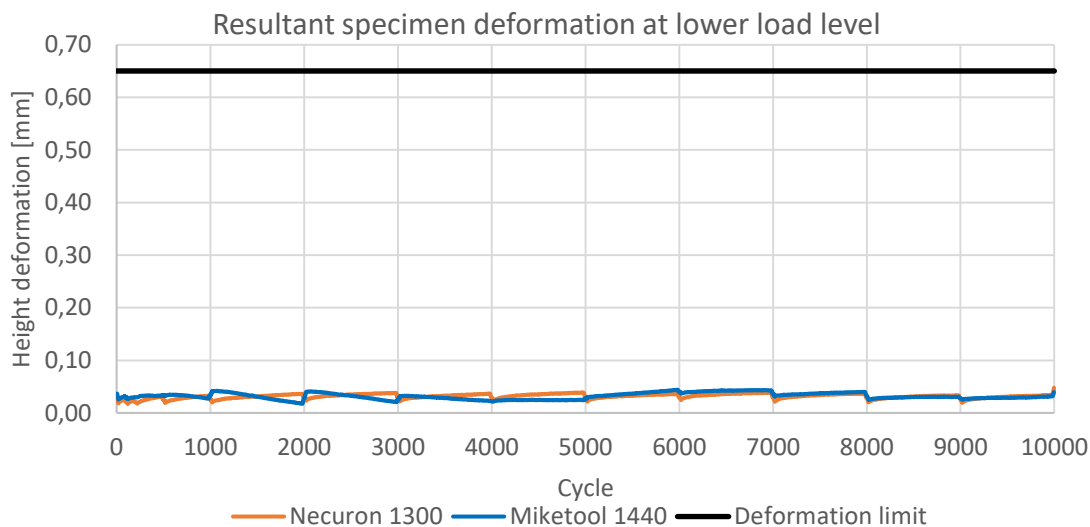


Figure 3. 92: specimens deformations resultant at the end of fatigue test performed at lower load level.

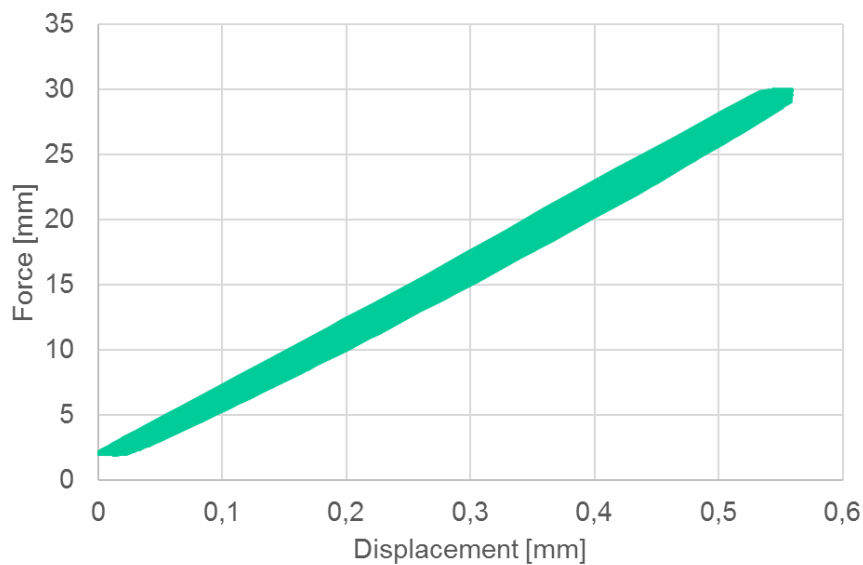


Figure 3. 93: Force vs Displacement diagram of compression fatigue cycles for Necuron 1300 at load level condition of 30 kN.

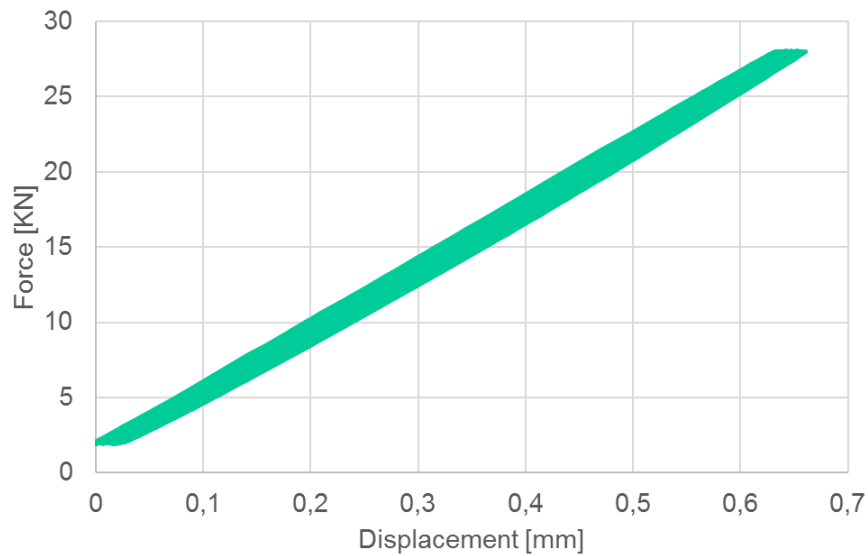


Figure 3. 94: Force vs Displacement diagram of compression fatigue cycles for Miketool 1440 at load level condition of 28 kN.

3.5 Conclusions

In this chapter, rapid tools have been developed for sheet metal stamping application. The experimental activities confirmed all the assumptions made in the first chapter. The rapid tools setup have been manufactured quickly at very low budget, if compared to the classic metal tools.

The numerical activities demonstrates that an FEM model can be implemented for predicting the process results in a reliable way. At the same experimental conditions, the FEM model shows that the tools structure is completely safe at the end of the process and no yield stress is reached. The developed compensation algorithm is able to drastically reduce the geometrical deviations between the stamped component and the designed one in automatic way. The implemented methodology simplifies the design phase by returning a tool with compensated shape with negligible effect on the final stress conditions at obtainable at the end of the process.

The fatigue tests shown that the material can resist for 10 000 cycle at the same experimental load conditions. It must be noted that the specimens have been tested at very high deformation rate, if compared to a stamping operation, which is from 5 to 10 time slower than the fatigue test rate experimented.

Finally, it has been demonstrated that rapid tools can be suitable for industrial stamping operation, because the disadvantages related to the design phase have been drastically reduced; no aesthetical defects have been seen on the stamped component also. If well designed the tools life is long enough for middle production volume. Further developments can be performed for improving the FEM model results, but the conditions for the industrialization of the rapid tools solution in sheet metal stamping process it is not so far **Errore. L'origine riferimento non è stata trovata.**-[39].

3.6 References

- [1] G.N. Levy, R. Schindel, P. Schleiss, F. Micari, L. Fratini, On the use of SLS Tools in Sheet Metal Stamping, *CIRP Annals - Manufacturing Technology*, Volume 52, Issue 1, 2003, Pages 249-252, ISSN 0007-8506, [http://dx.doi.org/10.1016/S0007-8506\(07\)60577-0](http://dx.doi.org/10.1016/S0007-8506(07)60577-0).
- [2] H. Müller, J. Sladojevic, Rapid tooling approaches for small lot production of sheet-metal parts, *Journal of Materials Processing Technology*, Volume 115, Issue 1, 22 August 2001, Pages 97-103, ISSN 0924-0136, [http://dx.doi.org/10.1016/S0924-0136\(01\)00749-X](http://dx.doi.org/10.1016/S0924-0136(01)00749-X).
- [3] DURGUN, I., et al. Prototype Tooling of Sheet Metal Components of Car Body. In: 7. International Conference and Exhibition on Design and Production of Machines and Dies/Molds, Antalya. 2013.
- [4] PINTO, Mário, et al. Study on the usability and robustness of polymer and wood materials for tooling in sheet metal forming. *Journal of Materials Processing Technology*, 2008, 202.1: 47-53.
- [5] QUADRINI, Fabrizio; SANTO, Loredana; SQUEO, Erica Anna. Flexible forming of thin aluminum alloy sheets. *International Journal of Modern Manufacturing Technologies*, 2010, 2.1: 79-84.
- [6] Material Removal Rate formula - http://www.sandvik.coromant.com/en-gb/knowledge/technologies/silent-tools/formulas_and_definitions accessed on 13/01/2018.
- [7] IORIO, Lorenzo; STRANO, Matteo; MONNO, Michele. Development of a Die Compensation Algorithm for Sheet Metal Stamping With Deformable Tools. In: ASME 2015 International Manufacturing Science and Engineering Conference. American Society of Mechanical Engineers, 2015. p. V001T02A089-V001T02A089.
- [8] IORIO, Lorenzo, et al. Design of Deformable Tools for Sheet Metal Forming. *Journal of Manufacturing Science and Engineering*, 2016, 138.9: 094701.
- [9] M. Oudjene, L. Penazzi, J.-L. Batoz, Towards the three-dimensional FE analysis of rapid prototyping tools for sheet metal stamping process, *Finite Elements in Analysis and Design*, Volume 43, Issue 8, May 2007, Pages 611-619, ISSN 0168-874X, <http://dx.doi.org/10.1016/j.finel.2006.12.012>.
- [10] ESI-Group, Visual-Mesh 11.0, User's Guide.
- [11] J. Witulski, M. Trompeter, A.E. Tekkaya, M. Kleiner, High wear resistant deep drawing tools made of coated polymers, *CIRP Annals - Manufacturing Technology*, Volume 60, Issue 1, 2011, Pages 311-314, ISSN 0007-8506, <http://dx.doi.org/10.1016/j.cirp.2011.03.149>.
- [12] ESI-Group, Pam-Stamp 2G 2015.1, User's Guide.
- [13] COLTON, J. S.; PARK, Y. Sheet metal forming using polymer composite rapid prototype tooling. *Journal of engineering materials and technology*, 2003, 125.July: 247-255.
- [14] PARK, Y.; COLTON, J. S. Failure analysis of rapid prototyped tooling in sheet metal forming-V-die bending. *TRANSACTIONS-AMERICAN SOCIETY OF MECHANICAL ENGINEERS JOURNAL OF MANUFACTURING SCIENCE AND ENGINEERING*, 2005, 127.1: 116.

- [15] PARK, Y.; COLTON, J. S. Failure Analysis of Rapid Prototyped Tooling in Sheet Metal Forming—Cylindrical Cup Drawing. *Journal of manufacturing science and engineering*, 2005, 127.1: 126-137.
- [16] Vialux Autogrid product - <https://www.vialux.de/en/autogrid-product-overview.html> accessed on 13/01/2018.
- [17] STANTON, M., et al. Modelling and Validation of Springback in Aluminium U-Profiles. *International Journal of Material Forming*, 2010, 3: 163-166.
- [18] BANABIC, Dorel. Sheet metal forming processes: constitutive modelling and numerical simulation. Springer Science & Business Media, 2010.
- [19] SCHNEIDER, M.; FRIEBE, H.; GALANULIS, K. Validation and optimization of numerical simulations by optical measurements of tools and parts. *International Deep Drawing Research Group*, 2008, 327-332.
- [20] Witulski, J., Trompeter, M., Tekkaya, A. E., & Kleiner, M. (2011). High wear resistant deep drawing tools made of coated polymers. *CIRP Annals - Manufacturing Technology*, 60(1), 311–314.
- [21] YANG, Xiang An; RUAN, Feng. A die design method for springback compensation based on displacement adjustment. *International Journal of Mechanical Sciences*, 2011, 53.5: 399-406.
- [22] R.A. Lingbeek, Aspects of a design tool for springback compensation, Master Thesis, University of Twente / INPRO.
- [23] SHEN, Guozhe, et al. Springback simulation and tool surface compensation algorithm for sheet metal forming. In: *AIP Conference Proceedings*. IOP INSTITUTE OF PHYSICS PUBLISHING LTD, 2005. p. 334.
- [24] Karafillis A.P., Boyce M.C., Tooling and binder design for sheet metal forming processes compensation springback error. *International Journal of Machine Tools & Manufacture* 1996; 36 (4): 503–36.
- [25] Wagoner RH, Gan W, Mao K, Price S, Rasouli F. Design of sheet forming dies for springback compensation. In: *6th international ESAFORM conference*. University of Salerno, Salerno; 2003. p. 7–12.
- [26] GanW, Wagoner RH. Die design method for sheet springback. *International Journal of Mechanical Sciences* 2004; 46(7): 1097–113.
- [27] W.H. Press, S.A. Teukolsky, W.T. Vetterling, B.P. Flannery, *Numerical Recipes in C*, Cambridge University Press, 1992.
- [28] LIU, Chuang, et al. A rapid and intelligent approach to design forming shape model for precise manufacturing of flanged part. *The International Journal of Advanced Manufacturing Technology*, 2017, 1-14.
- [29] LINGBEEK, R., et al. The development of a finite elements based springback compensation tool for sheet metal products. *Journal of Materials Processing Technology*, 2005, 169.1: 115-125.
- [30] IORIO, Lorenzo; STRANO, Matteo; MONNO, Michele. Development of a Die Compensation Algorithm for Sheet Metal Stamping With Deformable Tools. In: *ASME 2015 International Manufacturing Science and Engineering Conference*. American Society of Mechanical Engineers, 2015. p. V001T02A089-V001T02A089.
- [31] SINTEF, Geometry/GoTools, <https://github.com/SINTEF-Geometry/GoTools>.

- [32] Lee, S., Wolberg, G., & Shin, S. Y. (1997). Scattered data interpolation with multilevel B-splines. *Visualization and Computer Graphics, IEEE Transactions on*, 3(3), 228-244.
- [33] Luca P., Data fusion for process optimization and surface reconstruction, Doctoral Thesis, Politecnico di Milano.
- [34] IORIO, Lorenzo; STRANO, Matteo; MONNO, Michele. Rapid Tools Compensation in Sheet Metal Stamping Process. In: *MATEC Web of Conferences*. EDP Sciences, 2016. p. 10009.
- [35] Pilthammar J., Wall J., Sigvant M., Framework for Simulation-Driven Design of Stamping Dies Considering Elastic Die and Press Deformations, *ESAFORM 2017*
- [36] FDM Tooling - <http://www.stratasys.com/solutions/additive-manufacturing/tooling/metal-hydroforming> accessed on 13/01/2018.
- [37] Alro Plastics - www.alro.com/divgeneral/processingservices.aspx?div=pla accessed on 13/01/2018.
- [38] Ebalta tooling resis - http://www.ebalta.de/fileadmin/user_upload/7._Downloads/ebalta_Produktuebersicht_EN_171269_web.pdf accessed on 13/01/2018.
- [39] Obo-Werke Polyurethane boards - <https://www.obo-werke.de/fileadmin/templates/downloads/prospekte/renshape-brochure.pdf> accessed on 13/01/2018.
- [40] Necumer tooling boards - <http://necumer.com/index.php/en/products/board-materials/tooling> accessed on 13/01/2018.

Chapter 4

Rapid tools in air bending process

4.1 Introduction

In the previous chapter, the implementation of rapid tools in a sheet metal stamping process has been presented.

The economical evaluation conducted on the tests case showed that a stamping tooling setup made by polyurethane material could be manufactured with small amount of resources in terms of manufacturing time and costs.

The FEM activities demonstrated that the implemented simulation model is able to describe the behaviour of the polyurethane tools and the sheet metal during the stamping operation simultaneously.

Furthermore, the experimental fatigue tests performed on the polyurethane materials demonstrated that the designed rapid tools can resist over than 10 000 cycles, which correspond to the industrial middle production volume.

Thanks to the knowledge acquired in the study of the stamping process with the polyurethane tools, the main objective of this chapter is to enlarge the application of the polymeric dies and compare to other solutions.

Similar applications have been found in [1] and [2] where failure analysis has been conducted with the aid of experimental and numerical activities. The author presented a method for estimating the fatigue life of a polymeric die. A prototypal polymeric bending tools setup has been developed in order to validate experimentally the failure analysis conducted with FEA (Finite Element Analysis) techniques. As stated by the author, the study gives the basis of the possible application of the rapid tools in the sheet metal bending process, but more accurate predictions and detailed guidelines should be employed. For this reasons, a more industrialized solution will be presented in this chapter.

The bending tool solution developed in this section will consist in a V-shape bending die with a metal framework, which allows joining the tool to a standard press brake machine, and an interchangeable polyurethane insert, which will constitute the core of the tool where the bending operation will take place.

The developed solution will be economically compared with the equivalent commercial rigid metal solution. Experimental activities have been conducted in order to compare the results between the polyurethane die and the commercial metal, nylon and rubber solutions.

The results obtained by the experimental activities have been used for developing several FEM models able to describe all the solutions tested.

4.2 Economical comparison

The idea is to design a rapid tool solution composed by a rigid standard framework where interchangeable inserts can be put inside depending on the manufacturing needs. One of the requirements, which the rapid tool solution has to meet, is the low cost manufacturability with respect to the traditional metal ones. The commercial rigid die used as a reference product is the T80.06.88 made by Rolleri S.p.a., whose solution is the most common used in sheet metal bending. The company gave information about the cost weights of the manufacturing operations in percentage of the total tool cost (Table 4. 1).

The rapid tool/die concept, developed in this work (Figure 4. 1), consists in a composition of metal framework (grey component), which can be specifically manufactured or commercially bought, and a polyurethane insert (red component), which can be put inside its cavity.

The metal frame used for assembling the rapid die has been identified in the commercial framework MPG25 used normally for rubber dies. The cost of the MPG25 has been supposed by considering the commercial profit margin, subtracted the weight of the thermal treatment costs by obtaining the industrial cost of 37.42 €.

T80.06.88 data		
Rough dimensions		
Width	65	mm
Height	85	mm
Length	420	mm
Volume	$2.320 \cdot 10^3$	mm^3
Density	$7.870 \cdot 10^{-6}$	kg/mm^3
Weight	18.099	kg
Costs percentage coefficients		
Material	40%	Rolleri data
Machining operations	50%	
Thermal treatment	10%	
Costs data		
Material cost unit	0.857	€/kg
Material cost	15.524	€
Machining cost	19.405	€
Thermal treatment	3.881	€
Total cost	38.81	€

Table 4. 1: manufacturing costs of the die used in the experimental activities.

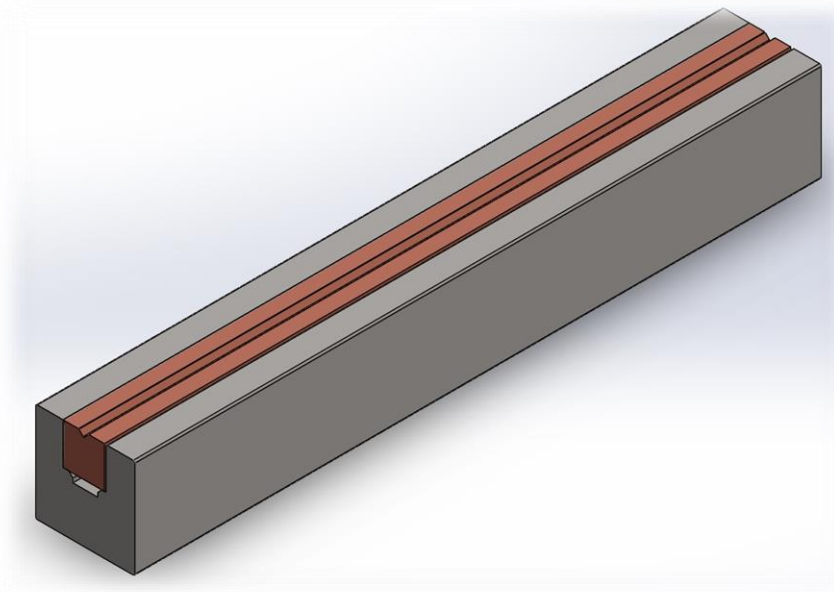


Figure 4. 1: bending rapid die concept.

The cost of the polyurethane insert has been calculated by considering the machining parameters suggested by the manufacturer company Necumer. In Table 4. 2, the costs unit of the different polyurethane, Necuron 1300, 1150 and 1050, and the commercial standard dimensions of the boards have been reported.

For the cost evaluation, the board with the maximum dimensions has been chosen, because it allows the manufacturing of 111 parallelepiped inserts with initial dimensions of 30x30x420 mm.

	Necuron		
	1300	1150	1050
Cost unit [€/m ³]	8100	8700	5960
Board dimensions (width x height x length) [mm]	400 x 75 x 800		
	400 x 100 x 800		
	500 x 75 x 1000		
	500 x 100 x 1000		

Table 4. 2: cost unit and available standard dimensions for Necuron boards.

Taking into account the cost of the polyurethane board with the maximum dimensions and the units reported in Table 4. 2, the cost of a single rough insert for each material has been approximatively calculated in Table 4. 3. Considering the machining parameters suggested by the manufacturer, the costs of the manufacturing cycle for obtaining a final insert dimensions 25x25x415 mm with a V-shaped cavity of 88° of opening angle and 6 mm width, have been reported in Table 4. 4. For having the total cost of the rapid die, the cost of the inserts should be added to the cost of the metal framework by obtaining a maximum cost of 48.69 € for the solution MPG25 + Necuron 1150.

Material	Cost
Necuron 1300	3,65 €
Necuron 1150	3,92€
Necuron 1050	2,68€

Table 4. 3: cost of each rough insert with dimensions of 30x30x420.

Manufacturing operations		
Flattening path	860.00	[mm]
Facing path	57.00	[mm]
Feed	2.83	[mm/s]
Cutting speed	0.83	[mm/s]
Facing time	20.15	[s]
Flattening time	303.95	[s]
Cutting path (bandsaw)	46.88	[mm]
Cutting time (bandsaw)	4.69	[s]
Setup time	60.00	[s]
Cutting time for V-shape cavity	293.35	[s]
Total time	661.98	[s]
Manufacturing costs		
Man power cost unit	40.00	[€/h]
Manufacturing cost for 1 insert	7.36	[€]
Total cost of Necuron 1300 insert	11	[€]
Total cost of Necuron 1150 insert	11.27	[€]
Total cost of Necuron 1050 insert	10.04	[€]

Table 4. 4: manufacturing operations data and total costs of the Necuron inserts.

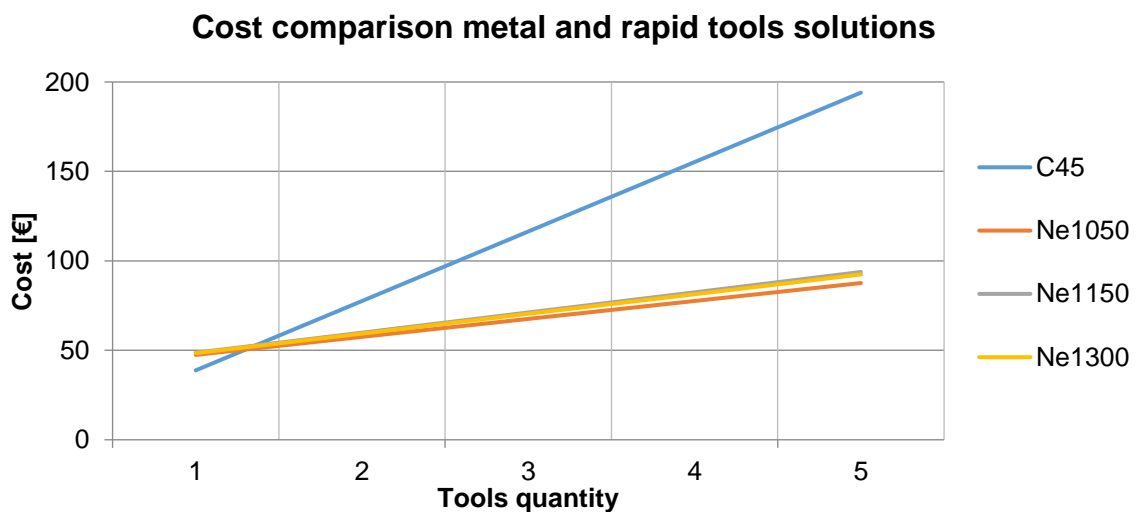


Figure 4. 2: comparison of the trend of the tools cost respect to the purchase quantities.

In Figure 4. 2, the cost comparison of the traditional metal and the rapid tools solutions has been presented. The cost of a single metal die is lower respect to the rapid die solution because the metal frame used in the rapid tool solution has a comparable price with the metal die solution. In order to reduce this difference on a single tool, a cheaper metal could be used for manufacturing the metal frame; otherwise, a completely polyurethane solution can be considered. It should be noted that in a company, more than one tool must be bought in order to bend blanks with different thicknesses at different angles. For this reason, the cost comparison between the metal and rapid tools solutions should be seen also in relation with the purchase quantity. The main advantage of the rapid tool solution is related to the interchangeability of the insert. When a different tools with different V-shaped cavity is needed only the polyurethane insert must be changed; instead, for the metal tool solution, a completely different die is need. From these considerations the rapid tools solution is more economically convenient respect to the traditional metal solution. In conclusion, the rapid tools solution seems to be again the more economical solution with respect yo of the rigid metal solution. In the next paragraphs, the described rapid die solution will be compared with the commercial solution (metal and rubber ones) in experimental and numerical activities.

4.3 Experimental plan and tools setup

The experimental bending tests have been implemented by using 7 types of bending dies made by different materials.

The main objective of the experiments is to compare the performances of commercial solution made by metal, nylon or rubber, with the rapid tool solution made by Necuron 1300, 1150 and 1050.

All the experiments have been carried out by the same V-metal punch P97.88.R08/C with radius of 0.8 mm and opening angle of 88° (Figure 4. 3).

The metal die is the commercial model T80.06.88/C, made by Rolleri, with a V-shaped cavity large 6 mm with angle of 88° (Figure 4. 4).

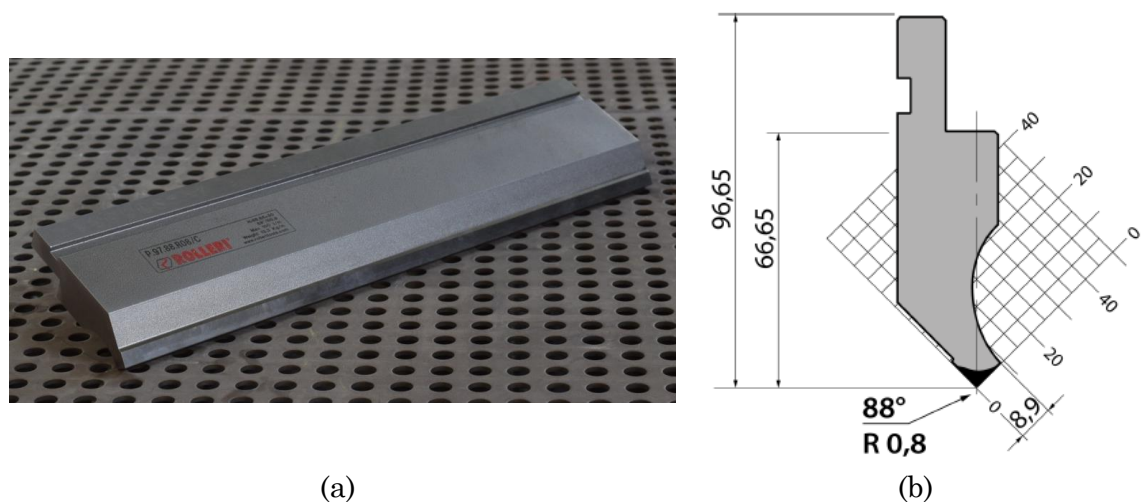


Figure 4. 3: metal punch P97.88.R08/C (a) used in the experimental activities with the geometrical dimensions (b).

The nylon die TN80-14-C is also a commercial solution composed by metal frame with a deformable insert, which is constrained by transversal screws passing inside the metal frame (Figure 4. 5). This kind of solution is normally used when no aesthetical defects, like scratches, are allowed on the final components. The main disadvantage of the nylon die is related to the low wear resistance of the insert, whose characteristic makes the solution suitable only for the production of small batches of components.

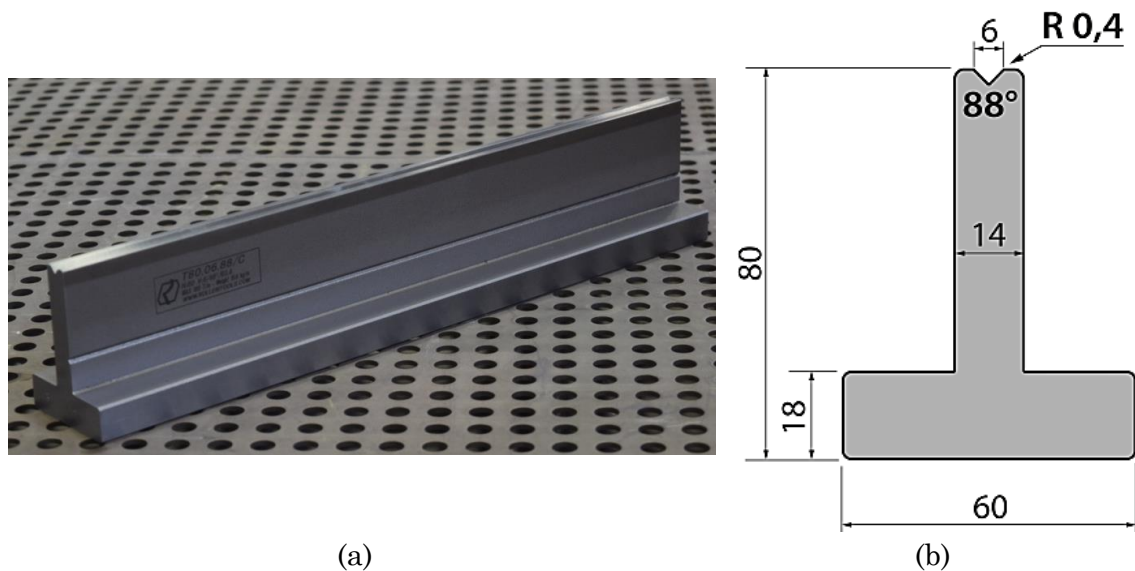


Figure 4. 4: metal die T80.R06.88/C (a) with geometrical dimensions (b).

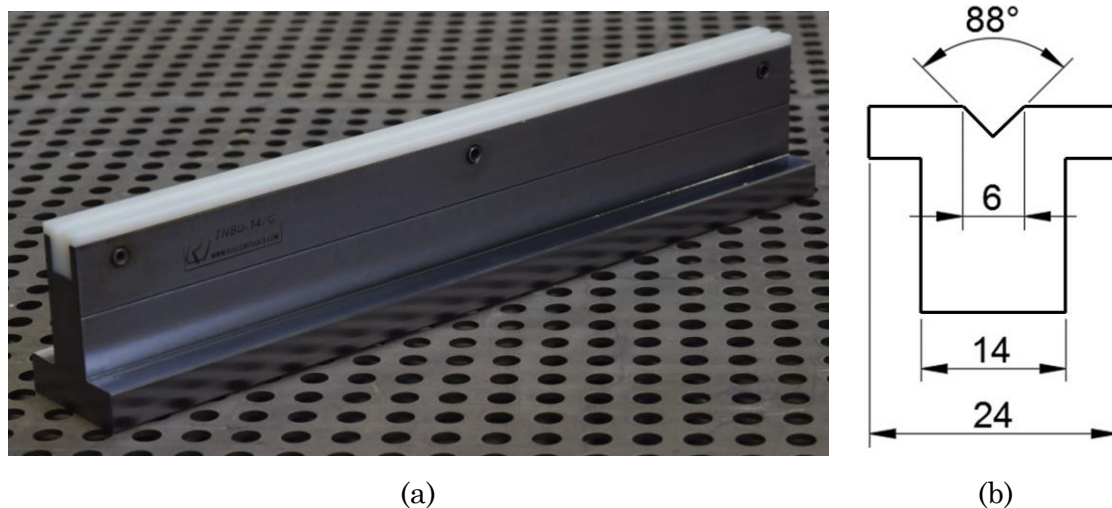


Figure 4. 5: metal frame with nylon insert TN80-14-C (a) with geometrical dimensions of the insert (b).

The rubber die used in the experimental activities is also composed by metal frame MPG25 (the same used for the rapid die) and a rubber insert named Kaylan D40-orange produced by Kay-Dee Engineering Plastics company. Two different rubber inserts have been used in the experiment (Table 4. 5), one with square section and the

other with square section with a hole at the center position. Actually the hole has been obtained by drilling, but it is not located exactly in the center; this defect will be taken in account during the simulation phase. Normally these kind of solutions are used in the bending of sheet metal component with large radius where no aesthetical defects are allowed, but a comparison with the other bending tools solution could be interesting due to the low availability data in the literature.

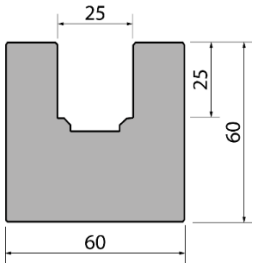
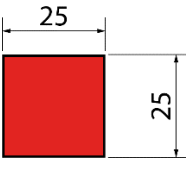
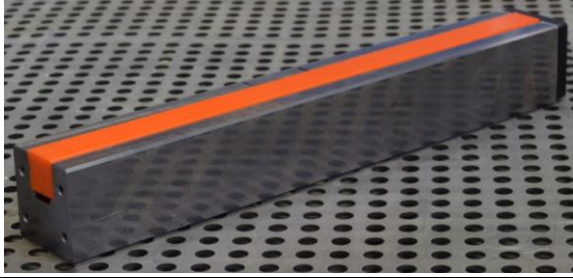
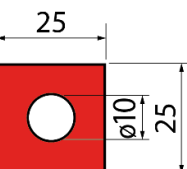
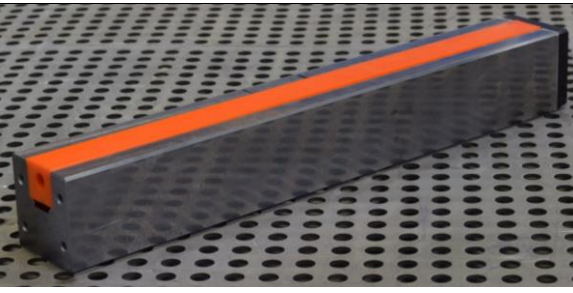
		
(a)	(b)	(d)
		
(a)	(c)	(e)

Table 4. 5: metal frame MPG45 (a) and rubber inserts dimensions (b), (c) and the assembly of the rubber dies (d) and (e).

The rapid die has been designed starting by the idea of the rubber die, by changing the hyper elastic insert (shore D 38-42) with the polyurethane ones (shore D 80-82). The polyurethane inserts have been milled in MUSP Laboratory of Piacenza and finished (Figure 4. 6), so that the V-shape cavity of the polyurethane inserts is the same respect to the metal die ones (T80.R06.88/C).

The polyurethane inserts, made by Necuron 1050, 1150 and 1300, does not need screws for being locked inside the metal frame, because the MPG45 is already provided with lateral plates, which close the insert inside the metal frame (Figure 4. 7).

In Table 4. 6 the comparison of the main tensile mechanical characteristics of the bending dies materials has been reported in order to show clearly the differences of the three material domains (metals, polymers and elastomers) already described in chapter 2.

The press brake supplied by the company is a prototypal machine normally involved for testing the special tools. The technical data of the press break have been reported in Table 4. 7.

The rectangular specimens with standard dimensions of 100x50 mm have been manufactured by waterjet cutting from a unique blank piece of each material considered.

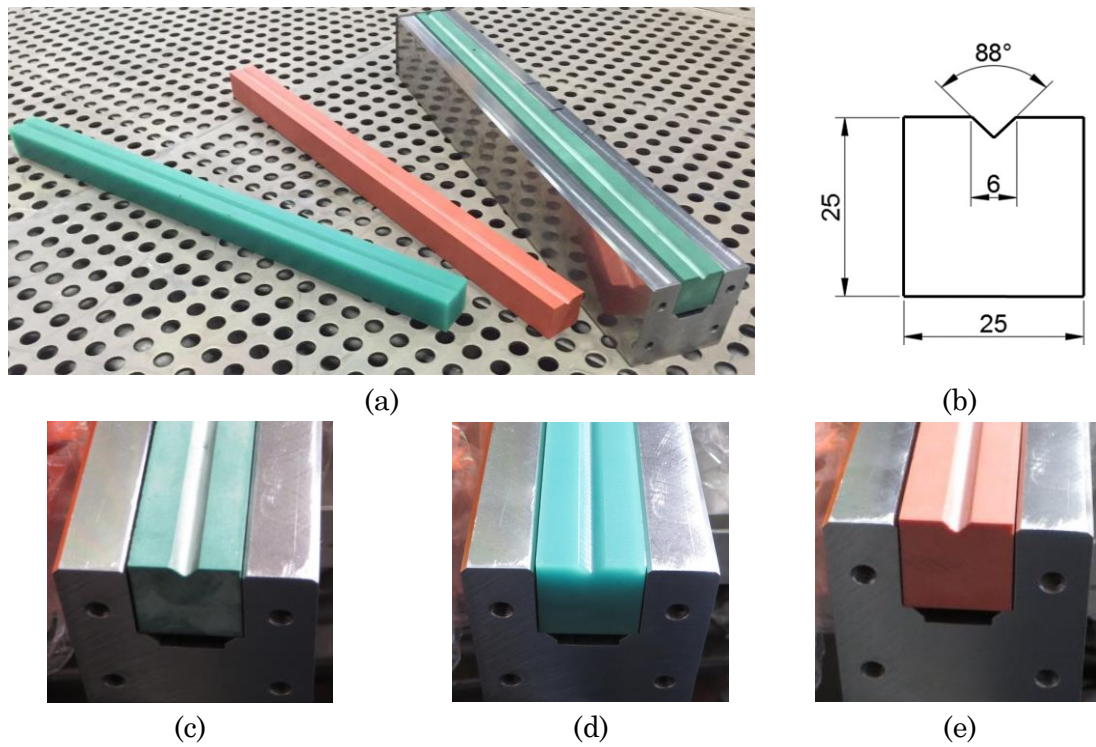


Figure 4. 6: rapid die solution (a) with the geometrical dimensions (b) and the detail of the V-shape cavity of each insert made by Necuron 1050 (c), 1150 (d) and 1300 (e).

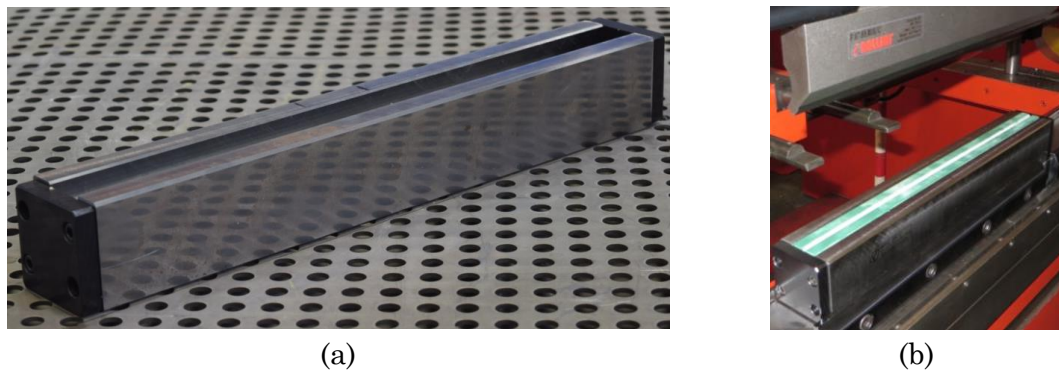


Figure 4. 7: detail of the MPG45 with the black locking plates (a) and rapid die with the Necuron 1050 insert inside the press brake (b).

Material	Density	Poisson's coefficient	Young's Modulus	Yield stress	Ultimate stress	Elongation
[-]	[kg/mm ³]	[-]	[MPa]	[MPa]	[MPa]	[%]
C40	7.8*10 ⁻⁶	0.28	208*10 ³	335	530	22
Nylon	1.15*10 ⁻⁶	0.4	2.50*10 ³	55	67.8	60
Necuron 1050	1.2*10 ⁻⁶	0.34	3.24*10 ³	30	38	3
Necuron 1150	1.2*10 ⁻⁶	0.34	2.91*10 ³	42.67	62.67	14.8
Necuron 1300	1.15*10 ⁻⁶	0.34	2.76*10 ³	37.33	49.33	12.07
Rubber Shore 90A	1.26*10 ⁻⁶	0.499	8.3	-	51.7	525

Table 4. 6: tensile material properties of the bending dies used in the experimental activities.

Four materials with a unique thickness have been considered. The reference of 0° for the rolling direction has been considered along the major dimension of 100 mm, as shown in Figure 4. 8. The resume of the available combinations in terms of the materials, thickness, rolling direction and quantity has been reported in Table 4. 8. The characterization of the specimens materials will be discussed in the paragraph related to the FEM activities. Due to the non-uniform availability of the specimen in terms of rolling direction the experimental plan has been designed in order to have at least 2 repetitions for each tool solution. Due to the low availability of the combination 4, the repetition has not been considered.

Technical data	
Maximum bending length	3100 mm
Maximum bending force	2000 kN
Pistons stroke	300 mm
Power	22 kW
Weight	3800 kg
Length	3750 mm
Width	1860 mm
Height	2950 mm

Table 4. 7: technical data of the press break involved in the experimental activities.

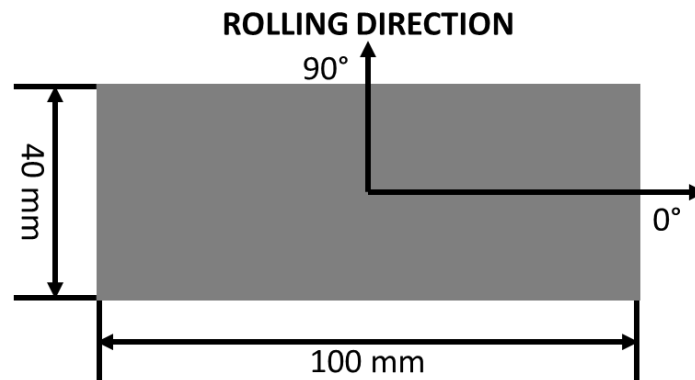


Figure 4. 8: schematization of the rolling direction and the dimensions of the standard specimen.

Material	Thickness	Rolling direction	Availability	Combination
[-]	[mm]	[°]	[-]	[-]
Al1050-0	1	0	4	1
Fe37	0.7	90	14	2
	0.8	0	14	3
		90	7	4
Fe37Z	1	0	14	5

Table 4. 8: available combinations of the specimen in terms of material, thickness, rolling direction and quantity

The complete experimental plan has been reported with the standard order in the Appendix C. The order of the experiment has been decided by considering the tool configuration as an hard to change factor.

The numerical control of the press brake needed the following parameters for calculating the punch stroke:

- Die geometry: height, width, opening angle and radius
- Punch geometry: height, opening angle and radius
- Blank material
- Blank thickness
- Desired angle

Initial tests have been performed with the metal tool solution in order to achieve the desired angle of 120° with a blank of 0.7 mm. The initial punch stroke was 1.77 mm and the obtained angle was smaller than 120°; for this reason the stroke has been adjusted gradually until 1.57 mm in order to reach an angle of 119.5°, very close to the target of 120°. The punch stroke has been maintained for all the experiments, in order to compare the resultant angle obtainable from the different solutions. For the polyurethane, nylon and metal solutions, the bending process can be defined as “air-bending” because the die supports the blank in two points along all the duration of the process and the tools do not reach the closure at the end of the process. On the contrary, for the rubber solutions (with and without the hole), the blank lean on the die surface during all the process, for this reason the first repetitions (standard order 7 and 9) performed with a punch stroke of 1.57 mm reach a very large opening angles of 174° and 173°. Due to these results, the punch strokes have been adjusted by the CN of the machine, by giving back a correction of 3.16 mm, which has been definitely used for all the experiments involving the rubber insert. The achieved angle results are reasonable because the rubber die surface is in contact with the blank since the beginning of the operation. The descending of the blank surface (due to the punch load) on the rubber die causes the uniform lowering of the entire upper surface of the surface, without any significant variation of the opening angle on the blank. This deformation of the rubber die reduces drastically the deformation of the blank given by the punch load, for this reason the resultant angle of the experiments involving rubber tools are so large.

After the experimental plan listed in Figure 4. 8, a set of 15 experiments have been performed with the die insert made by Necuron 1050, at punch stroke of 1.57 mm, in order to evaluate the repeatability of the cheaper polyurethane material used as a die insert.

4.4 Experimental results

The opening bend angle (α) of the specimens has been considered as the main response of the experiments. The opening angle has been measured by an analogic goniometer. The results of the experimental plan are reported in Table 4. 9. The ranges calculated between the correspondent experiments (Table 4. 9) show good repeatability but also demonstrate that the metal rigid solution can give the same magnitude with respect to the deformable solutions (standard order 5 and 6).

Std_order	Thickness [mm]	Material	Roll_dir [°]	Tool	Punch Stroke [mm]	Angle (α) [°]	Range [°]
1	1	Al1050	0	Rubber	3.16	165	0.00
2	1	Al1050	0	Rubber	3.16	165	
3	1	Al1050	0	Nylon	1.57	131.5	
4	1	Al1050	0	Nylon	1.57	131	0.50
5	0.7	Fe37	90	Metal	1.57	118	1.00
6	0.7	Fe37	90	Metal	1.57	119	
8	0.7	Fe37	90	Rubber	3.16	160.5	
10	0.7	Fe37	90	Rubber_hole	3.16	157.5	
11	0.7	Fe37	90	Ne1050	1.57	131.5	0.50
12	0.7	Fe37	90	Ne1050	1.57	132	
13	0.7	Fe37	90	Ne1150	1.57	132.75	1.25
14	0.7	Fe37	90	Ne1150	1.57	131.5	
15	0.7	Fe37	90	Ne1300	1.57	131	0.00
16	0.7	Fe37	90	Ne1300	1.57	131	
17	0.7	Fe37	90	Nylon	1.57	129.25	0.50
18	0.7	Fe37	90	Nylon	1.57	129.75	
19	1	Fe37Z	0	Metal	1.57	120	0.25
20	1	Fe37Z	0	Metal	1.57	119.75	
21	1	Fe37Z	0	Rubber	3.16	164.5	0.00
22	1	Fe37Z	0	Rubber	3.16	164.5	
23	1	Fe37Z	0	Rubber_hole	3.16	163.5	0.00
24	1	Fe37Z	0	Rubber_hole	3.16	163.5	
25	1	Fe37Z	0	Ne1050	1.57	133.25	0.50
26	1	Fe37Z	0	Ne1050	1.57	133.75	
27	1	Fe37Z	0	Ne1150	1.57	135	0.00
28	1	Fe37Z	0	Ne1150	1.57	135	
29	1	Fe37Z	0	Ne1300	1.57	133	0.00
30	1	Fe37Z	0	Ne1300	1.57	133	
31	1	Fe37Z	0	Nylon	1.57	134	0.00
32	1	Fe37Z	0	Nylon	1.57	134	
33	0.8	Fe37	0	Metal	1.57	121.25	0.00
34	0.8	Fe37	0	Metal	1.57	121.25	0.00
35	0.8	Fe37	90	Metal	1.57	121.25	
36	0.8	Fe37	0	Rubber	3.16	165	0.25
37	0.8	Fe37	0	Rubber	3.16	164.75	
38	0.8	Fe37	90	Rubber	3.16	165	
39	0.8	Fe37	0	Rubber_hole	3.16	164	0.75
40	0.8	Fe37	0	Rubber_hole	3.16	164.75	
41	0.8	Fe37	90	Rubber_hole	3.16	163.25	
42	0.8	Fe37	0	Ne1050	1.57	133.75	0.00
43	0.8	Fe37	0	Ne1050	1.57	133.75	
44	0.8	Fe37	90	Ne1050	1.57	133	
45	0.8	Fe37	0	Ne1150	1.57	133.5	0.00
46	0.8	Fe37	0	Ne1150	1.57	133.5	
47	0.8	Fe37	90	Ne1150	1.57	135	
48	0.8	Fe37	0	Ne1300	1.57	133	0.00
49	0.8	Fe37	0	Ne1300	1.57	133	
50	0.8	Fe37	90	Ne1300	1.57	133.5	
51	0.8	Fe37	90	Nylon	1.57	133	
52	0.8	Fe37	0	Nylon	1.57	133.5	0.50
53	0.8	Fe37	0	Nylon	1.57	133	

Table 4. 9: experimental results in terms of final bend angle.

The main objective of the experiments is the comparison of the obtainable bend angle respect to the used technology (tool solutions). In Figure 4. 9 it can be observed that the values of the bend angles can be divided in three macro groups: metal (grey), plastics (green) and rubber (yellow). This result has been anticipated by the consideration made in chapter 1 when the stiffness of the materials has been compared by giving back the same grouping. Inside the domain of the polyurethane materials the Necuron 1050 and Necuron 1300 show smaller variability respect to the Nylon and the Necuron 1150 (Figure 4. 9). This behaviour can be connected to the reinforcement inserted inside Necuron 1050 and 1300.

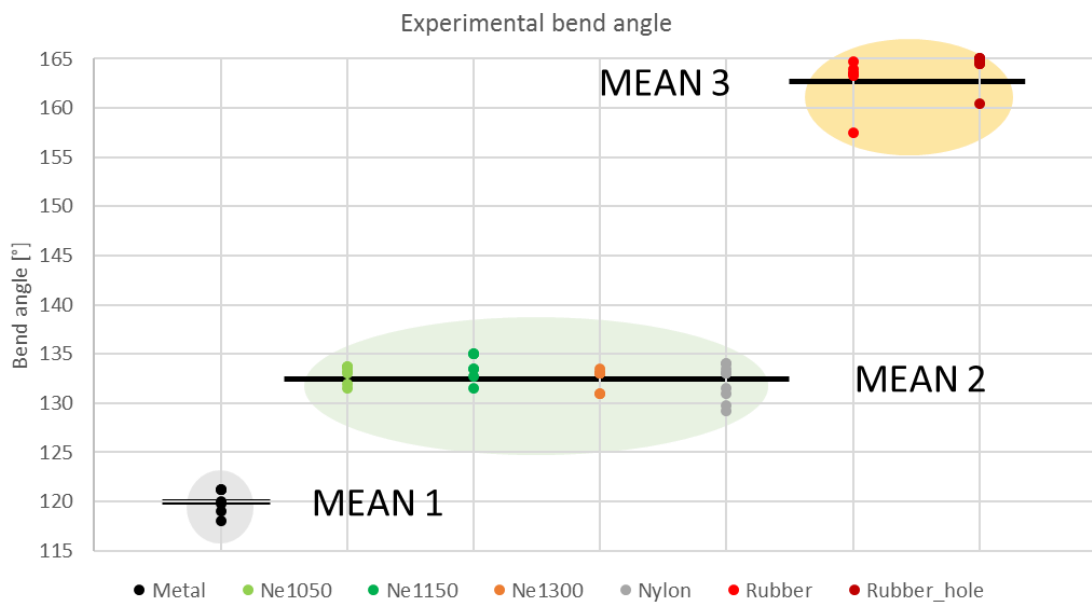


Figure 4. 9: bend angle results grouped by tools technology.

Considering the material groups identified in Figure 4. 9 a total of three mean angles can be calculated.

The metal solution (grey group) has a mean value of 120.07° (MEAN 1), which is in agreement with the criteria used for calculating the punch stroke by the numerical control of the press break. The mean value of the polymers solutions (green group) is 132.79° (MEAN 2), which is 10% higher with respect to the metal one, due to the local deformability of the polymer inserts.

For the rubber tools, it can be observed that for a punch stroke of 3.16 mm, the mean angle is 163.63° (MEAN 3), which value is so different respect to the values reached by the polymers and metal tools. This result demonstrates that the behaviour of the rubber tools is completely different from the polyurethane and metal ones, due to the hyper-elasticity of the material and to the different bending process mechanism.

The sheet metal bending with rubber tools is more similar to bottoming process where the bending tools reach the closure at the end of the process and the blank is in contact with them along its entire surface.

In Figure 4. 10, Figure 4. 11 and Figure 4. 12, the scatterplots of the tests made at the same condition has been presented only for the polymers solution in order to better show the differences between the rapid tools and the commercial nylon solutions.

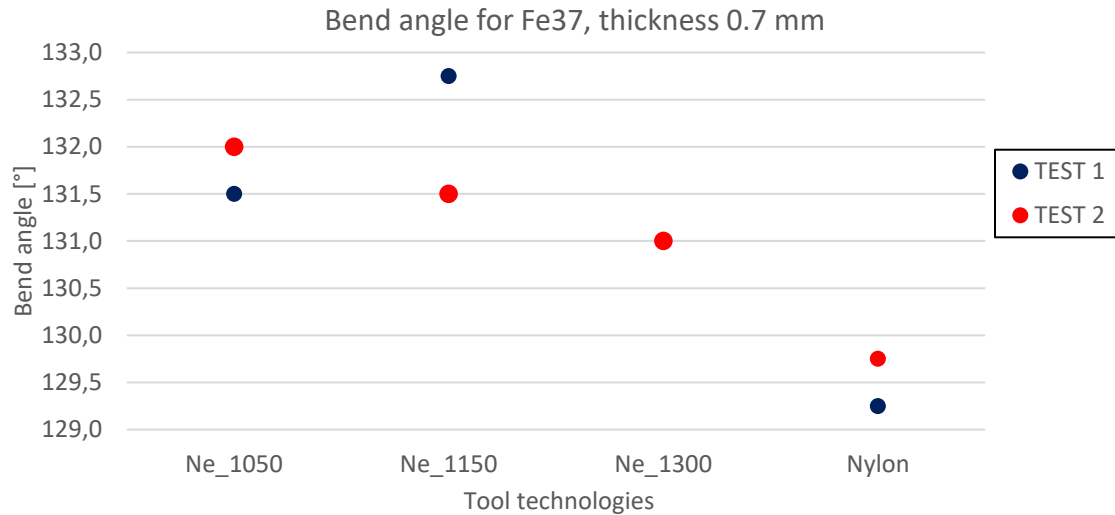


Figure 4. 10: measured bend angle of experiments made by Fe37 with thickness 0.7 mm.

In Figure 4. 11, the experiments with Necuron 1150, Necuron 1300 and Nylon dies showed very good repeatability so the results of Test 1 and Test 2 are overlapped. The Test 3 values, shown in Figure 4. 12, represents the experiment executed with specimens having rolling direction of 90°. Indeed, The bend angles measured for the experiments named test 3 in Figure 4. 12 show relevant deviations respect to Test 1 and Test 2 due to the effect of the different rolling direction of the blank, which effect has been observed also in other activities **Errore. L'origine riferimento non è stata trovata..**

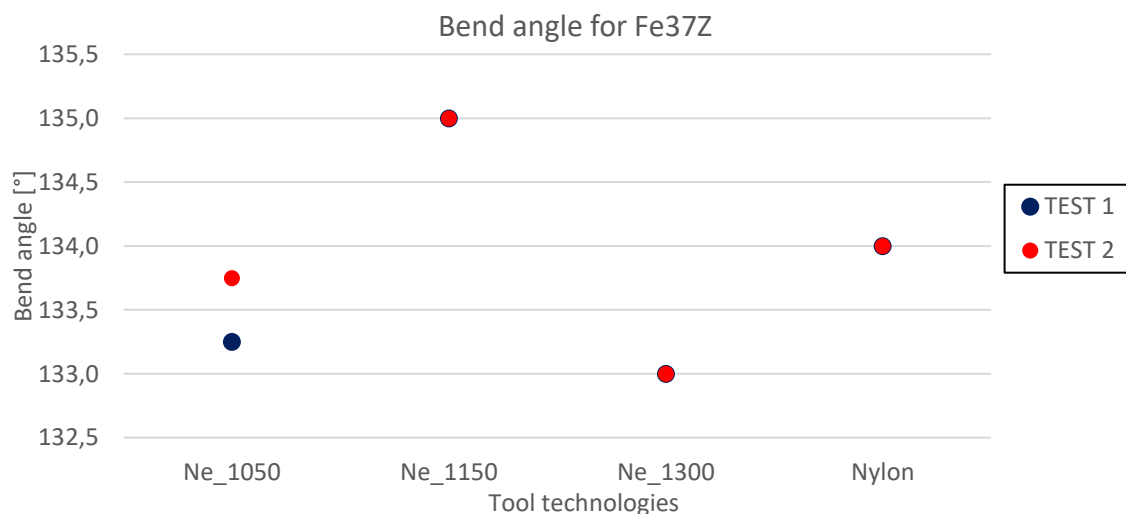


Figure 4. 11: measured bend angle of experiments made by Fe37Z with thickness 1 mm.

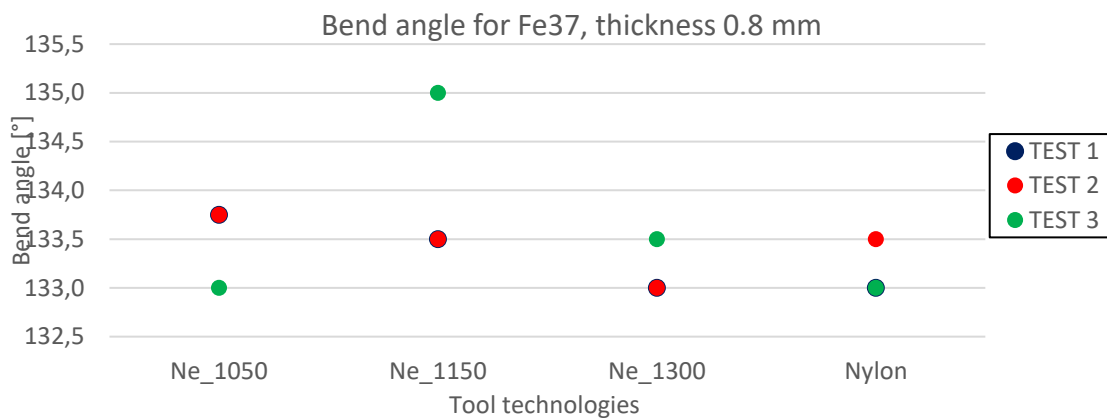


Figure 4. 12: measured bend angle of experiments made by Fe37 with thickness 0.8 mm.

After a first look of the bend angles measured from the experiment performed on the polymeric inserts (Nylon, Necuron 1050, Necuron 1150 and Necuron 1300), a statistical regression analysis with the software Minitab 17 has been performed only on the polyurethane inserts (Necuron 1050, Necuron 1150 and Necuron 1300) in order to calculate a statistical standard deviation of the process. The extracted bend angles have been reported in Table 4. 10.

Thickness	Material	Rolling direction	Necuron	Punch stroke	α_{exp}
0.7	Fe37	90	1050	1.57	131.5
0.7	Fe37	90	1050	1.57	132
0.7	Fe37	90	1150	1.57	132.75
0.7	Fe37	90	1150	1.57	131.5
0.7	Fe37	90	1300	1.57	131
0.7	Fe37	90	1300	1.57	131
1	Fe37Z	0	1050	1.57	133.25
1	Fe37Z	0	1050	1.57	133.75
1	Fe37Z	0	1150	1.57	135
1	Fe37Z	0	1150	1.57	135
1	Fe37Z	0	1300	1.57	133
1	Fe37Z	0	1300	1.57	133
0.8	Fe37	0	1050	1.57	133.75
0.8	Fe37	0	1050	1.57	133.75
0.8	Fe37	90	1050	1.57	133
0.8	Fe37	0	1150	1.57	133.5
0.8	Fe37	0	1150	1.57	133.5
0.8	Fe37	90	1150	1.57	135
0.8	Fe37	0	1300	1.57	133
0.8	Fe37	0	1300	1.57	133
0.8	Fe37	90	1300	1.57	133.5

Table 4. 10: experimental results of the specimen bended with Necuron inserts.

In the regression analysis, the thickness and the rolling direction have been considered as continuous predictors, instead the material and the Necuron type as categorical predictors. In the regression the interactions and the factors until the square order have been considered; the data have been filtered using the Stepwise method implemented in the software with α equal to 0.05 as a removal and entering criterion. The results of the analysis of variance have been reported in Table 4. 11. The R^2 of the analysis is 90.84% which means that the regression model underestimates the standard deviation of the process. The normal distribution of the residual has been showed in Figure 4. 13 and the sparse distribution of the residual versus the fitted values is showed in Figure 4. 14. The standard deviation of 0.339° can be calculated as the square root of the mean square error.

Source	DF	Adj SS	Adj Ms	F-Value	P-Value
Regression	9	26.5104	2.9456	23.04	0
Thickness	1	4.9603	4.9603	38.8	0
Rol_dir	1	0.1808	0.1808	1.41	0.259
Material	1	6.8571	6.8571	53.64	0
Tool	2	1.9475	0.9738	7.62	0.008
Thickness*Tool	2	2.3819	1.191	9.32	0.004
Rol_dir*Tool	2	1.5997	0.7999	6.26	0.015
Error	11	1.4062	0.1278		
Lack-of-Fit	2	0.375	0.1875	1.64	0.248
Pure Error	9	1.0313	0.1146		
Total	20	27.9167			

Table 4. 11: analysis of variance coming from the regression analysis.

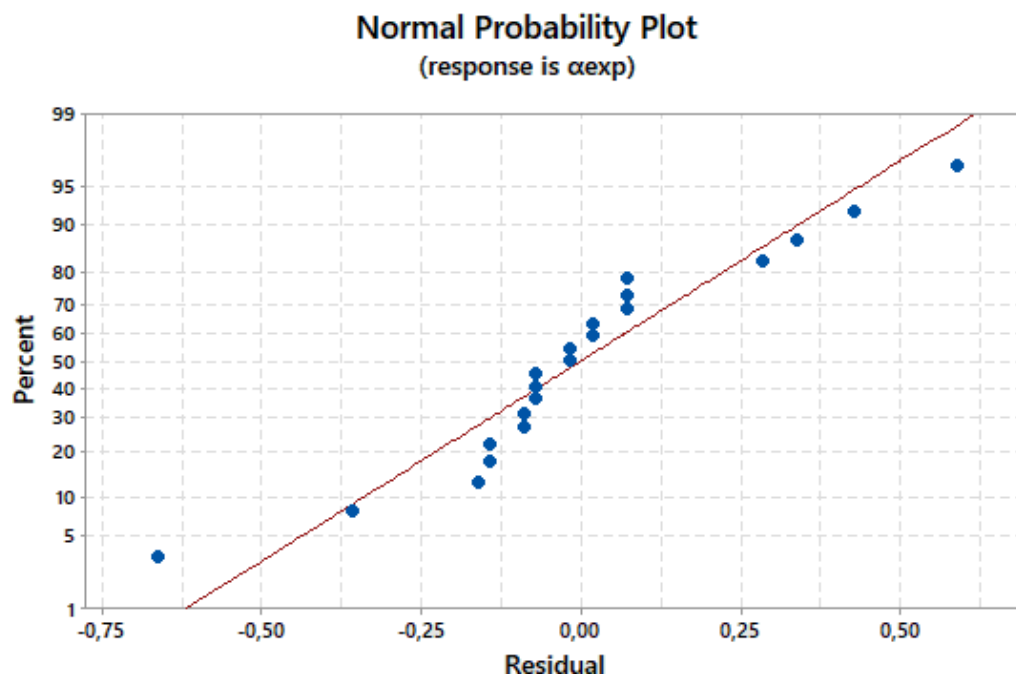


Figure 4. 13: normal distribution of the residuals.

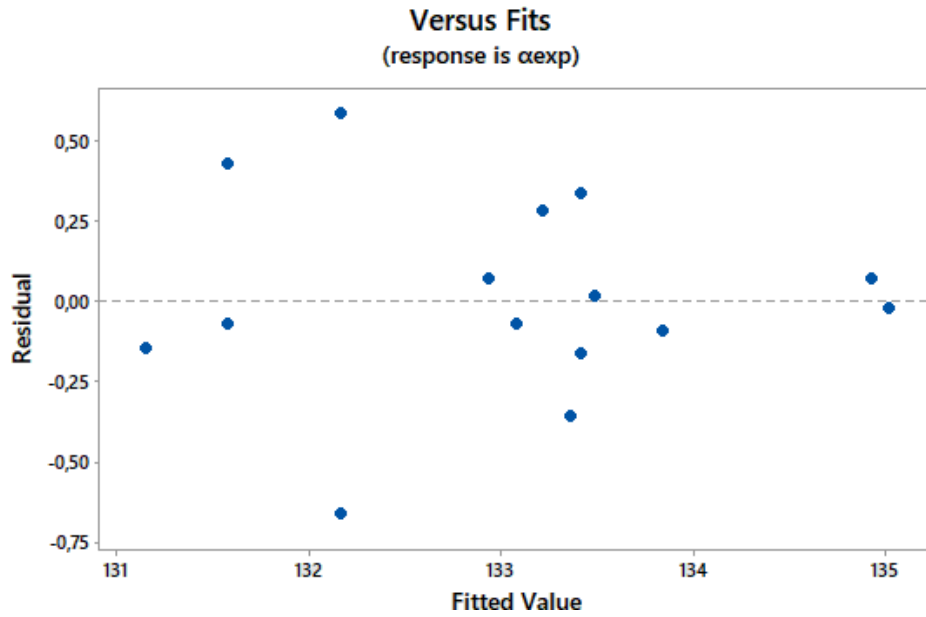


Figure 4. 14: distribution of the fitted vales versus residuals.

The analysis of variance showed the relevance of the interaction between the thickness and the tools and the interaction with the rolling direction and the tools. This result has been highlighted in the interaction plots shown in Figure 4. 15 and Figure 4. 16. Another interesting result which can be observed in the interaction plots is the line slope of Necuron 1150. This effect suggests that the experimental angle is more sensitive to the variation of thickness and rolling direction when the specimen is bended with Necuron 1150 insert, so the performance of this material are lower respect to the other two materials (Necuron 1050 and 1300) in terms of the stability of the process result.

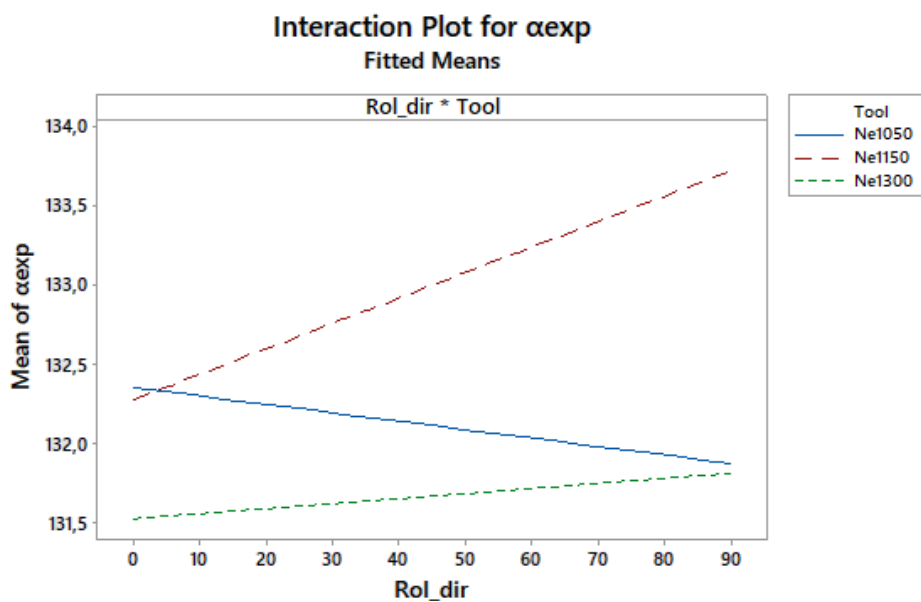


Figure 4. 15: interaction plot of the angle versus the rolling direction at different insert materials.

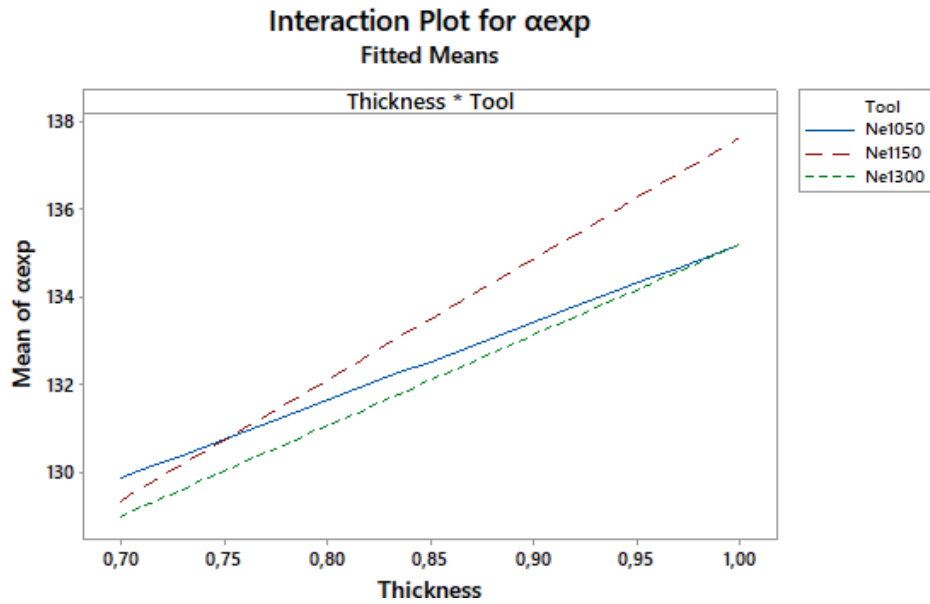


Figure 4. 16: interaction plot of the angle versus the thickness at different insert materials.

The result of a bending process is not limited only on the resultant bend angle. In some applications, the aesthetical results are also fundamental in terms of presence of scratches on the blank surface.

As expected, all the specimens bent with metal tools presented scratches near the round zone, due to the contact between the blank surface and the rigid metal die (Figure 4. 17). The polymer dies are normally used when aesthetical defects are not allowed, but surprisingly some specimen bent with the nylon die presented soft scratches on the surface zone in contact with the nylon surface (Figure 4. 18). Instead, no specimens bent with polyurethane and rubber dies presented scratches or other aesthetical defects on the external surface (from Figure 4. 19 to Figure 4. 23).

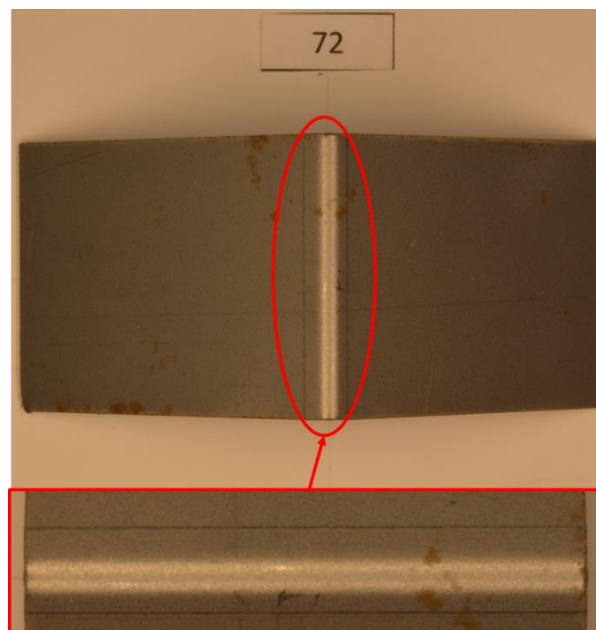


Figure 4. 17: example of aesthetical defects on a specimen bent with metal tool.

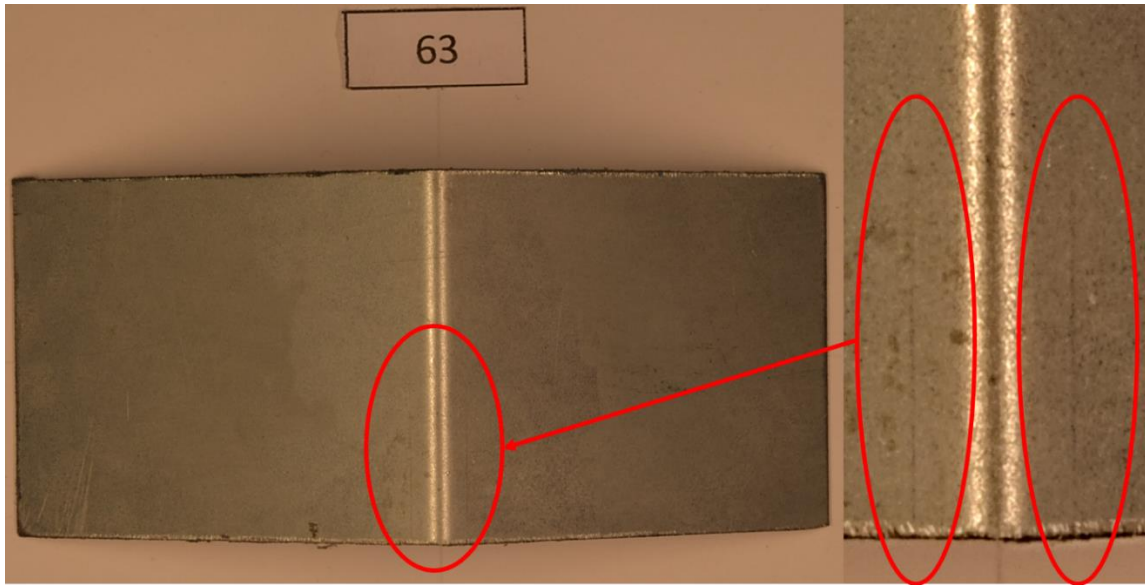


Figure 4. 18: example of aesthetical defects on a specimen bent with nylon insert (white) tool.

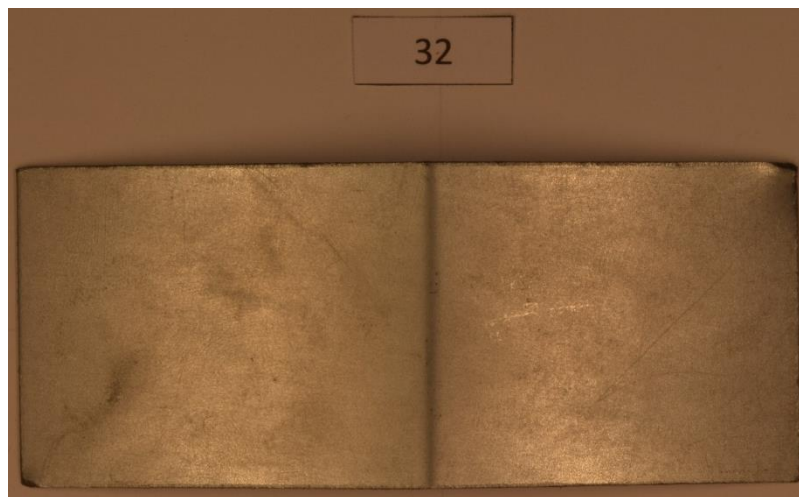


Figure 4. 19: specimen 32 bent with rubber tool with no defects.



Figure 4. 20: specimen 33 bent with drilled rubber tool with no defects.



Figure 4. 21: specimen 41 bent with die Necuron 1050 with no defects.



Figure 4. 22: specimen 51 bent with die Necuron 1150 with no defects.



Figure 4. 23: specimen 61 bent with die Necuron 1300 with no defects.

During the experimental activities, two marks have been drawn on the polyurethane and rubber dies in order to perform the bending operations always in the same position of the tools (bending zone). This operation allowed evaluating if the performed bending operations could deform or leave some scratches on the inserts surface. As supposed from the results of the fatigue tests described in chapter 3, no relevant plastic deformations have been observed on the polyurethane inserts. Very soft scratches have been observed on the corners of the V-shape cavity, due to the sliding with the blank surface. The sliding between the blank surface and the polyurethane inserts deforms microscopically the corners of the V-shape cavity by making it more rounded. This phenomenon can affect the results in terms of repeatability of the bend for large batches, so it should be deeper explored with larger experimental plan. The scratches have been observed only on one side of the V-shape cavity, these asymmetrical defects can be linked to a non-correct positioning of the tools on the press break.

In Figure 4. 24, the top view of the V cavity of the Necuron 1050 insert has been presented. It can be noted that no particular differences can be observed between the bending zone, where the specimens have been bended, and the rest of the insert surface (unbending zone), where no bending operations have been performed. Instead, in Figure 4. 25, some scratches can be observed in the bending zone on the top view of the V cavity of Necuron 1150 insert. Normally the scratches should be present on both side of the die V cavity, because the sliding of the blank should be symmetric during the bending process. The presence of scratches only on one side of the V cavity suggests that a positioning error has been done during the experiments. Similar result can be observed also in Figure 4. 26 for the Necuron 1300.

The rubber dies have been marked by the punch along all their surfaces, due to the bottoming mechanism described before which makes indistinguishable the bending and the free zone of the insert (Figure 4. 27). At the end, very pronounced scratches have been observed on the nylon die (Figure 4. 28) which suggest very high tendency of wearing mechanism of this kind of material.

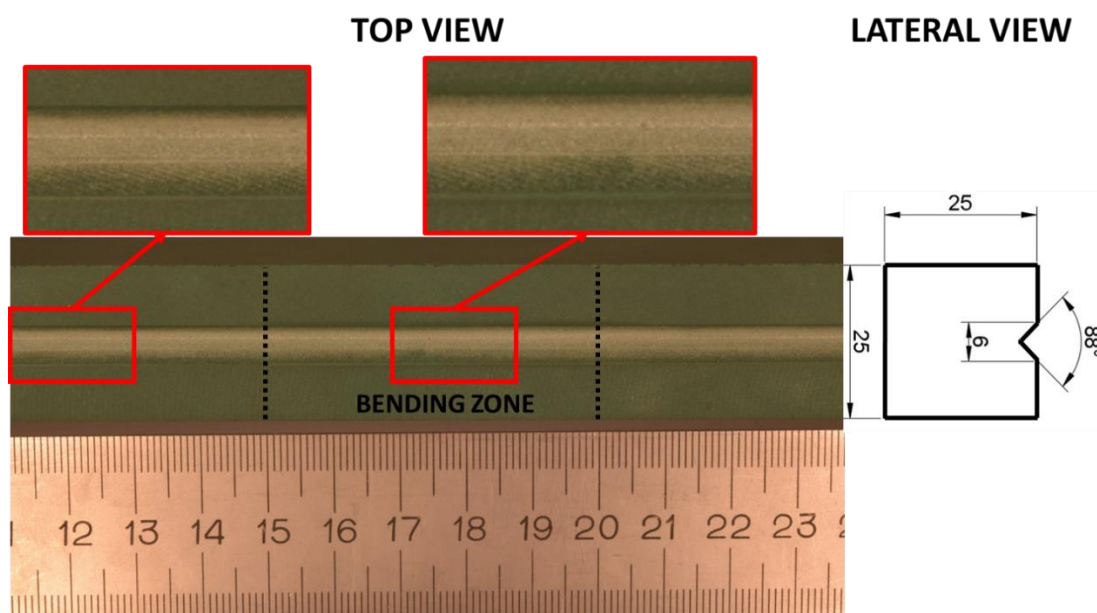


Figure 4. 24: comparison of the bending zone and the free zone of the Necuron 1050 insert.

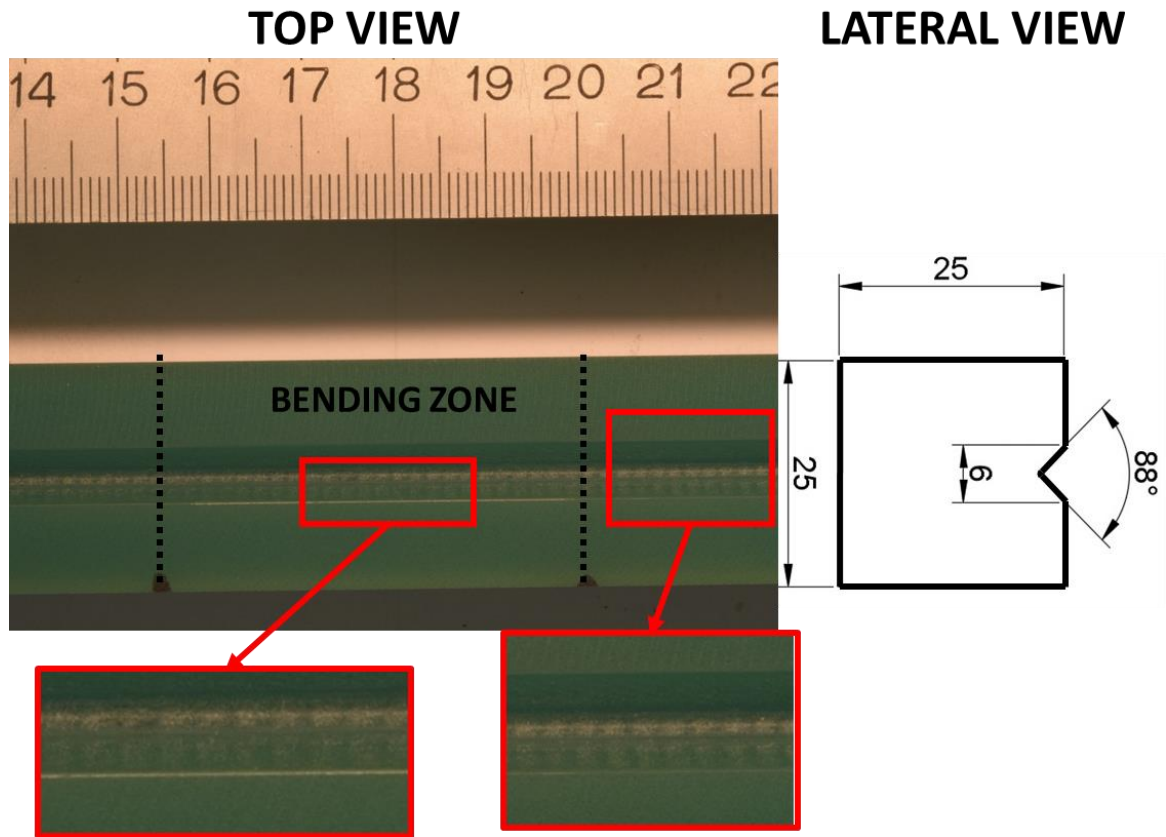


Figure 4. 25: comparison of the bending zone and the free zone of the Necuron 1150 insert.

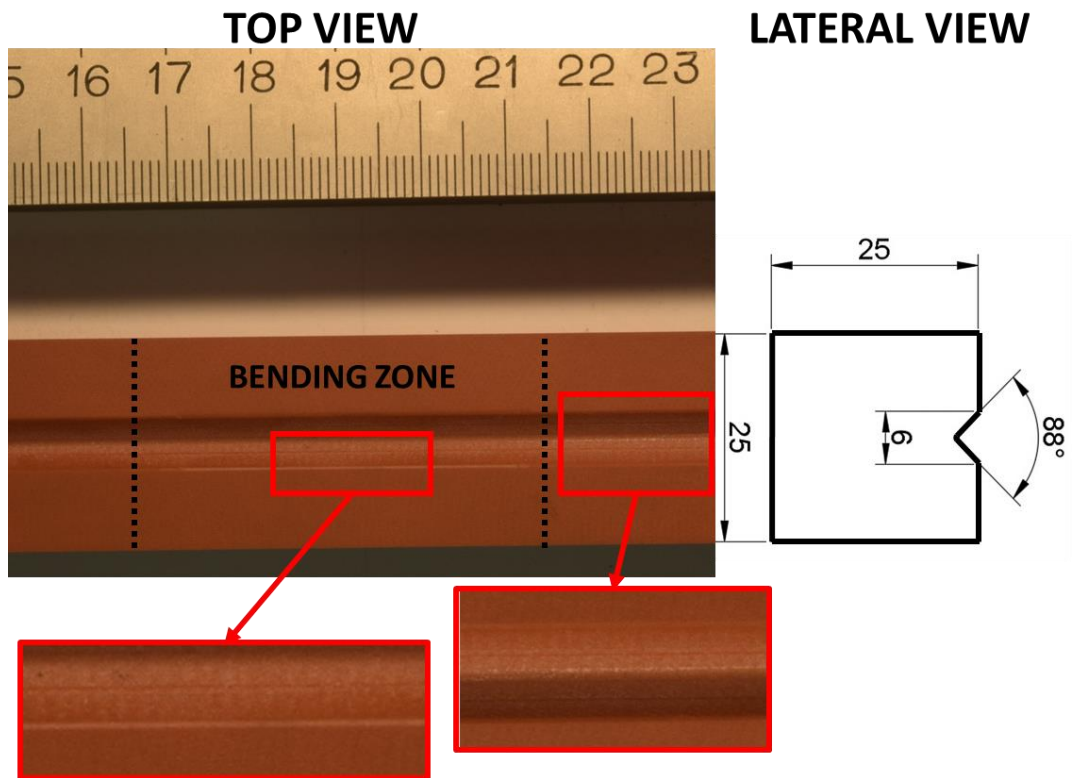


Figure 4. 26: comparison of the bending zone and the free zone of the Necuron 1300 insert.

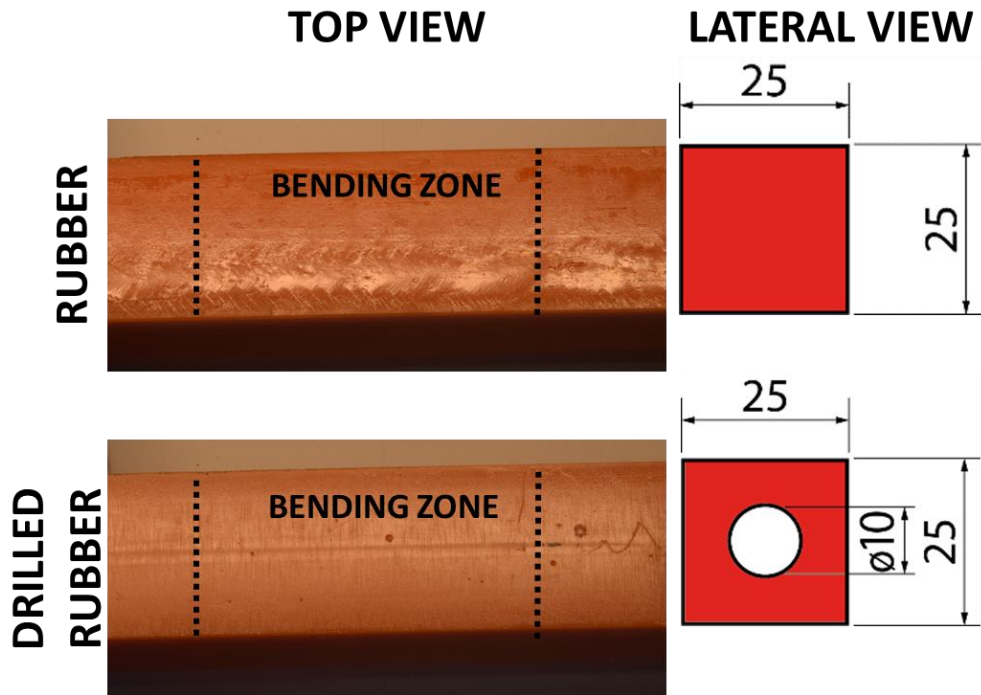


Figure 4. 27: rubber (a) and rubber drilled (b) dies marked by the punch.

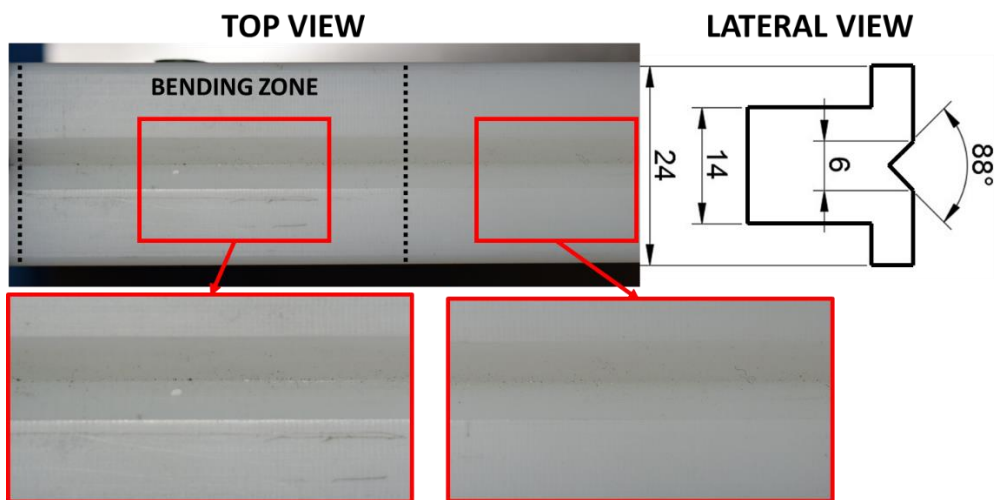


Figure 4. 28: nylon die after the experimental activities.

After the execution of the experimental plan described in Table 4. 9, a batch of 15 specimens has been used for a repeatability tests.

The repeatability test consist in 15 specimens bent at the same condition of punch stroke of 1.57 mm with the same die insert of Necuron 1050. The insert material has been chosen for testing the performances of the cheaper polyurethane available. The results of the 15 tests are reported in Table 4. 12 and in Figure 4. 29.

From a first look, the measurement bend angles coming from the repeatability tests showed a large variability in a rage within $[139; 138]^{\circ}$. However, the standard

deviation of 0.306° (Table 4. 12) is compatible with the 0.339 obtained from the statistical analysis performed on the bend angles of the specimens bended with Necuron inserts. This compatibility suggests that the obtained values could be the natural standard deviation of the bending process with the polyurethane inserts.

Specimen	Bend angle	Punch stroke	Mean	Standard deviation
1	139.00°	1.57 mm	138.77°	0.306°
2	139.00°			
3	138.75°			
4	139.00°			
5	139.00°			
6	139.00°			
7	138.75°			
8	139.00°			
9	138.50°			
10	138.50°			
11	139.00°			
12	138.50°			
13	138.50°			
14	139.00°			
15	138.00°			

Table 4. 12: results of the repeatability test plan.

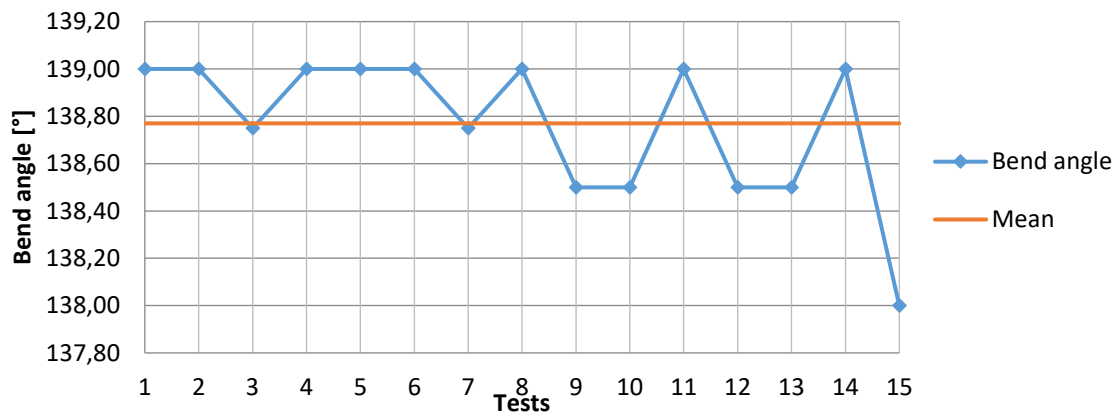


Figure 4. 29: trend of the measured bend angle in the repeatability test plan performed with the die insert of Necuron 1050.

These standard deviations have been also compared with the one obtained from a statistical analysis performed on a batch of 23 experiments extracted from a bigger plan of 288 sheet metal bending experiments performed in collaboration with AMADA Engineering EU in an another project **Errore. L'origine riferimento non è stata trovata..** The calculation of the standard deviation of 0.301° of the 23 experiments has been described in Appendix C. The three standard deviations obtained from the experimental plan, repeatability tests and AMADA experiments are very similar to

each other. This results demonstrates that the performances of the polyurethane tools are very similar with the metal ones in terms of the variability of the process.

In conclusion, the results of the experimental activities are very interesting in terms of the achieved values and process investigations.

The different bend angle results demonstrate the different behaviour of the die materials involved. The three main die material domains (metal, plastics and rubber) can be easily identified inside the sets of the angles measurements. The nylon commercial solution gives back similar results respects to the polyurethane dies in terms of bend angles, so an introduction of the polyurethane inserts in the industrial bending tools scenario can be expected, especially if the high machinability of the polyurethane is considered.

The results achieved with the rubber dies suggests that different approaches based on FEM simulation must be used for studying the behaviour of this kind of tools.

The repeatability tests and the comparison of the standard deviations give back interesting results for deeper investigations in the future.

4.5 FEM model

4.5.1 Geometry and mesh

The FEM model has been implemented with the commercial code PAM-STAMP 2G V2015.1, which allows defining the rectangular geometry of the blank directly in the graphical unit interface in a parametric way.

The solid models of the tools have been generated with reverse engineering operations by measuring, in order to reach better precise results from the simulation models:

1. the external dimensions of the deformable inserts;
2. the width of the V-shape cavity of the dies, for polymers tools;
3. the positioning of the hole in the drilled rubber insert.

The measurements of the external dimensions have been performed with a micrometre. In order to measure the width of the V-shape cavity, each polymeric tool has been positioned on a platform, manually moved along x and y planar directions with micrometric slides, where a dial indicator has been mounted for measuring the z vertical direction (Figure 4. 30a, Figure 4. 30b, Figure 4. 30c). The movement of the platform along the y direction (Figure 4. 30d) allowed the dial indicator to identify, with the oscillation of the needle, the vertexes of the V-shape (point 1 and 2 in figure). The measurement of the transversal movement of the platform allowed to measure the distance between the identified vertexes, corresponding to the width of the V-shape cavity (Figure 4. 30d).

The measured dimensions of the rigid metal die T80.06.88, the metal frameworks MPG25 (used for rubber and polyurethane inserts) and TN80.14 (for nylon insert) and the punch P97.88.r08 complied with the scheme presented in Figure 4. 31.

The dimensions deformable inserts shown small deviations from the nominal ones already presented in Figure 4. 5b, Table 4. 5 and Figure 4. 6b. The deviations of the dies width respect to the nominal ones can affect the process results in terms of bend angle [1]. The dimensions of the measured inserts have been presented in Figure 4. 32.

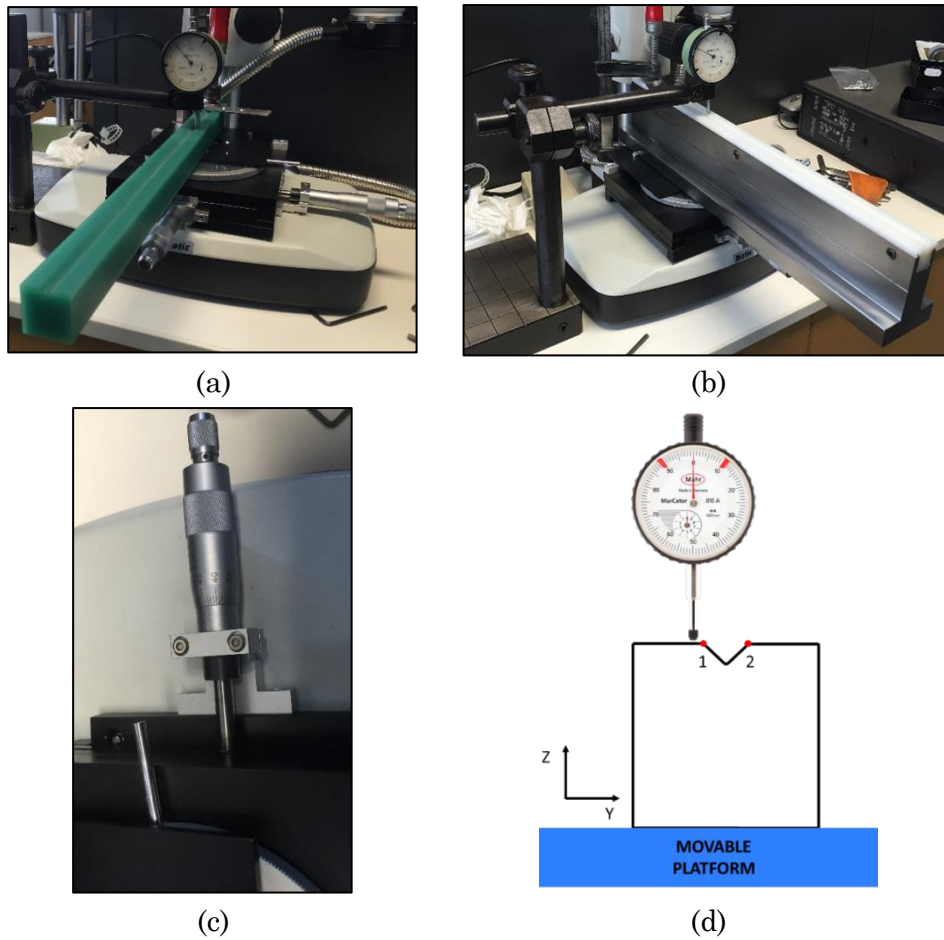


Figure 4. 30: positioning of the Necuron 1150 (a) and nylon (b) inserts on the platform moved with micrometric slides (c) and the scheme of the measuring operation (d).

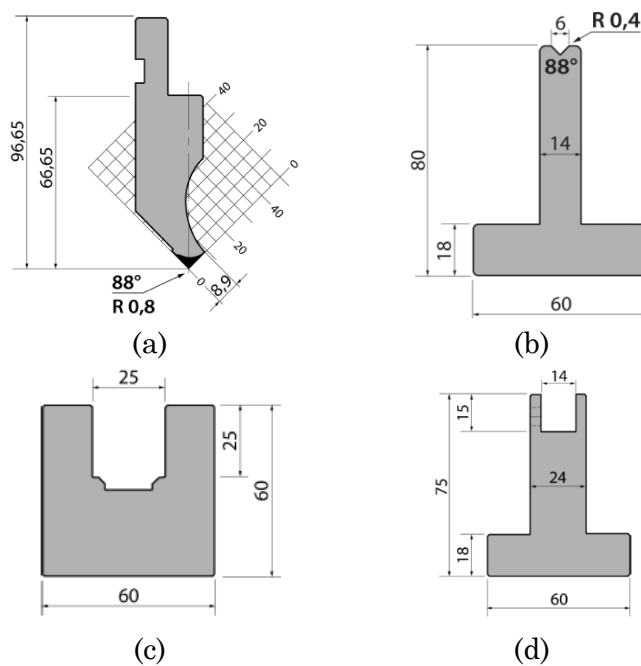


Figure 4. 31: main dimensions of the metal tools: punch (a), die (b), metal framework for polyurethane and rubber inserts (c) and framework for nylon insert (d).

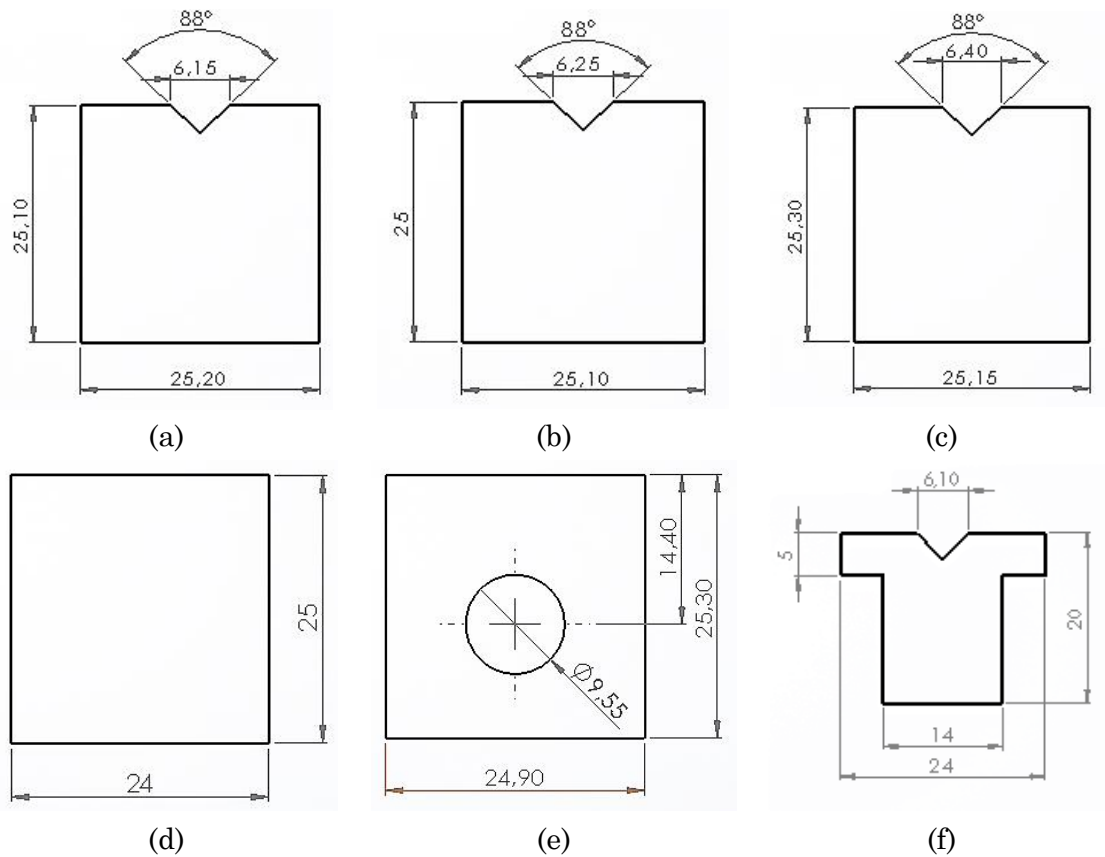


Figure 4. 32: measured dimensions of the inserts made by Necuron 1050 (a), 1150 (b), 1300 (c), Rubber (d), drilled rubber (e) and Nylon (f).

The metal tools presented in Figure 4. 31 have been meshed with for noded shell elements and the constraint of rigid body has been imposed. In order to reduce the dimension of the simulation model, only the surfaces in contact with the blank and the inserts have been considered in the mesh generation of the metal tools (Figure 4. 33).

The polymer inserts (Necuron and Nylon) have been meshed with four noded tetrahedral elements by using the same methodology described in chapter 3. Instead, the rubber tools have been meshed with eight noded hexahedral elements in order to better describe per non-linear hyper elastic behaviour of the rubber material [3].

The dimensions of the rectangular blank are 50x25 mm, due to the double symmetry, and the surface area of each initial element is 100 mm² with a total number of 10 initial elements. The shell elements chosen for the blank have 4 nodes with three degrees of freedom in translation and three degrees of freedom in rotation and bi-linear interpolation polynomials, the same elements formulation used for simulate the aluminium blank in chapter 3. Refinement will be also applied to the blank in order to split each quadrangular element into five smaller quadrangular shells, by an automatic refinement algorithm. In Figure 4. 33, the schematizations of all simulations setup have been presented, for the polyurethane solutions (Necuron 1050, 1150 and 1300); only one general setup has been shown. Double symmetry has been applied on planes XY and YZ (Figure 4. 33). The number of elements and nodes for each object has been resumed in Table 4. 13.

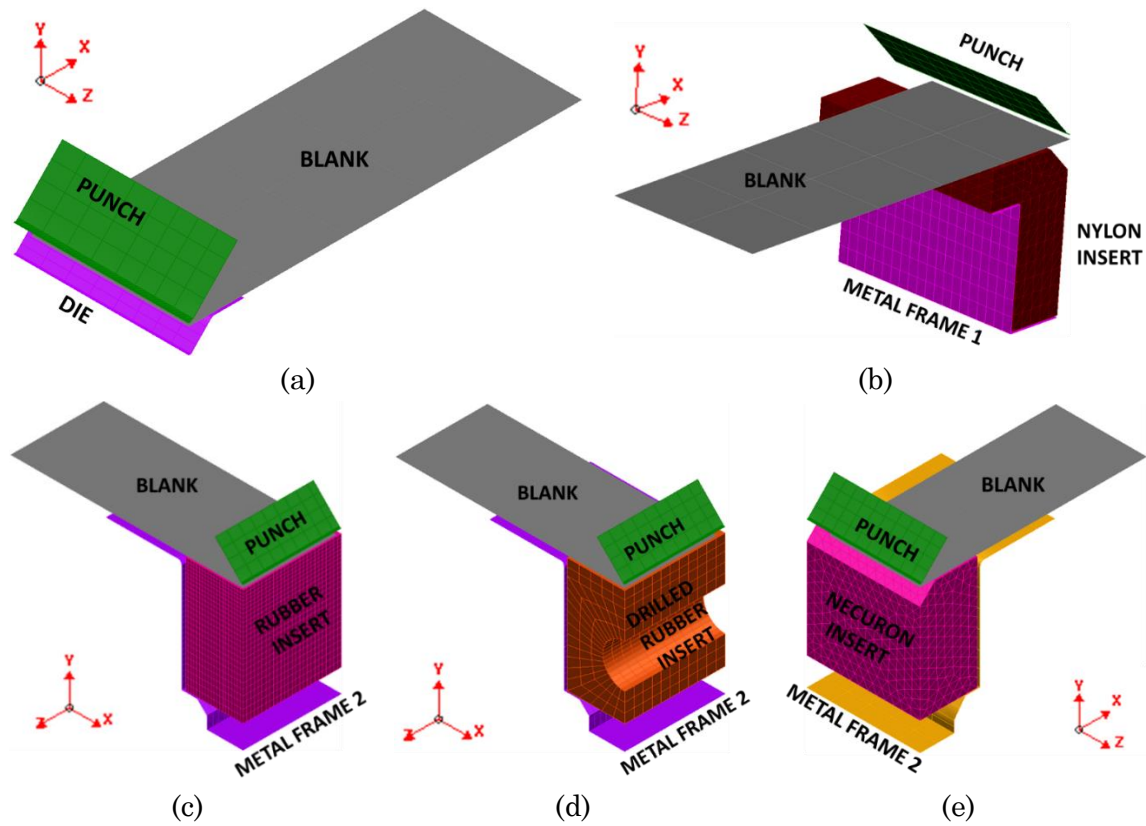


Figure 4. 33: schematization of the simulations setup with metal tools (a), nylon die (b), rubber die (c), drilled rubber die (d) and Necuron die (e).

Tool	Body type	Elements type	N. elements	N. nodes
Punch	Rigid	Shell	162	190
Metal Die	Rigid	Shell	128	153
Blank	Deformable	Shell	10	18
Nylon insert	Deformable	Tetrahedral	4045	1056
Metal frame 1	Rigid	Shell	320	357
Rubber insert	Deformable	Hexahedral	13000	14742
Drilled rubber insert	Deformable	Hexahedral	770	1152
Metal frame 2	Rigid	Shell	120	150
Necuron insert	Deformable	Tetrahedral	6406	1504

Table 4. 13: number of elements and nodes used for meshing the object of the simulations.

4.5.2 Material properties

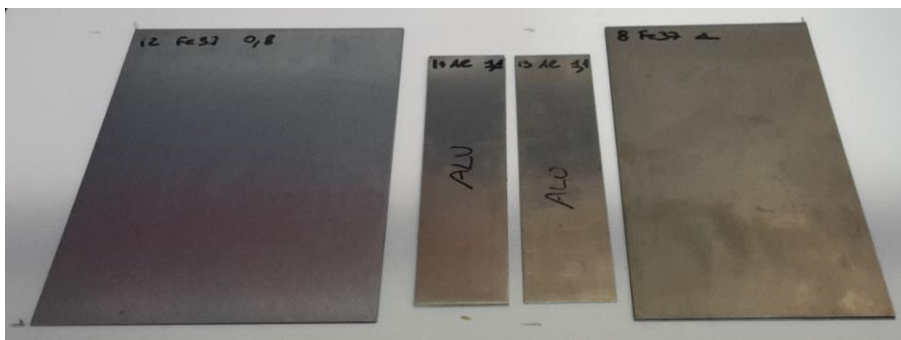
The material characterization has been performed only for blank materials and rubber insert. The nylon material has not been mechanical characterized due to the reduced dimension of the nylon insert. For this reason the material parameters of the Nylon

insert have been retrieved in the “CES EduPack” (Table 4. 14) material database using as input the material code “Nylon6” given by the company.

The characterization of the Necuron inserts has been already presented in chapter 2. The profile of the blank specimen have been cut by waterjet (Figure 4. 34).

Material	Young Modulus (E)	Yield Stress (R _s)	Peak Stress (R _m)	Elongation (A%)	Poisson coeff (ν).	Density (ρ)
	[MPa]	[MPa]	[MPa]	[%]		[g/cm ³]
Nylon 6	2500	55	67.8	60	0.4	1.15

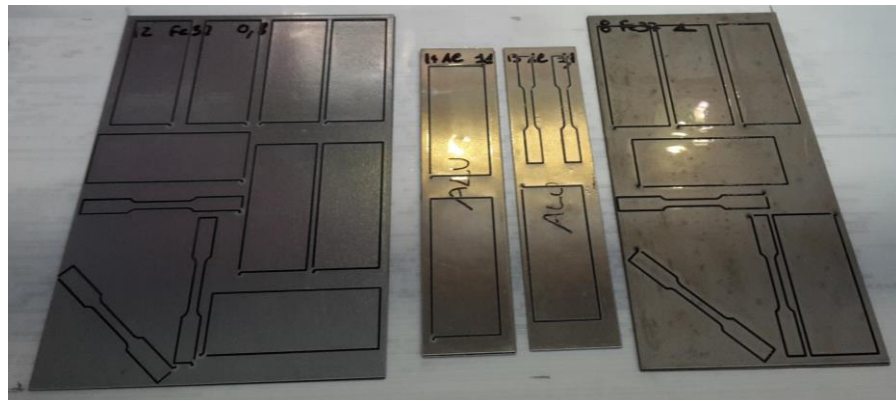
Table 4. 14: material properties of the Nylon insert.



(a)



(b)



(c)

Figure 4. 34: blank before (a) the waterjet cutting operation (b) and after (c).

The dimensions of the subsize specimens according to the standard [5] are presented in Figure 4. 35.

The waterjet process has been preferred to the laser cut in order to prevent any alterations of the metallurgical morphology of the material for the anisotropy tests.

The waterjet process parameters used for cutting the tensile specimens are resumed in Table 4. 15.

The rolling direction of the specimens has been chosen according with the Figure 4. 36. The anisotropy has been evaluated only for the specimen made by Fe37 and Fe37Z, because the aluminium was annealed (1050-O). The tensile test have been performed with MTS Alliance RT/100 (Figure 4. 37a) tensile machine and the elongation of the specimens has been measured with an extensometer MTS 634.12F-54 (Figure 4. 37b). The material data resultant from the tensile tests have been resumed in table, and the complete numerical and graphic results have been reported in the appendix. The Krupkowsky's constitutive law has not been used this time, due to the availability of the complete Hardening curve obtained directly from the tensile tests.

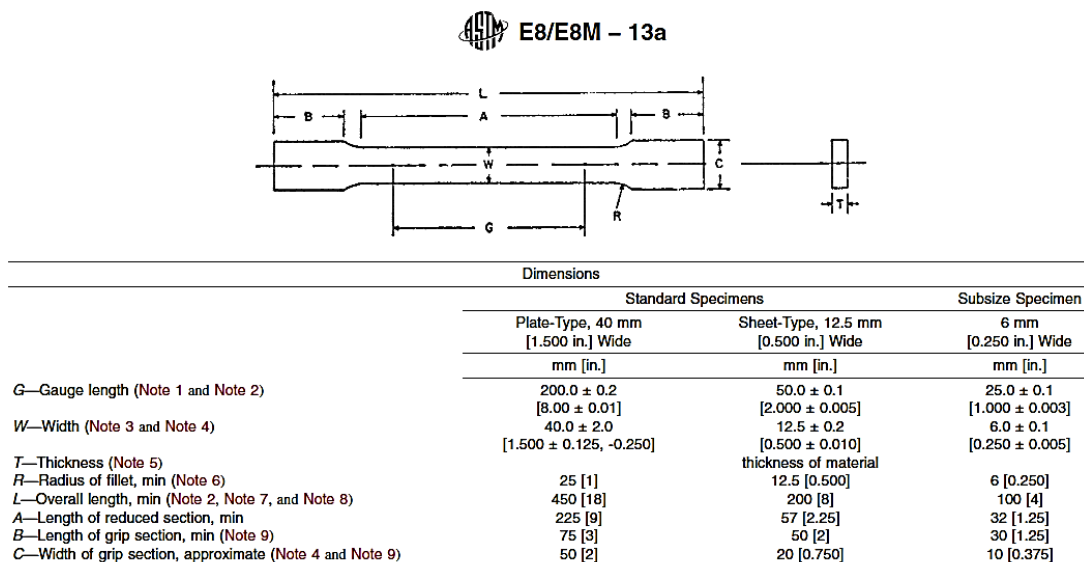


Figure 4. 35: tensile specimen dimensions cited in the standard ASTM E8.

Parameter	Value
Nozzle diameter	0.33 mm
Focuser diameter	1.02 mm
Abrasive flow rate	350 g/min
Abrasive dimension	300-150 μ m
Pressure	380 MPa
Feed rate	600 mm/min

Table 4. 15: process parameters of the waterjet operation.

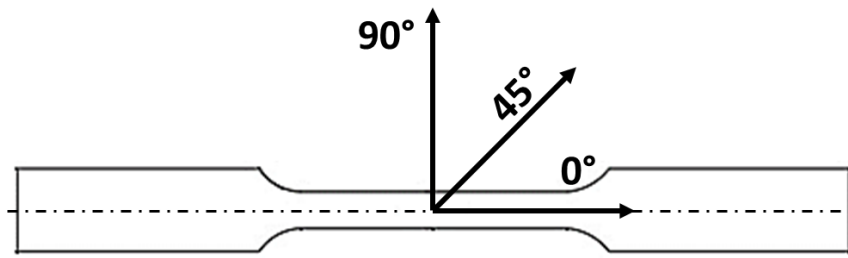


Figure 4. 36: references for the rolling direction of the tensile specimens.



(a)



(b)

Figure 4. 37: machine (a) and extensometer (b) used for tensile tests.

Material	Specimen ID	Rolling direction	Thickness	Young's Modulus (E)	Yield Stress (R _s)	Peak Stress (R _m)	Elongation (A%)
		[°]					
Fe37	1	0	0.7	102927	134	237	37.7
Fe37	2	45	0.7	138501	137	240	34.1
Fe37	3	90	0.7	151108	140	243	***
Fe37	4	0	0.7	109427	120	216	38.8
Fe37	5	45	0.7	144359	142	247	35.6
Fe37	6	90	0.7	130411	140	243	27.5
Fe37Zn	7	0	1.0	194807	180	283	27.5
Fe37Zn	8	45	1.0	203418	188	301	***
Fe37Zn	9	90	1.0	196840	189	300	29.1
Fe37	10	0	0.8	175125	258	307	27.4
Fe37	11	45	0.8	187058	269	331	24.2
Fe37	12	90	0.8	178782	257	323	26.3
Al	13	0	1.0	64283	104	203	15.1
Al	14	0	1.0	64534	99	194	15.3

Table 4. 16: material properties resultant from the tensile tests.

The anisotropy tests have been performed accordingly with the standard [6], where the specimens cut along different principal rolling direction must be pulled until reaching the 10% of elongation.

The anisotropy coefficient r_α along the general rolling direction α is defined as the ratio between the strain along the width (ε_w) and the strain along the thickness (ε_t) of the specimen:

$$r_\alpha = \frac{\varepsilon_w}{\varepsilon_t} \quad (4.1)$$

where ε_w and ε_t can be defined as the logarithm of the ratio between the final and the initial value of width (w) or thickness (t):

$$\varepsilon_w = \ln\left(\frac{w_f}{w_0}\right) \quad (4.2)$$

$$\varepsilon_t = \ln\left(\frac{t_f}{t_0}\right) \quad (4.3)$$

assuming the constancy of the volume for small deformations, the ratio t_f/t_0 can be written as:

$$\frac{t_f}{t_0} = \frac{l_0 w_0}{l_f w_f} \quad (4.4)$$

where l_0 and l_f are the initial and final length of the specimen, corresponding with the initial and final length of the extensometer. From these considerations, ε_t can be finally written as:

$$\varepsilon_t = \ln\left(\frac{l_0 w_0}{l_f w_f}\right) \quad (4.5)$$

In the Table 4. 17, the results of the anisotropy tests have been resumed. The initial and final measurement of the length l are the same for each specimen due the imposition of the 10% of strain as stop criteria of the tests, as requested in the standard [6]. Due to the low availability, only the specimens Fe37 with thickness 0.7 have been replicated 2 times for the anisotropy tests.

In literature, there are several polynomial models to represent hyper-elastic behaviour of the elastomers [7] which include the Arruda-Boyce, Mooney Rivlin, Neo-Hookean, Ogden, polynomial, reduced polynomial, Yeoh and Van der Waals.

The formulation implemented in Pam-Stamp is the Mooney-Rivlin polynomial model, which is normally used for rubber-pad forming simulations. In the Mooney Rivlin model, the strain energy potential W is defined as a function of strain invariants I :

Material	Thickness [mm]	w ₀ [mm]	w _f [mm]	l ₀ [mm]	l _f [mm]	r _α	Rolling direction [°]
Fe37	0.8	4.504	4.280	25	27.439	1.207	0°
Fe37	0.8	4.562	4.367	25	27.439	0.889	45°
Fe37	0.8	4.613	4.367	25	27.439	1.431	90°
Fe37	0.7	4.679	4.373	25	27.439	2.636	0°
Fe37	0.7	4.637	4.373	25	27.439	1.701	45°
Fe37	0.7	4.591	4.377	25	27.439	1.053	90°
Fe37	0.7	4.627	4.370	25	27.439	1.595	0°
Fe37	0.7	4.628	4.353	25	27.439	1.922	45°
Fe37	0.7	4.599	4.353	25	27.439	1.436	90°
Fe37Zn	1	4.473	4.177	25	27.439	2.804	0°
Fe37Zn	1	4.570	4.357	25	27.439	1.051	45°
Fe37Zn	1	4.562	4.273	25	27.439	2.365	90°

Table 4. 17: calculation of the anisotropy r₀, r₄₅ and r₉₀ coefficients.

$$\begin{aligned}
W &= W(I_1, I_2, I_3) \\
&= A(I_1 - 3) + B(I_2 - 3) \\
&\quad + W(I_3)
\end{aligned} \tag{4.6}$$

where A and B are material coefficient and W(I₃) is a penalty function for incompressibility (using ν=0,499: Poisson's ratio) [8]. The right Cauchy-Green strain invariants are defined as [9]:

$$I_1 = \lambda_1^2 + \lambda_2^2 + \lambda_3^2 \tag{4.7}$$

$$I_2 = (\lambda_1\lambda_2)^2 + (\lambda_2\lambda_3)^2 + (\lambda_1\lambda_3)^2 \tag{4.8}$$

$$I_3 = (\lambda_1\lambda_2\lambda_3)^2 \tag{4.9}$$

where λ_i are stretch ratios for the unit fibers that are initially oriented along the directions of three axis in the coordinate systems.

The A and B coefficient can be retrieved in literature or they can be calculated with a curve fitting data by using the least square method from experimental uniaxial or equi-biaxial tests [10]-[11].

The characterization of the rubber material has been performed with a compression test by following the standard [12]. The stress-strain curve coming from the compression test has been reported in Figure 4. 38. The compression test have been performed with the same machine described in chapter 2 at the same condition.

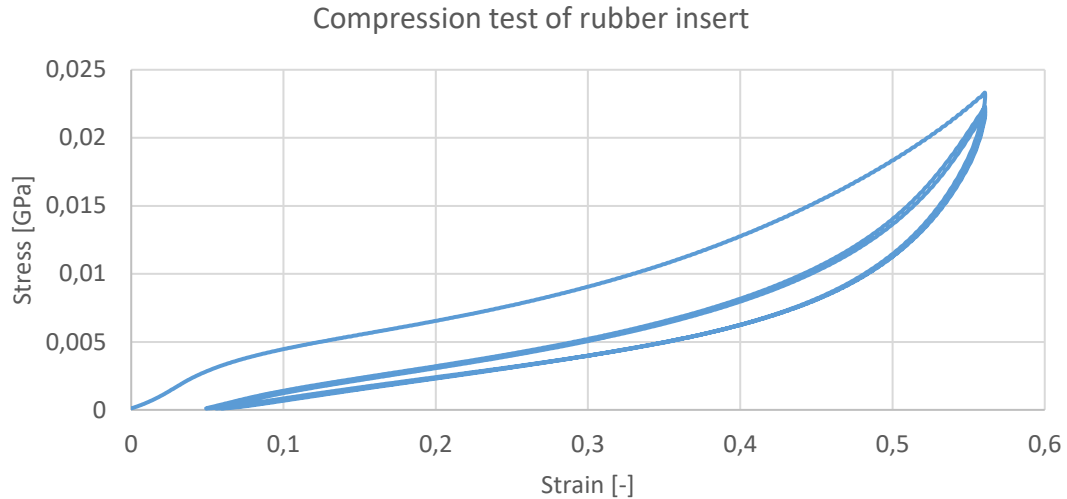


Figure 4. 38: stress-strain curves resultant from the compression test.

In Figure 4. 38, the results of the three load and unload cycles have been represented. The specimen shown hysteresis effect with a little permanent deformation after the first cycle. More stable material behaviour can be observed at the second and third cycles.

The compression test has been simulated with PAM-STAMP in order to test the capability of the software to describe the rubber material behaviour. In PAM-STAMP, there is a software tool able to calculate the A and B Mooney Rivlin coefficients (equation 4.6) at load and unload condition, by importing the stress and strain curve coming from the compression test. The calculation of the Mooney Rivlin coefficient has been performed using as an input the stress-strain data of the third compression cycle (load and unload) shifted to the point (0; 0) as shown in Figure 4. 39. The coefficient A and B of the Mooney Rivlin constitutive law, calculated by PAM-STAMP, and the material properties imposed in the simulation have been reported in Table 4. 18.

The simulation setup is composed by the cylindrical specimen between the lower and upper plate without symmetry, in order to converge the simulation without elements distortion. In Figure 4. 40 the upper plate (equal to the lower plate) has been represented in transparent view in order to show the mesh geometry of the specimen. The rigid upper and lower plate have been modelled by shell elements with thickness of 0.2 mm for improving the contact compatibility with the solid elements of the specimen. The specimen has been modelled with hexahedral 8 noded elements and the rigid plates with rectangular 4 noded shell elements. The quantities of nodes and elements for each component have been reported in Table 4. 19. All the displacements of the lower plate have been locked, instead the upper plate has been imposed a displacement curve as shown in Figure 4. 41. The Accurate algorithm has been chosen for modelling the contact between the rigid plates and the deformable specimen, by imposing a friction of 0.15 according to [13].

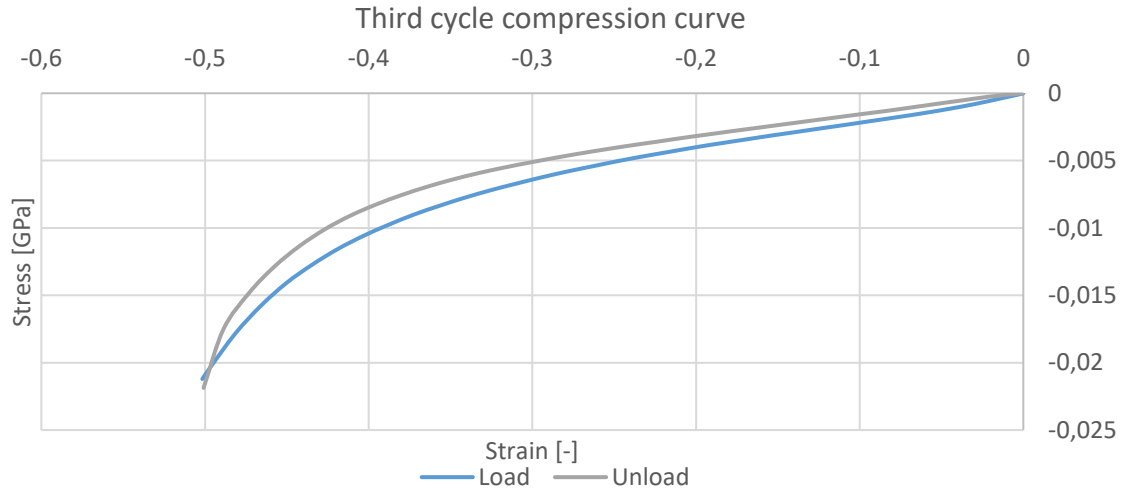


Figure 4. 39: compression stress-strain curves used for calculate the Mooney Rivlin coefficients in PAM-STAMP.

Material	A	B	Poisson coeff (v).	Density (ρ)
	[GPa]	[GPa]		[kg/mm ³]
Rubber Shore A90 (Load)	0.003708	-0.000671	0.499	1.26*10 ⁻⁶
Rubber Shore A90 (Unload)	0.001404	0.000479	0.499	1.26*10 ⁻⁶

Table 4. 18: material properties of the rubber shore 90 used in the simulation.

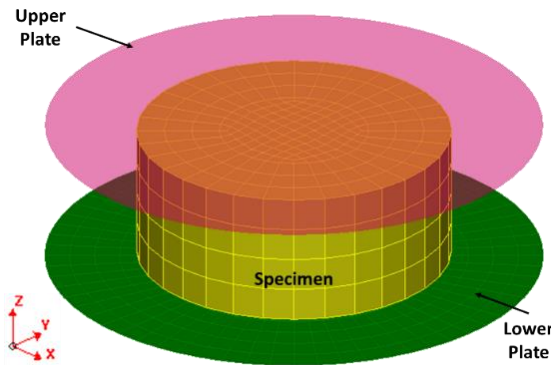


Figure 4. 40: scheme of the compression simulation setup of rubber material.

Object	Behaviour	Elements	Nodes
Upper plate	Rigid	640	641
Lower plate	Rigid	640	641
Specimen	Deformable	768	1045

Table 4. 19: number of elements and nodes used for meshing the object in the compression simulation.

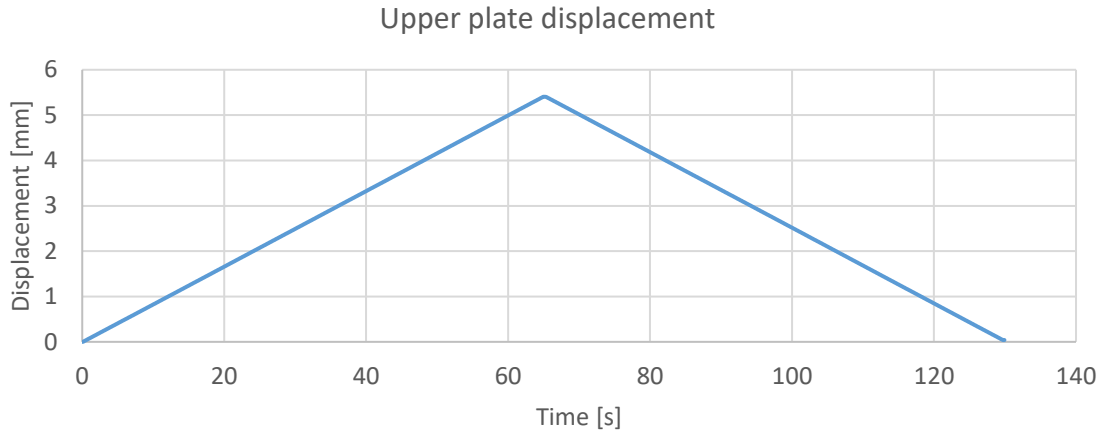


Figure 4. 41. imposed displacement for the upper plate.

In Figure 4. 42, the comparison between the forces resultant from the experimental and numerical compression tests is presented. Due the inertia effect, the FEM distribution is more scattered respect to the experimental one, but the experimental curve is well replicated by the model. Little deviations can be observed in the unload zone, where the force decreasing trend is observed, instead the load zone is very well represented. The registered deviations in the unload zones are not relevant for the application described in this chapter, because the bending process correspond to a load condition for the rubber insert; usually the study of load and unload condition are typical of structural application where the rubber component represent a fundamental part of an assembly. In the bending process simulation the rubber insert is loaded by the descent of the punch during the process, but the unloading is not considered because the springback is simulated by releasing the blank from the tools, so the bend angle will be independent from the rubber unloading conditions. In conclusion, the simulation results demonstrate that the PAM-STAMP is able to simulate the rubber material behaviour subjected to compression load.

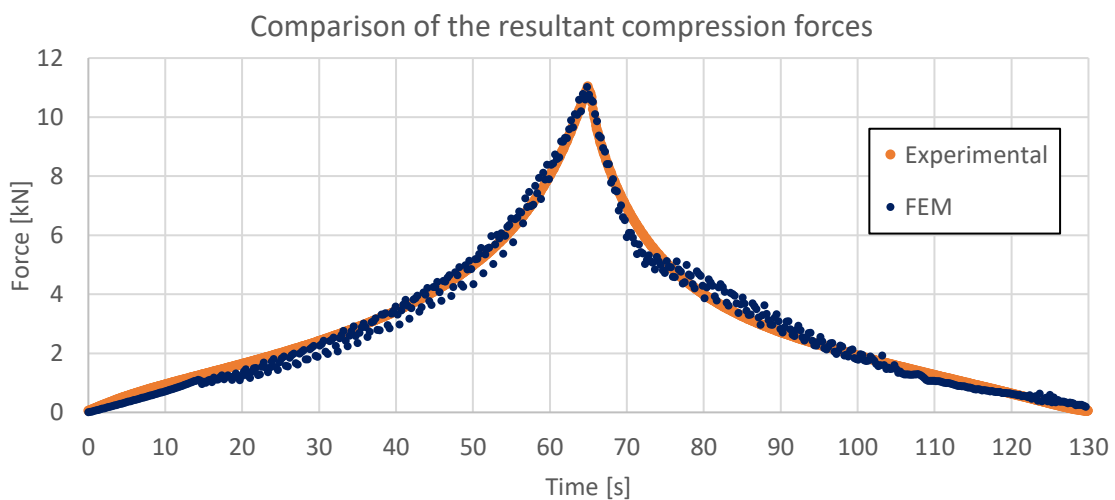


Figure 4. 42: comparison of the resultant forces on the upper plate at the end of the experimental and simulated compression test for Rubber shore 90A.

4.5.3 Boundary conditions

Each simulation setup starts when the blank is held between the punch and the die (rigid or deformable). Then the punch moves down with the constant velocity of 0.1 mm/ms. The translation and rotation of the rigid tools (die and metal frame) have been locked along all the directions.

The contact algorithm between the objects is defined by accurate algorithm described in chapter 2, taking into account a Coulomb friction coefficient of 0.25 between the deformable insert and the blank, 0.15 between the deformable bodies (blank or insert) and the rigid tools (punch, die and metal frames) according with [1]-**Errore. L'origine riferimento non è stata trovata.**

The springback analysis has been run with the “Advanced Implicit” algorithm, implemented in the FEM software, by removing one degree of freedom at one nodal location on the blank, due to the double symmetry (Figure 4. 43). For clarification, the resume of the boundary conditions and the interaction matrix of the simulation are presented in Table 4. 20 and Table 4. 21.

Stage	Object	Rigid Body	Cartesian kinematic	Refinement	Springback	Boundary conditions
Bending	Blank			Level 5		
	Die (rigid)		Locked translations: X, Y, Z Locked rotations: X, Y, Z			
	Punch		Locked translations: X, Z Locked rotations: X, Y, Z Imposed velocity: -Y			
	Metal Frame	Simplified	Locked translations: X, Y, Z Locked rotations: X, Y, Z			
Springback	Blank				Advanced Implicit	Node 1: TY and TZ locked Node 2: TZ locked

Table 4. 20: resume of the complete boundary conditions imposed in the simulation setup.

Master / Slave	Blank	Nylon insert	Necuron insert	Rubber insert
Die	0.15			
Metal Frame		0.25	0.25	0.25
Punch	0.15			
Nylon insert	0.25			
Necuron insert	0.25			
Rubber insert	0.25			

Table 4. 21: master and slave contact relations.

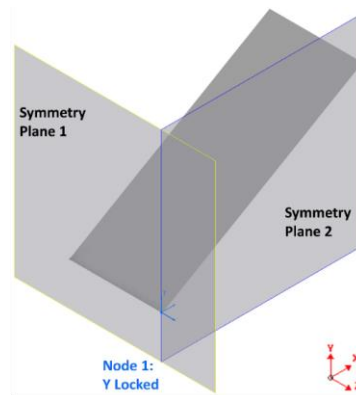


Figure 4. 43: scheme of the boundary condition applied on the blank in springback step.

4.5.4 Simulation results

In this paragraph, the results in terms of bend angle and the final stresses on the deformable inserts will be described. In Table 4. 22 the resultant bend angles (α_{FEM}) and the deviations with the experimental ones (α_{EXP}) have been presented. From Figure 4. 44 to Figure 4. 50, the experimental (α_{EXP}) and simulated (α_{FEM}) bend angle values have been represented. The experimental angles have been shown as mean values of the replications with bars representing the range of the measures; instead, the FEM values have been represented as unique values for their deterministic nature.

The experiments number 7 and 9 (Table 4. 9) have not been considered in the simulation activities due to bend angle close to 180° , which value is irrelevant from an engineering point of view.

The results of the simulations are very representative of the real cases. The bend angle deviations between the α_{EXP} and α_{FEM} are smaller than 1° , which value is very similar with the ones found in literature [3] and [14]. The results achieved in terms of bend angle demonstrates that the FEM model can be used as a reliable tool for evaluating the deformations of the tools insert and the residual stresses.

Std_order	Thickness [mm]	Material	Rol_dir [°]	Tool	Punch stroke [mm]	α_{exp} [°]	α_{FEM}	Deviations exp - fem
1	1	Al1050	0	Rubber	3.16	165	165.72	-0.72
2	1	Al1050	0	Rubber	3.16	165	165.72	-0.72
3	1	Al1050	0	Nylon	1.57	131.5	131.39	0.11
4	1	Al1050	0	Nylon	1.57	131	131.39	-0.39
5	0.7	Fe37	90	Metal	1.57	118	119.36	-1.36
6	0.7	Fe37	90	Metal	1.57	119	119.36	-0.36
8	0.7	Fe37	90	Rubber	3.16	160.5	159.87	0.63
10	0.7	Fe37	90	Rubber_hole	3.16	157.5	157.1	0.4
11	0.7	Fe37	90	Ne1050	1.57	131.5	131.93	-0.43
12	0.7	Fe37	90	Ne1050	1.57	132	131.93	0.07
13	0.7	Fe37	90	Ne1150	1.57	132.75	132.13	0.62
14	0.7	Fe37	90	Ne1150	1.57	131.5	132.13	-0.63
15	0.7	Fe37	90	Ne1300	1.57	131	131.88	-0.88
16	0.7	Fe37	90	Ne1300	1.57	131	131.88	-0.88
17	0.7	Fe37	90	Nylon	1.57	129.25	129.42	-0.17
18	0.7	Fe37	90	Nylon	1.57	129.75	129.42	0.33
19	1	Fe37Z	0	Metal	1.57	120	119.86	0.14
20	1	Fe37Z	0	Metal	1.57	119.75	119.86	-0.11
21	1	Fe37Z	0	Rubber	3.16	164.5	165.15	-0.65
22	1	Fe37Z	0	Rubber	3.16	164.5	165.15	-0.65
23	1	Fe37Z	0	Rubber_hole	3.16	163.5	162.88	0.62
24	1	Fe37Z	0	Rubber_hole	3.16	163.5	162.88	0.62
25	1	Fe37Z	0	Ne1050	1.57	133.25	132.93	0.32
26	1	Fe37Z	0	Ne1050	1.57	133.75	132.93	0.82
27	1	Fe37Z	0	Ne1150	1.57	135	134.8	0.2
28	1	Fe37Z	0	Ne1150	1.57	135	134.8	0.2
29	1	Fe37Z	0	Ne1300	1.57	133	133.21	-0.21
30	1	Fe37Z	0	Ne1300	1.57	133	133.21	-0.21
31	1	Fe37Z	0	Nylon	1.57	134	134.07	-0.07
32	1	Fe37Z	0	Nylon	1.57	134	134.07	-0.07
33	0.8	Fe37	0	Metal	1.57	121.25	122.11	-0.86
34	0.8	Fe37	0	Metal	1.57	121.25	122.11	-0.86
35	0.8	Fe37	90	Metal	1.57	121.25	122.21	-0.96
36	0.8	Fe37	0	Rubber	3.16	165	165.65	-0.65
37	0.8	Fe37	0	Rubber	3.16	164.75	165.65	-0.9
38	0.8	Fe37	90	Rubber	3.16	165	165.87	-0.87
39	0.8	Fe37	0	Rubber_hole	3.16	164	164.56	-0.56
40	0.8	Fe37	0	Rubber_hole	3.16	164.75	164.56	0.19
41	0.8	Fe37	90	Rubber_hole	3.16	163.25	164.12	-0.87
42	0.8	Fe37	0	Ne1050	1.57	133.75	133.97	-0.22
43	0.8	Fe37	0	Ne1050	1.57	133.75	133.97	-0.22
44	0.8	Fe37	90	Ne1050	1.57	133	133.82	-0.82
45	0.8	Fe37	0	Ne1150	1.57	133.5	134.28	-0.78
46	0.8	Fe37	0	Ne1150	1.57	133.5	134.28	-0.78
47	0.8	Fe37	90	Ne1150	1.57	135	134.14	0.86
48	0.8	Fe37	0	Ne1300	1.57	133	133.96	-0.96
49	0.8	Fe37	0	Ne1300	1.57	133	133.96	-0.96
50	0.8	Fe37	90	Ne1300	1.57	133.5	133.97	-0.47
51	0.8	Fe37	90	Nylon	1.57	133	132.8	0.2
52	0.8	Fe37	0	Nylon	1.57	133.5	133.07	0.43
53	0.8	Fe37	0	Nylon	1.57	133	133.07	-0.07

Table 4. 22: simulation results and deviations with the experimental values of blanks bend angle.

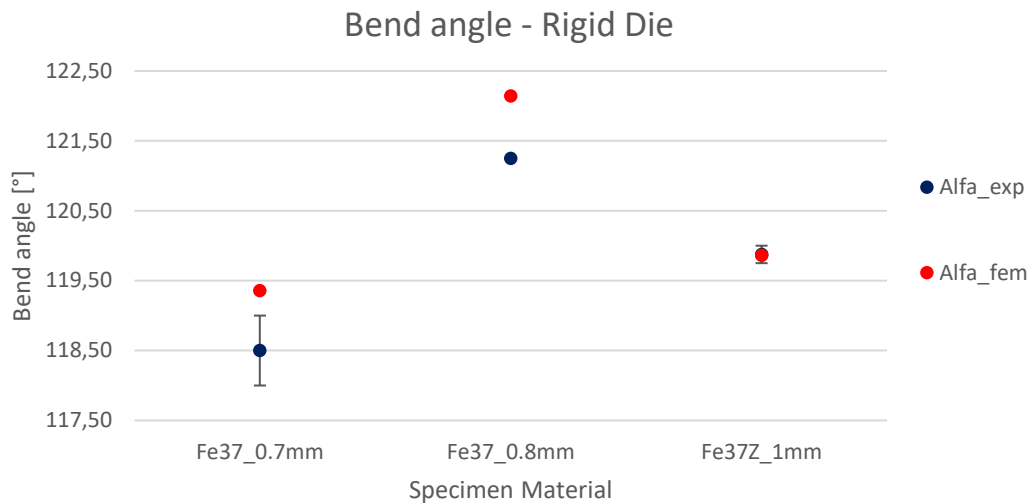


Figure 4. 44: experimental (alfa_exp) and simulated (alfa_fem) comparison for specimen bent by rigid die.

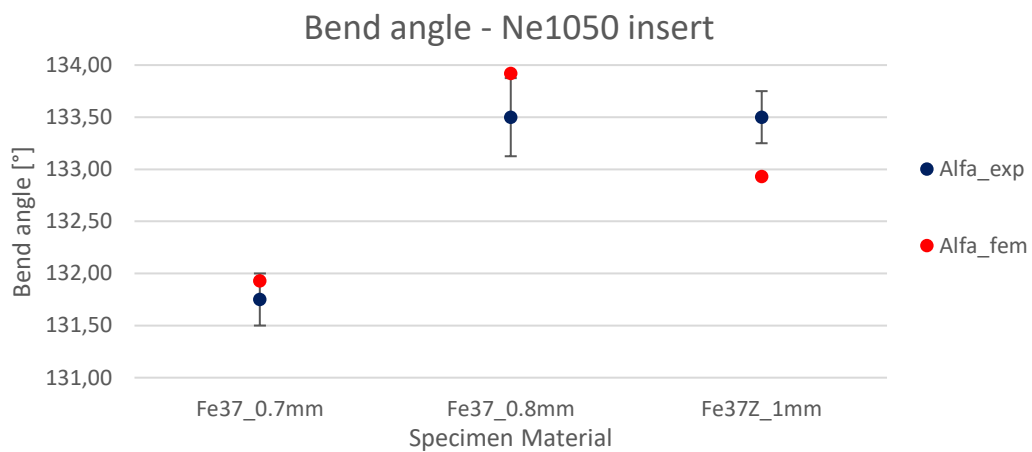


Figure 4. 45: experimental (alfa_exp) and simulated (alfa_fem) comparison for specimen bent by Necuron 1050 insert.

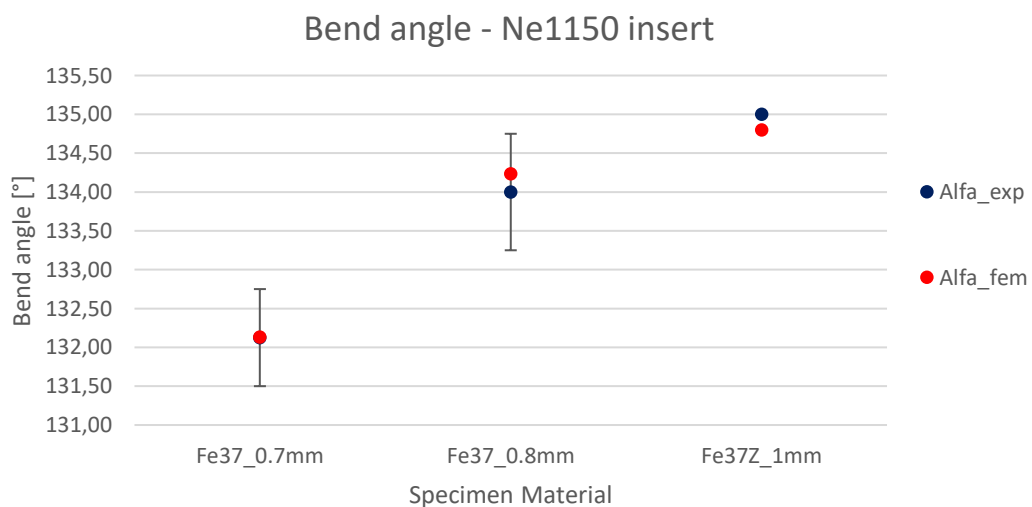


Figure 4. 46: experimental (alfa_exp) and simulated (alfa_fem) comparison for specimen bent by Necuron 1150 insert.

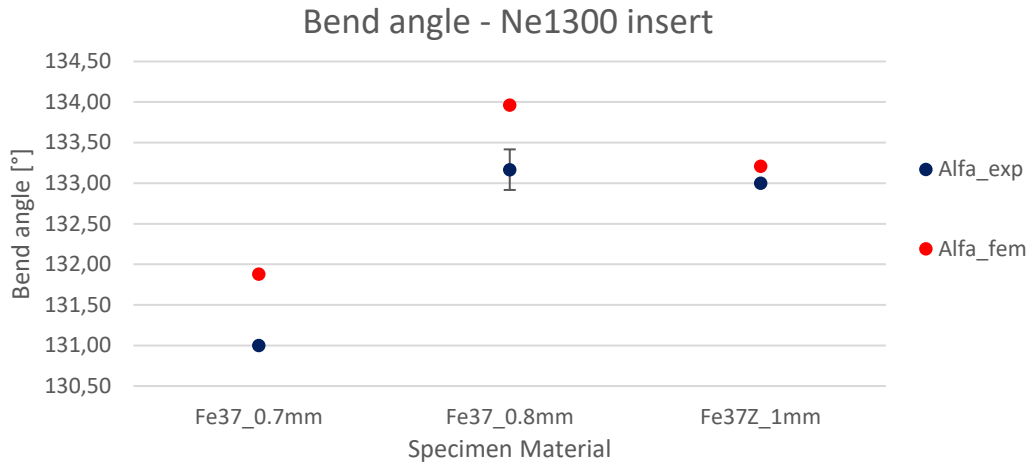


Figure 4. 47: experimental (alfa_exp) and simulated (alfa_fem) comparison for specimen bent by Necuron 1300 insert.

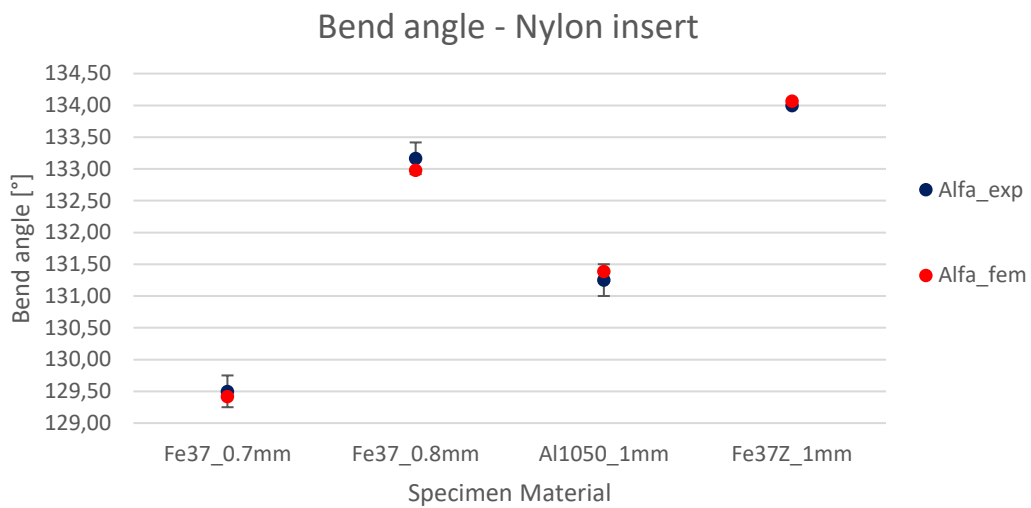


Figure 4. 48: experimental (alfa_exp) and simulated (alfa_fem) comparison for specimen bent by Nylon insert.

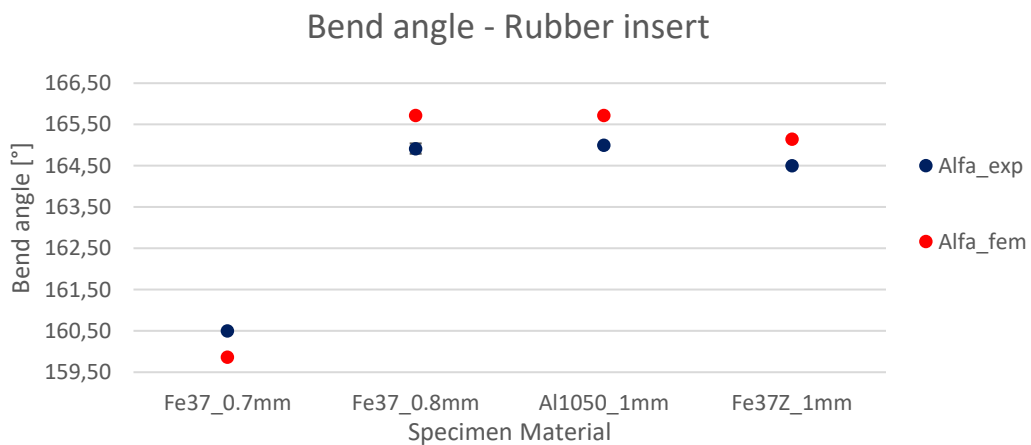


Figure 4. 49: experimental (alfa_exp) and simulated (alfa_fem) comparison for specimen bent by Rubber insert.

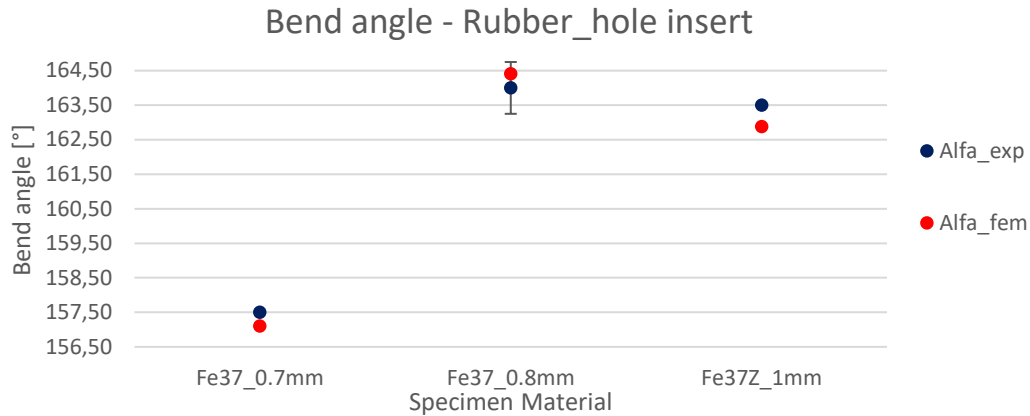


Figure 4. 50: experimental (alfa_exp) and simulated (alfa_fem) comparison for specimen bent by drilled Rubber insert.

In the Figure 4. 51, Figure 4. 52 and Figure 4. 53, the stress maps on the polyurethane inserts at the end of the bending operation have been presented only for the experiments with material Fe37Z thickness 1 mm. The stress maps on the polyurethane inserts for the other experiments have been presented in the appendix. No polyurethane insert reached the Yield stress, a stress value of 18 MPa can be observed in the upper cavity of the die corresponding to the contact zone with the blank. According with the fatigue tests described in chapter 3, the load level of 18 MPa suggests that the polyurethane insert are able to bend more than 10 thousand pieces, without the arising of relevant permanent deformations. An increment of the stress value can be registered in all insert in the contact zone between the lower surface of the insert and the edge of the cavity of the metal frame. The metal frame, used in the experimental activities, is normally coupled with the rubber inserts, because the lower cavity must accommodate the hyper-elastic material of the insert when very high deformation are performed (Figure 4. 54). Actually, the thermoset polyurethane cannot be deformed like the rubber insert so a redesign of the metal frame, without the cavity, must be considered in order to avoid the increments of the stresses registered in the simulations.

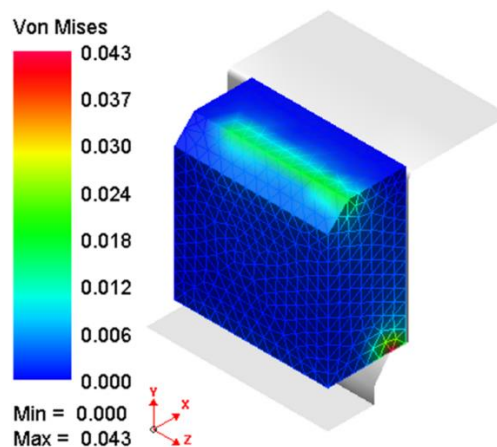


Figure 4. 51: stress map (GPa) of the Necuron 1050 insert at the end of bending operation for specimen Fe37Z.

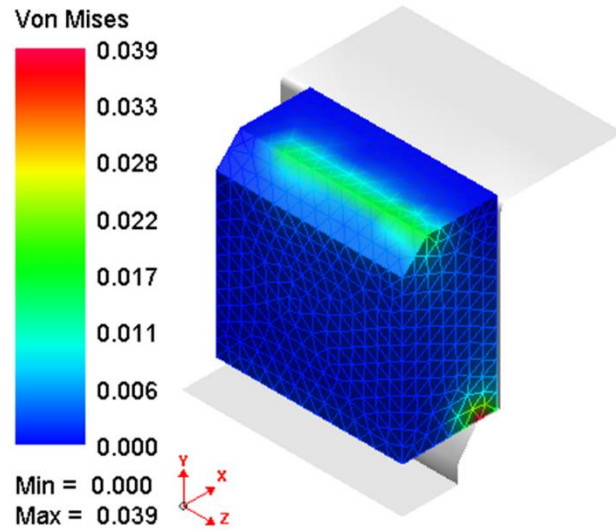


Figure 4. 52: stress map (GPa) of the Necuron 1150 insert at the end of bending operation for specimen Fe37Z.

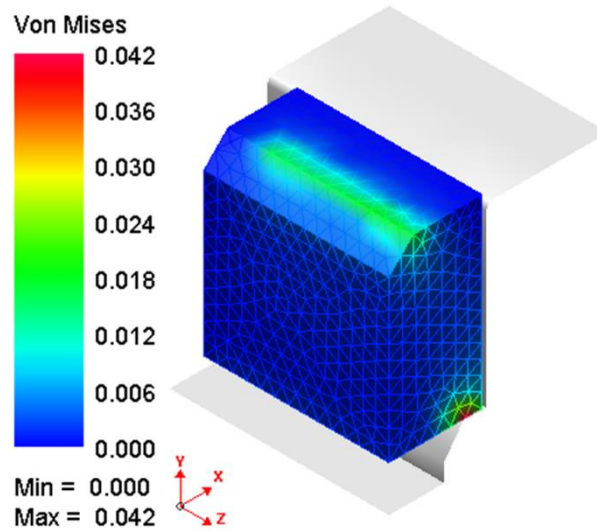


Figure 4. 53: stress map (GPa) of the Necuron 1300 insert at the end of bending operation for specimen Fe37Z.

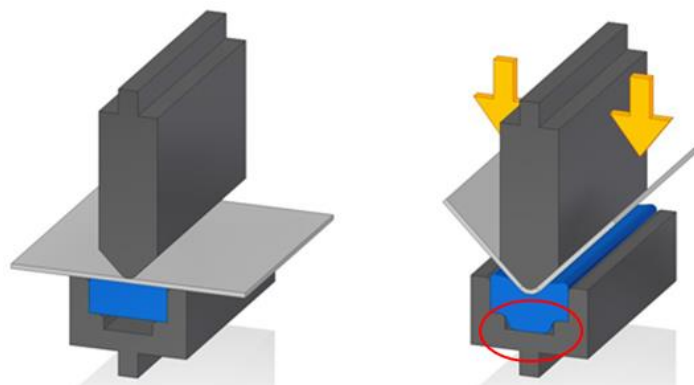


Figure 4. 54: example of the rubber flow inside the metal frame cavity when high sheet metal deformation are performed [15].

In the Figure 4. 55, Figure 4. 56 and Figure 4. 57, the deformation maps of the polyurethane inserts have been shown in terms of normal displacement. The displacement maps registered the max displacement, approximatively of 0.07 mm, on the contact zone with the blank. The deformations reached by the polyurethane inserts demonstrate why the experimental bend angle are out of 10° respect to the initial target angle of 120° .

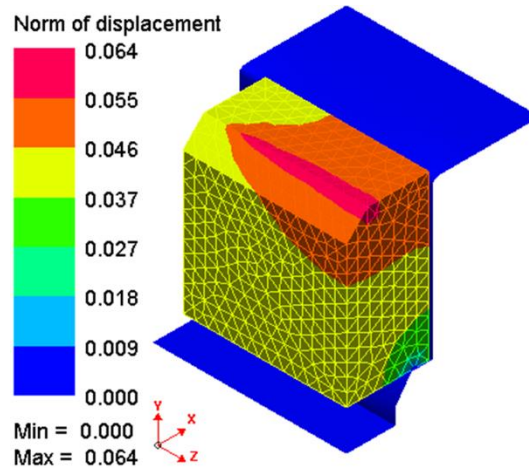


Figure 4. 55: displacement map (mm) of the Necuron 1050 insert at the end of bending operation for specimen Fe37Z.

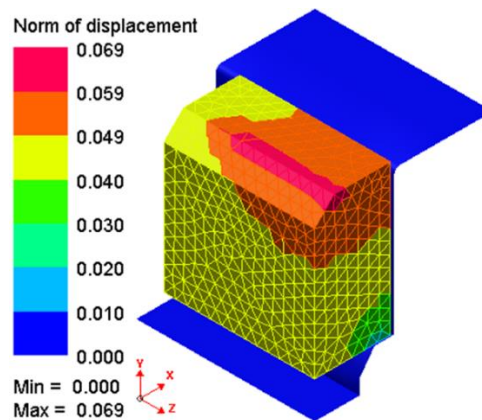


Figure 4. 56: displacement map (mm) of the Necuron 1150 insert at the end of bending operation for specimen Fe37Z.

A geometrical compensation of the insert, similar with the one described in chapter three, cannot be considered as a possible solution because generally this kind of die are normally used for bending different product at different angles. A geometrical compensation could solve only this particular case, but it will introduce errors when a different component will be bent at different angle respect to 120° . The punch stroke is the main parameter which influences the sheet metal bend angle, when the tools have been selected. Normally the punch stroke is calculated geometrically with trial and errors or with prediction algorithms similar to the ones developed in **Errore. L'origine riferimento non è stata trovata.**, [16]-[22]. These kind of algorithm are

normally developed on a very large experimental and/or numerical campaign. For example the research work described in **Errore. L'origine riferimento non è stata trovata.** required two years for performing and analysing 288 experiments and 507 simulations, in order to generating a Hierarchical metamodel able to predict the bend angle and the bend deduction of sheet metal bending operation with a rigid metal tools setup. A further development of this research could be focused on a development of prediction algorithm, which will take in account also the deformation of the inserts during the process.

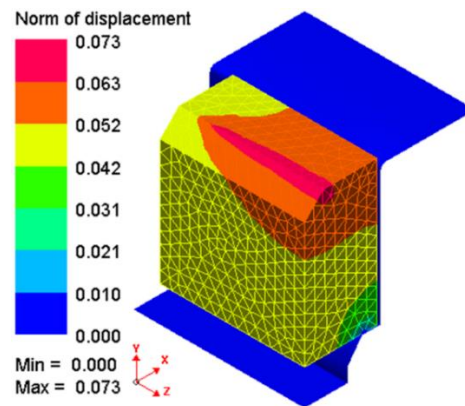


Figure 4. 57: displacement map (mm) of the Necuron 1300 insert at the end of bending operation for specimen Fe37Z.

In Figure 4. 58, the stress and displacement maps have been reported for the Nylon insert. The material characteristics are very similar with the polyurethane ones, indeed the stress values reached are similar. In this case the metal frame is different respect to the one used for polyurethane and rubber insert, for this reason no stress concentration have been registered in the lower surface of the insert like the polyurethane cases. Also the displacement in Figure 4. 58b are lower respect to the ones registered for polyurethane insert, due to the higher rigidity of the metal frame supplied in the purchase phase.

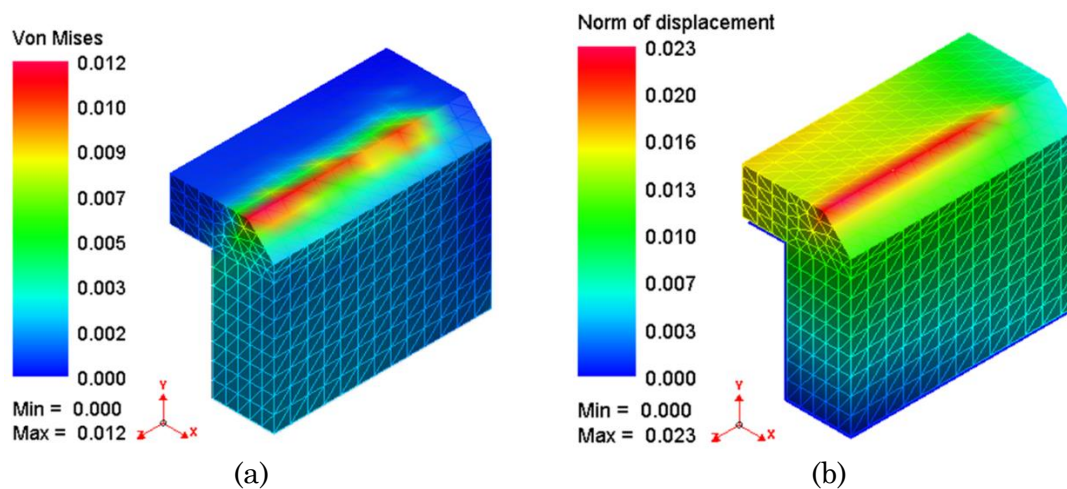


Figure 4. 58: stress (GPa) (a) and displacement (mm) (b) maps of the Nylon insert at the end of bending operation for specimen Fe37Z.

Finally, the stress and displacement maps have been presented in Figure 4. 59 for rubber and drilled rubber inserts. The stress values reached by the rubber inserts are very low (at least 7 MPa), this demonstrate the capacity of the rubber material in absorbing the loads. If the loads are very low, the deformations are huge respect to the ones observed for the polyurethane and nylon material. This phenomenon is obviously related to the hyper-elastic material behaviour described in paragraph 4.5.2 and shown in Figure 4. 38, where has been shown that to a very low load level corresponds a very huge deformation. In the Figure 4. 59b, lower values of displacements can be observed for the rubber insert, respect to the drilled one in Figure 4. 59d. This is obviously related to the presence of the longitudinal hole, which makes the insert structure less stiff; indeed the drilled rubber insert are suitable when bend angle minor than 90° must be reached. In both rubber insert cases, it can be observed the role of the lower cavity of the metal frame. Indeed, both of the rubber inserts presents displacements major than 0 in the lower surfaces, because they tend to flow along the lower cavity (during the bending process) in order to simply the deformation mechanism of the material.

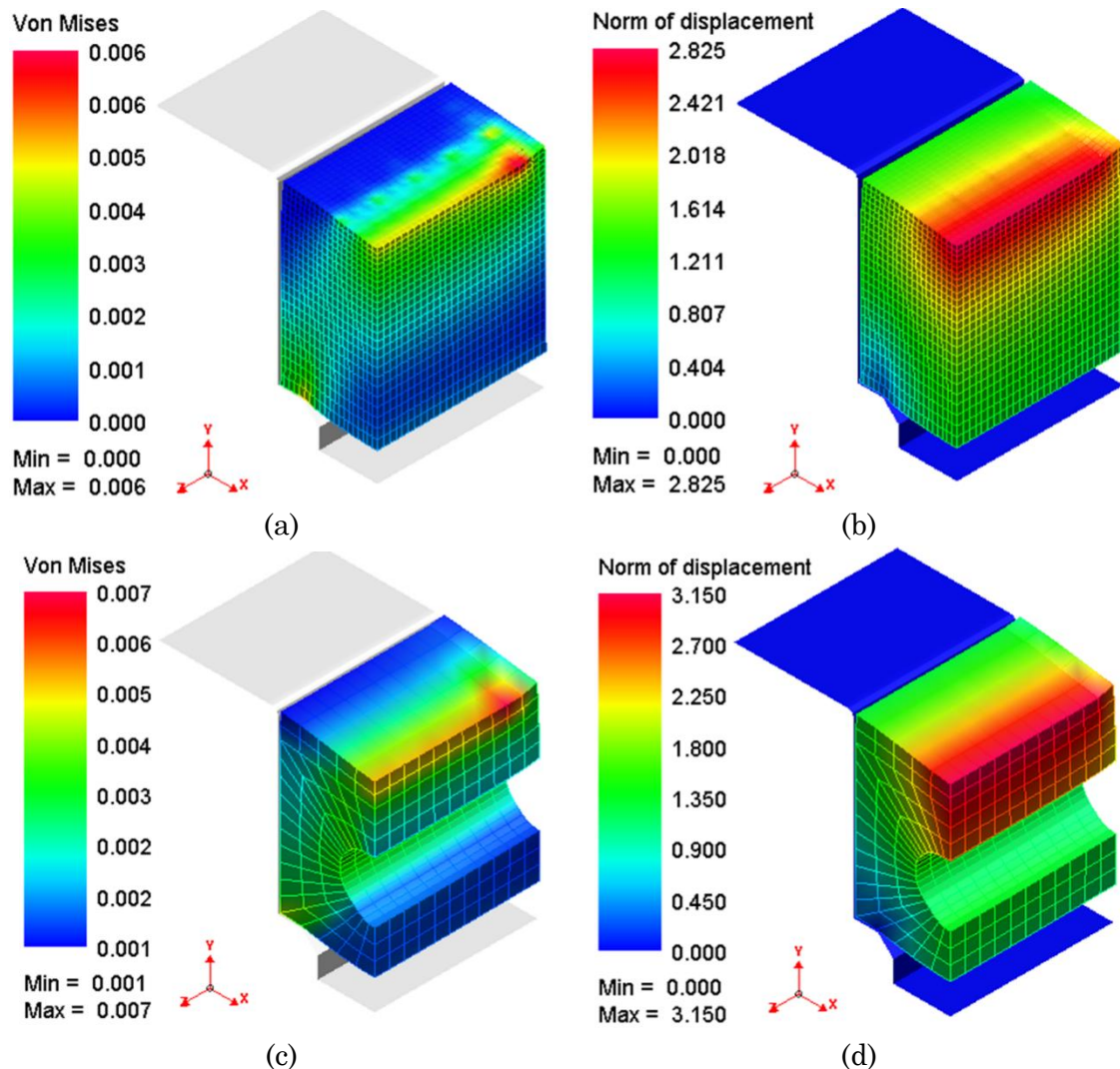


Figure 4. 59: stress (GPa) (a) and displacement (mm) (b) maps of the Rubber inserts at the end of bending operation for specimen Fe37Z.

4.6 Conclusions

In this chapter, the rapid tools have been introduced in the sheet metal bending process as a new tools setup concept solution. The rapid tools setup has been compared with the commercial tools solutions, already used in the sheet metal bending industry. The experimental activities demonstrates that the performances of the rapid tools are similar with the nylon tools solution. Using the same process parameters, the rapid tools shown similar values of bend angles, without any aesthetical defects, like scratches, on the product surface, which defects have been observed for some specimen bend with the nylon solution. The traditional metal tools presented best performances in terms of obtained bend angle, closer to the initial target of 120°. It should be noted that the numerical controls of the press brakes are normally developed for metal tools, this is the main reason why the metal tools obtained the best results in term of bend angle. The specimens bent with rapid tools showed bend angles 15 degrees bigger than the specimens bent with metal tools. This result demonstrates than the traditional rules used for evaluating the bending process parameters (like the punch stroke) cannot be used for rapid tools, for this reason a simulation model has been studied. The developed simulation model is able to evaluate the final angle of blanks bended with polyurethane tools within a range of error of $[-1; 1]^{\circ}$, This result is similar to the others found in literature. The experiments performed with the rubber inserts demonstrate that different approaches should be used in design and manufacturing phases, because in this case the bending process becomes similar to the bottoming one. The experiments showed that the same process parameters, designed for metal tools, give back very bad results in terms of final bend angle in case of rubber tools. The simulation activities demonstrates that modelling the behaviour of rubber material is not trivial, due to the completely different approach used in the available constitutive models which are very complex respect to the traditional elasto-plastic model used for metals and polymers. The results obtained from the simulations in terms of load and displacement for rapid tools demonstrate that the V-shaped cavity can resist for middle-volume industrial productions, according with the fatigue tests described in chapter 3.

All the activities described in this chapter demonstrate that there is wide margin of the rapid tools usage in sheet metal bending process. The performances are close with commercial solutions already existing. Simulation model can be implemented in the design phase in order to evaluate the process parameters. As a future development, it could be interesting to introduce the deformation of the tools inside the prediction algorithm of the numerical controls of the press brakes, in order to improve the productivity of the rapid tools. At the end of the research, the company, which collaborated during the experimental activities, decided to introduce the rapid tools solution in its catalogue. This result is very encouraging for the performed research activity and it demonstrates clearly that the rapid tools are awakening interest for the manufacturing industry.

4.7 References

- [1] PARK, Young-Bin; COLTON, Jonathan S. Fatigue of reinforced-polyurethane-based, sheet metal forming dies. *International journal of fatigue*, 2006, 28.1: 43-52.
- [2] PARK, Y.; COLTON, J. S. Failure analysis of rapid prototyped tooling in sheet metal forming-V-die bending. *Transactions-American Society Of Mechanical Engineers Journal Of Manufacturing Science And Engineering*, 2005, 127.1: 116.
- [3] STRANO, Matteo, et al. Fusion metamodeling of the bend deduction in air bending. In: *AIP Conference Proceedings*. AIP Publishing, 2017. p. 100003.
- [4] IRTHIEA, Ihsan, et al. Experimental and numerical investigation on micro deep drawing process of stainless steel 304 foil using flexible tools. *International Journal of Machine Tools and Manufacture*, 2014, 76: 21-33.
- [5] ASTM, E8. 8M: Standard test method for tension testing of metallic materials (Metric). *Annual Book of ASTM Standards*, Philadelphia, 1991.
- [6] ASTM E517-00. Standard test method for plastic strain ratio r for sheet metal, 2000.
- [7] RAMEZANI, Maziar; RIPIN, Zaidi Mohd. *Rubber-pad forming processes: Technology and applications*. Elsevier, 2012.
- [8] ESI-Group, Pam-Stamp 2G 2015.1, User's Guide.
- [9] Sasso, M., et al. "Characterization of hyperelastic rubber-like materials by biaxial and uniaxial stretching tests based on optical methods." *Polymer Testing* 27.8 (2008): 995-1004.
- [10] Feng, William W., and John O. Hallquist. "On Mooney-Rivlin Constants for Elastomers." *stress (force per unit undeformed area)* 1 (2012): 5.
- [11] Seibert, H., T. Scheffer, and S. Diebels. "Biaxial testing of elastomers- Experimental setup, measurement and experimental optimisation of specimen's shape." *Technische Mechanik* 34.2 (2014): 72-89.
- [12] ASTM D395, "Standard Test Methods for Rubber Property-Compression Set," 2008.
- [13] LIU, Yanxiong, et al. Studies of the deformation styles of the rubber-pad forming process used for manufacturing metallic bipolar plates. *Journal of Power Sources*, 2010, 195.24: 8177-8184.
- [14] NILSSON, Annika; MELIN, Lars; MAGNUSSON, Claes. Finite-element simulation of V-die bending: a comparison with experimental results. *Journal of Materials Processing Technology*, 1997, 65.1-3: 52-58.
- [15] Rubber Pad Forming advantaged and disadvantages - <https://jimmysmits.wordpress.com/2014/07/30/rubber-pad-forming-advantages-and-disadvantages/> accessed on 13/01/2018.
- [16] Raghupathi, P. S., Karima, M., Akgerman, N., and Altan, T., 1983, "A Simplified Approach to Calculate Springback in Brake Bending," *Proc. of NAMRC XI*, May, SME, Madison, Wisconsin, pp. 165–170.
- [17] Gary Harlow, D. (2004). The effect of statistical variability in material properties on springback. *International Journal of Materials and Product Technology*, 20(1–3), 180–192.

- [18] Lin, Z.-C., & Chang, D.-Y. (1996). Application model in of a neural network machine learning the selection system of sheet metal bending tooling. *Artificial Intelligence in Engineering*, 10, 21–37.
- [19] LEU, Daw-Kwei. A simplified approach for evaluating bendability and springback in plastic bending of anisotropic sheet metals. *Journal of Materials Processing Technology*, 1997, 66.1: 9-17.
- [20] YILAMU, K., et al. Air bending and springback of stainless steel clad aluminum sheet. *Journal of Materials Processing Technology*, 2010, 210.2: 272-278.
- [21] Wiebenga H, Boogaard A, Klaseboer G (2012) Sequential robust optimization of a v bending process using numerical simulations. *Struct Multidiscip Optim* 46:137–156
- [22] Kennedy M, O'Hagan A (2000) Predicting the output from a complex computer code when fast approximations are available. *Biometrika* 87:1–13.

Chapter 5

Rapid tools in tube bending

5.1 Introduction

In the previous chapters, the rapid tools have been introduced in sheet metal forming processes like stamping and air bending.

The experimental activities demonstrated that a rapid tools setup can be easily implemented with a smaller amount of time and cost with respect to the traditional metal tools solutions. The polyurethane tools (rapid tools) showed better results respect the commercial tools made by Nylon in terms of aesthetical defects on the final component. The numerical activities demonstrated that the rapid tools behaviour could be simulated with FEM model in order to predict the deformation of the tools and the final geometry of the sheet metal component at the same time. The prediction of the rapid tools behaviour is fundamental for implementing corrective actions like the tool compensation algorithm for stamping process and punch stroke compensation for bending process.

In this chapter, the rapid tools will be introduced in the rotary tube bending process. The application of polymeric tools in rotary draw bending has been found in [1], where two different types of polymeric mandrel (with and without spheres) have been studied in order to investigate their effect when Yoshida-Uemori material model is applied in the FEM modelling. In this chapter, the feasibility analysis of a rotary draw bending process with completely polymeric tools setup will be presented and compared with the results obtained in the previous study performed by the author during the bachelor degree, where the same process with rigid tools has been studied experimentally and numerically [2].

5.2 Brief description of the previous study on rotary draw bending process

The previous study on rotary draw bending process, made in collaboration with BLM S.p.a of Cantù (CO), had as objective the analysis of the phenomena which could appear when tube with non-circular transversal section are bended.

In the case of traditional rotary draw bending process, where tube with circular transversal section are bended, the design and manufacturing of the tools setup is a standard procedure, because the process parameters are well known and the process results are controllable [3]. Same assertion cannot be said where tube with non-circular section are bended, because the deformation of the section cannot be easily predicted. In order to give information about the mechanical behaviour of a bended welded tube with non-circular section, an FEM model able to predict the results of the rotary draw bending process has been generated.

The FEM model of the rotary draw bending process of a tube with non-circular section (Figure 5. 1) has been largely validated by comparing the simulated bent tube with the prototypal ones manufactured by the company. The FEM described in [2] is able to predict the final shape of the bended tube in terms of thickness distribution along the tube axis, and the final deformation of the tube section, by taking in account the different mechanical behaviour along the tube section introduced by the welding line used for closing the tube profile during previous rolling operation.

After some years, the company B.L.M. GROUP, which collaborated in the experimental activities, revealed the interest of a feasibility analysis turn towards the application of rapid tools in the analysed process.

Starting by the FEM model generated during the bachelor degree, an FEM model with polyurethane tools setup of the same process will be implemented and validated with the results of the previous one. The FEM model will give information about the possible advantages of the process in order to introduce the rapid tools also in the tube bending industry.

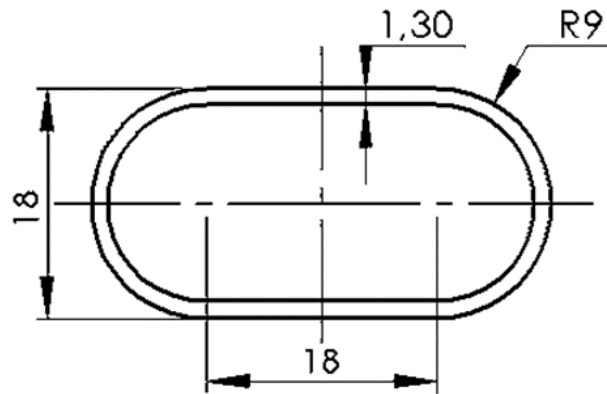


Figure 5. 1: tube section.

5.3 FEM model with Rapid Tools

5.3.1 Geometry and mesh

The case study consists in the rotary draw bending tools setup whose assembly has been represented in Figure 5. 2 in exploded view. The objective of the company was to investigate the possibility to change the material of the bend die, clamp dies, pressure dies and mandrel tools from metal to polyurethane, in order to reduce the tools costs for a low volume production. It should be noted that the product has not the traditional circular shape and so the tools setup has been manufactured expressly for this

component. The wiper die has been excluded from the study because it was considered of scarce interest from the company.

In order to study the feasibility of the rapid tools solution the deformable tools (bend die, clamp dies, pressure die and the mandrel) have been modelled with solid elements, instead the wiper die has been modelled as a rigid discrete surface.

As for the previous case, the solid mesh of the plastic tools has been generated with Visual Mesh 11, by using the integrated automatic tetra mesh algorithm. The symmetry plane has been applied perpendicular to the rotation axis of the bend die (Figure 5. 3)

The number of elements and the number of nodes for each deformable and rigid tool are shown in Table 5. 1.

The tube section is flattened oval with nominal dimensions reported in Figure 5. 1. The surface area of each element is 1.48 mm^2 with a total number of 9468 squared shell elements. The refinement has not been applied for the tube object due to the incompatibility of the Pam-Stamp refinement algorithm, which could generate bad results in post processing.

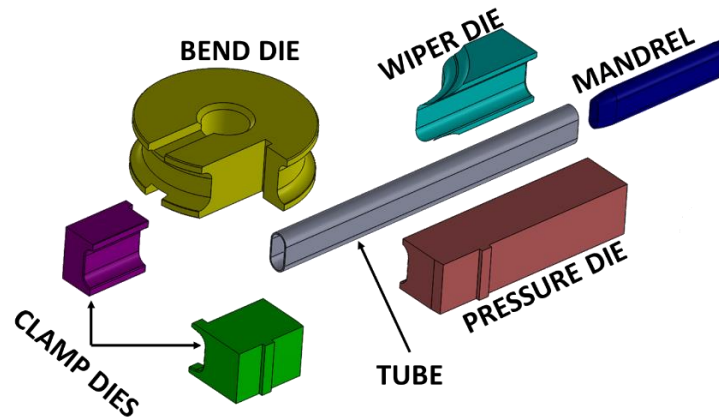


Figure 5. 2: case study tools setup (exploded view).

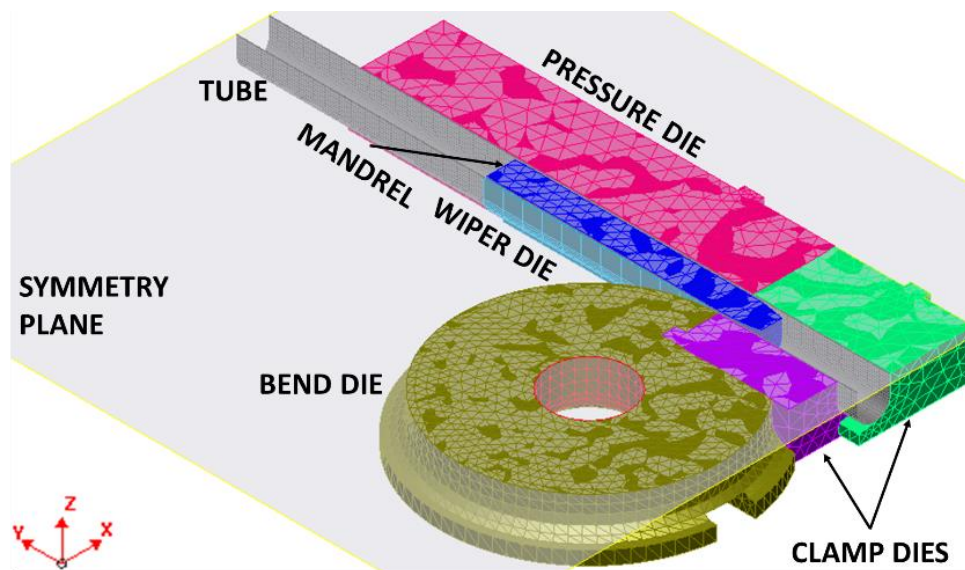


Figure 5. 3: Scheme of the tube bending simulation setup.

Tool	N. elements	N. nodes	Elements Type
Bend die	16462	3911	Tetrahedral
Wiper die	213	226	Rigid shell
Mandrel	2198	672	Tetrahedral
Pressure die	3138	954	Tetrahedral
Clamp die 1 (purple)	1590	496	Tetrahedral
Clam die 2 (green)	910	302	Tetrahedral

Table 5. 1: number of elements and nodes used for meshing the tools.

5.3.2 Material properties

All the deformable tools have been modelled with the material properties of Necuron 1050, described in chapter 2, because it is the most economical polyurethane material studied in this doctoral research with very good behaviour in terms of fatigue life (chapter 3).

The tube material (RSt37-2) has been modelled as elastic-plastic by the Krupkowsky's constitutive law, whose coefficients n , K , ϵ_0 have been retrieved in [2]. The hardening curve of the tube material is shown in Figure 5. 4. The rolling direction of the tube has been considered along the Y axis (Figure 5. 3) by imposing the Lankford's coefficients reported in Table 5. 2 together with all the material properties of the tube.

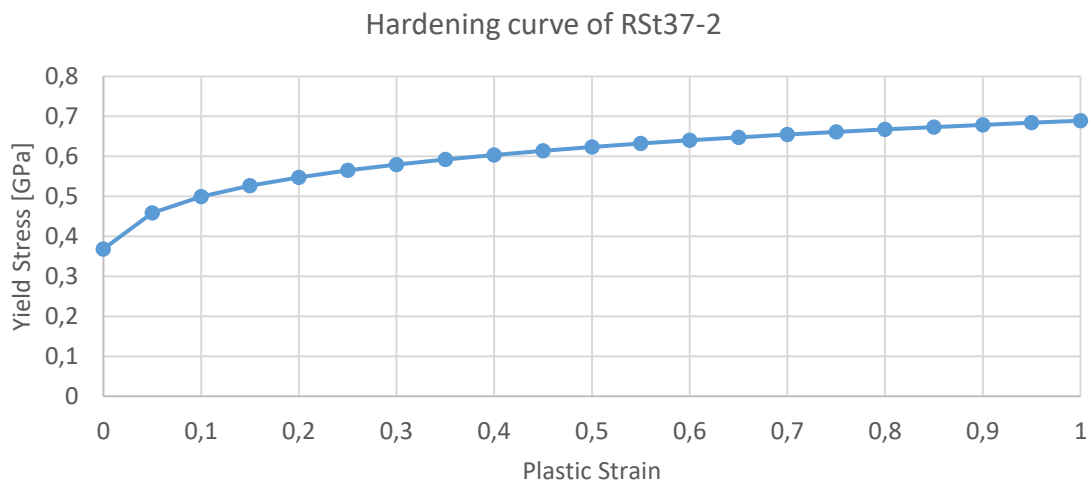


Figure 5. 4: Rst37-2 hardening curve calculated with the Krupkowsky's constitutive law.

Material	Poisson coeff (ν)	Density (ρ) [g/cm ³]	Young Modulus (E) [MPa]	Krupkowsky coefficients			Lankford coefficients		
				n	K	ϵ_0	r ₀	r ₄₅	r ₉₀
					[MPa]				
RSt37-2	0.3	7.8	210000	0.148	687.7	0.0147	0.831	0.951	0.921

Table 5. 2: material properties of the tube.

5.3.3 Boundary conditions

The simulation starts at the end of the closing stage, where the tube is held between the tools. The bend die rotates around the z-axis with center in the point with Cartesian coordinates (0; 0; 0) by following the velocity profile shown in Figure 5. 5. In order to simulate the deformation of the bend die, the rotational kinematics has been applied only on the elements faces belonging to the center hole of the tool (Figure 5. 6a). The same boundary condition has been imposed on the external elements faces of the clamp die 2 (green), as shown in Figure 5. 6b). The rigid wiper die has been constrained along all directions, as the nodes positioned on the rear surface of the mandrel (Figure 5. 7). The pressure die should move parallel with the tube axis, for this reason all the degree of freedom, except of the translation along the Y axis, of the nodes belonging to the rear surface of the pressure die have been locked (Figure 5. 8).

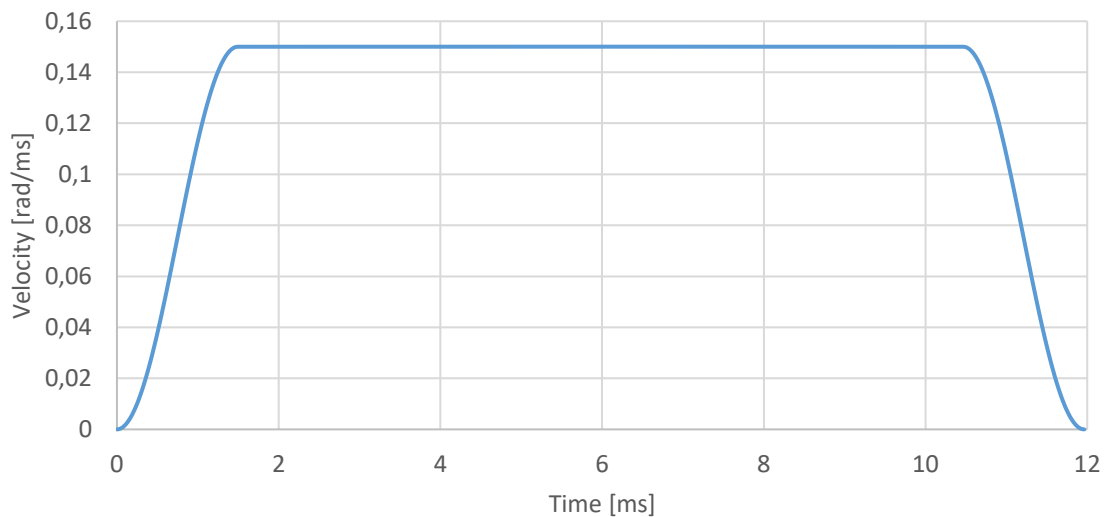


Figure 5. 5: velocity profile applied at the rotational axis of the bend die.

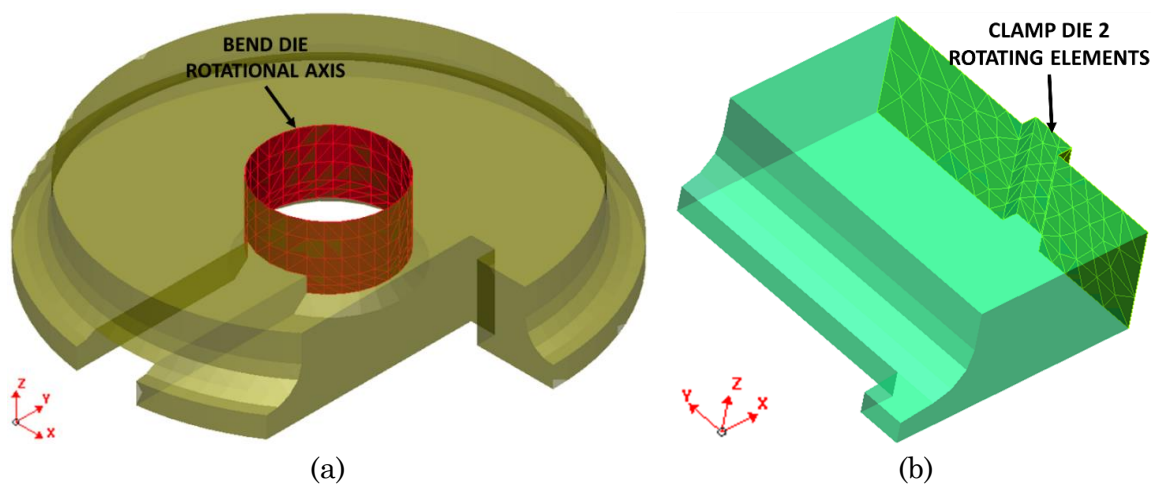


Figure 5. 6: elements where the rotational kinematics along the z-axis has been applied.

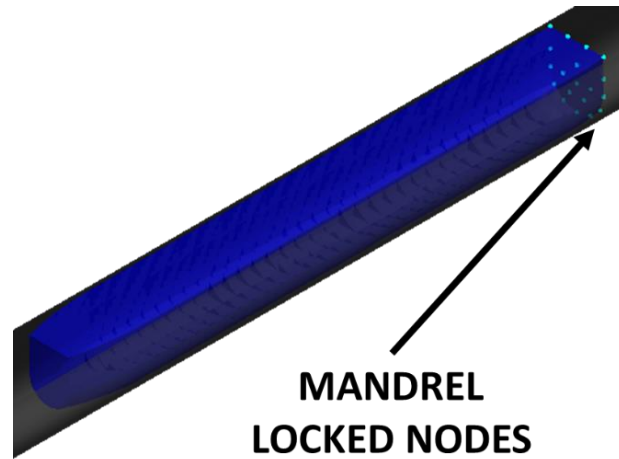


Figure 5. 7: Locking condition applied on the nodes of the mandrel.

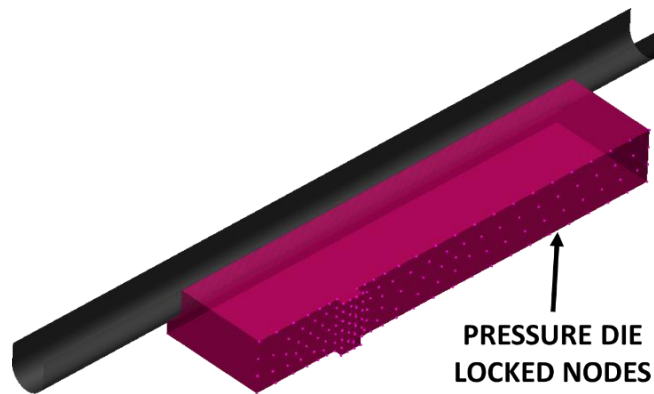


Figure 5. 8: locked nodes belonging to the rear surface of the pressure die.

The clamp die 1 will be moved by the rotation of the bend die, for this reason no kinematic boundary conditions have been imposed. The Accurate contact algorithm has been chosen for modelling the interaction between the objects by following the contact matrix in Table 5. 3, where all the friction coefficients have been reported. The values of the friction coefficient have been already validated in [2]. The resume of the boundary conditions has been presented in Table 5. 4.

Master / Slave	Tube	Clamp die 1	Clamp die 2
Bend Die	0.5	0.99	
Clamp die 1	0.99		0.99
Clamp die 2	0.99		
Wiper die	0.12		
Pressure die	0.5		
Mandrel	0.08		

Table 5. 3: master and slave contact relations.

Stage	Object	Rigid Body	Cartesian kinematic	Rotational kinematic
Bending	Bend die (axis elements)	User-defined		Axis position: (0; 0; 0) Axis direction: (0; 0; -1)
	Wiper die	Simplified	Locked translations: X, Y, Z Locked rotations: X, Y, Z	
	Mandrel (rear nodes)		Locked translations: X, Y, Z Locked rotations: X, Y, Z	
	Pressure die (rear nodes)		Locked translations: X, Z Locked rotations: X, Y, Z	
	Clamp die 2 (rear elements)	User-defined		Axis position: (0; 0; 0) Axis direction: (0; 0; -1)

Table 5. 4: resume of the complete boundary conditions imposed in the tube bending simulation setup.

5.4 Comparison of the results between rigid and deformable tools setup

In this paragraph, the results of the rotary drawn bending model with deformable tools will be compared with the ones obtained in [2], where the rigid setup has been analysed and validated.

For clarity, in the following analysis the tube surface will be divided in 3 main zones (Figure 5. 9) as follow:

1. Extrados (orange): the external zone where maximum curvature radius can be measured;
2. Intrados (blue): it is located at the opposite side of the extrados, where minimum curvature radius can be measured;
3. Neutral zone (green): it can be found in the lower part of the tube, where no significant thickness variation can be observed.

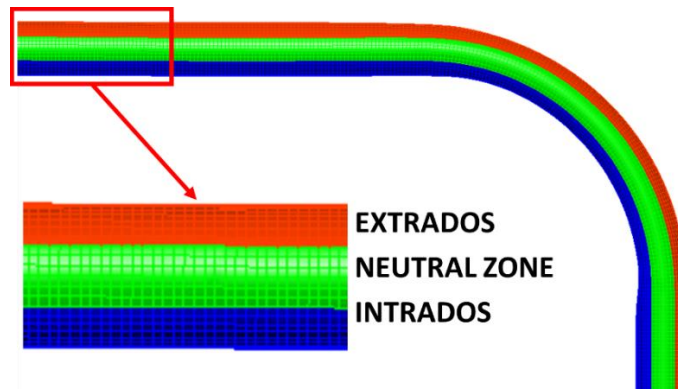


Figure 5. 9: description of the zone on the tube surface.

In Figure 5. 10, the comparison between the thickness profiles of the deformable and rigid cases has been presented. The thickness trends are typical of all tube bending processes. The extrados is the tube zone mainly subjected to stretching, so the thinning phenomenon is normally expected in the bent zone. The thickness profiles are very similar to each other; the maximum difference of 0.03 mm is located at abscissa 75. This maximum difference can be considered negligible at the final usage of the bent component.

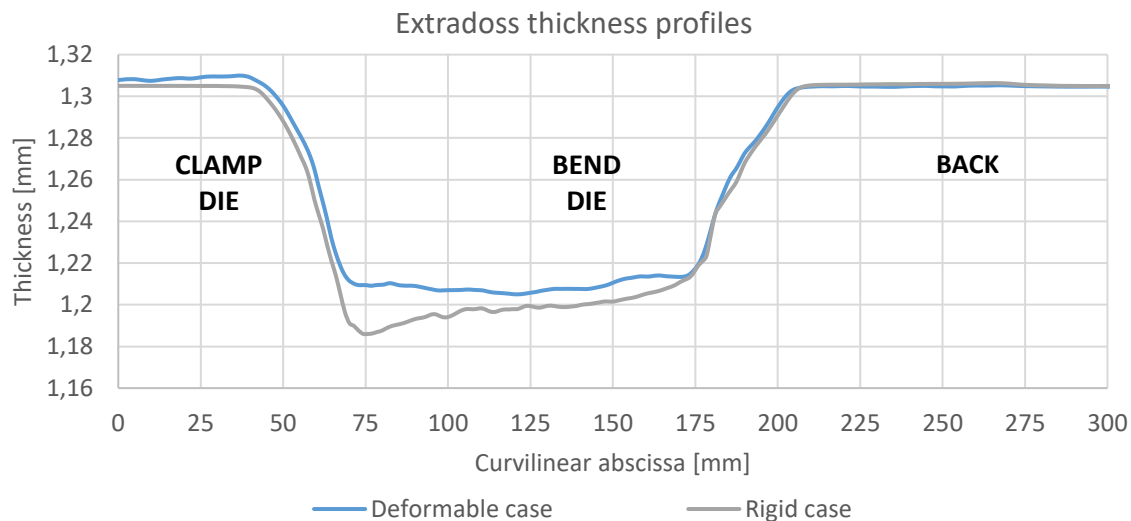


Figure 5. 10: comparison of the extrados thickness profiles between the rigid and deformable cases.

In this case, the material flux on the extrados is controlled by the internal plug, which has been positioned 10 mm over the wiper die due to its smoothed shape. During the bending process, the material tends to lean over the plug surface as shown in Figure 5. 11. The constant thinning observed in the bent zone (Figure 5. 10, BEND DIE zone) of the deformable case suggests that the mandrel is subjected to a local curvature, which gives uniform deformation to the extrados of the tube due to the sliding contact between the mandrel and tube. This result is really positive because the extrados structural behaviour will be more homogeneous due to the constant thinning.

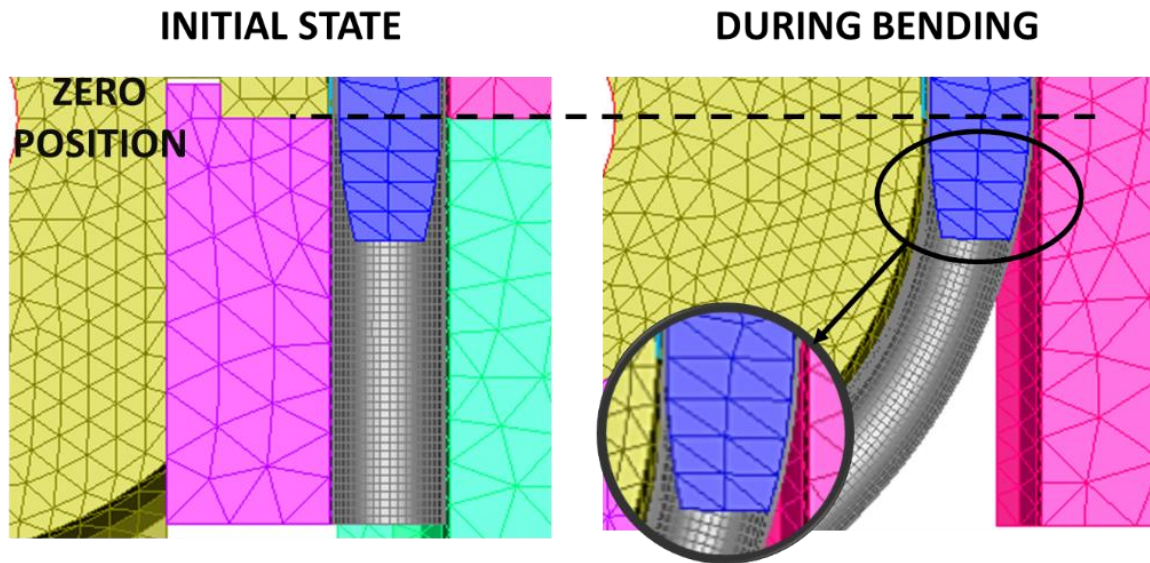


Figure 5. 11: Enlarged view of the mandrel at the initial state and during the bending process.

If on one hand, the introduction of the deformable mandrel represent a good solution for the thinning of the extrados, on the other hand it seems not rigid enough to support the intrados tube wall. In Figure 5. 12, comparison of the intrados thickness profiles has been represented for deformable and rigid case. Two peaks can be observed in the curvilinear abscissa interval [50; 75] mm, which corresponds to the initial bent zone between the clamp and bend dies.

These two differs from the rigid case of 0.02 mm, whose value could be considered negligible from a structural point of view, because the thinning of the higher peak is very close to the maximum thinning values.

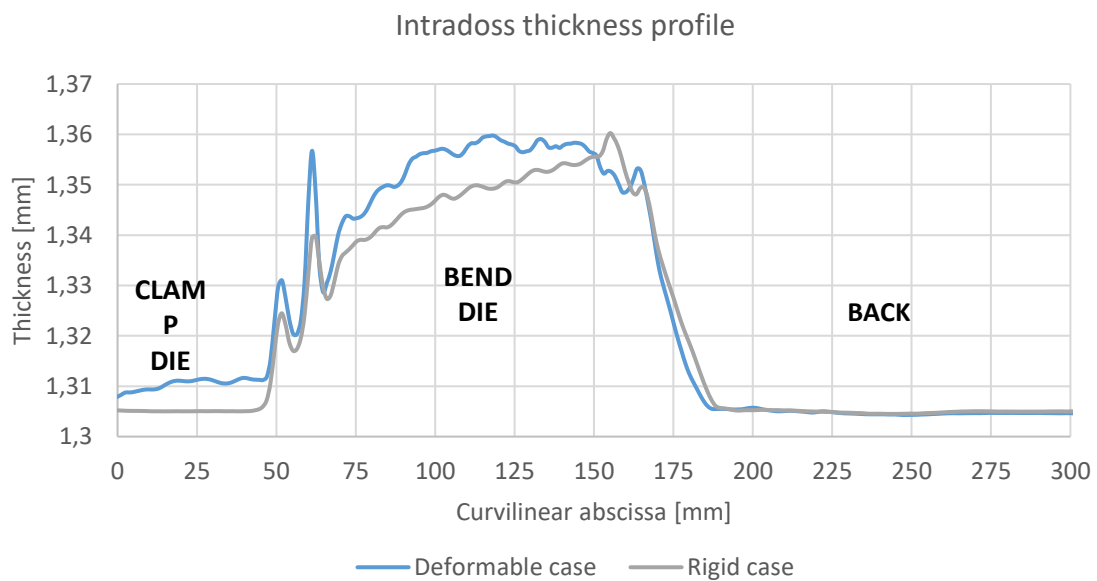


Figure 5. 12: comparison of the intrados thickness profiles between the rigid and deformable cases.

However, from an aesthetical point of view, these two pronounced peaks correspond to higher risk of wrinkling, which normally should be reduced or avoided in the tube bending processes.

The analysis of the FLD diagrams in Figure 5. 13 demonstrates the observations done on the analysis of the intrados and extrados. The deformable case (Figure 5. 13a) presents higher probability of wrinkling with respect to the rigid one (Figure 5. 13b). Higher and non-constant deformation of the extrados in the rigid case. Both cases reveal very scarce use of the material deformability, especially for the deformable case which presents lower deformation along the principal direction (ordinate axis in Figure 5. 13a).

In Figure 5. 14, the geometry of the deformable case after the spingback analysis has been compared with the rigid one in terms of distance map. In the intrados zone a wave trend of the distance map can be observed which corresponds to a very high wrinkling trend of the deformable case. The negative values on the extrados zone and the positive values in the neutral zone (referring to Figure 5. 9 for the nomenclature) indicates respectively a compression and stretching of the section of the tube.

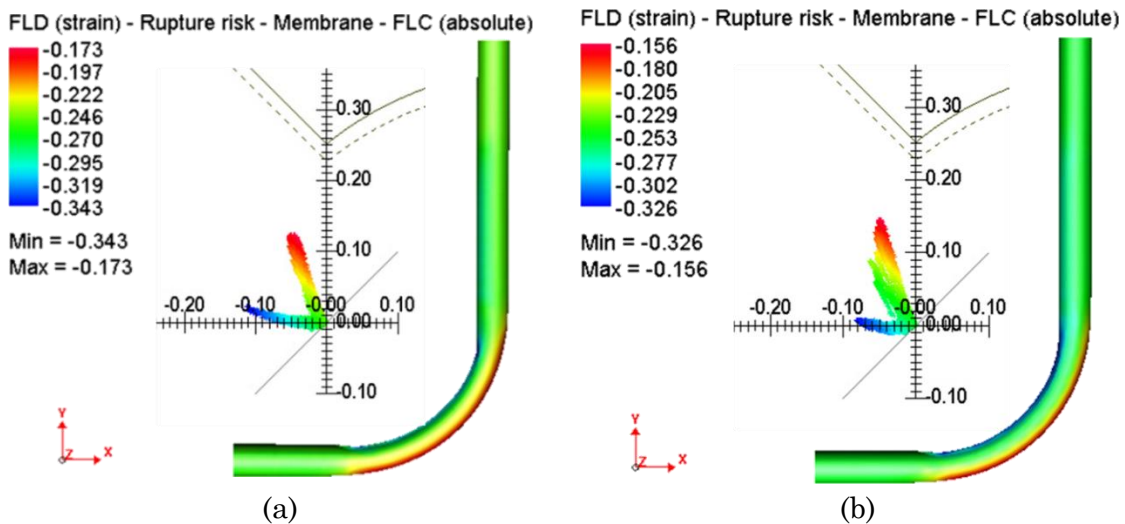


Figure 5. 13: FLD diagram of the bent tube in the deformable (a) and rigid (b) cases.

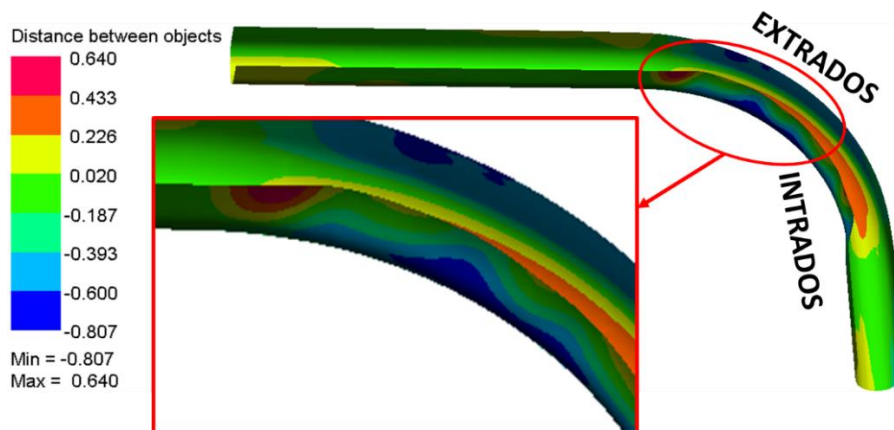


Figure 5. 14: distance analysis between the tube bended with rigid tools and the one bended with deformable tools.

These effects indicate a high ovalization trend of the section of the tube bended with deformable tools. In order to better explain the phenomenon, the simulated tubes sections of the deformable case and the rigid one, obtained at 45° of the bend zone (Figure 5. 15a), have been compared in Figure 5. 15b. The section of the deformable case (red line in Figure 5. 15b) is more compressed along the X direction and more stretched along the Y direction.

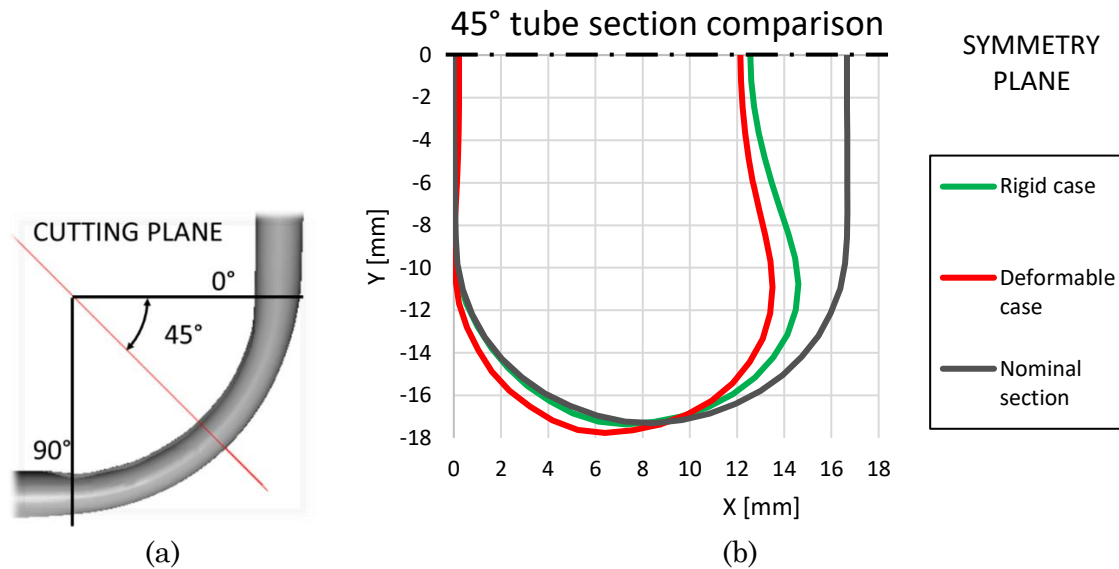


Figure 5. 15: schematization of the section at 45° (a) and comparison between the simulated tubes section with the nominal one.

The comparison of the two test cases demonstrates that the rigid and deformable setups can give back very similar results in terms global deformations of the bent tube, but different result in terms of esthetical defects, like wrinkling and ovalization of the section. From these first considerations, it can be affirmed that the deformable tools could not be suitable for esthetical components.

In order to evaluate which tool can tolerate the rotary bending process, a final stress analysis on the deformable tools has been presented.

In Figure 5. 16, the Von Mises stress maps have been presented for deformable tools. The pressure die (Figure 5. 16a) presents a stress concentration in the rear zone of the tools, which is in contact with the tube at the end of the process. The maximum value of the stress concentration is far from the elastic limit of the material, so the polyurethane material can be used for manufacturing these kind of tools. Same results have been achieved for the clamp die 1 (Figure 5. 16b), the one linked to the bend die. The stress concentration is located in the contact zone between the clamp die 1 and the bend die; the maximum stress value does not reach the elastic limit of the material, so this result suggests that also the clamp die 1 could be manufactured with polyurethane material. It should be noted that the tools as the clamp die 1 are can be included in the structure of the bend die; so the stress concentration, registered in this case, could be avoided. Similar result can be observed in the clamp die 2 (Figure 5. 16c), where the stress concentration is located in the protrusion in contact with the

clamp die 1. The maximum value of 53 MPa is near to the elastic limit of the material, so the modification of the topology of the component is required (e.g. suppression of the protrusion where the stress concentration is located) in order to eliminate or reduce the stress concentration.

The mandrel (Figure 5. 16d) presents maximum value of stress concentration of 57 MPa in the zero position zone (Figure 5. 11) due to the flexural load given by the interaction with the tube. The maximum value of the Von Mises stress registered on the mandrel suggests that the polyurethane material cannot substitute the metal. Similar result has been observed on the bend die where the maximum Von Mises stress is 55 MPa located on the round corner corresponding with contact interface with the tube. This stress concentration close to the elastic limit on the flange of the bend die is due to the stretching of the tube section observed previously in Figure 5. 15b. This concentration could produce the plasticization and, consequently, the break of the bend die after few cycles.

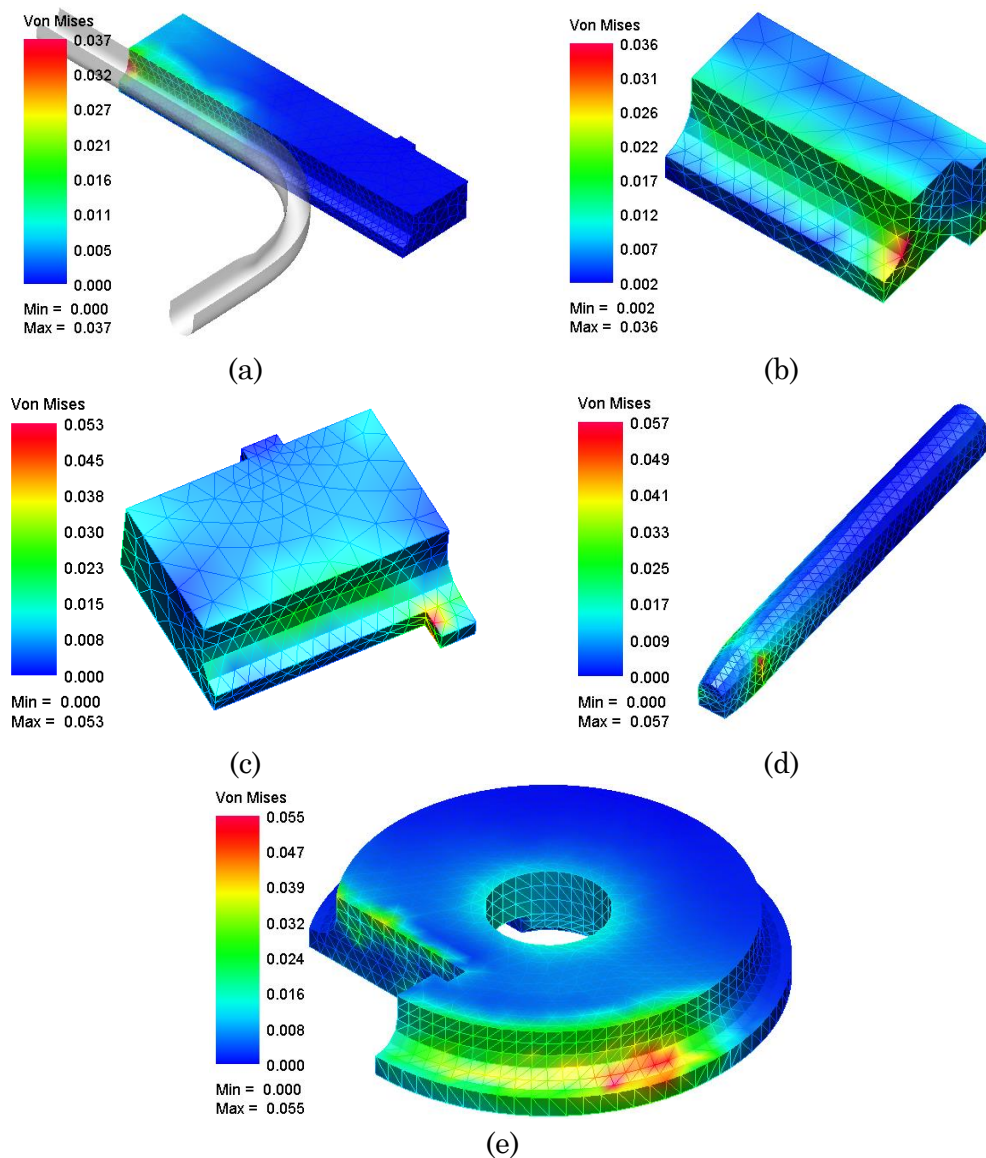


Figure 5. 16: Von Mises stress maps on the pressure die (a), clamp die 1 (b), clam die 2 (c), mandrel (d) and bend die (e).

5.5 Design improvement

The results obtained from the simulation model of the rotary draw bending process with deformable tools demonstrates that only the clamp and the pressure dies made by polyurethane material can be used in the bending process without any or few modification to the original design.

In this paragraph, the modifications of the design concept of the bend die and the mandrel will be proposed in order to solve the issues found in the previous numerical activities.

As described before in paragraph 5.4, the high stress concentration on the bend die (Figure 5. 16e) can produce the break after few cycles of the lower zone of the tool. For this reason, a modification to the design of the bend die has been proposed in Figure 5. 17 with a protrusion of 10 mm of the lower surface (blue) in order to reinforce the structure. The reinforced bend die will be made by polyurethane material, but it will be bigger and rigid respect to the original design.

The reinforced bend die has been substituted in the simulation model without any other changes. In Figure 5. 18, the Von Mises stress maps of the reinforced bend die at the end of the rotary draw bending process has been presented. The maximum value of the Von Mises stress is reduced at 38 MPa, which is compatible with the ones obtained for the pressure die and clamp die 1. The stress values reached with the reinforced bend indicate that the tool can reach a medium volume batch production, according with the fatigue tests described in chapter 3. Considering the density of the polyurethane material, the modification performed has small impact on the weight of the tool, if compared with the initial one made by steel. This is an interesting result because a reduced weight could allow higher velocity of movement of the bending machine (compatibly with the deformation behaviour of the tube material) by increasing the performance of the process.

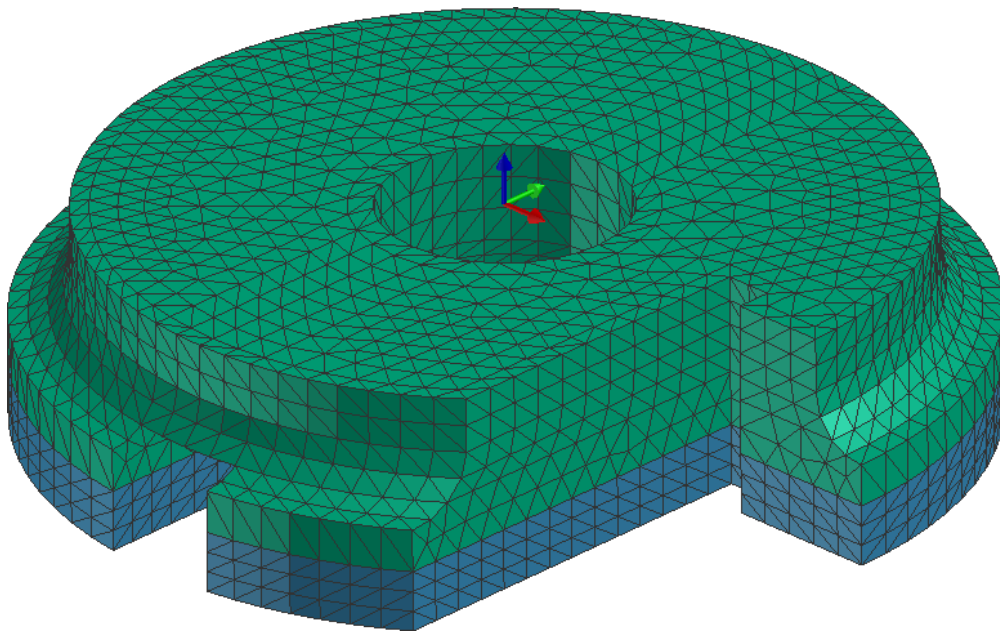


Figure 5. 17: reinforced bed die.

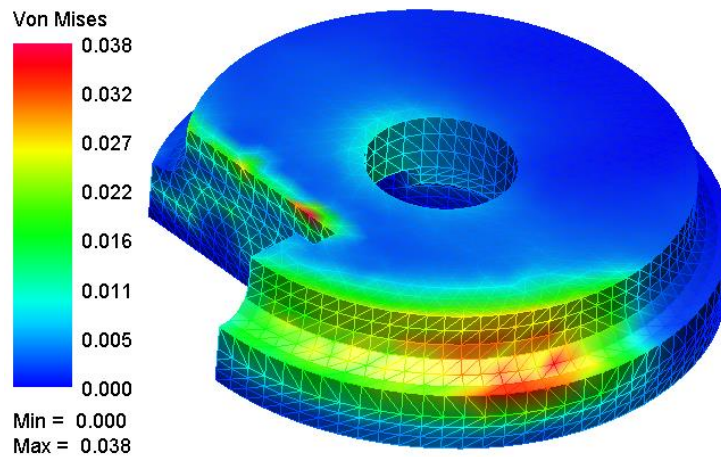


Figure 5. 18: Von Mises stress map on the reinforced bend die obtained from the rotary draw bending simulation model with deformable tools.

The stress maps observed on the mandrel (Figure 5. 16d) suggests that the Necuron 1050 could not be the best substitute of the traditional steel, because the maximum Von Mises stress reached is very close to the maximum compression strength of the material. For this reason, two main possibilities can be investigated:

1. **Necuron 1150:** according with the compression test results, this material presented higher resistance respect to Necuron 1050. The maximum compression strenght found for the Necuron 1150 is 87 MPa, which is 30 MPa higher respect to the maximum Von Mises stress obtained from the simulation. According with the results of the fatigue tests described in chapter 3, this solution could guarantee a tool life for an middle industrial production volume;
2. **Rubber:** using a hyper-elastic mandrel could be an interesting solution, because it can support the tube walls during all the process, but more simulation activity is required for make more consideration.

A first trial has been done by modelling a rubber mandrel presented in Figure 5. 19 having the same length and positioning of the polyurethane ones. The solid mesh is composed by 4620 hexahedral 8 noded elements with edge dimension of 2 mm.

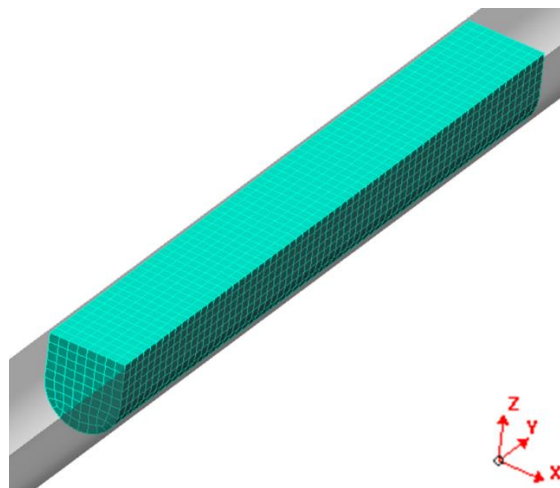


Figure 5. 19: rubber mandrel.

The material behaviour has been modelled with Mooney Rivlin constitutive law by using the same coefficients presented in chapter 4.

The rubber mandrel is dragged by tube during the process, in order to sustain the tube walls in the bent zone.

In Figure 5. 20 the geometrical results of the simulation with rubber mandrel are shown in terms of FLD analysis. The analysis of the FLD diagram shows clearly an accentuated wrinkling phenomenon on the intrados of the bent zone of the tube; the stretching of the extrados (red zone) is very similar with the simulation where polyurethane mandrel. In order to reduce the wrinkling phenomenon, a more rigid mandrel able to support the tube wall in the bent zone should be used. For this reason, the concept of mandrel composed by a pressurized rubber membrane has been modelled (Figure 5. 21a). The length of the rubber membrane is 130 mm, equal to the solid rubber mandrel (described before) and the polyurethane one.

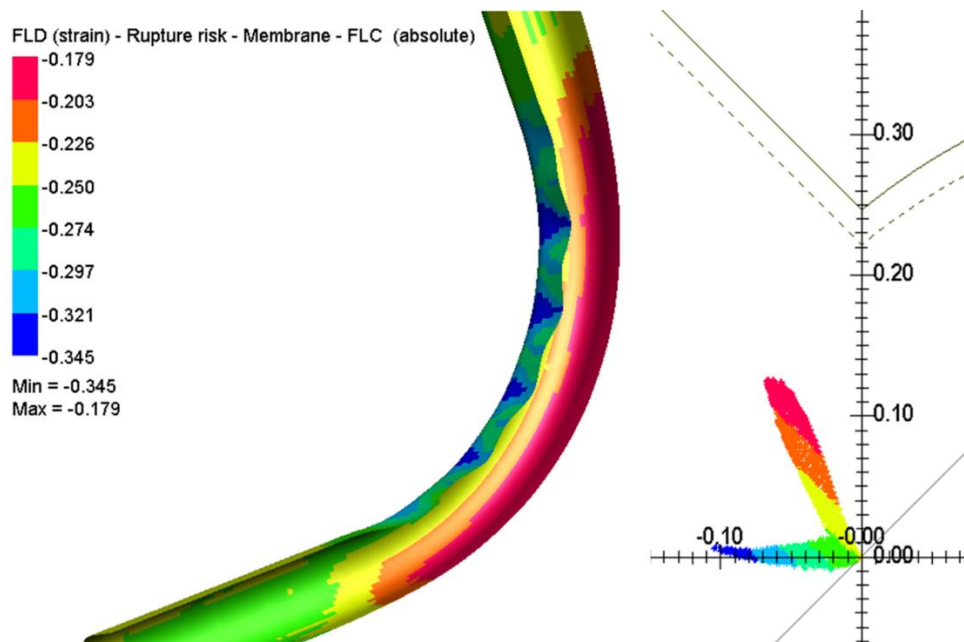


Figure 5. 20: tube FLD diagram of the simulation with rubber mandrel.

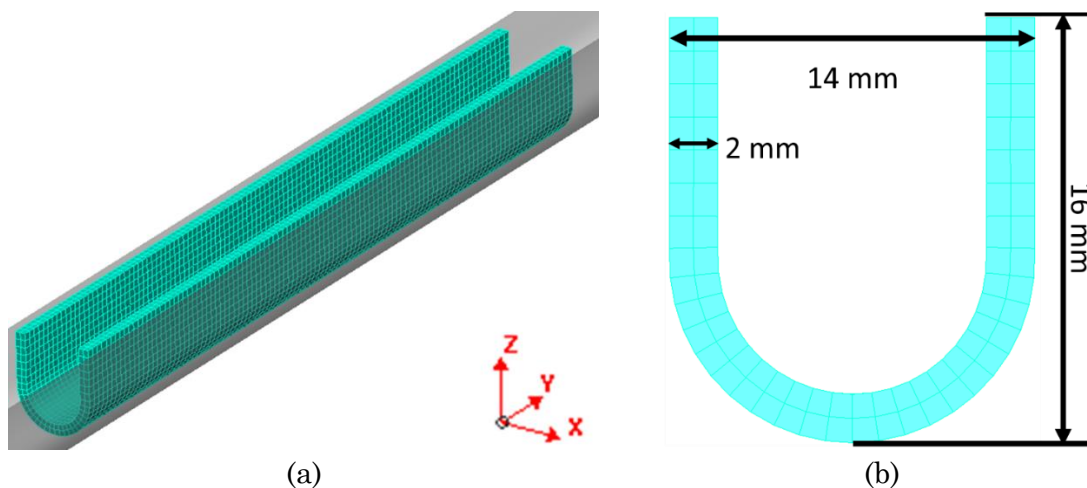


Figure 5. 21: rubber membrane (a) dimensions (b).

The dimensions of the section of the rubber membrane are reported in Figure 5. 21b. The external dimensions of the rubber membrane have been reduced respect to the internal dimensions of the tube in order to ease the extraction of it at the end of the bending process, when the pressure will be released.

The pressure value applied at the end of the rubber membrane has been evaluated by analyzing the major stress values on the tube section along the Plane XY coming from the simulation with the rubber mandrel (Figure 5. 22). The pressure value of 120 MPa, to be applied in the internal surface of the rubber membrane (Figure 5. 23a), has been calculated as a mean value of the major stress measured on the tube section in the bent zone. In order to apply the pressure on the internal surface of the membrane, a shell mesh with the same elements edge dimensions of the rubber membrane has been designed and successively merged in each nodal position with the rubber membrane, as schematized in Figure 5. 23b.

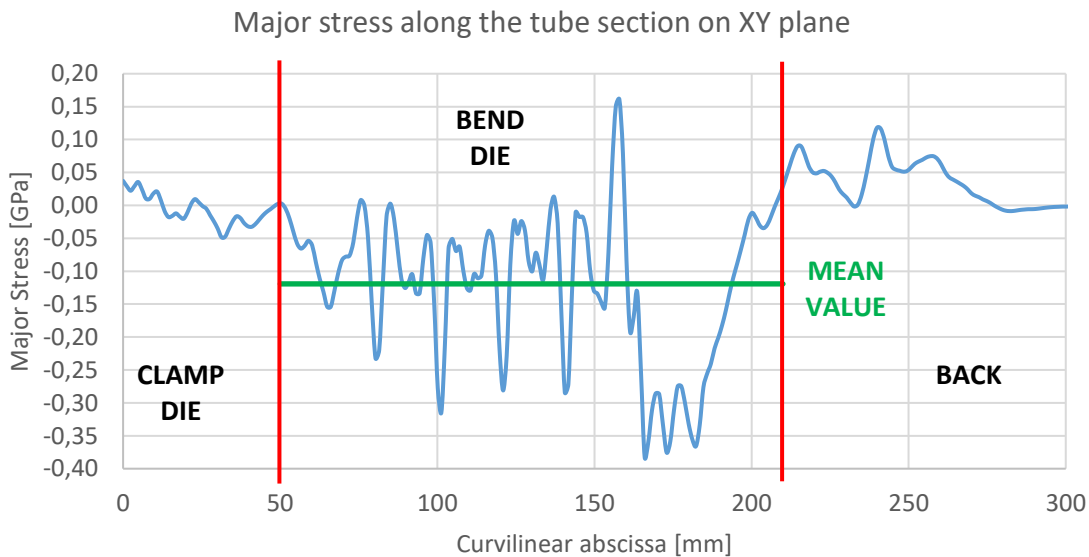


Figure 5. 22: Major stress measured on the tube section along the plane XY.

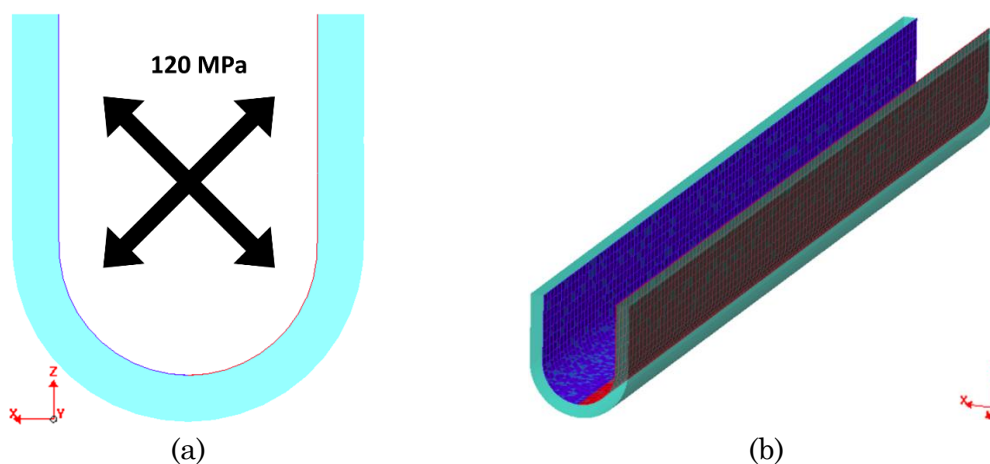


Figure 5. 23: application of the internal pressure of 120 MPa (a) and schematization of the internal surface modelled with shell elements.

In Figure 5. 24 the results of the simulation with the pressurized rubber membrane have been presented in terms of FLD analysis. The results of the FLD diagram shows that the wrinkling phenomenon is drastically reduced on the tube intrados. The reduced wrinkling phenomenon causes higher thickening on the intrados respect to the rigid (metal tools) and deformable case (polyurethane tools) (Figure 5. 25). Similar results can be observed on the extrados where the thinning is more severe (Figure 5. 26) because the tube wall are subjected to free stretching without any control. If on the aesthetical point of view the reduction of the wrinkling on the intrados is a very positive result, the higher thinning on the extrados reveal a very important criticality of this case, which can causes the fracture of the tube. The results obtained from intrados and extrados demonstrate that the pressure value should be a compromise between the appearing of wrinkling phenomenon, due to low level of pressure, and the risk of fracture (on extrados), due to high level of pressure.

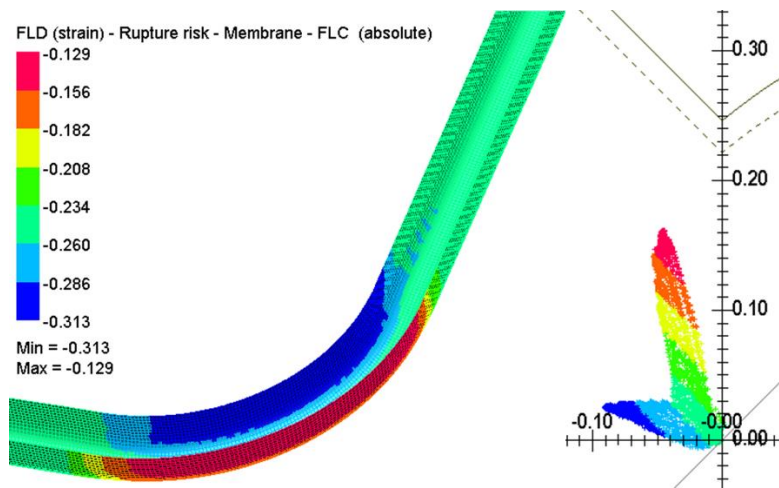


Figure 5. 24: FLD diagram of the tube bent with the pressurized rubber membrane.

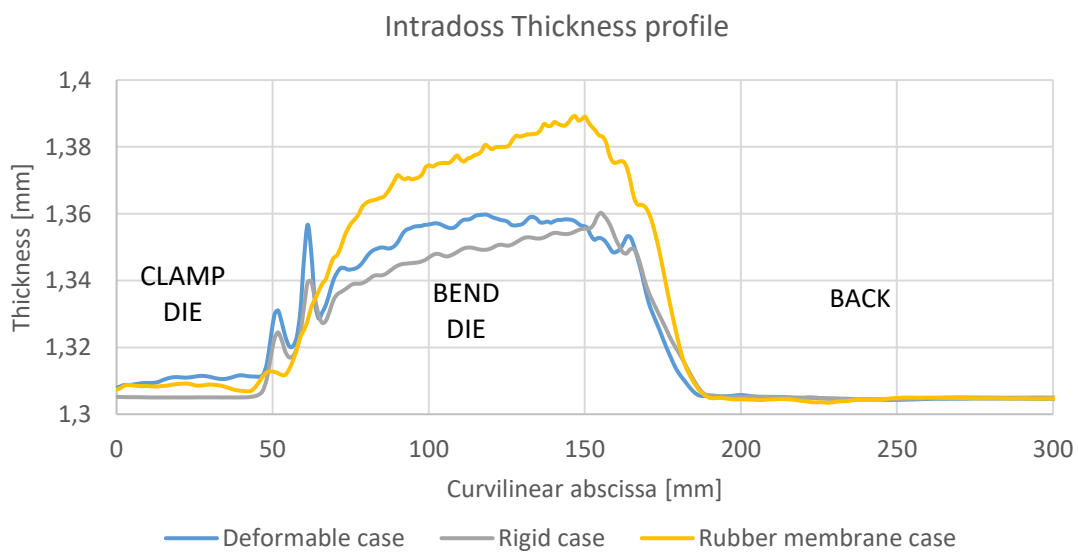


Figure 5. 25: comparison of the thickness distribution on the tube intrados for rigid, deformable and rubber membrane cases.

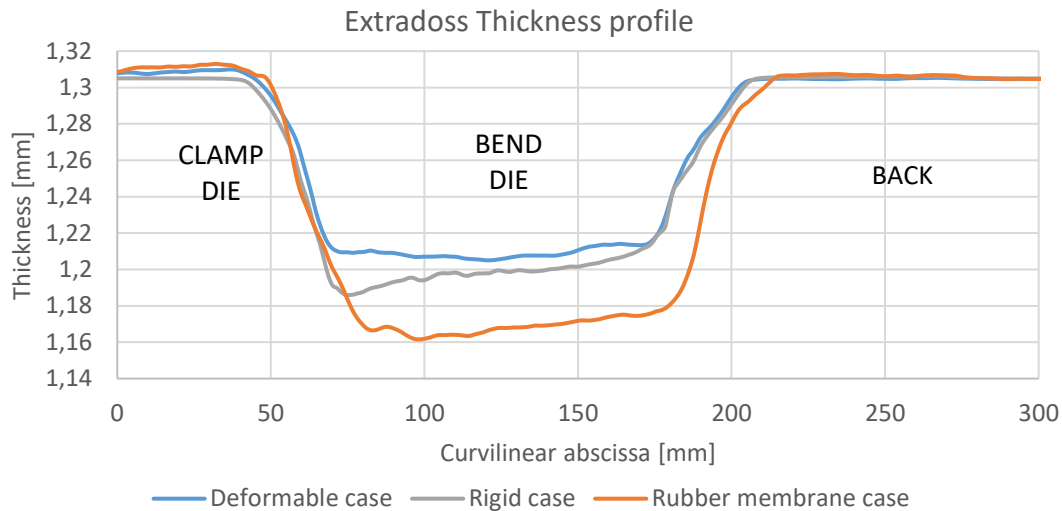


Figure 5. 26: comparison of the thickness distribution on the tube extradoss for rigid, deformable and rubber membrane cases.

5.6 Conclusions

In this chapter, the analysis of the rotary draw bending tube process with rapid tool has been carried out. The simulation model of the bending process with deformable tools has been compared with the one with rigid tools, which has been largely validated in [2]. The geometrical results of the bent tube with deformable tools is very similar with the one bent with rigid tools setup in terms of thinning. Higher risk of wrinkling has been observed in the deformable case due to a scarce support of the tube wall from the deformable mandrel. The stress analysis performed on the deformable tools suggests that only the clamp and pressure die can tolerate the bending process with very low impact on their structure. For this reason a modification of the topology of the bend die and the mandrel have been proposed. The simulation demonstrated that a stiffening of the bend die structure can reduce the magnitude of the stress concentrations in order to use the tool for middle volume industrial productions. More complicated study has been done for the mandrel where an initial substitution of the initial polyurethane mandrel with a rubber ones did not give back any positive results in terms of wrinkles phenomenon. The transformation of the rubber mandrel in a pressurized rubber membrane allowed reducing the wrinkling phenomenon with very positive impact on the aesthetic point of view. Unfortunately, the introduction of a rubber membrane in the rotary draw bending process leads a lot of complications on the process planning, which can be partly solved with the aid of virtual simulation, and on the design of the bending machine where a water pressure control system should be considered. In this case, a complete transformation of the tools setup from traditional to “rapid” cannot lead in an economic setup because the complications introduced on the machine structure may cause the increment of the process costs. Therefore, if the tools concepts introduced in this chapter can be considered rapid tools, these same concepts (rubber membrane included) cannot be considered “smart tools” because the implementation costs of them can exceed the ones of the traditional rigid solutions.

5.7 References

- [1] ZHU, Y. X., et al. Springback prediction for rotary-draw bending of rectangular H96 tube based on isotropic, mixed and Yoshida–Uemori two-surface hardening models. *Materials & Design*, 2013, 47: 200-209.
- [2] L. Iorio, *Curvatura Di Tubi A Sezione Non Circolare: Analisi Fem E Sperimentale*, 2009. Bachelor Thesis at Università di Cassino.
- [3] A. Mentella, *Metodi di Progettazione Avanzata per la Curvatura di Tubi a Controllo Numerico*, 2009. Doctoral Thesis at Università di Cassino.

Conclusions

In this doctoral thesis, the rapid tools have been studied as an alternative possible solution to the traditional rigid metal tools setup and rubber ones, normally used in sheet metal forming process.

Initially, a general state of the art about the rigid and rubber tools setups has been performed by analysing the cold sheet metal forming processes most diffused in the industrial scenario. The analysis of the sheet metal forming processes with metal and rubber tools allowed to identify the advantages and disadvantages of these two macro categories of tools setup intended to outline the necessity of the investigation of new solutions based on different tools materials. For this reason, an analysis of possible innovative materials suitable for tooling purpose has been conducted. The analysis has been performed by comparing the main properties normally evaluated for tools manufacturing (i.e. Young Modulus, Yield strength, Fatigue strength and Price) and identifying three main material domains: metal, plastics and elastomer. The analysis of the materials demonstrates that some reinforced plastic materials can be suitable for tooling purpose thanks to their material properties equivalent with commercial aluminium alloys and their low price respect to traditional metal tools. Consequently, the choice of plastic materials, as possible alternative solution to the traditional metal alloys and elastomers, identified the rapid tooling as suitable technology for tooling purpose. The state of the art of the rapid tools demonstrated that a lot of literature is available about the concept of the rapid tools, but very few design methods or design guidelines have been developed. Furthermore, the resin tooling methodology has been chosen as most convenient technology for manufacturing the case study analysed in this thesis, thanks to his similarity with the traditional milling operations normally used for manufacturing the metal tools.

After the analysis of the rapid tools technologies, a review of polymer materials has been presented in order to define their classification and the attended mechanical behaviour, which will be encountered during the subsequent mechanical compression and tensile tests. As described before, three types polyurethane materials, one pure polyurethane (Necuron 1150) and two reinforced polyurethanes (Necuron 1050 and 1300) have been chosen for the case studies analysed in this doctoral thesis. Destructive tensile and compression tests have been performed in order to compare their elastic response to typical load, because the FEM software, which has been used for the numerical simulations, calculates the effective stress in a symmetrical way with respect to mean tensile and compression states of stress. In other words, a unique Young's modulus for tension and

compression can be defined. In order to tests the capability of the FEM software PAM-STAMP in predicting the deformation of the characterized polyurethane materials, the simulations of the compression tests have been performed by testing the software response at different elements formulations. These numerical tests demonstrated that the tetrahedral and hexahedral linear elements formulation give back the same results in the elastic behaviour of the materials tested. Tetrahedral elements formulation has been chosen for describing the tools geometry of the case studies

because the free shape of the tools surfaces did not allowed the mesh generation of only hexahedral elements.

Consequently to the choice of tools manufacturing technology, the materials and the software to be used for numerical simulations, three representative sheet (blanks and tubes) metal stamping processes, stamping, air bending and tube rotary draw bending, have been chosen for the development of the case studies for practically testing the capabilities of the rapid tools.

The first case study, composed by a standard stamping tools setup (die, punch and blankholder), made by reinforced polyurethane, has been designed by the author and implemented at MUSP Laboratory of Piacenza. A series of experiments has been conducted in the MUSP Lab at different values of blankholder force, in order to obtain the necessary data for validating the FEM model of the process. The validation of the FEM models has been performed by various comparisons with the experimental results:

1. Dimensional comparison: the components profiles have been measured by the CMM (Coordinate Measuring Machine) available at the Measure Lab in the Mechanical Department of Politecnico di Milano;
2. Strain maps comparison: with the collaboration the German company ViALUX, the strain maps of the stamped component has been obtained by analysing the deformation of a mesh previously applied on the flat blanks;
3. Analysis of fracture: only one experimental condition reach the fracture of the blank, the same experiment has been simulated with the software, which identified, with the analysis of the FLD, the same fracture shape at the same zones.

After the validation of the FEM model of the stamping process with rapid tools, the analysis of the residual stress on the polymeric tools and the analysis of the deviations between the stamped component and the designed one have been performed. The stress analysis demonstrated that the tools did not reach the plastic field deformations; but the deviation analysis identified the main disadvantage of a rapid tools setup in the stamping process related to the large deviations between the stamped component to the designed one. This phenomenon can be related to the local elastic deformations of the tools and blank springback effect visible in the analysis of the simulation models. In order to overcome this issue, a compensation algorithm, integrated with the simulation model, has been presented. No compensation algorithm able to compensate at the same time the errors related to the springback of the stamped blank and the tools deformations has been found in literature by the author. For this reason, a state of the art about the compensation methods developed for rigid tools has been presented in order to justify the compensation method chosen and readapted to the case study. The same methodology, numerical and experimental, has been used in the second, but more complex, stamping case study developed in collaboration with DALF srl. In both cases, the compensation algorithm gave back very good results comparable with the other commercial algorithms developed for rigid tools configurations.

The simulation models developed for the analysis of the two stamping case studies allowed to evaluated the typical loads acting on the rapid tools during the process. This load values have been used as input data in the fatigue tests performed on

standard specimen composed by the same stamping tools materials, for the evaluation of the expected tools life in a hypothetical industrial scenario. The fatigue tests demonstrated that the tools developed in the case studies could resist more than 10^4 cycles, which order of magnitude corresponds to the ones found in the state of the art of the plastic material and it represents a typical medium industrial production volume.

The case studies based on stamping process allowed obtaining enough knowledge about the behaviour of the rapid tools in sheet metal forming so that a new solution based on them as been proposed for air bending process. The polymer die concept developed for the air bending process consisted in a rigid metal frame with interchangeable polymers inserts having the same shape of traditional tools. This rapid tool configuration has been tested with others commercial solutions consisted in dies made by metal, nylon or rubber. The results obtained by the experiments demonstrated again the different behaviours registered in the selection of tools materials presented in the first chapter. The rapid tool configuration returned the same results obtained with the nylon tools, which results was different to the ones obtained with metal and rubber tools configurations. The statistical analysis conducted on the experimental results demonstrated that the performances of the rapid tools, in terms of standard deviations of the air bending process, are similar with the traditional metal tools. The results of the simulations have been in agreement with the experimental ones in terms of final opening angles values. This allowed the validation of the FEM model, which has been used for the evaluation of the residual stresses on the tools. The values of the residual stresses on the polymer bending dies have been compared with the fatigue tests, which revealed the same tools life value calculated for the stamping tools described in the first two case studies.

At the end, a case study based on rotary tube bending process has been created in order to study the behaviour of the rapid tools in the field of tube forming processes. This last case study allowed understanding the limit of the polymer tools. An FEM model of the process, where all tools have been modelled with the cheaper material (Necuron 1050), has been generated and validated with the experimental data obtained in a previous work. The simulation demonstrated that the tube bended with polymer tools is more subjected to wrinkling and ovalization, but the analysis of the FLD shown similar magnitude of deformation. This result suggests that, differently from the stamping processes where esthetical defects can be avoided with the use of polymers die, in tube bending process the rapid tools increase the esthetical defects; but, according by the FLD analysis, maintain the performance of the bended product. The analysis of the residual stresses was in according with the industrial experiences registered with BLM, which collaborated in the experiments conducted in the previous work. Only the clamps and pressure dies can be manufactured with plastics material by saving the original shape of the metal tools configuration. The deformations registered on the bend die tends to open the tools along the direction of the rotation axis. This phenomenon has been justified by the analysis of the tube section, which was more stretched along the same direction exactly in the most stressed zones of the bend die. Similar results has been registered by the company during the design phase of the tools. An improvement of the die design has been presented and tested in a new simulation, whose results demonstrated the feasibility of the modifications. The

analysis of the mandrel revealed residual stresses close to the elastic limit of the material which could be traduced in very scarce tool life, according with the results of the fatigue tests. For this reason, the use of another material like Necuron 1150 has been firstly suggested by the author. Afterward, a design improvement has been proposed with the substitution of rubber plug, which solution gave back very bad results with respect to the initial plastic configuration. For this reason, the possibility of a pressurized rubber membrane as a plug has been investigated. The simulation results demonstrated that the pressurized rubber membrane could remove totally the wrinkles and ovalization defects with a very bad impact on the entire process costs. The implementation of a pressurized solution could complicate to much the entire machine structure with the consequently increase of process costs.

All the results obtained on the case studies demonstrated that design a rapid tools setup with any guidelines could be not trivial operation. The experiments and numerical simulations conducted for stamping and air bending case studies revealed very good performances of the rapid tools for small-medium production, especially if the tools costs are compared with the traditional metal solution. The development of FEM models and compensation algorithm make easier and faster the design phase. This improvement, if added with the very fast manufacturing time registered during the experimental activities, has a great impact on the reduction of the total development time. On the other side, the experience matured with the tube rotary draw bending process demonstrated that, sometimes, the rapid tools could substitute only some components of a tools setup, without the risk of useless process complications.

As future development, it could be very interesting to apply all the knowledge acquired in the stamping process on the production of real commercial components.

On the point of view of the air bending process, according with the results achieved in the another project made in collaboration with AMADA Engineering EU and largely cited in the chapter 4, the possible future development of the modular polymers dies could be related to the developments of prediction algorithm able to predict the final opening angles and elongation which could take in account the deformation of the tools and so improving the actual algorithm currently implemented in the commercial numerical control of the press brakes.

From the results obtained on the tube bending process, it is clear that a dedicated research on tube forming processes with rapid tools is needed, because the types of tube forming processes are so numerous and different to each other that a dedicated research on rapid tools should be conducted only for them.

The author hopes that all the results obtained in this doctoral thesis could be helpful for the diffusion of the rapid tools as a real alternative solution to the tooling setup traditionally used in the sheet metal forming processes.

Appendix A

A-1. Tensile Tests results of polyurethane material

Specimen ID: Necuron 1050 - T1

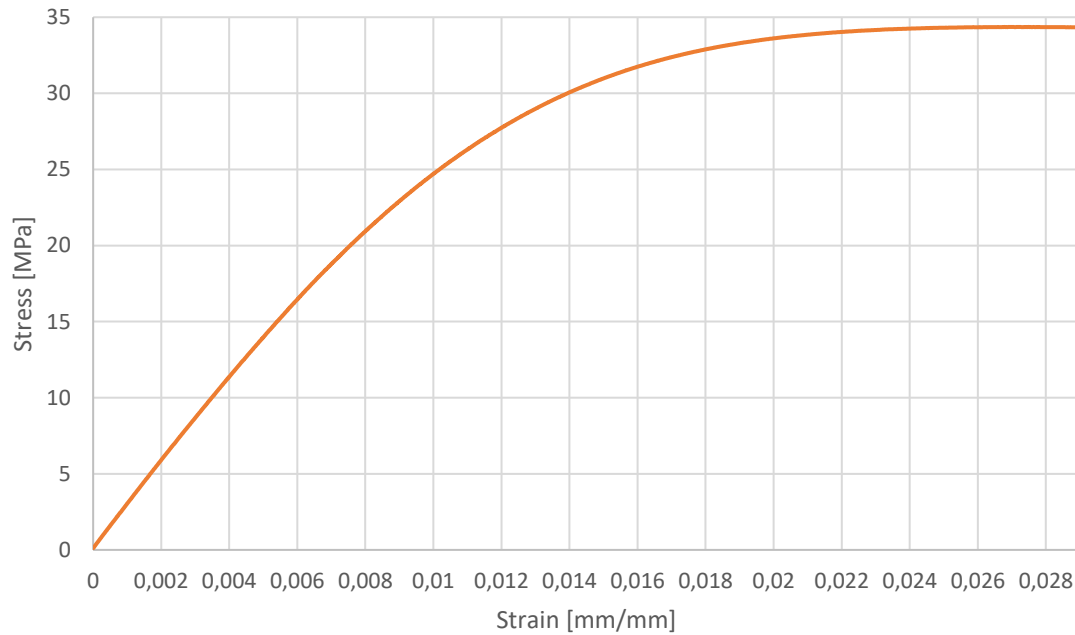


Figure A- 1: Stress strain curve obtained from tensile tests on specimen Necuron 1050 – T1.

Name	Value	Units
Speed	2.00	mm/min
Specimen thickness	14.04	mm
Specimen width	18.95	mm
Young's Modulus	2929	MPa
Rp02	26	MPa
Rp1	34	MPa
Peak Stress	34	MPa
Strain At Break	2.9	%
Stress At Break	34	MPa

Table A- 1: tensile mechanical properties of Necuron 1050 - T1.

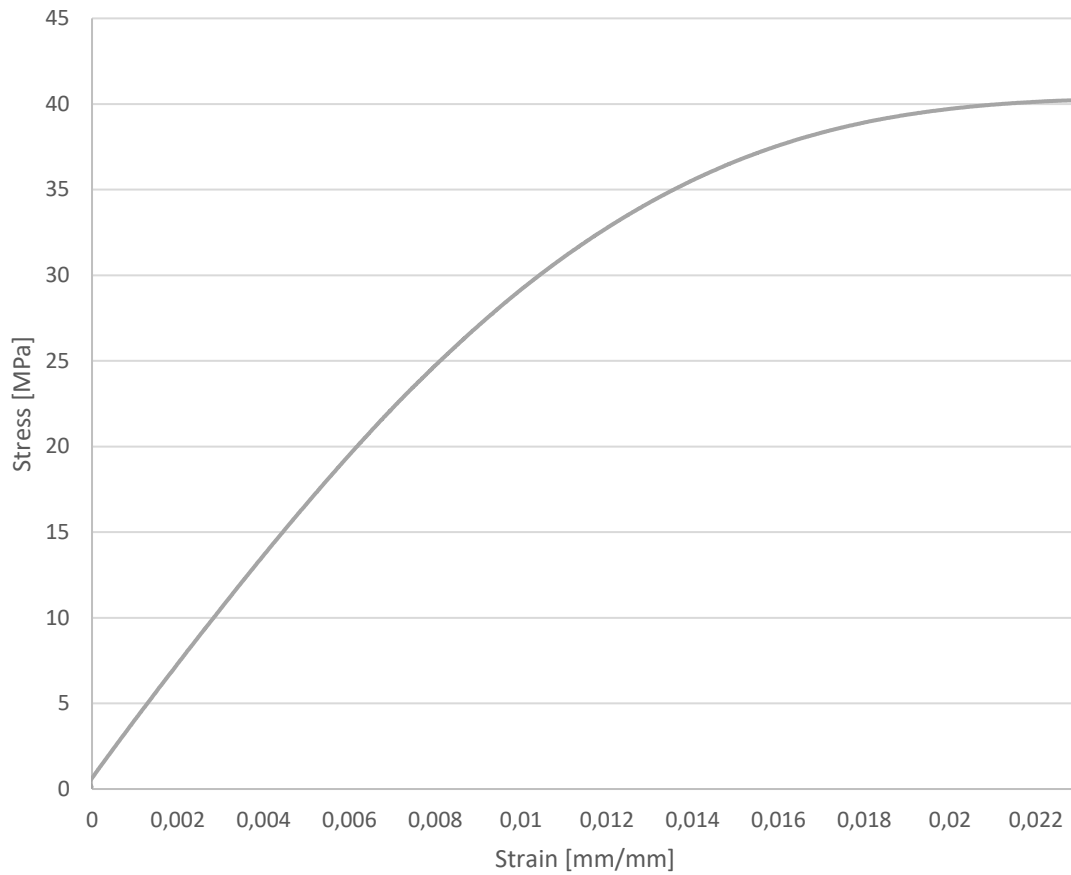
Specimen ID: Necuron 1050 - T2

Figure A- 2: Stress strain curve obtained from tensile tests on specimen Necuron 1050 – T2.

Name	Value	Units
Speed	2.00	mm/min
Specimen thickness	14.01	mm
Specimen width	18.98	mm
Young's Modulus	3413	MPa
Rp02	31	MPa
Rp1	40	MPa
Peak Stress	40	MPa
Strain At Break	2.3	%
Stress At Break	40	MPa

Table A- 2: tensile mechanical properties of Necuron 1050 - T2.

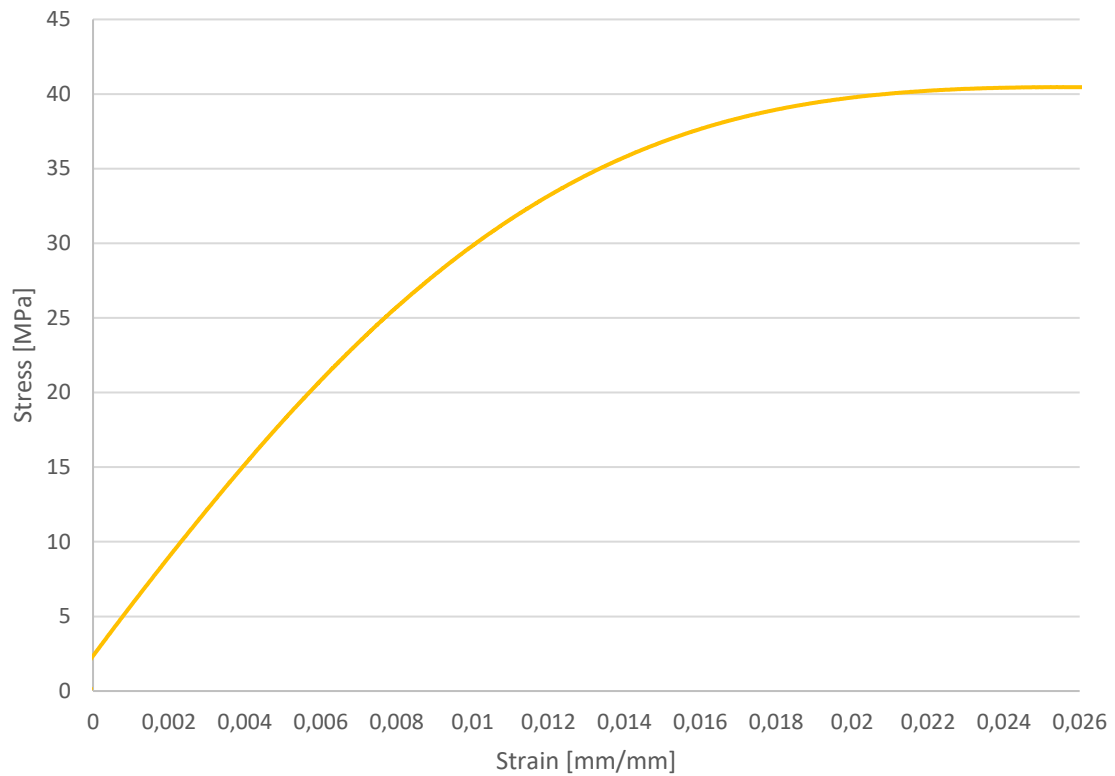
Specimen ID: Necuron 1050 - T3

Figure A- 3: Stress strain curve obtained from tensile tests on specimen Necuron 1050 – T3.

Name	Value	Units
Speed	2.00	mm/min
Specimen thickness	14.02	mm
Specimen width	18.97	mm
Young's Modulus	3400	MPa
Rp02	33	MPa
Rp1	40	MPa
Peak Stress	40	MPa
Strain At Break	2.6	%
Stress At Break	40	MPa

Table A- 3: tensile mechanical properties of Necuron 1050 - T3.

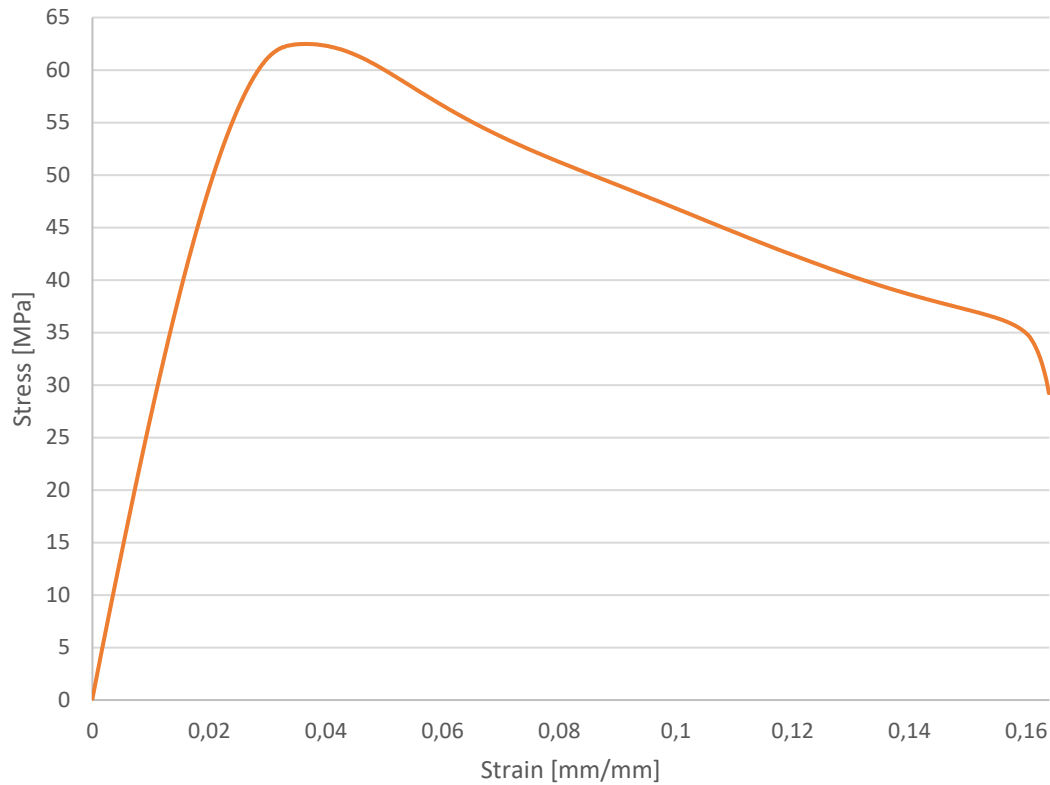
Specimen ID: Necuron 1150 - T1

Figure A- 4: Stress strain curve obtained from tensile tests on specimen Necuron 1150 – T1.

Name	Value	Units
Speed	2.00	mm/min
Specimen thickness	14.13	mm
Specimen width	18.97	mm
Young's Modulus	2875	MPa
Rp02	43	MPa
Rp1	62	MPa
Peak Stress	62	MPa
Strain At Break	16.4	%
Stress At Break	29	MPa

Table A- 4: tensile mechanical properties of Necuron 1150 - T1.

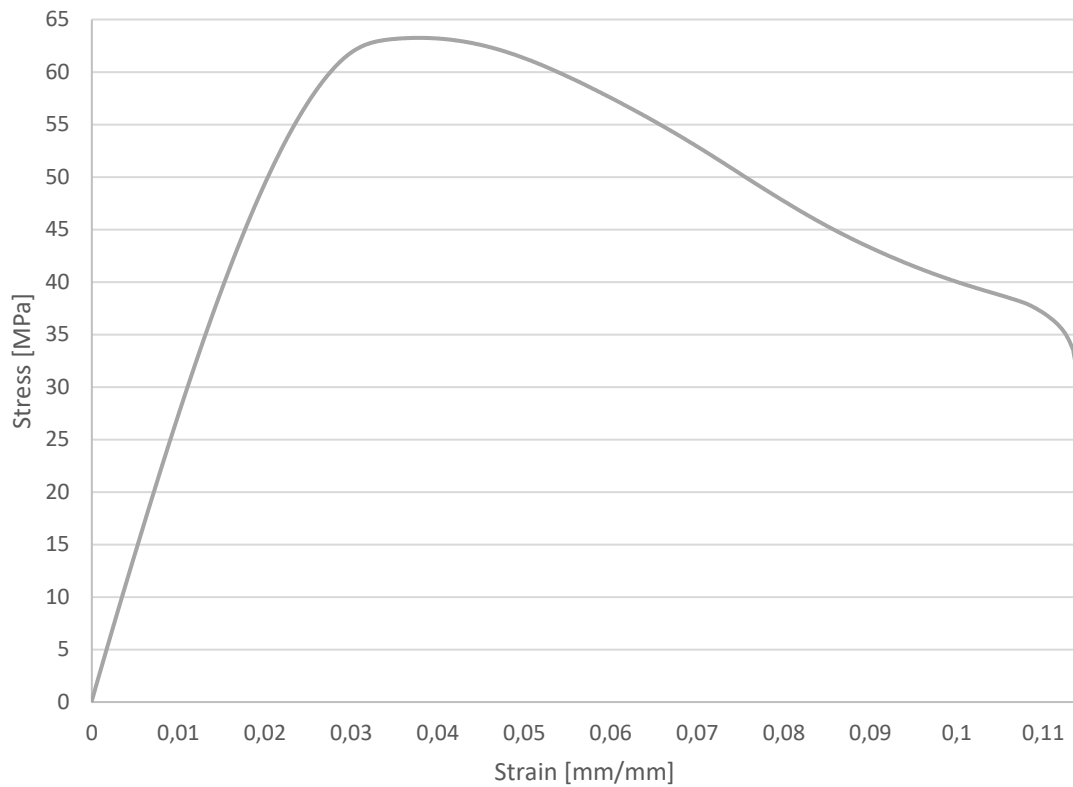
Specimen ID: Necuron 1150 - T2

Figure A- 5: Stress strain curve obtained from tensile tests on specimen Necuron 1150 – T2.

Name	Value	Units
Speed	2.00	mm/min
Specimen thickness	14.02	mm
Specimen width	18.97	mm
Young's Modulus	2918	MPa
Rp02	43	MPa
Rp1	63	MPa
Peak Stress	63	MPa
Strain At Break	11.4	%
Stress At Break	32	MPa

Table A- 5: tensile mechanical properties of Necuron 1150 - T2.

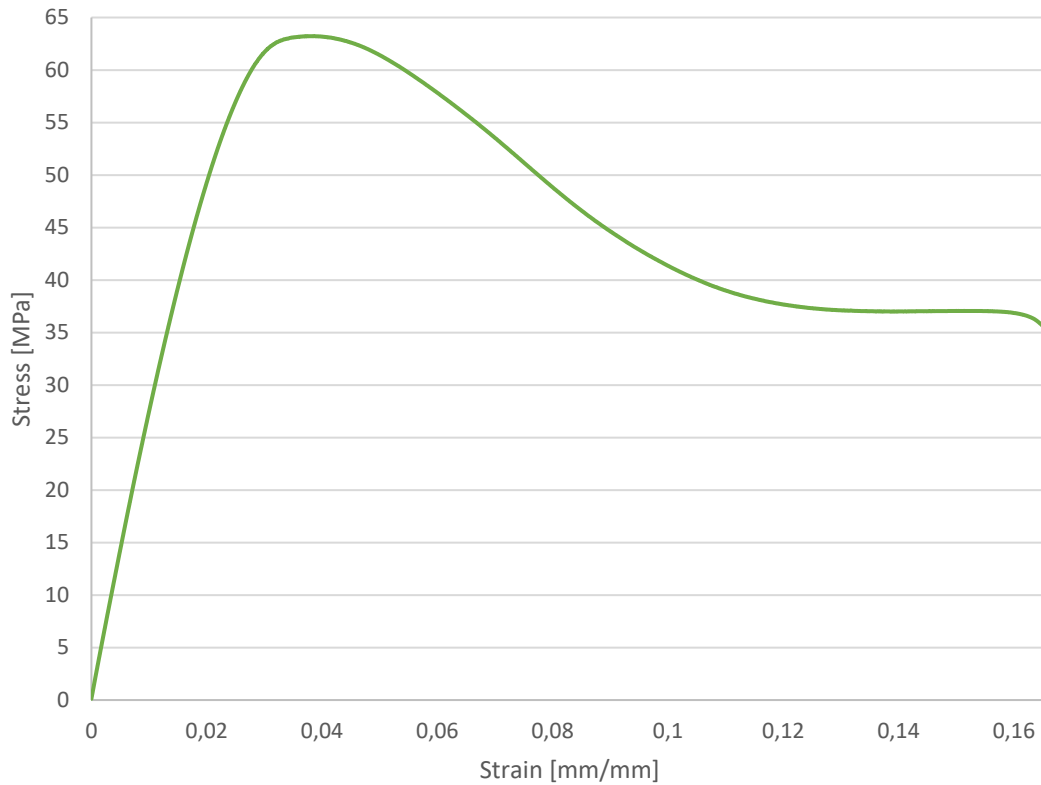
Specimen ID: Necuron 1150 – T3

Figure A- 6: Stress strain curve obtained from tensile tests on specimen Necuron 1150 – T3.

Name	Value	Units
Speed	2.00	mm/min
Specimen thickness	14.06	mm
Specimen width	19.00	mm
Young's Modulus	2952	MPa
Rp02	42	MPa
Rp1	62	MPa
Peak Stress	63	MPa
Strain At Break	16.6	%
Stress At Break	35	MPa

Table A- 6: tensile mechanical properties of Necuron 1150 - T3.

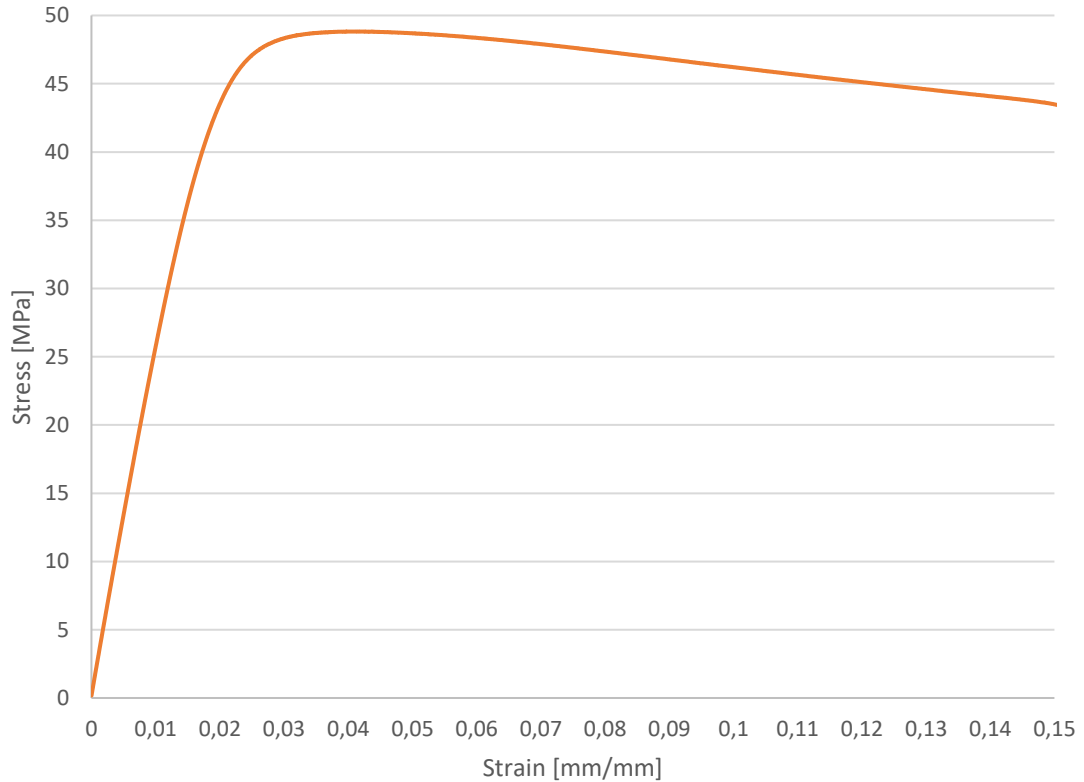
Specimen ID: Necuron 1300 – T1

Figure A- 7: Stress strain curve obtained from tensile tests on specimen Necuron 1300 – T1.

Name	Value	Units
Speed	2.00	mm/min
Specimen thickness	14.00	mm
Specimen width	19.04	mm
Young's Modulus	2752	MPa
Rp02	37	MPa
Rp1	48	MPa
Stress0.2	6	MPa
Strain At Break	15.1	%
Stress At Break	43	MPa

Table A- 7: tensile mechanical properties of Necuron 1300 - T1.

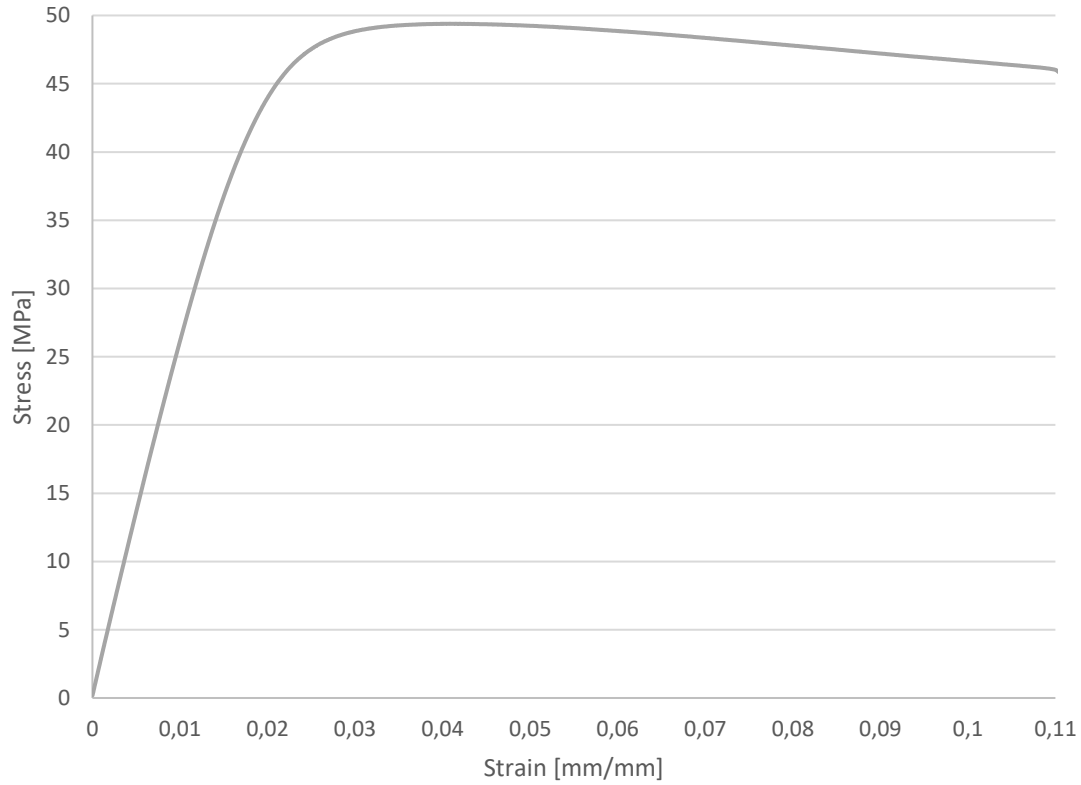
Specimen ID: Necuron 1300 – T2

Figure A- 8: Stress strain curve obtained from tensile tests on specimen Necuron 1300 – T2.

Name	Value	Units
Speed	2.00	mm/min
Specimen thickness	13.98	mm
Specimen width	19.04	mm
Young's Modulus	2783	MPa
Rp02	38	MPa
Rp1	48	MPa
Peak Stress	49	MPa
Strain At Break	11.0	%
Stress At Break	46	MPa

Table A- 8: tensile mechanical properties of Necuron 1300 - T2.

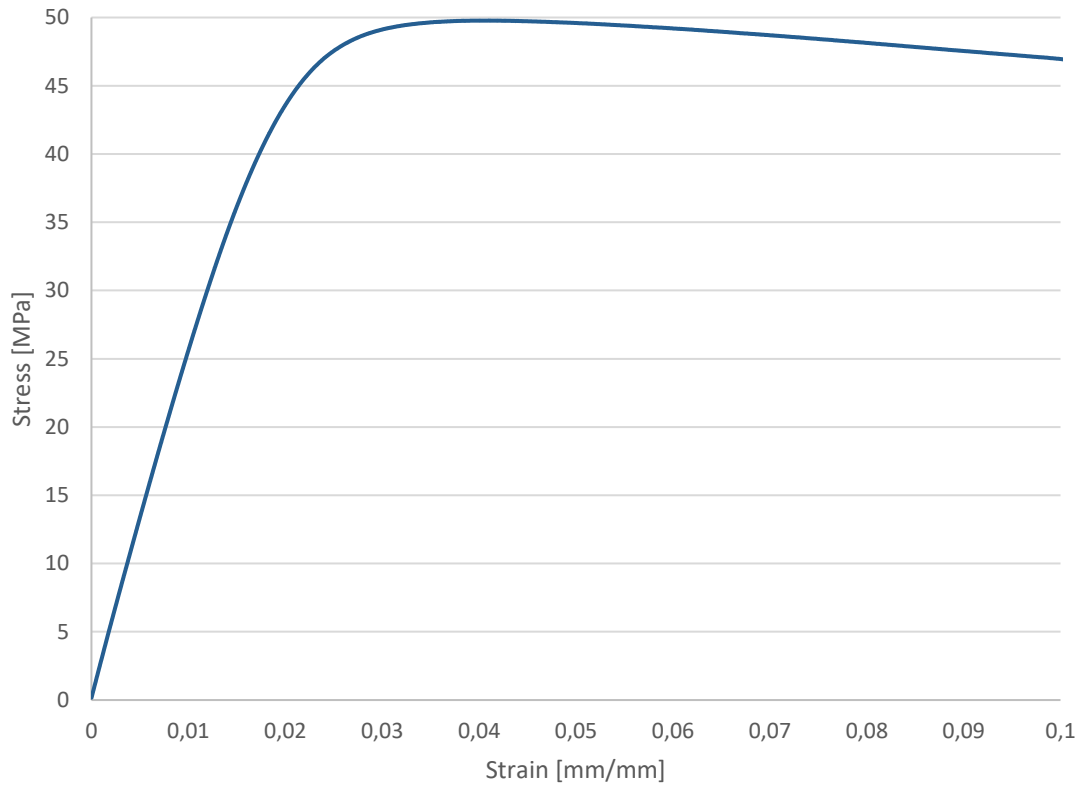
Specimen ID: Necuron 1300 – T3

Figure A- 9: Stress strain curve obtained from tensile tests on specimen Necuron 1300 – T3.

Name	Value	Units
Speed	2.00	mm/min
Specimen thickness	14.00	mm
Specimen width	18.98	mm
Young's Modulus	2747	MPa
Rp02	37	MPa
Rp1	49	MPa
Peak Stress	50	MPa
Strain At Break	10.1	%
Stress At Break	47	MPa

Table A- 9: tensile mechanical properties of Necuron 1300 - T3.

A-2. Compression Tests results of polyurethane material

Specimen ID: Necuron 1050 – C1

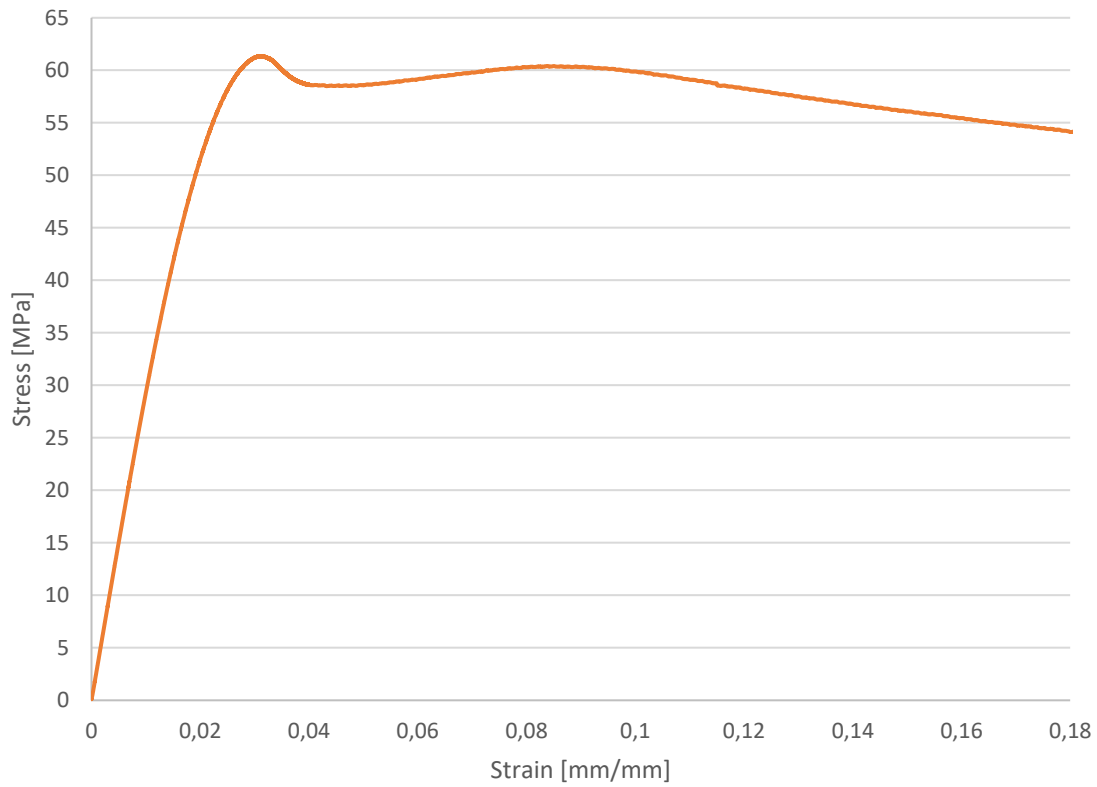


Figure A- 10: Stress strain curve obtained from compression tests on specimen Necuron 1050 – C1.

Name	Value	Units
Speed	1.3	mm/min
Specimen Diameter	12.70	mm
Young's Modulus	2907	MPa
Rp02	50	MPa
Peak Stress	61	MPa

Table A- 10: compression mechanical properties of Necuron 1050 – C1.

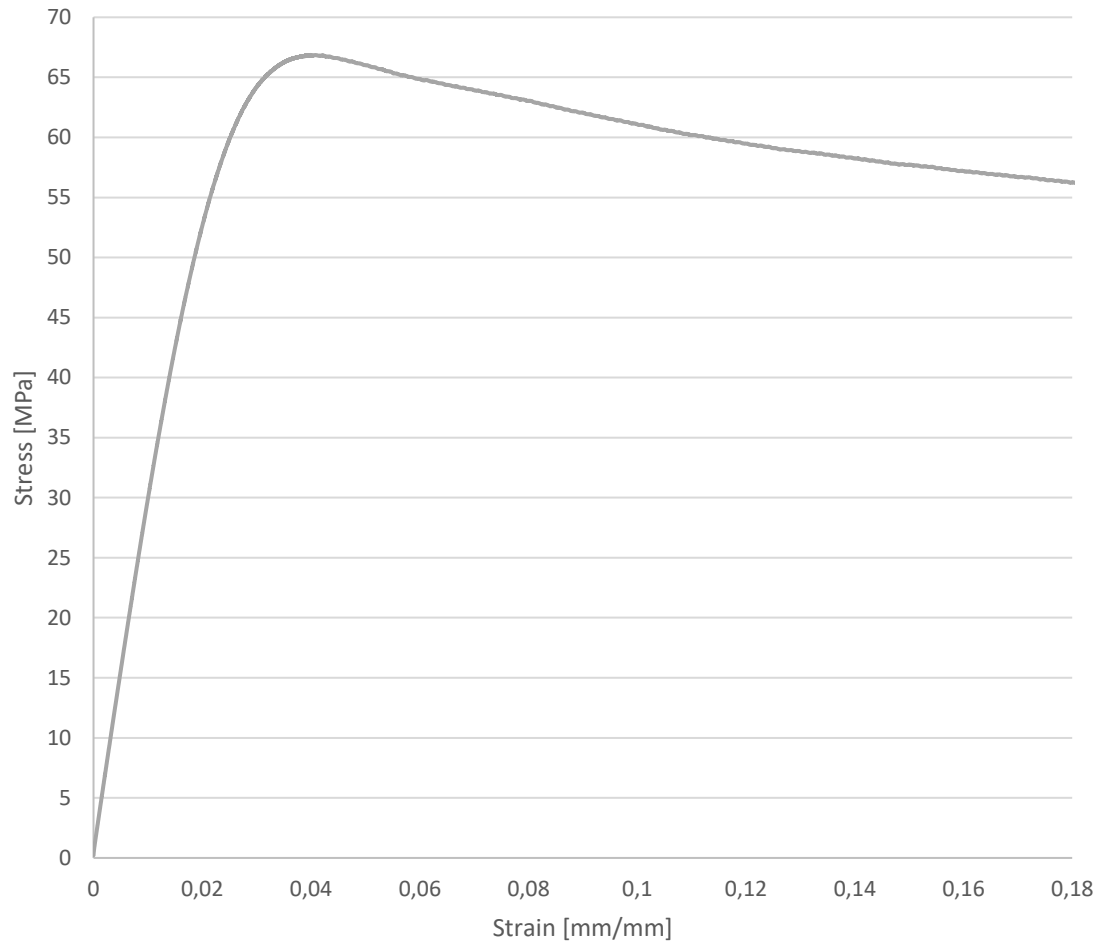
Specimen ID: Necuron 1050 – C2

Figure A- 11: Stress strain curve obtained from compression tests on specimen Necuron 1050 – C2.

Name	Value	Units
Speed	1.3	mm/min
Specimen Diameter	12.70	mm
Young's Modulus	3174	MPa
Rp02	45	MPa
Peak Stress	67	MPa

Table A- 11: compression mechanical properties of Necuron 1050 – C2.

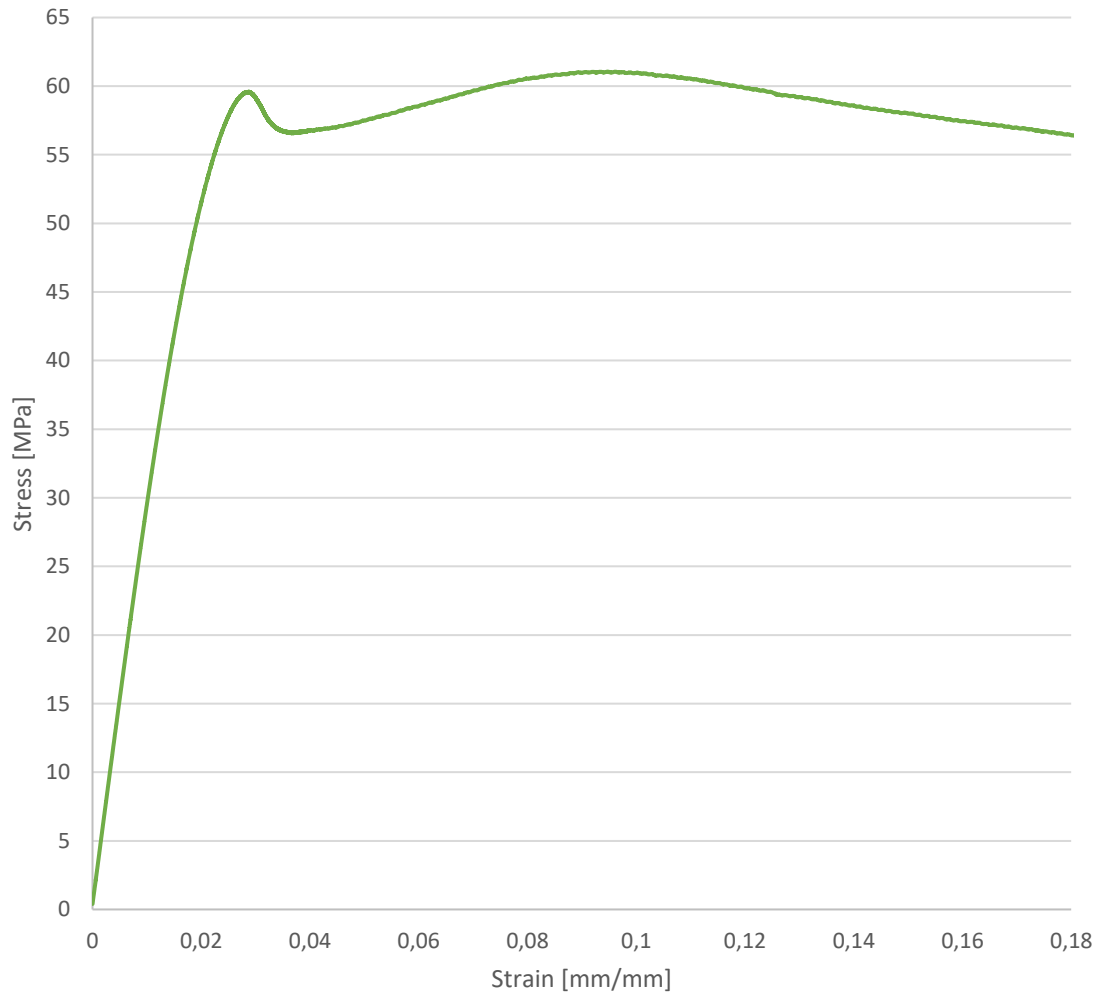
Specimen ID: Necuron 1050 – C3

Figure A- 12: Stress strain curve obtained from compression tests on specimen Necuron 1050 – C2.

Name	Value	Units
Speed	1.3	mm/min
Specimen Diameter	12.70	mm
Young's Modulus	2898	MPa
Rp02	51	MPa
Peak Stress	61	MPa

Table A- 12: compression mechanical properties of Necuron 1050 – C2.

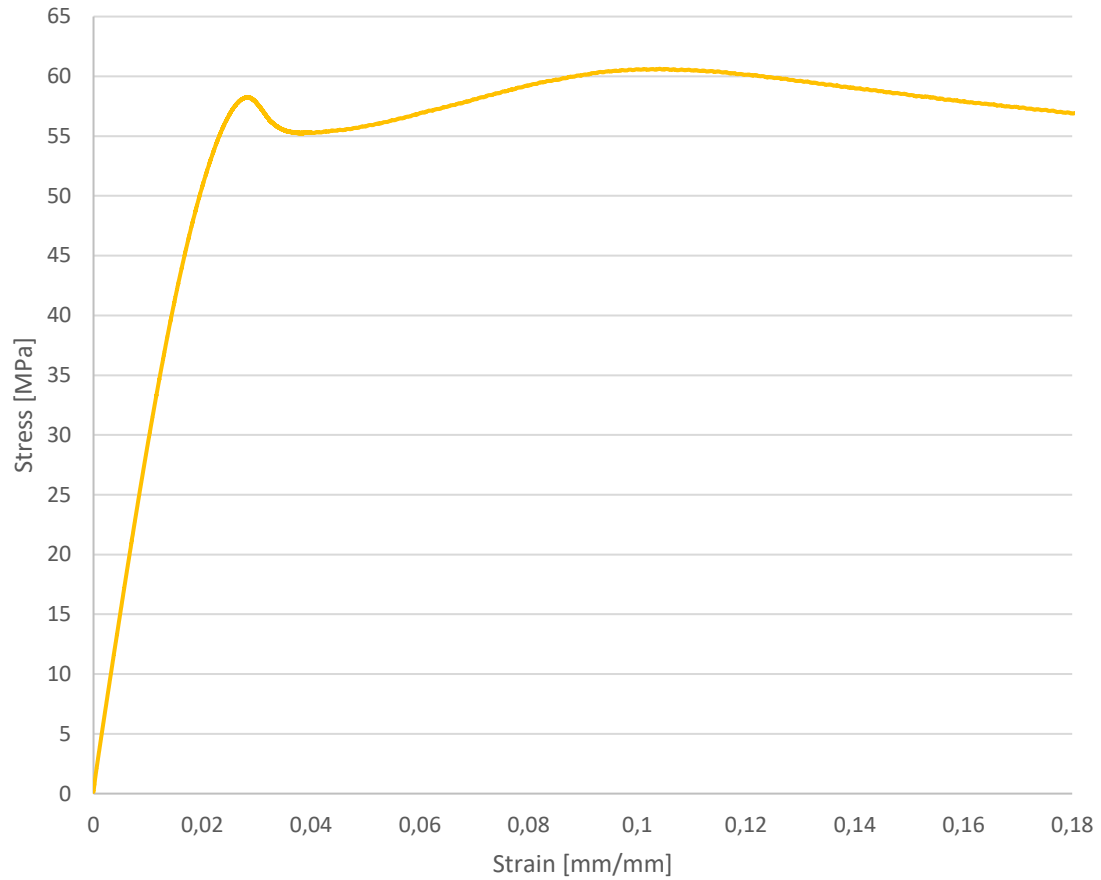
Specimen ID: Necuron 1050 – C4

Figure A- 13: Stress strain curve obtained from compression tests on specimen Necuron 1050 – C4.

Name	Value	Units
Speed	1.3	mm/min
Specimen Diameter	12.70	mm
Young's Modulus	3422	MPa
Rp02	35	MPa
Peak Stress	61	MPa

Table A- 13: compression mechanical properties of Necuron 1050 – C4.

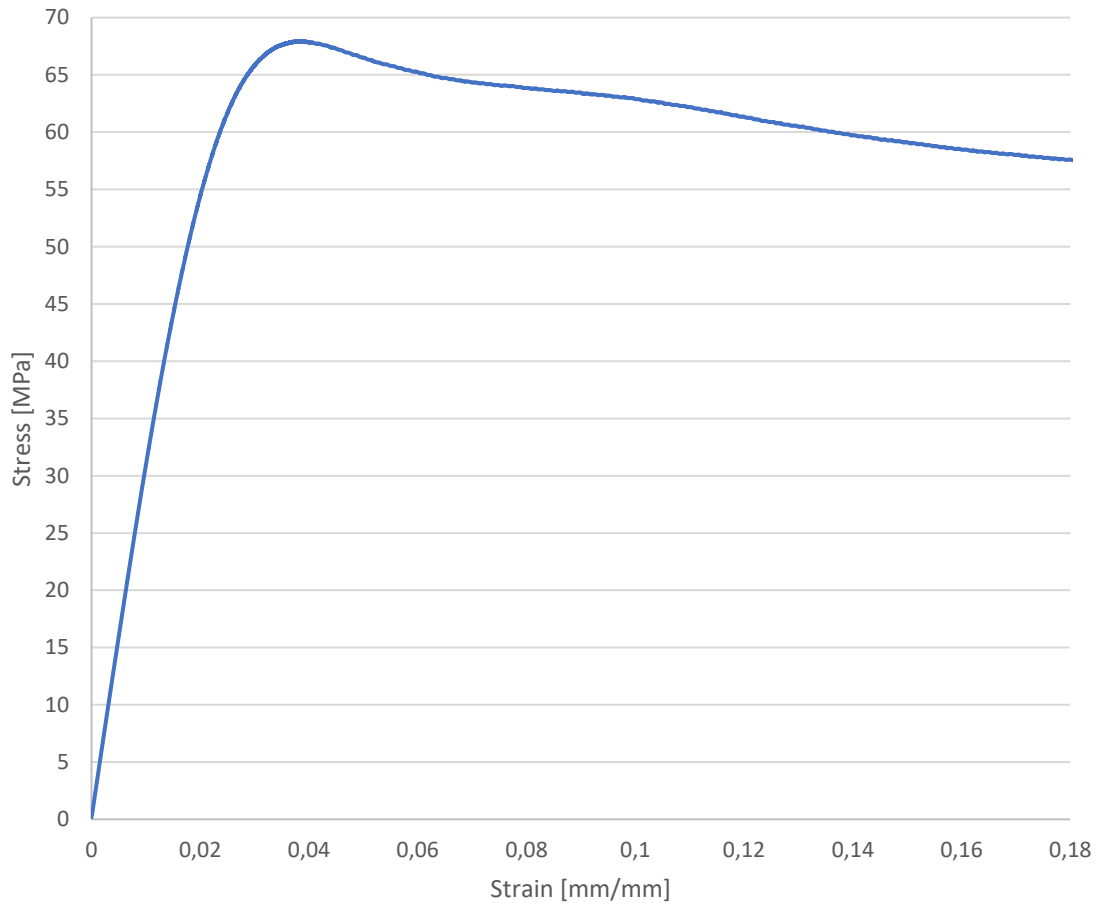
Specimen ID: Necuron 1050 – C5

Figure A- 14: Stress strain curve obtained from compression tests on specimen Necuron 1050 – C5.

Name	Value	Units
Initial Speed	1.3	mm/min
Diameter	12.70	mm
Young's Modulus	3037	MPa
Rp02	54	MPa
Peak Stress	68	MPa

Table A- 14: compression mechanical properties of Necuron 1050 – C5.

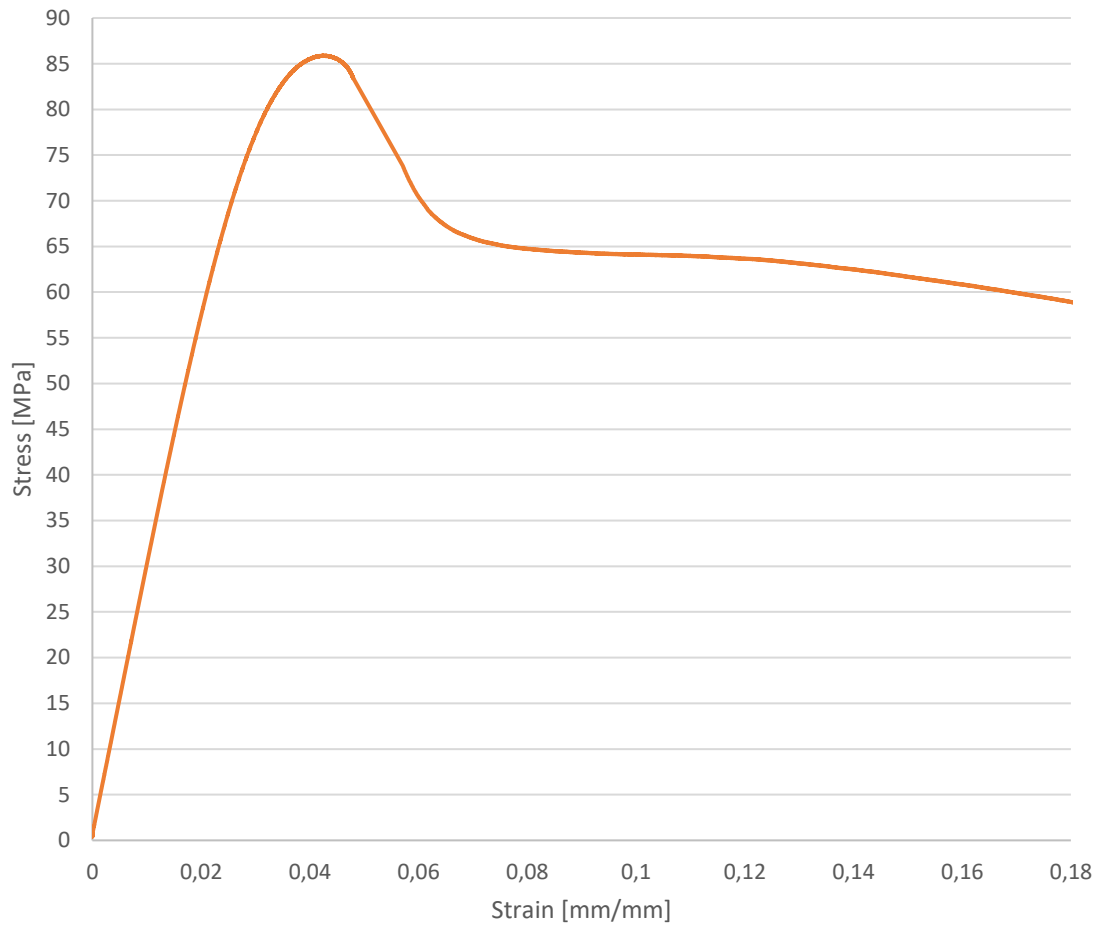
Specimen ID: Necuron 1150 – C1

Figure A- 15: Stress strain curve obtained from compression tests on specimen Necuron 1150 – C1.

Name	Value	Units
Speed	1.3	mm/min
Specimen Diameter	12.70	mm
Young's Modulus	2747	MPa
Rp02	77	MPa
Peak Stress	86	MPa

Table A- 15: compression mechanical properties of Necuron 1150 – C1.

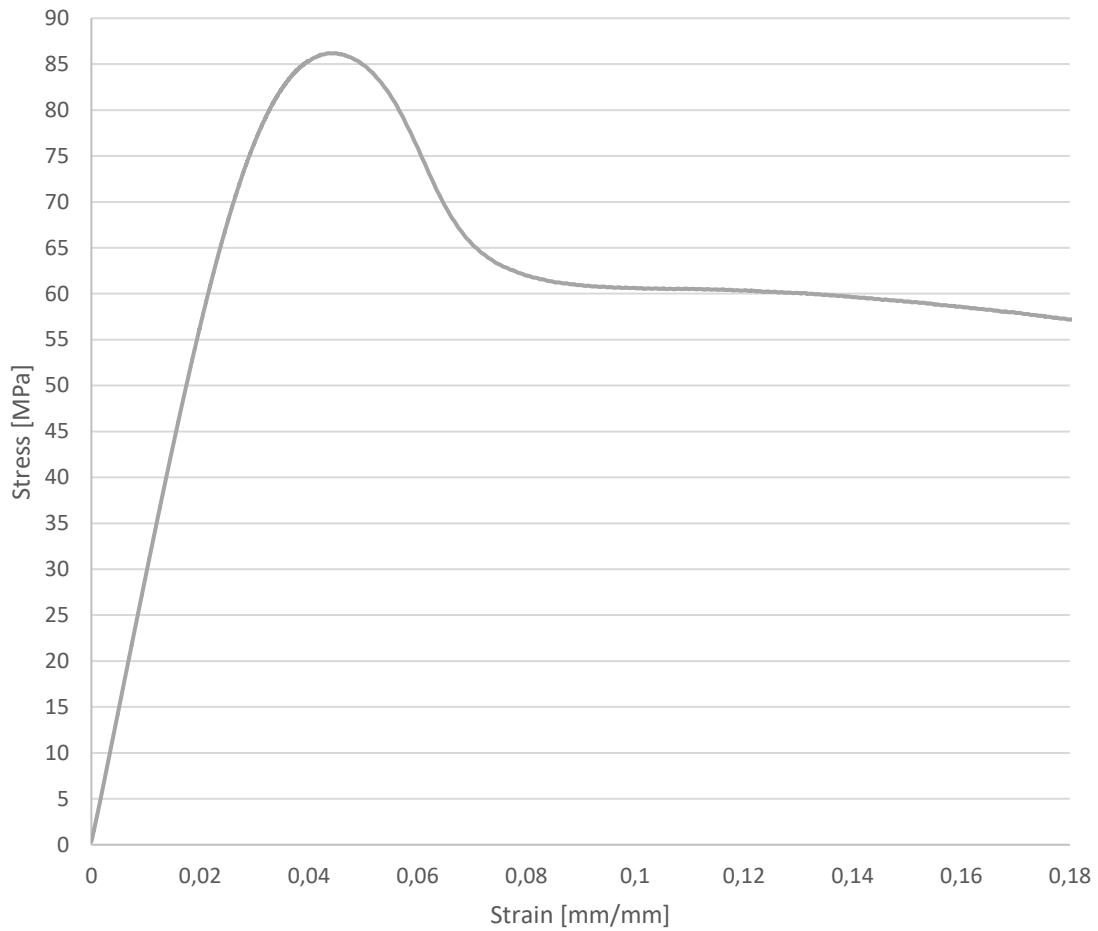
Specimen ID: Necuron 1150 – C2

Figure A- 16: Stress strain curve obtained from compression tests on specimen Necuron 1150 – C2.

Name	Value	Units
Speed	1.3	mm/min
Specimen Diameter	12.70	mm
Young's Modulus	2587	MPa
Rp02	80	MPa
Peak Stress	86	MPa

Table A- 16: compression mechanical properties of Necuron 1150 – C2.

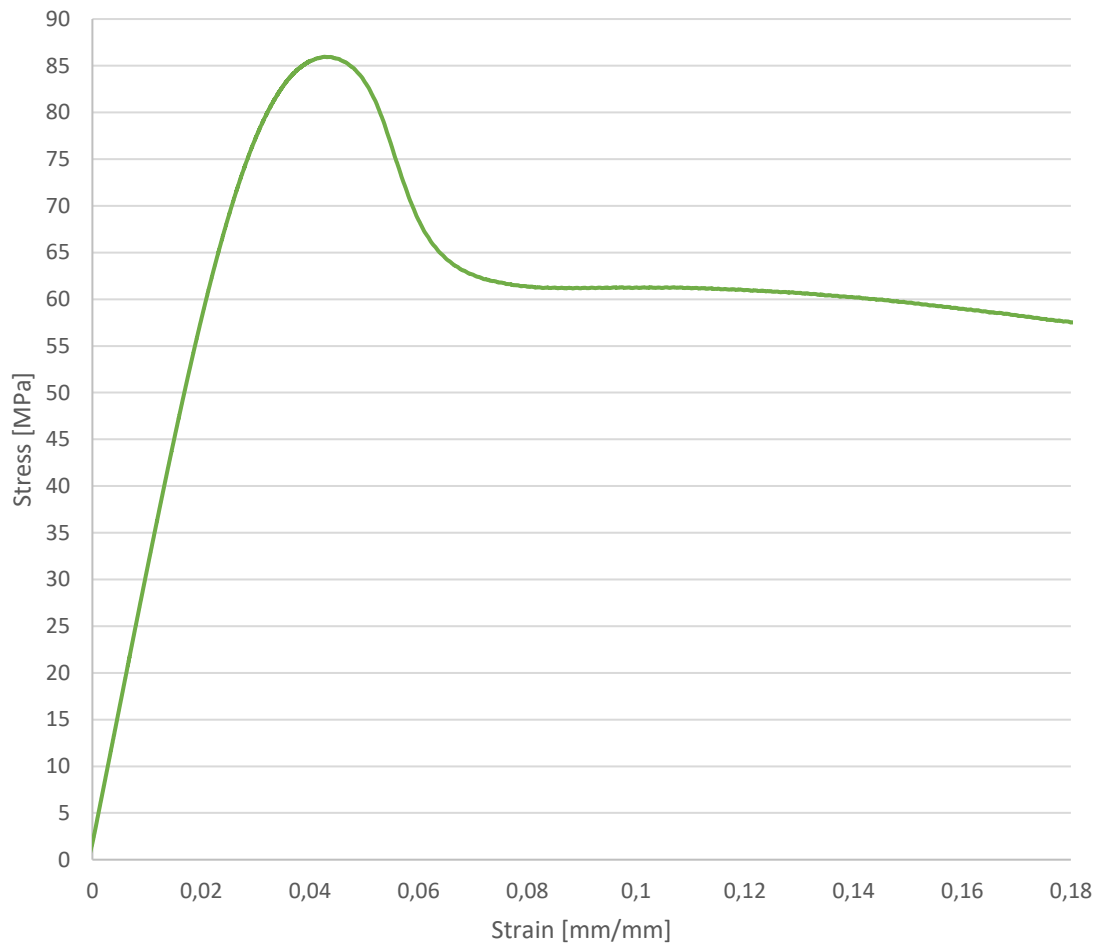
Specimen ID: Necuron 1150 – C3

Figure A- 17: Stress strain curve obtained from compression tests on specimen Necuron 1150 – C3.

Name	Value	Units
Speed	1.3	mm/min
Specimen Diameter	12.70	mm
Young's Modulus	2847	MPa
Rp02	74	MPa
Peak Stress	86	MPa

Table A- 17: compression mechanical properties of Necuron 1150 – C3.

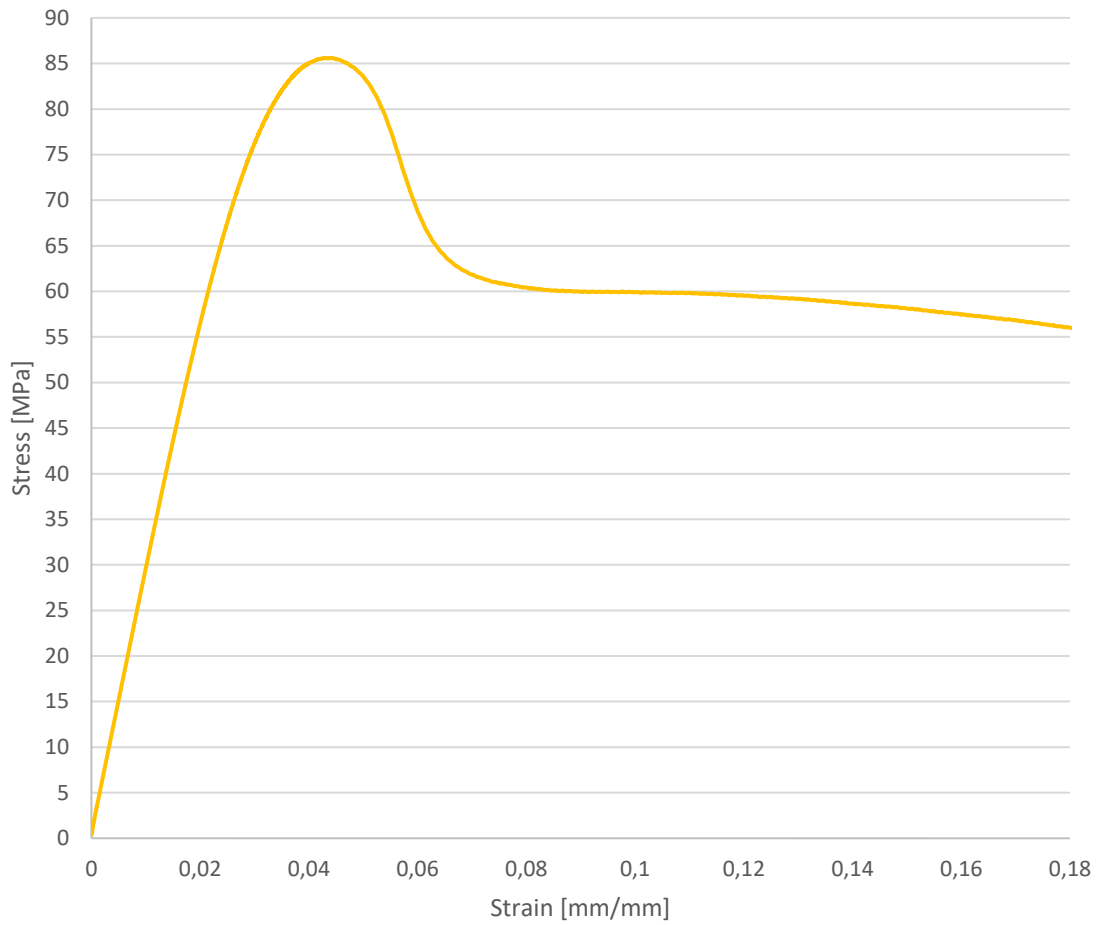
Specimen ID: Necuron 1150 – C4

Figure A- 18: Stress strain curve obtained from compression tests on specimen Necuron 1150 – C4.

Name	Value	Units
Speed	1.3	mm/min
Specimen Diameter	12.70	mm
Young's Modulus	3104	MPa
Rp02	58	MPa
Peak Stress	86	MPa

Table A- 18: compression mechanical properties of Necuron 1150 – C4.

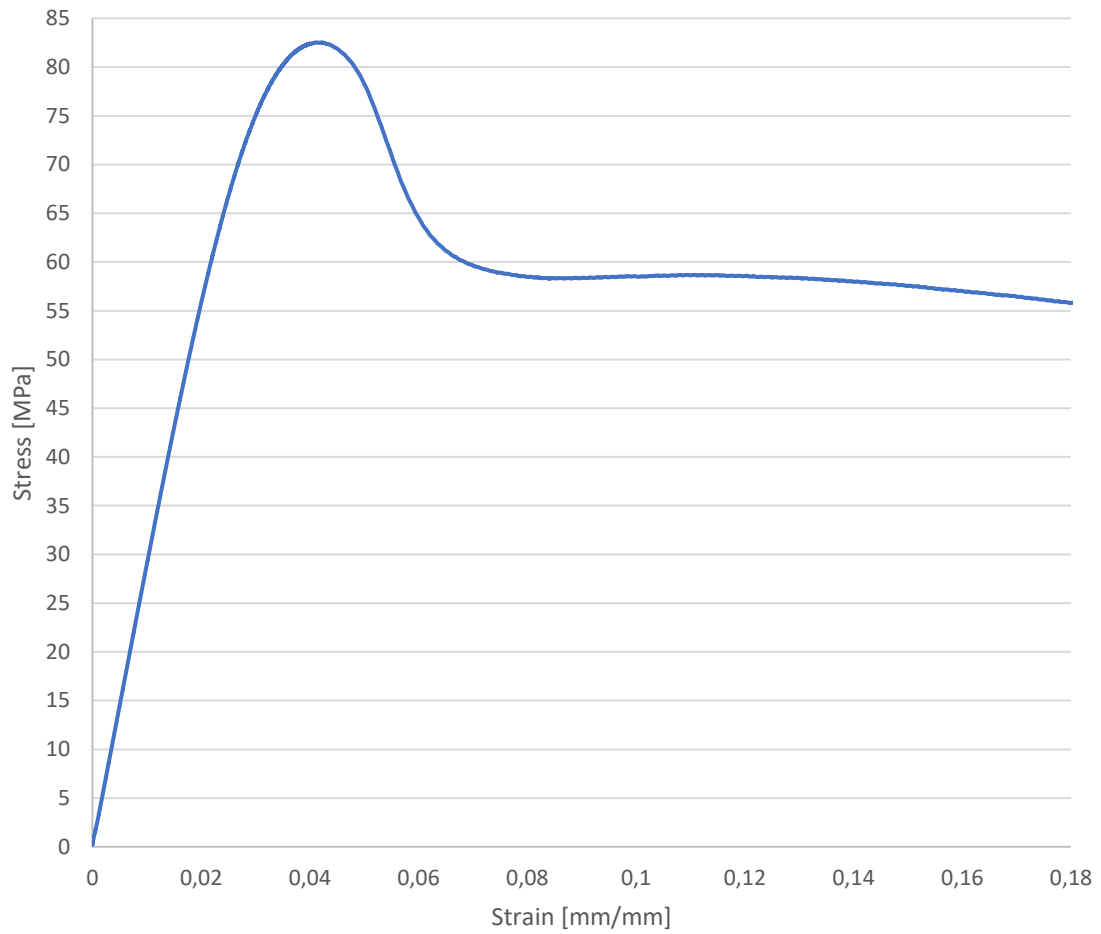
Specimen ID: Necuron 1150 – C5

Figure A- 19: Stress strain curve obtained from compression tests on specimen Necuron 1150 – C5.

Name	Value	Units
Speed	1.3	mm/min
Specimen Diameter	12.70	mm
Young's Modulus	2387	MPa
Rp02	81	MPa
Peak Stress	83	MPa

Table A- 19: compression mechanical properties of Necuron 1150 – C5.

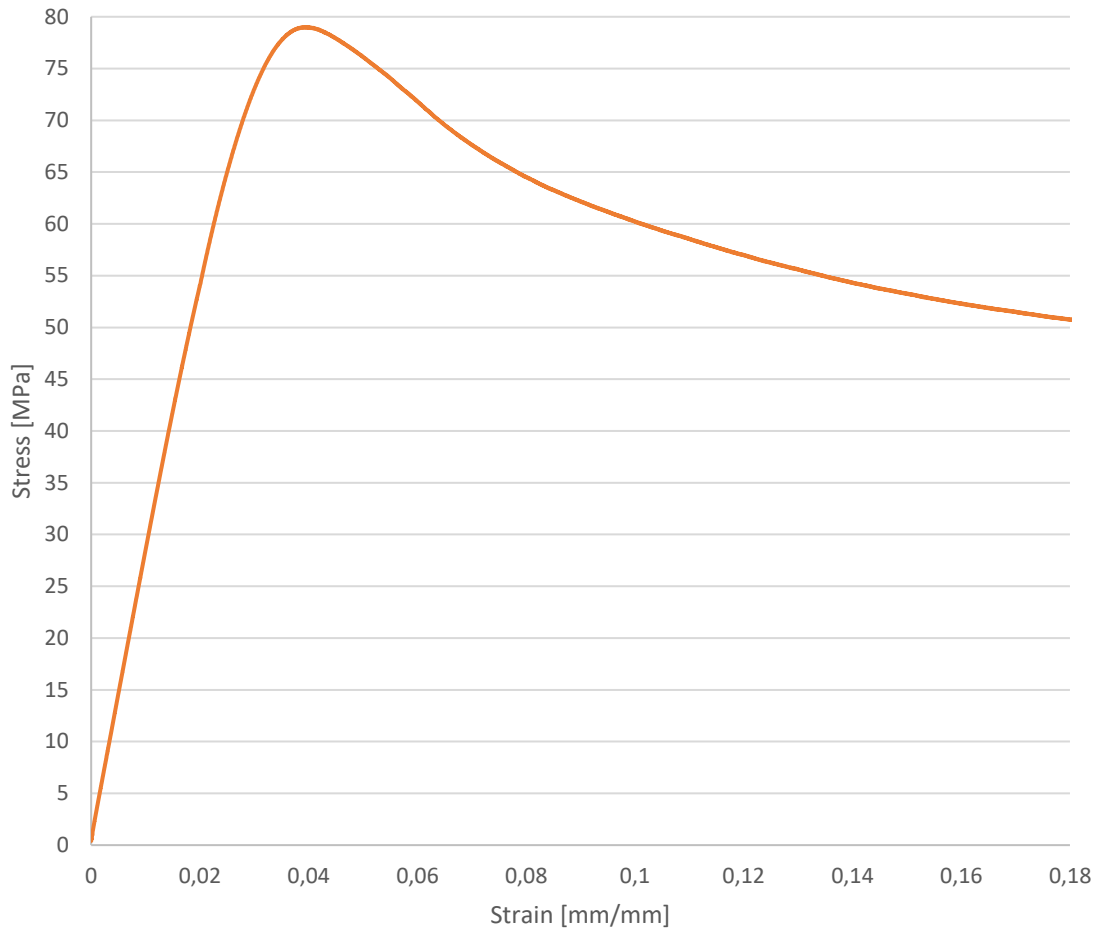
Specimen ID: Necuron 1300 – C1

Figure A- 20: Stress strain curve obtained from compression tests on specimen Necuron 1300 – C1.

Name	Value	Units
Speed	1.3	mm/min
Specimen Diameter	12.70	mm
Young's Modulus	2810	MPa
Rp02	61	MPa
Peak Stress	73	MPa

Table A- 20: compression mechanical properties of Necuron 1300 – C1.

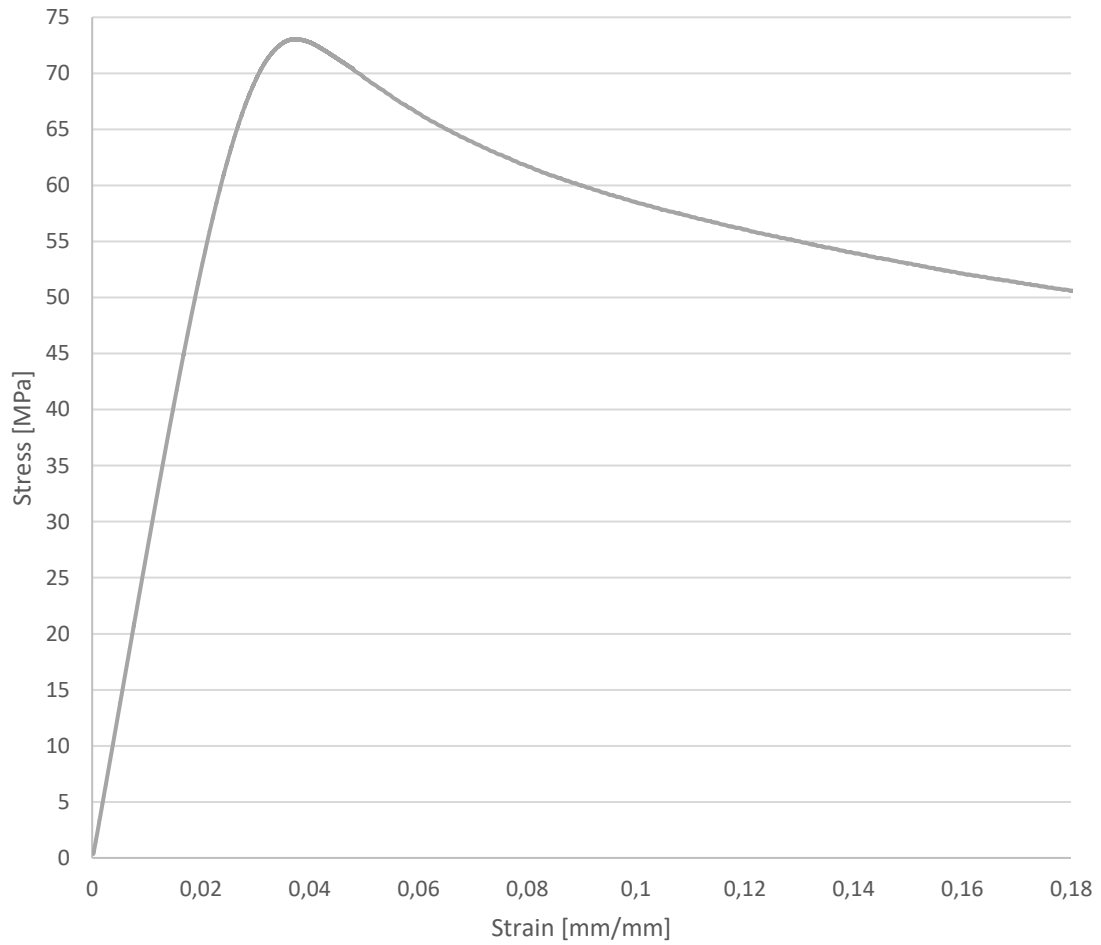
Specimen ID: Necuron 1300 – C2

Figure A- 21: Stress strain curve obtained from compression tests on specimen Necuron 1300 – C2.

Name	Value	Units
Speed	1.3	mm/min
Specimen Diameter	12.70	mm
Young's Modulus	2794	MPa
Rp02	66	MPa
Peak Stress	79	MPa

Table A- 21: compression mechanical properties of Necuron 1300 – C2.

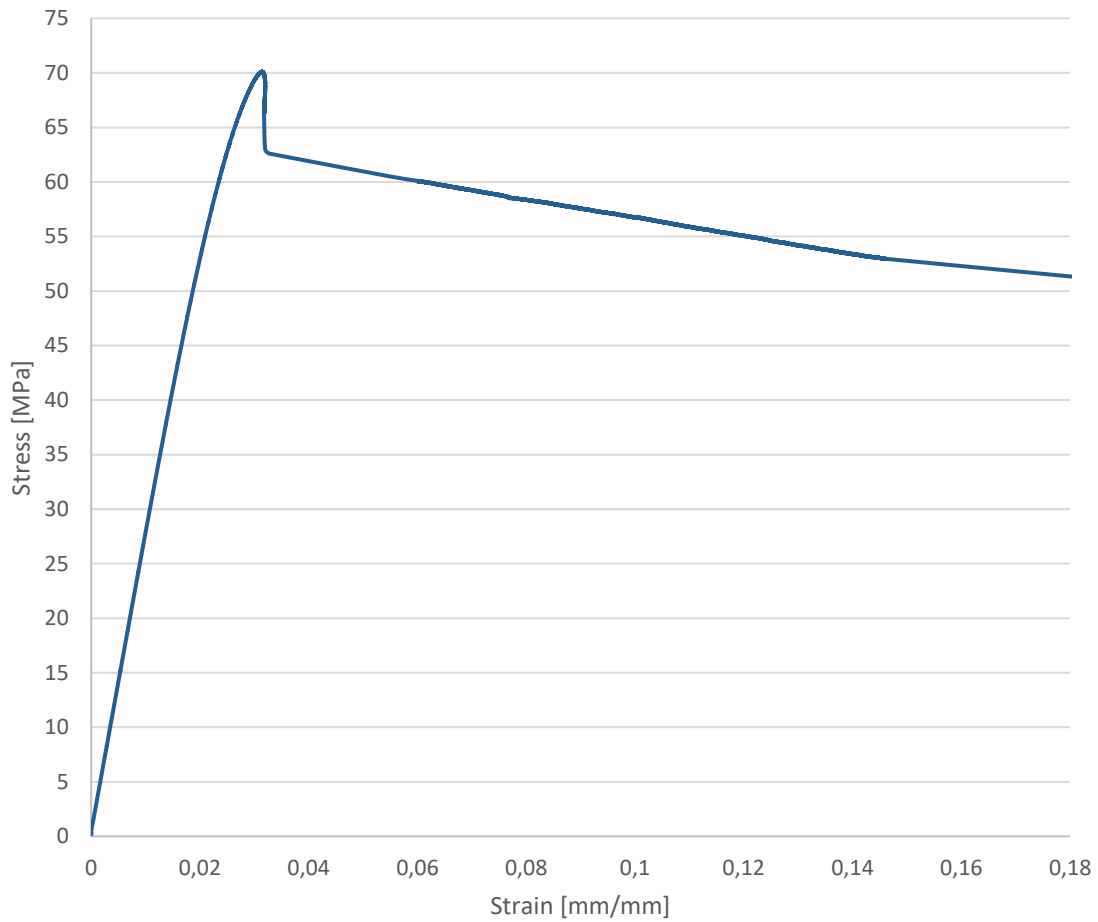
Specimen ID: Necuron 1300 – C3

Figure A- 22: Stress strain curve obtained from compression tests on specimen Necuron 1300 – C3.

Name	Value	Units
Speed	1.3	mm/min
Specimen Diameter	12.70	mm
Young's Modulus	2565	MPa
Rp02	68	MPa
Peak Stress	70	MPa

Table A- 22: compression mechanical properties of Necuron 1300 – C3.

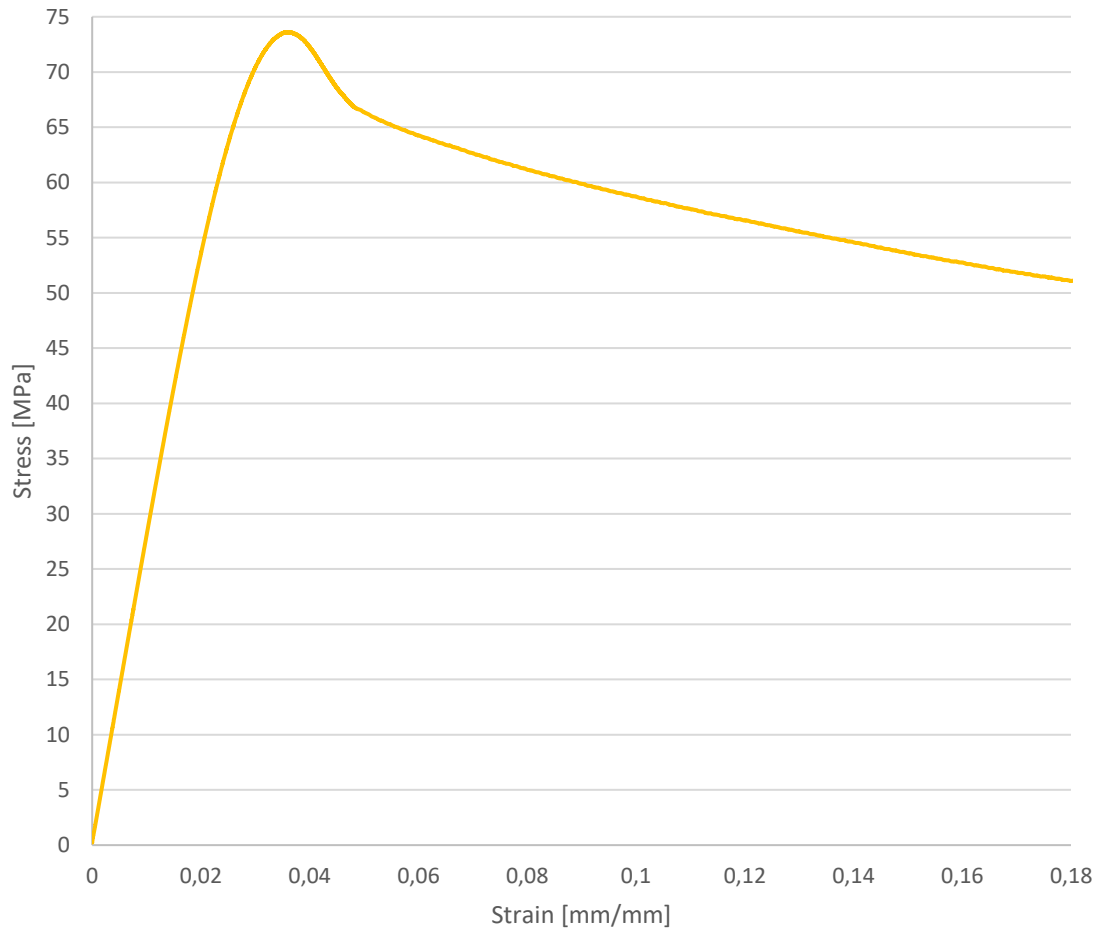
Specimen ID: Necuron 1300 – C4

Figure A- 23: Stress strain curve obtained from compression tests on specimen Necuron 1300 – C4.

Name	Value	Units
Speed	1.3	mm/min
Specimen Diameter	12.70	mm
Young's Modulus	2607	MPa
Rp02	68	MPa
Peak Stress	74	MPa

Table A- 23: compression mechanical properties of Necuron 1300 – C4.

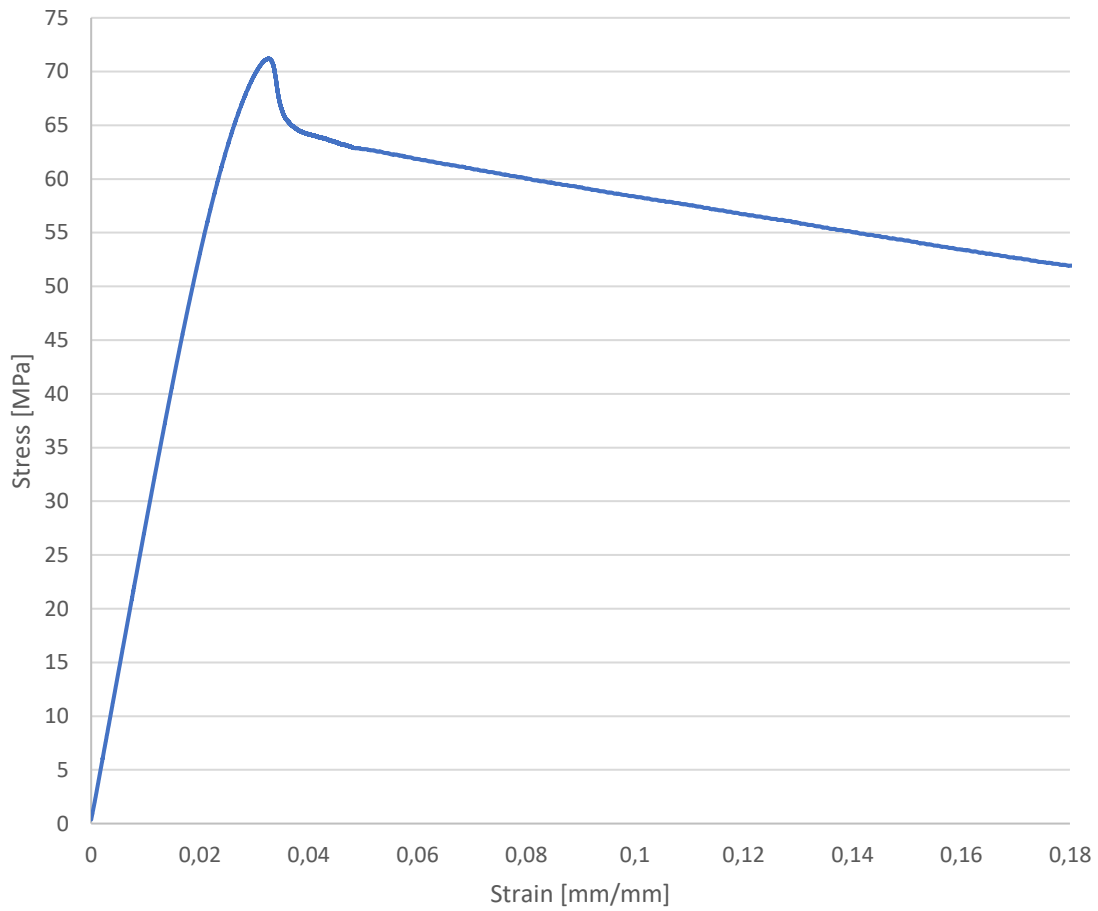
Specimen ID: Necuron 1300 – C5

Figure A- 24: Stress strain curve obtained from compression tests on specimen Necuron 1300 – C5.

Name	Value	Units
Speed	1.3	mm/min
Specimen Diameter	12.70	mm
Young's Modulus	2543	MPa
Rp02	69	MPa
Peak Stress	71	MPa

Table A- 24: compression mechanical properties of Necuron 1300 – C5.

Appendix B

B-1. Description of the measurement method used for calculate the geometrical errors

All the FEM simulations of the sheet metal forming processes have been performed by using shell elements for discretizing the blanks. An FEM shell surface is the representation of a middle surface of a component, this mean that half thickness should be considered on each face of generic shell elements in order to obtain the external or internal surface of a simulated part. The experimental profiles have been measured on the external shell of the blanks by using a CMM machine.

In order to compare the profiles of the experimental components, measured by a CMM machine, with the simulated ones, the numerical shell profile have been offsetted along the “external” normal direction, point by point according with the scheme presented in Figure B- 1.

In Figure B- 1, a general portion composed by three generic nodes (N_1 , N_2 and N_3) of a generic simulated profile is presented. The FEM software allows exporting the 2D shell profile section of the simulated component as a matrix of Cartesian (x , y), corresponding to the nodes coordinates. At the same time, it is possible to export the thickness contour of the section as a matrix of (x , t) coordinates, where x are the same abscissa of the previous (x , y) Cartesian profile and t is the thickness value calculated on the profile.

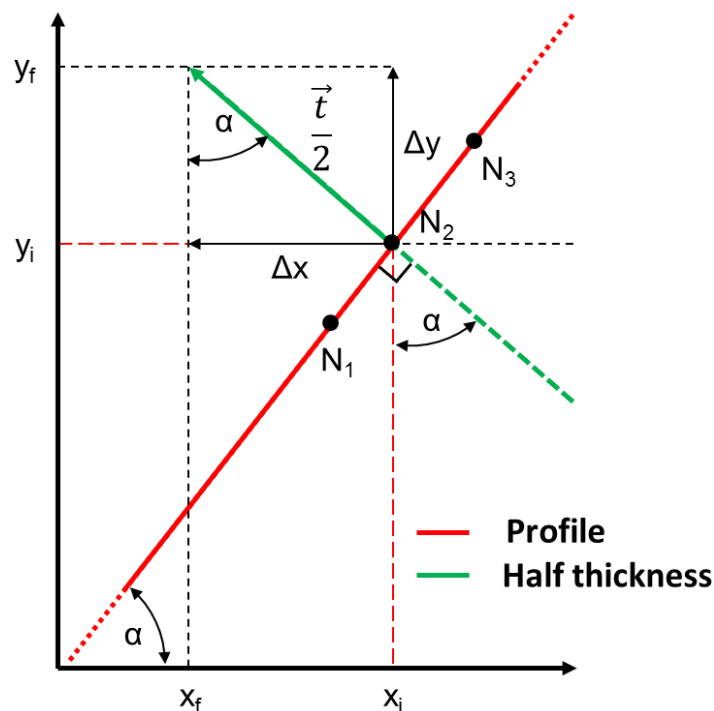


Figure B- 1: schematization of the punctual profile offset operation.

Referring to Figure B- 1, the profile portion can be discretized with a sum of small straight lines passing through consecutive nodes. In order to obtain the external shell of the blank needed for the experimental comparisons, each node must be offsetted, with a quantity equal to half of the thickness “ $t/2$ ” along normal direction. So each node must be translated along abscissa axis with a Δx magnitude, and along ordinate axis with Δy magnitude. Considering the scheme in Figure B- 1, the translation magnitude for the node N_2 can be calculated as:

$$\Delta x_2 = (x_{f,2} - x_{i,2}) = -\frac{t_2}{2} \cdot \sin \alpha_2 \quad (\text{B.1})$$

$$\Delta y_2 = (y_{f,2} - y_{i,2}) = \frac{t_2}{2} \cdot \cos \alpha_2 \quad (\text{B.2})$$

where the subscript 2 indicates the local value of each quantity referred to the node 2. The angle α_2 should correspond to the local angular coefficient of the straight line passing between the three nodes N_1 , N_2 and N_3 , but this assumption is impossible because 3 general points will never be aligned along the profile. For this reason, 2 straight lines have been considered $\overline{N_1N_2}$ and $\overline{N_2N_3}$, where the corresponding angular coefficients (m_1 and m_3) and the corresponding slope angles (α_1 and α_3) are:

$$m_1 = \frac{y_{i,2} - y_{i,1}}{x_{i,2} - x_{i,1}}; m_3 = \frac{y_{i,3} - y_{i,2}}{x_{i,3} - x_{i,2}} \quad (\text{B.3})$$

$$\alpha_1 = \arctan(m_1); \alpha_3 = \arctan(m_3) \quad (\text{B.4})$$

In order to obtain a smoothed offset, the mean can be calculated:

$$\Delta x_2 = \frac{1}{3} \cdot \left(\frac{t_1 + t_2 + t_3}{2} \right) \cdot \frac{(\sin -\alpha_1 + \sin -\alpha_3)}{2} = -\frac{(t_1 + t_2 + t_3) \cdot (\sin \alpha_1 + \sin \alpha_3)}{12} \quad (\text{B.5})$$

$$\Delta y_2 = \frac{1}{3} \cdot \left(\frac{t_1 + t_2 + t_3}{2} \right) \cdot \frac{(\cos \alpha_1 + \cos \alpha_3)}{2} = \frac{(t_1 + t_2 + t_3) \cdot (\cos \alpha_1 + \cos \alpha_3)}{12} \quad (\text{B.6})$$

The equations (B.5) and (B.6) are valid only if the following hypothesis is respected:

- If the blank profile is well refined (refer to the refinement operation explained in the section 3.2.4.2):
 - 1) Reasonable small thickness variations between the consecutive nodes can be found
 - 2) The straight lines passing through consecutive nodes have small slope variations, so the sine and cosine do not vary significantly.

At the end the final coordinates of the node N_2 are:

$$x_{f,2} = x_{i,2} + \Delta x_2 \quad (\text{3.17})$$

$$y_{f,2} = y_{i,2} + \Delta y_2 \quad (3.18)$$

In order to complete the offset of the entire profile, the operation can be repeated recursively for all consecutive nodes. In Figure B- 2 and Figure B- 3 the results of the variable offset operation is shown for the test case 1 and 2 described in chapter 3.

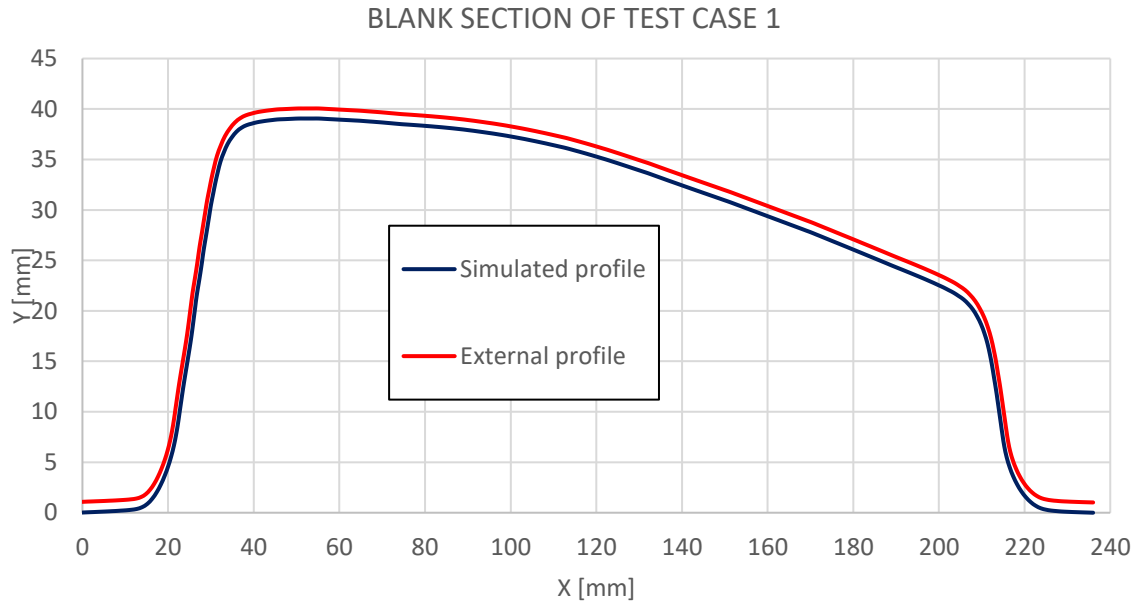


Figure B- 2: result of the variable offset of the blank profile for the test case 1.

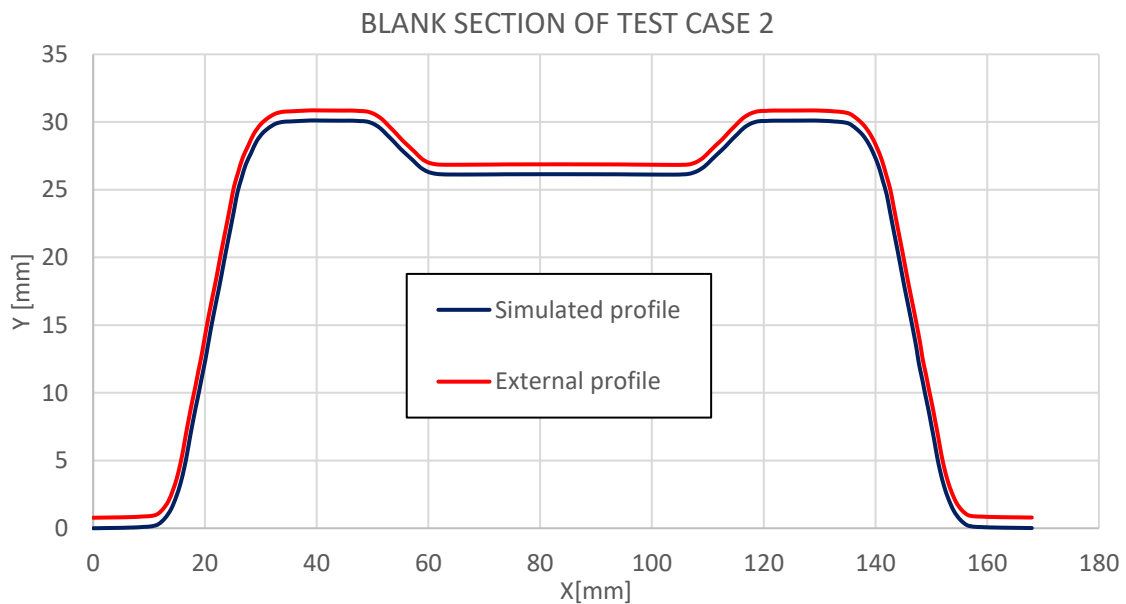


Figure B- 3: result of the variable offset of the blank profile for the test case

This variable offsetting operation correspond to an easy application of a 2D Displacement Adjustment method algorithm for thickness compensation.

All of these operations have been described for further discuss about the errors between the simulated and experimental components shown in chapter 3 for both cases. The deviations calculated for the simulated components contains the contribution of the errors related to the geometrical approximation of the mesh, but also the errors related to the calculation of the thinning of the blank, which is directly related to the material properties of the blank. The results obtained until now from the FEM models are very impressive if these two errors are considered in the calculation of the deviations of the numerical and experimental profiles.

All of these observations suggests that the blank material should be better described with experimental tensile test. For this reason, the material used in the experimental bending case presented in the chapter 4 have been characterized by tensile tests.

Appendix C

C-1. Tensile Tests results of metal specimens used in the bending experiments

Specimen ID: Fe37 – 0.7 mm – 1

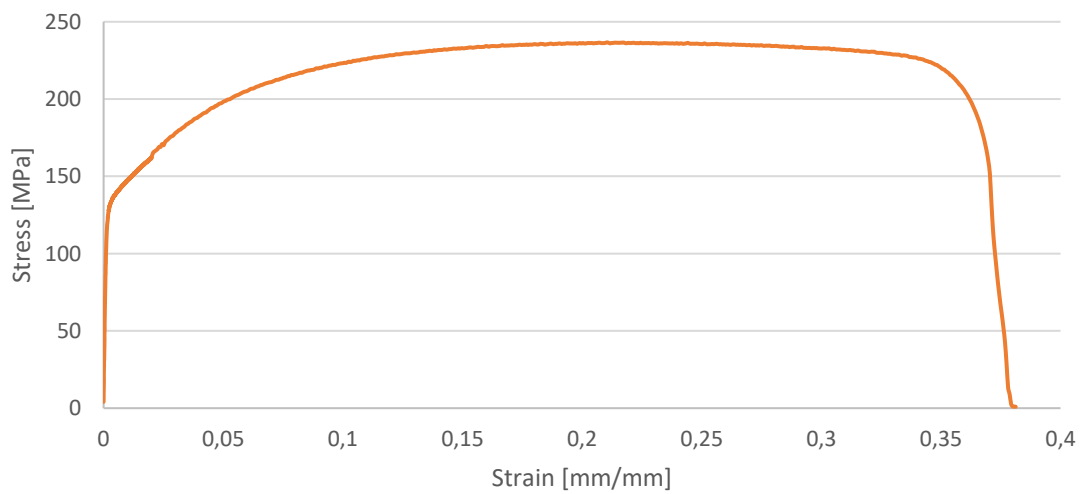


Figure C- 1: Stress strain curve obtained from the tensile test for specimen 1 made by FE37 thickness 0.7 mm.

Name	Value	Units
Speed	1.00	mm/min
Specimen Thickness	0.70	mm
Specimen Width	4.58	mm
Young's Modulus	102927	MPa
Rp02	134	MPa
Stress0.2	127	MPa
Peak Stress	237	MPa
Strain At Break	37.7	%
A%	54.0	%

Table C- 1: tensile properties of specimen 1 made by FE37 thickness 0.7 mm.

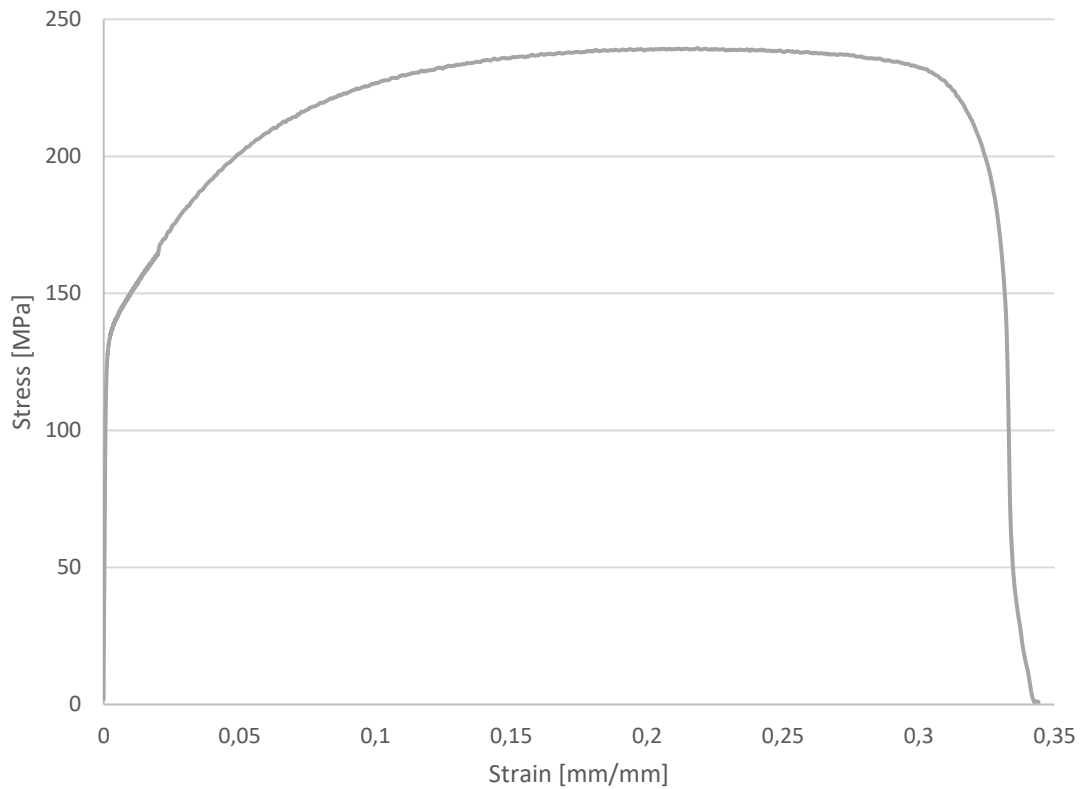
Specimen ID: Fe37 – 0.7 mm – 2

Figure C- 2: Stress strain curve obtained from the tensile test for specimen 2 made by FE37 thickness 0.7 mm.

Name	Value	Units
Speed	1.00	mm/min
Specimen Thickness	0.69	mm
Specimen Width	4.57	mm
Young's Modulus	138501	MPa
Rp02	137	MPa
Stress0.2	133	MPa
Peak Stress	240	MPa
Strain At Break	34.1	%
A%	43.6	%

Table C- 2: tensile properties of specimen 2 made by FE37 thickness 0.7 mm.

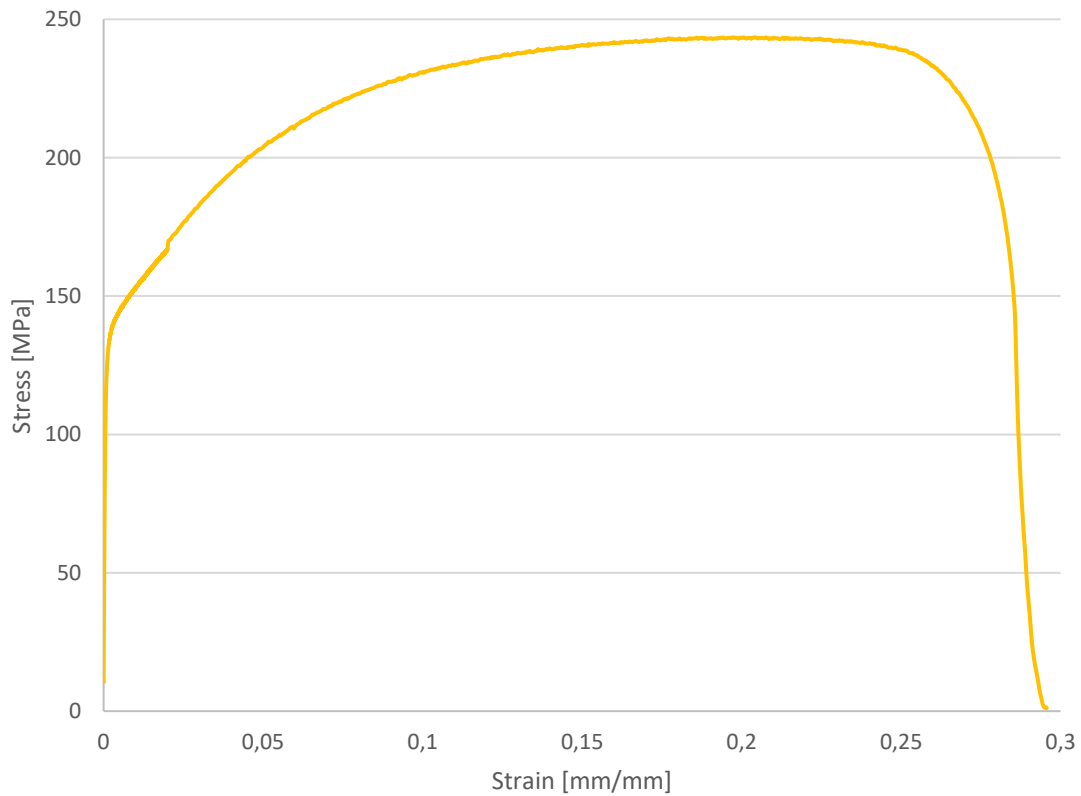
Specimen ID: Fe37 – 0.7 mm – 3

Figure C- 3: Stress strain curve obtained from the tensile test for specimen 3 made by FE37 thickness 0.7 mm.

Name	Value	Units
Speed	1.00	mm/min
Specimen Thickness	0.67	mm
Specimen Width	4.58	mm
Young's Modulus	151108	MPa
Rp02	140	MPa
Stress0.2	135	MPa
Peak Stress	243	MPa
Strain At Break	30	%
A%	35.2	%

Table C- 3: tensile properties of specimen 3 made by FE37 thickness 0.7 mm.

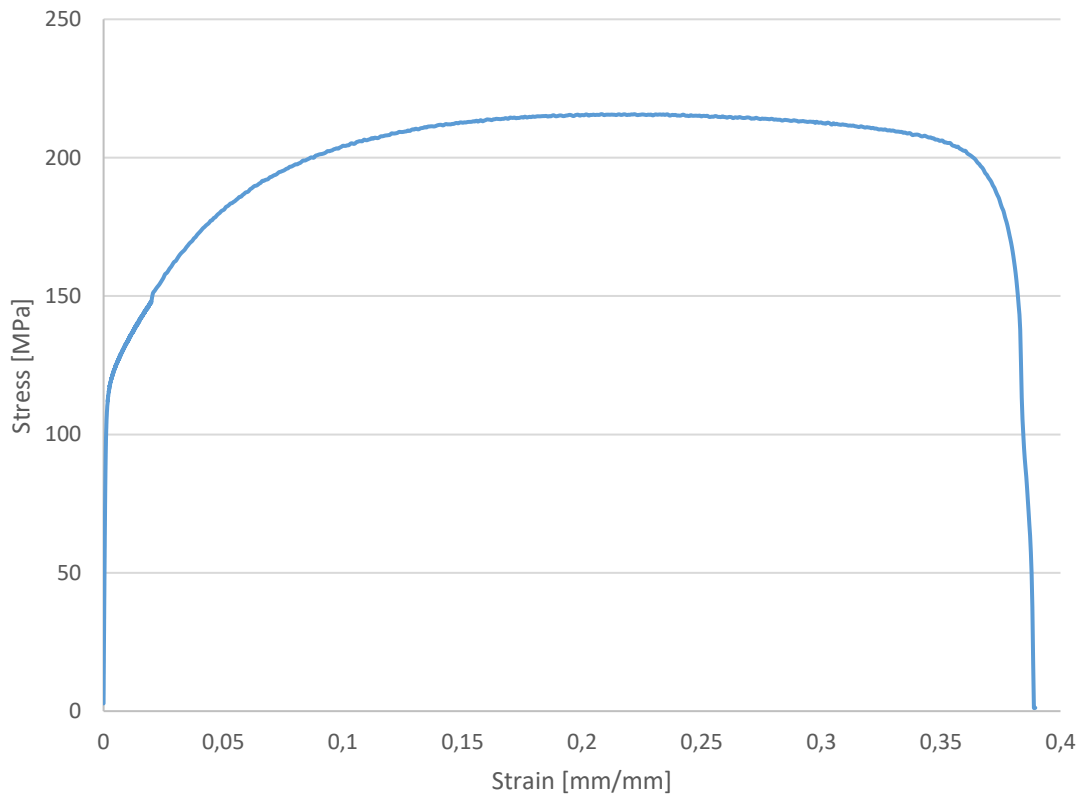
Specimen ID: Fe37 – 0.7 mm – 4

Figure C- 4: Stress strain curve obtained from the tensile test for specimen 4 made by FE37 thickness 0.7 mm.

Name	Value	Units
Speed	1.00	mm/min
Specimen Thickness	0.78	mm
Specimen Width	4.57	mm
Young's Modulus	109427	MPa
Rp02	120	MPa
Stress0.2	114	MPa
Peak Stress	216	MPa
Strain At Break	38.8	%
A%	52.0	%

Table C- 4: tensile properties of specimen 4 made by FE37 thickness 0.7 mm.

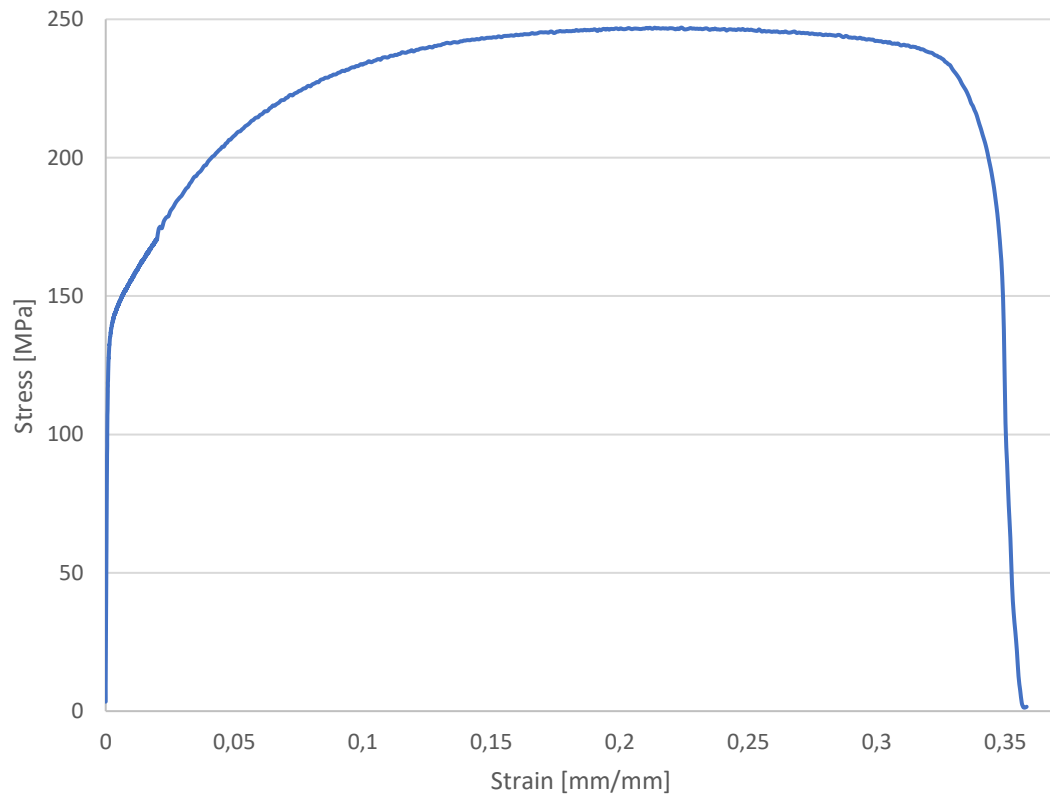
Specimen ID: Fe37 – 0.7 mm – 5

Figure C- 5: Stress strain curve obtained from the tensile test for specimen 5 made by FE37 thickness 0.7 mm.

Name	Value	Units
Speed	1.00	mm/min
Specimen Thickness	0.77	mm
Specimen Width	4.57	mm
Young's Modulus	144359	MPa
Rp02	142	MPa
Stress0.2	137	MPa
Peak Stress	247	MPa
Strain At Break	35.6	%
A%	47.6	%

Table C- 5: tensile properties of specimen 5 made by FE37 thickness 0.7 mm.

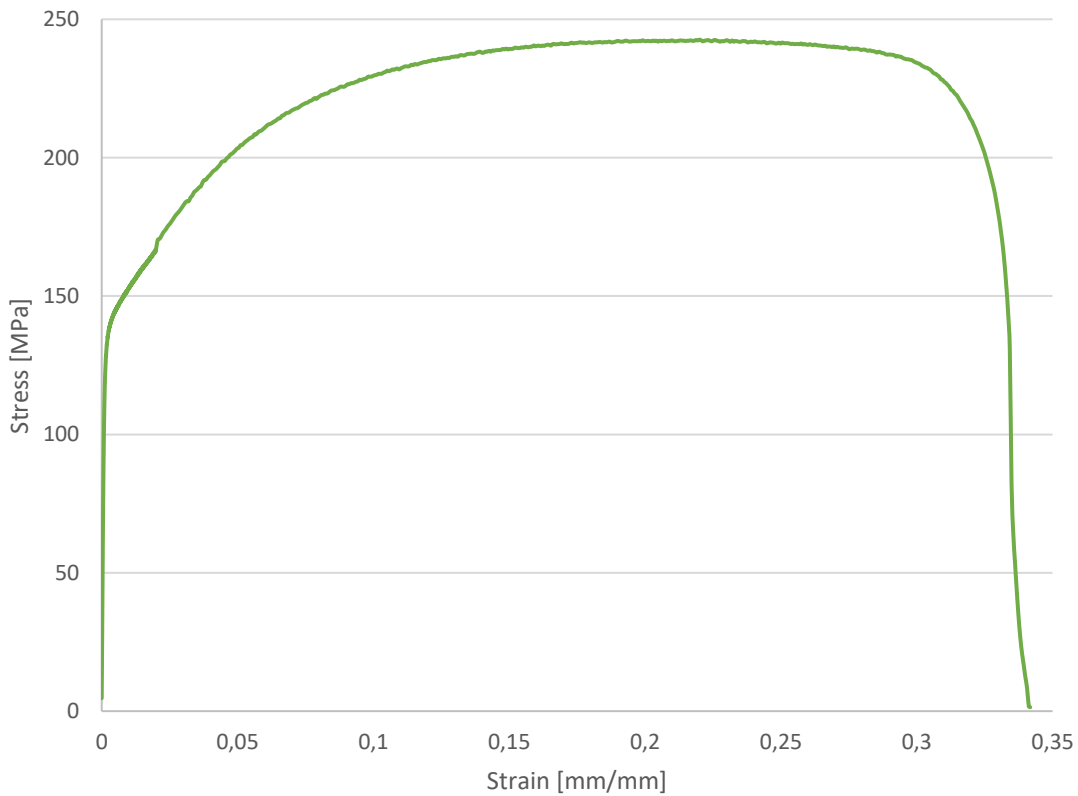
Specimen ID: Fe37 – 0.7 mm – 6

Figure C- 6: Stress strain curve obtained from the tensile test for specimen 6 made by FE37 thickness 0.7 mm.

Name	Value	Units
Speed	1.00	mm/min
Specimen Thickness	0.68	mm
Specimen Width	4.61	mm
Young's Modulus	130411	MPa
Rp02	140	MPa
Stress0.2	133	MPa
Peak Stress	243	MPa
Strain At Break	34.1	%
A%	45.6	%

Table C- 6: tensile properties of specimen 6 made by FE37 thickness 0.7 mm.

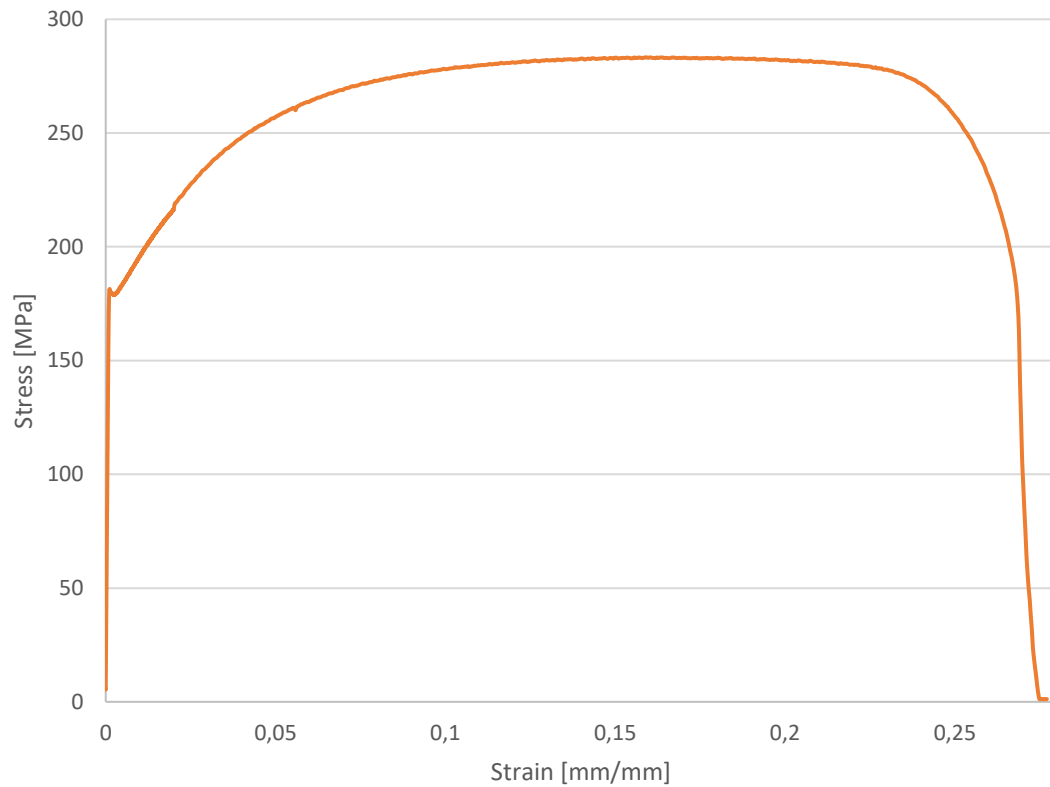
Specimen ID: Fe37Z – 1 mm – 7

Figure C- 7: Stress strain curve obtained from the tensile test for specimen 7 made by FE37Z thickness 1 mm.

Name	Value	Units
Speed	1.00	mm/min
Specimen Thickness	1.02	mm
Specimen Width	4.64	mm
Young's Modulus	194807	MPa
Rp02	180	MPa
Stress0.2	179	MPa
Peak Stress	283	MPa
Strain At Break	27.5	%
A%	38.4	%

Table C- 7: tensile properties of specimen 7 made by FE37Z thickness 1 mm.

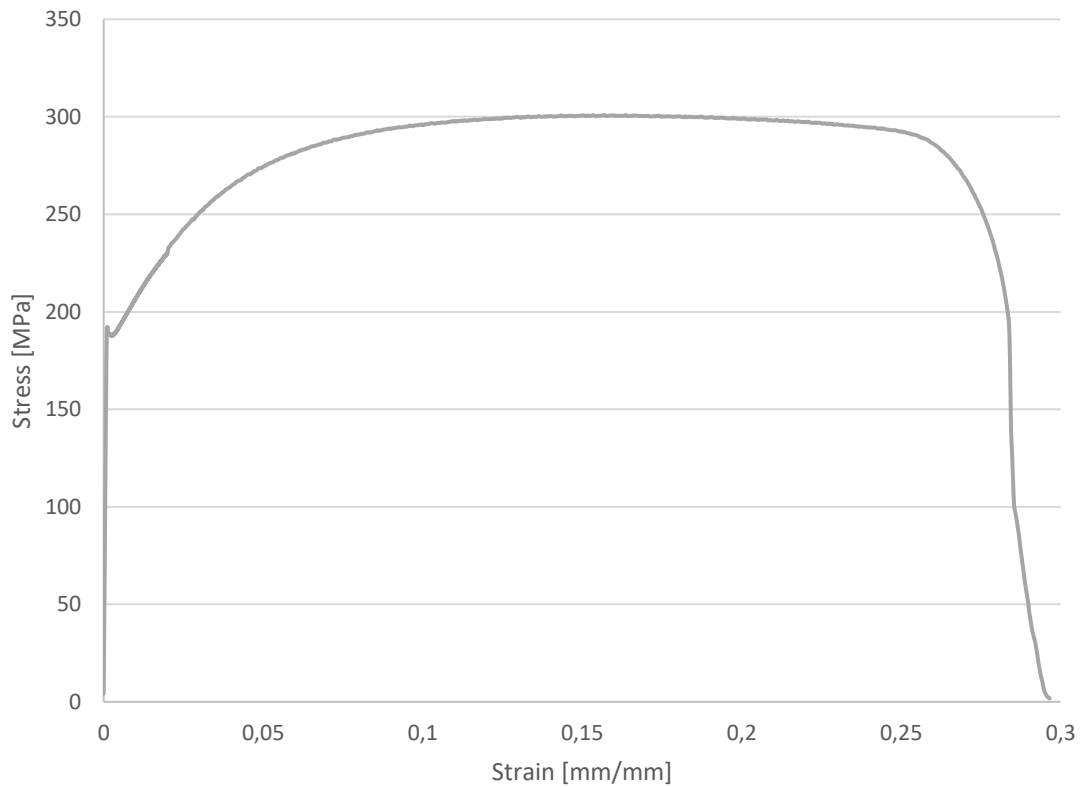
Specimen ID: Fe37Z – 1 mm – 8

Figure C- 8: Stress strain curve obtained from the tensile test for specimen 8 made by FE37Z thickness 1 mm.

Name	Value	Units
Speed	1.00	mm/min
Specimen Thickness	1.00	mm
Specimen Width	4.69	mm
Young's Modulus	203418	MPa
Rp02	188	MPa
Stress0.2	188	MPa
Peak Stress	301	MPa
Strain At Break	30	%
A%	40.0	%

Table C- 8: tensile properties of specimen 8 made by FE37Z thickness 1 mm.

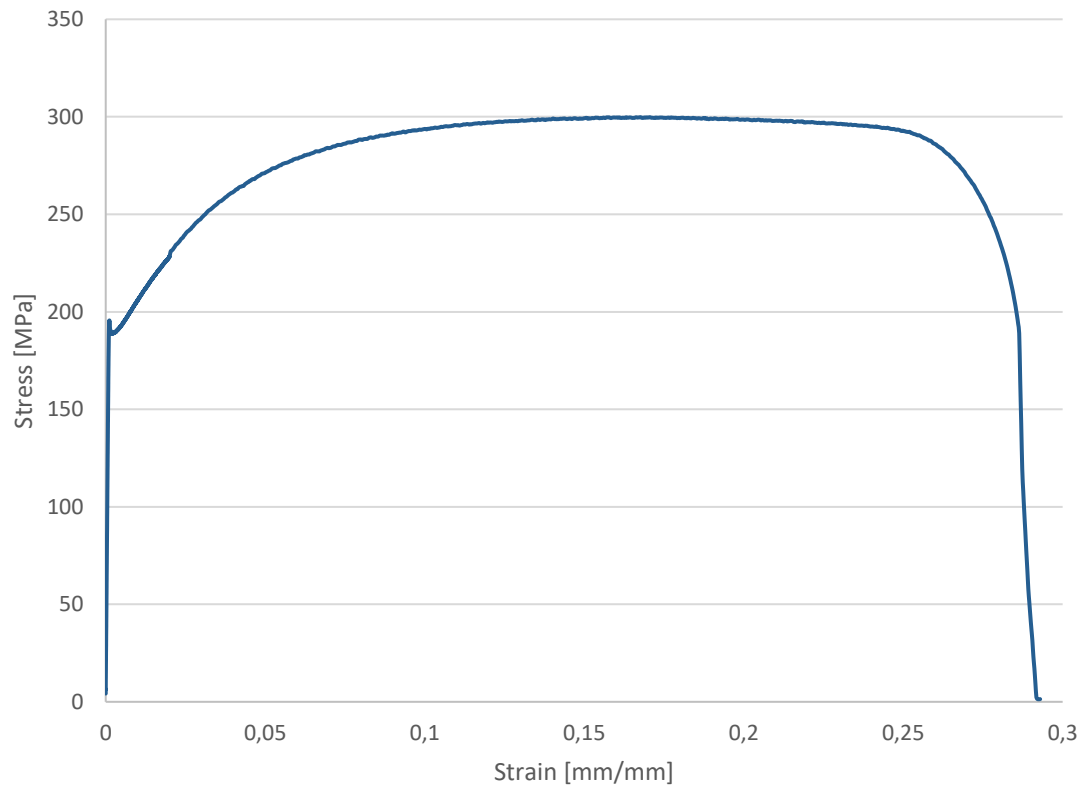
Specimen ID: Fe37Z – 1 mm – 9

Figure C- 9: Stress strain curve obtained from the tensile test for specimen 9 made by FE37Z thickness 1 mm.

Name	Value	Units
Initial Speed	1.00	mm/min
Thickness	1.07	mm
Width	4.69	mm
Young's Modulus	196840	MPa
Rp02	189	MPa
Stress0.2	189	MPa
Peak Stress	300	MPa
Strain At Break	29.1	%
A%	39.1	%

Table C- 9: tensile properties of specimen 9 made by FE37Z thickness 1 mm.

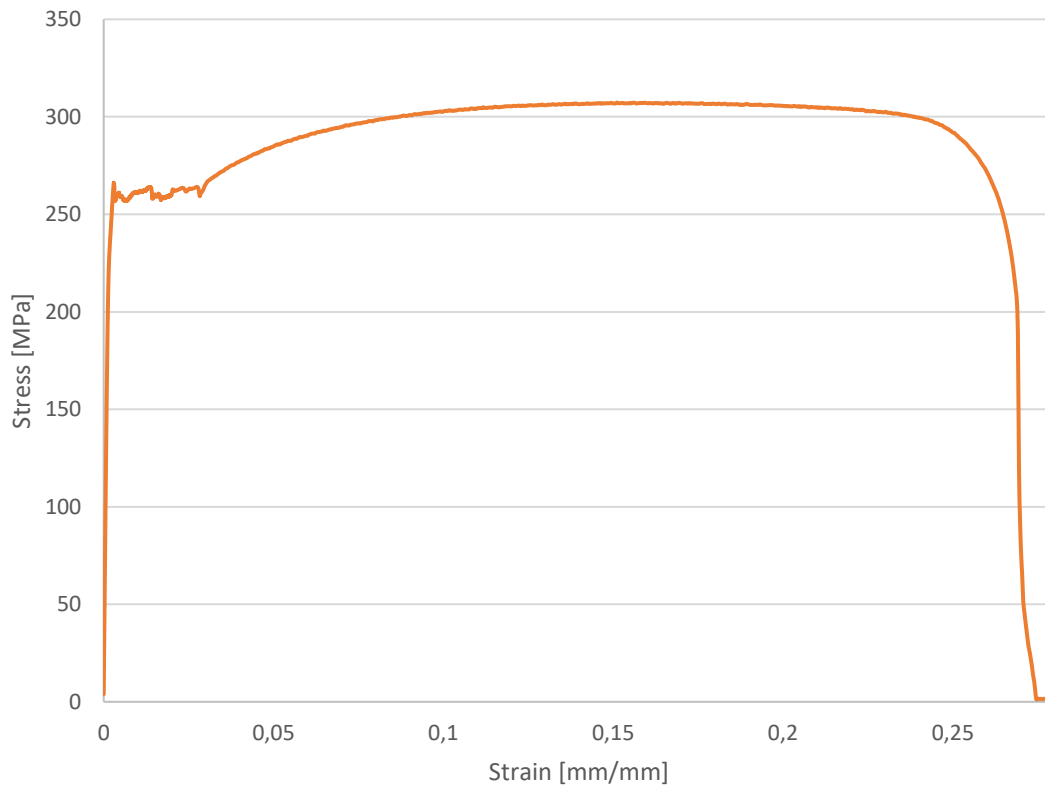
Specimen ID: Fe37 – 0.8 mm – 10

Figure C- 10: Stress strain curve obtained from the tensile test for specimen 10 made by FE37 thickness 0.8 mm.

Name	Value	Units
Speed	1.00	mm/min
Specimen Thickness	0.83	mm
Specimen Width	4.68	mm
Young's Modulus	175125	MPa
Rp02	258	MPa
Stress0.2	240	MPa
Peak Stress	307	MPa
Strain At Break	27.4	%
A%	37.0	%

Table C- 10: tensile properties of specimen 11 made by FE37 thickness 0.8 mm.

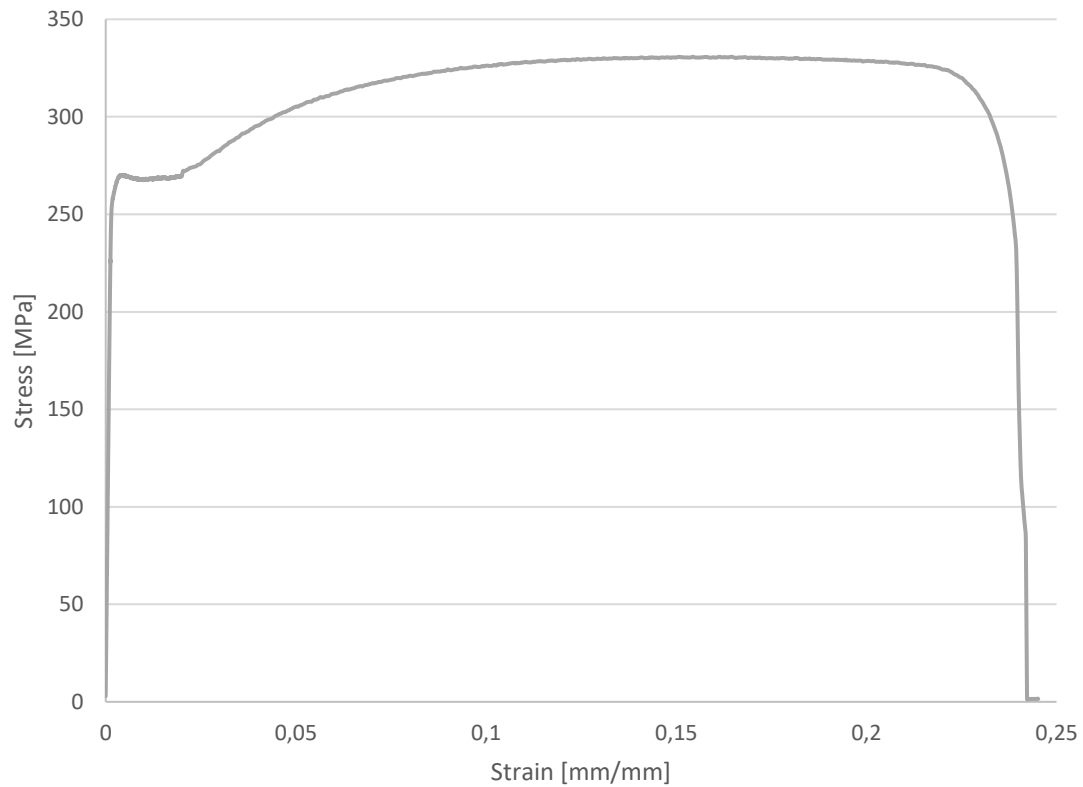
Specimen ID: Fe37 – 0.8 mm – 11

Figure C- 11: Stress strain curve obtained from the tensile test for specimen 11 made by FE37 thickness 0.8 mm.

Name	Value	Units
Speed	1.00	mm/min
Specimen Thickness	0.79	mm
Specimen Width	4.69	mm
Young's Modulus	187058	MPa
Rp02	269	MPa
Stress0.2	259	MPa
Peak Stress	331	MPa
Strain At Break	24.2	%
A%	30.6	%

Table C- 11: tensile properties of specimen 11 made by FE37 thickness 0.8 mm.

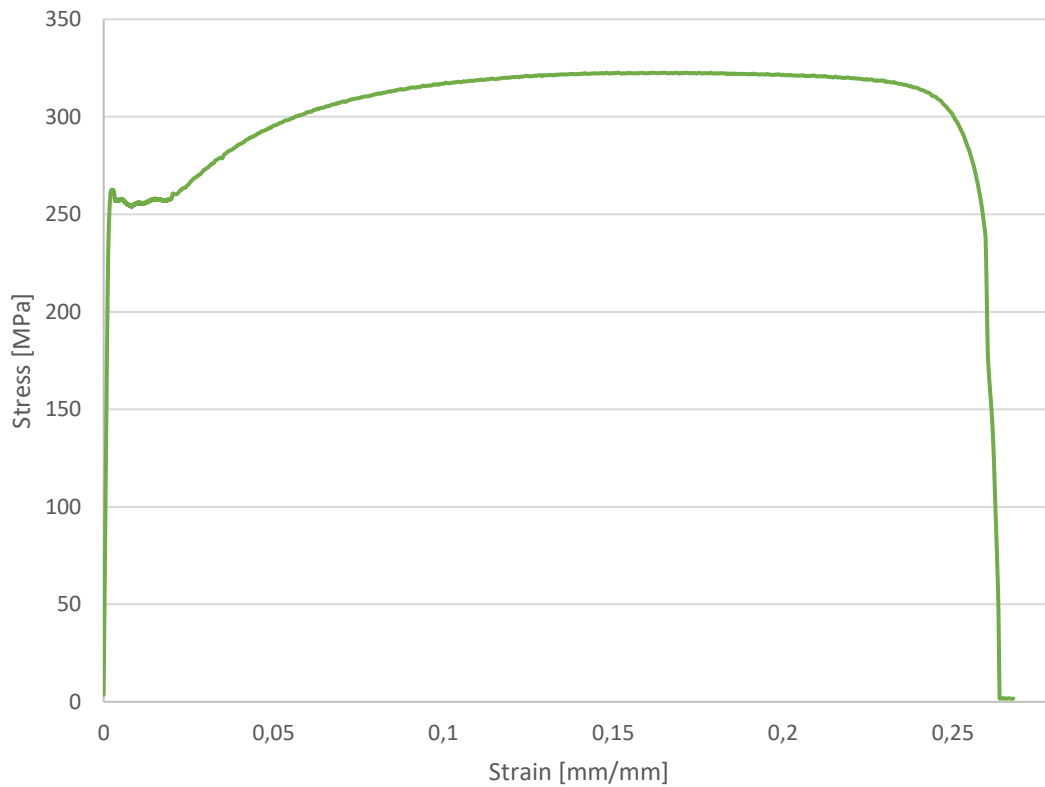
Specimen ID: Fe37 – 0.8 mm – 12

Figure C- 12: Stress strain curve obtained from the tensile test for specimen 12 made by FE37 thickness 0.8 mm.

Name	Value	Units
Speed	1.00	mm/min
Specimen Thickness	0.79	mm
Specimen Width	4.70	mm
Young's Modulus	178782	MPa
Rp02	257	MPa
Stress0.2	261	MPa
Peak Stress	323	MPa
Strain At Break	26.3	%
A%	38.2	%

Table C- 12: tensile properties of specimen 12 made by FE37 thickness 0.8 mm.

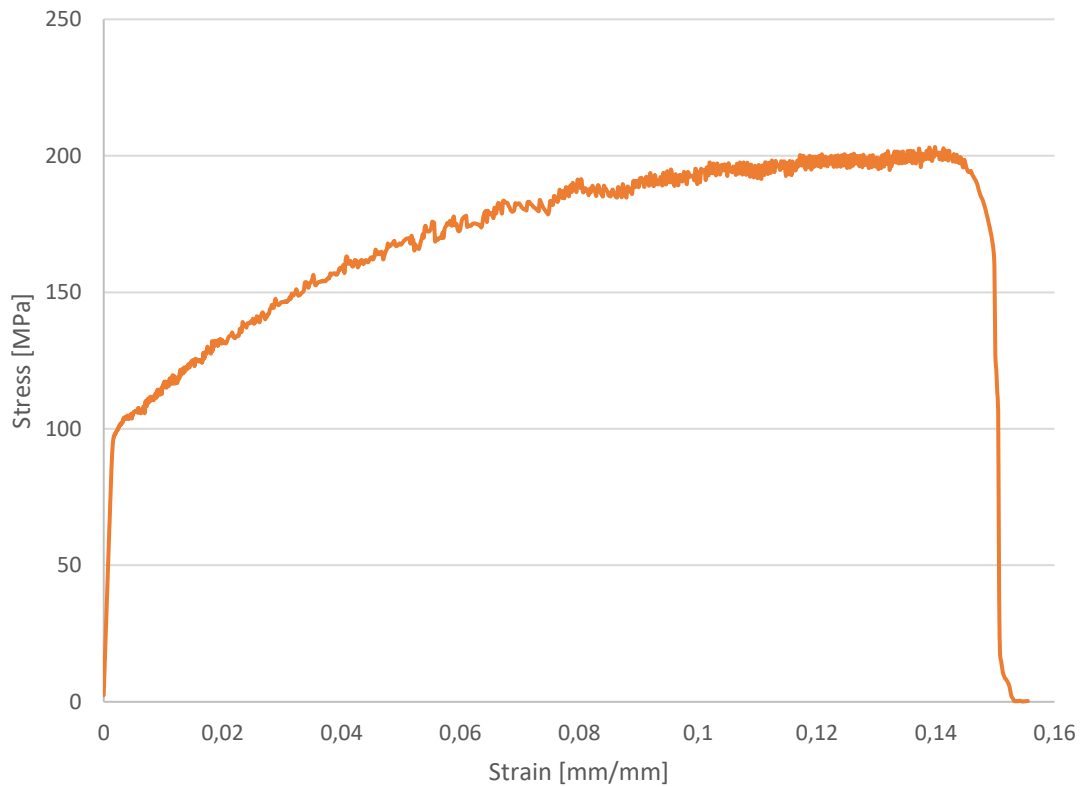
Specimen ID: Al – 1 mm – 13

Figure C- 13: Stress strain curve obtained from the tensile test for specimen 13 made by Al thickness 1 mm.

Name	Value	Units
Speed	1.00	mm/min
Specimen Thickness	1.04	mm
Specimen Width	4.62	mm
Young's Modulus	64283	MPa
Rp02	104	MPa
Stress0.2	98	MPa
Peak Stress	203	MPa
Strain At Break	15.1	%
A%	16.6	%

Table C- 13: tensile properties of specimen 13 made by Al thickness 1 mm.

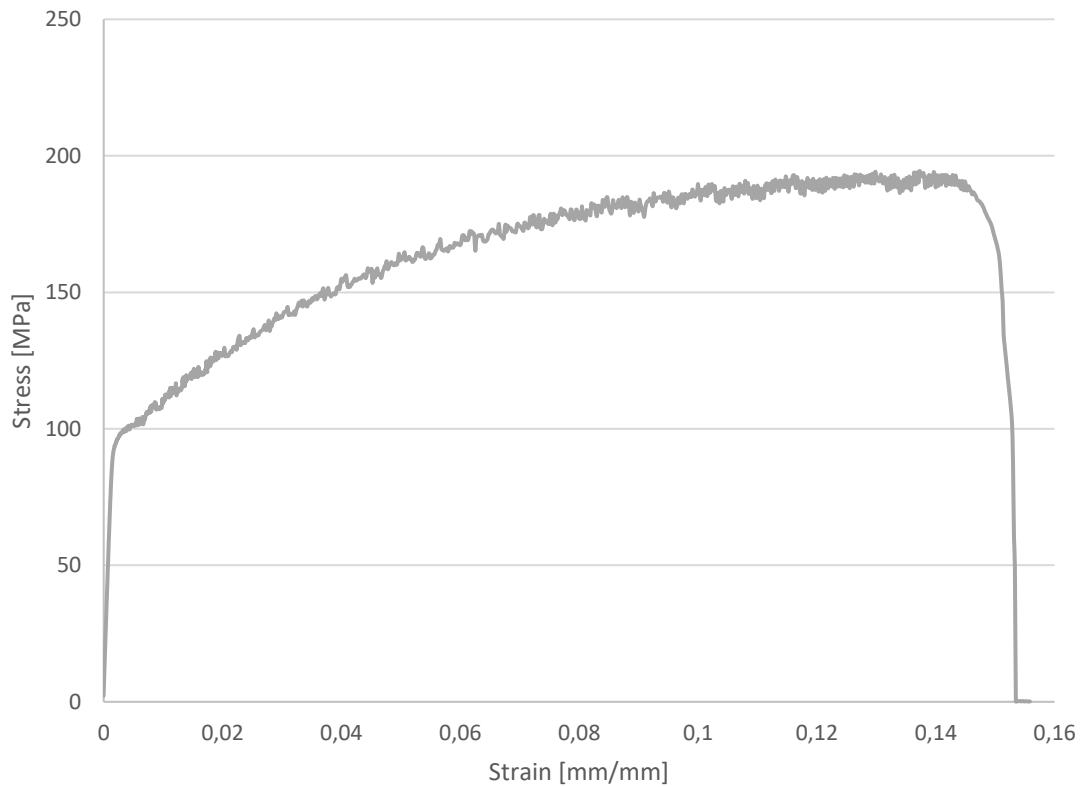
Specimen ID: Al – 1 mm – 14

Figure C- 14: Stress strain curve obtained from the tensile test for specimen 14 made by Al thickness 1 mm.

Name	Value	Units
Speed	1.00	mm/min
Specimen Thickness	1.07	mm
Specimen Width	4.66	mm
Young's Modulus	64534	MPa
Rp02	99	MPa
Stress0.2	95	MPa
Peak Stress	194	MPa
Strain At Break	15.3	%
A%	17.6	%

Table C- 14: tensile properties of specimen 14 made by Al thickness 1 mm.

C-2. Plan designed for sheet metal bending experiments

Std_order	Run order	Specimen	Thickness [mm]	Material	Rolling_dir [°]	Tool	Punch stroke [mm]
1	45	141	1	Al1050	0	Rubber	3.16
2	46	142	1	Al1050	0	Rubber	3.16
3	29	151	1	Al1050	0	Nylon	1.57
4	30	152	1	Al1050	0	Nylon	1.57
5	1	11	0.7	Fe37	90	Metal	1.57
6	2	21	0.7	Fe37	90	Metal	1.57
7	47	31	0.7	Fe37	90	Rubber	1.57
8	48	32	0.7	Fe37	90	Rubber	3.16
9	38	33	0.7	Fe37	90	Rubber_hole	1.57
10	39	34	0.7	Fe37	90	Rubber_hole	3.16
11	8	41	0.7	Fe37	90	Ne1050	1.57
12	9	42	0.7	Fe37	90	Ne1050	1.57
13	15	51	0.7	Fe37	90	Ne1150	1.57
14	16	52	0.7	Fe37	90	Ne1150	1.57
15	22	61	0.7	Fe37	90	Ne1300	1.57
16	23	62	0.7	Fe37	90	Ne1300	1.57
17	31	63	0.7	Fe37	90	Nylon	1.57
18	32	64	0.7	Fe37	90	Nylon	1.57
19	3	71	1	Fe37Z	0	Metal	1.57
20	4	72	1	Fe37Z	0	Metal	1.57
21	49	73	1	Fe37Z	0	Rubber	3.16
22	50	74	1	Fe37Z	0	Rubber	3.16
23	40	81	1	Fe37Z	0	Rubber_hole	3.16
24	41	82	1	Fe37Z	0	Rubber_hole	3.16
25	10	83	1	Fe37Z	0	Ne1050	1.57
26	11	84	1	Fe37Z	0	Ne1050	1.57
27	17	91	1	Fe37Z	0	Ne1150	1.57
28	18	92	1	Fe37Z	0	Ne1150	1.57
29	24	93	1	Fe37Z	0	Ne1300	1.57
30	25	94	1	Fe37Z	0	Ne1300	1.57
31	33	95	1	Fe37Z	0	Nylon	1.57
32	34	96	1	Fe37Z	0	Nylon	1.57
33	5	102	0.8	Fe37	0	Metal	1.57
34	6	107	0.8	Fe37	0	Metal	1.57
35	7	124	0.8	Fe37	90	Metal	1.57
36	51	103	0.8	Fe37	0	Rubber	3.16
37	52	104	0.8	Fe37	0	Rubber	3.16
38	53	108	0.8	Fe37	90	Rubber	3.16
39	42	105	0.8	Fe37	0	Rubber_hole	3.16
40	43	106	0.8	Fe37	0	Rubber_hole	3.16
41	44	117	0.8	Fe37	90	Rubber_hole	3.16
42	12	111	0.8	Fe37	0	Ne1050	1.57
43	13	112	0.8	Fe37	0	Ne1050	1.57
44	14	118	0.8	Fe37	90	Ne1050	1.57
45	19	113	0.8	Fe37	0	Ne1150	1.57
46	20	114	0.8	Fe37	0	Ne1150	1.57
47	21	121	0.8	Fe37	90	Ne1150	1.57
48	26	115	0.8	Fe37	0	Ne1300	1.57
49	27	116	0.8	Fe37	0	Ne1300	1.57
50	28	122	0.8	Fe37	90	Ne1300	1.57
51	35	123	0.8	Fe37	90	Nylon	1.57
52	36	125	0.8	Fe37	0	Nylon	1.57
53	37	126	0.8	Fe37	0	Nylon	1.57

C-3. Statistical analysis of experimental data with metal tools

In Table C- 15 the list of data extracted from a bigger experimental plan performed in collaboration with AMADA Engineering EU has been presented. The original experimental plan is composed by 288 experiments where 5 materials (Young Modulus E, Yield Stress R_s , Peak stress R_m , elongation A% and mean anisotropy r_{ave}), 3 thicknesses (t_0), 3 tools setup (punch radius R_p , die width w and die shoulders radius R_d) and 4 nominal angles (75° , 90° , 120° and 165°) are combined in order to generate a fusion hierarchical metamodel able to predict in reliable way the effective bend angle (Alfa), the bend deduction (BD) and the punch stroke (s) in the sheet metal bending process. From this 288 experiments, 23 have been extracted where similar material, thickness and nominal angle are investigated. These experiments have been used in a regression analysis in order to evaluate a typical standard deviation of a bending process where metal tools are used. In the regression analysis, the thickness (t_0), the Young's Modulus (E), die width (w) and the punch stroke (s) have been considered as predictors. As for the analysis performed in chapter 4, the interactions and the factors until the square order have been also considered the data have been filtered using the Stepwise method implemented in the software with α equal to 0.05 as a removal and entering criterion. The results of the analysis of variance have been reported in Table C- 16.

t_0	E	R_s	R_m	A%	r_{ave}	R_p	w	R_d	s	alfa	BD
[mm]	[Mpa]	[Mpa]	[Mpa]			[mm]	[mm]	[mm]	[mm]	[°]	[mm]
0.8	170242	198	300	0.36	1.3905	0.6	6	1.5	1.541	118.15	1.0969
0.8	170242	198	300	0.36	1.3905	0.6	6	1.5	1.541	118.18	1.095136
0.8	170242	198	300	0.36	1.3905	0.6	8	1.5	2.025	120.22	0.970697
0.8	170242	198	300	0.36	1.3905	0.6	8	1.5	2.025	120.34	1.089683
0.8	170242	198	300	0.36	1.3905	0.8	10	2	2.618	120.08	0.8517
0.8	170242	198	300	0.36	1.3905	0.8	10	2	2.618	119.95	0.8283
0.8	170242	198	300	0.36	1.3905	0.8	10	2	2.618	119.98	0.8023
0.8	178719	188	305	0.4	1.3905	0.6	6	1.5	1.541	117.37	0.851407
0.8	178719	188	305	0.4	1.3905	0.6	6	1.5	1.541	118.10	0.656043
0.8	178719	188	305	0.4	1.3905	0.6	8	1.5	2.025	120.28	0.837174
0.8	178719	188	305	0.4	1.3905	0.6	8	1.5	2.025	120.34	0.800851
0.8	178719	188	305	0.4	1.3905	0.8	10	2	2.618	120.60	0.5564
0.8	178719	188	305	0.4	1.3905	0.8	10	2	2.618	119.73	0.7326
0.8	178719	188	305	0.4	1.3905	0.8	10	2	2.618	120.35	0.6348
1.2	177322	183	298	0.44	1.289	0.8	10	2	2.57	117.58	1.2307
1.2	177322	183	298	0.44	1.289	0.8	10	2	2.57	118.11	1.3345
1.2	177322	183	298	0.44	1.289	0.8	10	2	2.57	117.10	1.1005
1.2	188709	191	297	0.5	1.289	0.8	10	2	2.57	118.09	0.9945
1.2	188709	191	297	0.5	1.289	0.8	10	2	2.57	118.17	0.9903
1.2	188709	191	297	0.5	1.289	0.8	10	2	2.57	118.31	1.0382
2	202729	245	366	0.384	0.656	0.8	10	2	2.504	117.79	1.52
2	202729	245	366	0.384	0.656	0.8	10	2	2.504	117.42	1.6991
2	202729	245	366	0.384	0.656	0.8	10	2	2.504	117.66	1.5882
2	215550	260	370	0.38	0.656	0.8	10	2	2.504	118.20	1.6148
2	215550	260	370	0.38	0.656	0.8	10	2	2.504	118.74	1.9282
2	215550	260	370	0.38	0.656	0.8	10	2	2.504	118.30	1.4556

Table C- 15: data extracted from experimental plan.

Source	DF	Adj SS	Adj Ms	F-Value	P-Value
Regression	6	32.3708	5.3951	63.44	0
t0	1	18.4091	18.4091	216.48	0
E	1	0.4722	0.4722	5.55	0.029
w	1	5.226	5.226	61.46	0
s	1	3.0315	3.0315	35.65	0
t0*t0	1	10.5328	10.5328	123.86	
E*s	1	0.6807	0.6807	8	
Error	19	1.6157	0.085		
Lack-of-Fit	3	0.1637	0.0546	0.6	0.623
Pure Error	16	1.452	0.0907		
Total	25	33.9865			

Table C- 16: analysis of variance coming from the regression analysis.

Only the Young's Modulus has been considered for the material analysis because it perform the main influence on the spingback effect of the specimen; also different values of the Young's Modulus at the same thickness give information on the rolling direction. The die with and the punch stroke are the main tools and process parameters which influence the results of a sheet metal air-bending process because they give information on the three points where the blank lean during the bending operation. The R^2 of the analysis is 93.74% which means that the regression model underestimates the standard deviation of the process.

The normal distribution of the residual has been showed in Figure C- 15 and the sparse distribution of the residual versus the fitted values is showed in Figure C- 16. The standard deviation of 0.301° can be calculated as the square root of the mean square error.

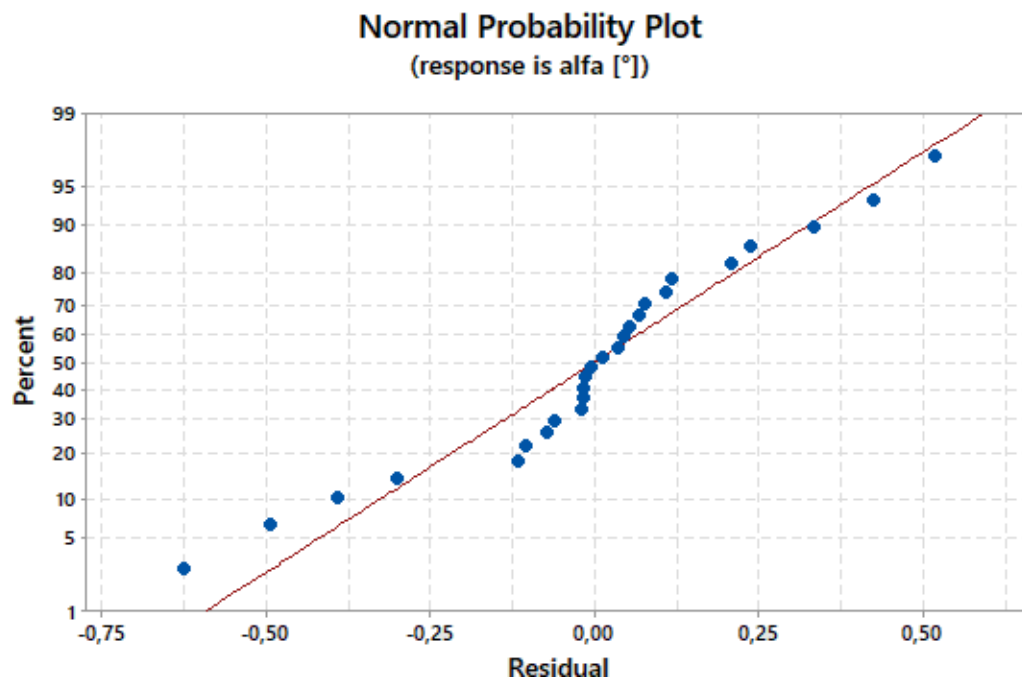


Figure C- 15: normal distribution of the residuals.

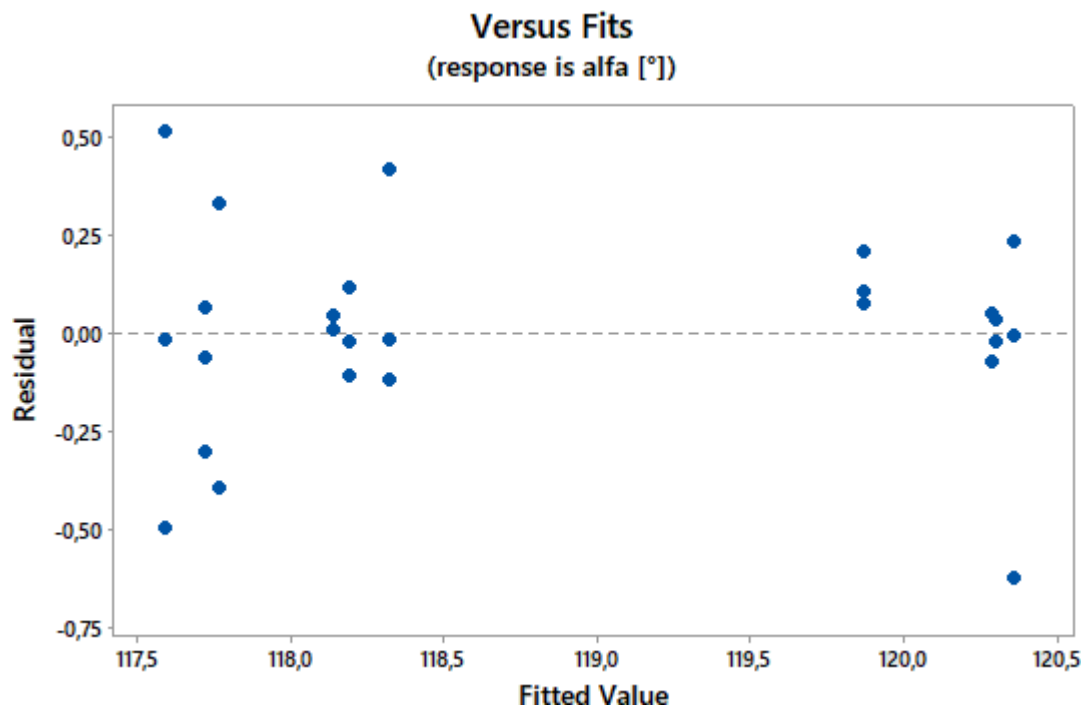


Figure C- 16: distribution of the fitted vales versus residuals.